# NEW CONCEPTS AND ADVANCED STUDIES IN ENGINEERING





# NEW CONCEPTS AND ADVANCED STUDIES IN ENGINEERING

Editor
Asst. Prof. Dr. Umut ÖZKAYA





New Concepts and Advanced Studies in Engineering Editor: Asst. Prof. Dr. Umut ÖZKAYA

Design: All Sciences Academy Design

Published Date: October 2025

**Publisher's Certification Number: 72273** 

**ISBN:** 978-625-5794-60-4

© All Sciences Academy

www.allsciencesacademy.com allsciencesacademy@gmail.com

### **CONTENT**

1. Chapter  Reactive Power Compensation: Fundamentals and Simulation Insights  Adem DÖNMEZ, Uğur ERKARSLAN	8
2. Chapter An Emission Analysis Study of School Buses Adem UĞURLU	31
3. Chapter A Study on Emissions of Refuse Trucks Adem UĞURLU	42
<b>4. Chapter</b> Geochemical Studies of Mangan Bearing Sediments Around Durmuştepe Village (Maden-Elazığ)  Dicle BAL AKKOCA, Pelin BİNGÖL	56
5. Chapter  Basic Applications in Simulink Environment for Raspberry Pi Pico W  Erdem ILTEN	80
6. Chapter Application of High-Entropy Perovskite Oxides in Enegy Fatma MEYDANERİ TEZEL	91
7. <b>Chapter</b> Metamaterials, applications and sustainability Fehim FINDIK	109
8. Chapter Wheel exploration and development Fehim FINDIK	124

10. Chapter	161
Roof Systems in Agricultural Buildings; Literature Review  Israfil KOCAMAN	
ISTAJU KOCAMAN	
11. Chapter	181
Electrical Energy Efficiency, Smart Systems and Artificial Intelligence Metin DEMİRTAS	
12. Chapter	202
Examination of an Off-Grid Solar Energy System for a Rural Residence <i>Muhammed Arslan OMAR</i>	
13. Chapter	216
Geopolymer Concrete For Sustainable Infrastructure: A Chemical Review Ömer LAÇİN, Fatih DEMİR, Fatih SEVİM	W
14. Chapter	230
Geopolymer Concrete for Sustainable Infrastructure: Functional Role of Components and Optimum Design Parameters	
Ömer LAÇİN, Fatih DEMİR, Fatih SEVİM	
15. Chapter	245
Magnetic-depth estimation and geophysical investigations of Timor Islan surrounding area, eastern Indonesia	d and
Sercan KAYIN, M. Nuri DOLMAZ, Ezgi ERBEK-KIRAN	
16. Chapter	259
Stabilization of AVR Systems Using Proportional-Integral-Retarded Controller	
Sevgi Gursul KALAC, Serdar Ethem HAMAMCI	

An Economic Production Quantity Model with Defectives and Backordering

under Non-Synchronized Production and Screening Activities

Harun SULAK, Abdullah EROĞLU

9. Chapter

145

Search for Low-Mass Resonances in Proton-Proton Collisions at $\sqrt{s}$ =137 with the CMS Detector	ГeV
Serdal DAMARSECKIN	
18. Chapter	294
Rationale for Model Development in Accuracy Assessment of Optical Ro Encoders Under Vibration: A Literature Perspective	otary
Violeta KRCHEVA, Stojance NUSEV, Miša TOMIĆ	
19. Chapter	316
Automatic Detection and Classification of Mango Diseases Using Deep Learning Methods	
Halil Talha GÜNDÜZ, Selim SÜRÜCÜ, Esra GÜNEY	
20. Chapter	326
Particle Swarm Optimization-Based Modulation Classification in 5G Communication Systems	
Asuman SAVAŞCIHABEŞ	

17. Chapter

21. Chapter

273

335

Electrochemical Wastewater Treatment and Hydrogen Production

Ziya Mert ÖZGEN, Ümran Tezcan ÜN, Özlem ONAY

# Reactive Power Compensation: Fundamentals and Simulation Insights

Adem DÖNMEZ<sup>1</sup>

Uğur ERKARSLAN<sup>2</sup>

Assoc. Prof. Dr Adem Donmez - Department of Electricity and Energy, Yatagan Vocational School, Mugla Sıtkı Koçman University, Mugla, Turkey. adonmez@mu.edu.tr ORCID No: 0000-0002-9773-0493

Assoc. Prof. Dr Ugur Erkarslan - Department of Physics, Molecular Nano-Materials Laboratory, Mugla Sıtkı Kocman University, Mugla, Turkey. eugur@mu.edu.tr ORCID No: 0000-0001-7667-2151

### ABSTRACT

This chapter introduces the fundamental principles of reactive power compensation in low-voltage electrical networks and demonstrates their technical implications through MATLAB/Simulink simulations. Reactive power, although necessary for sustaining electromagnetic fields, does not perform useful work and leads to increased losses, reduced efficiency, and higher operating costs. Compensation methods are therefore indispensable for improving the power factor, enhancing energy quality, and ensuring more efficient utilization of electrical infrastructure.

Simulation studies compared conventional contactor-switched capacitor banks with modern thyristor-switched systems. The results showed that contactor-based switching generates severe inrush currents, up to 30,000 A when switching occurs near the voltage maximum, causing overheating, shortened equipment life, and decreased system stability. The inclusion of preinsertion resistors reduced this current to approximately 3,500 A but did not fully eliminate the transient risk. In contrast, thyristor-switched systems, triggered precisely at voltage zero-crossings, limited inrush currents to about 500 A, effectively ensuring smooth operation and extending equipment lifespan.

In addition, harmonic distortion was minimized when resonance filters were integrated, further improving voltage stability and system reliability. These findings highlight that while conventional methods offer partial solutions, thyristor-based systems provide superior technical and economic performance.

In conclusion, reactive power compensation remains a fundamental strategy for sustainable and efficient energy management. The simulation results presented here confirm the advantages of modern semiconductor-based approaches, offering valuable insights for both researchers and practitioners.

 $\label{lem:keywords-Reactive power compensation, energy efficiency, power factor, thyristor switching, Simulink analysis$ 

### INTRODUCTION

Global energy demand has been rising rapidly due to population growth, industrialization, and technological development. The increasing need for housing, the expansion of production capacities, and the widespread use of technological devices in daily life have significantly accelerated electricity consumption. Electricity, as one of the most essential energy sources, plays a central role in meeting this demand. However, the limited availability of resources and the environmental impacts of fossil fuels have

made energy efficiency and sustainable energy utilization increasingly critical (Yılkıran and Doğan, 2020).

In this context, minimizing losses in generation, transmission, and distribution has become a necessity. One of the most effective strategies to reduce losses and enhance energy efficiency is reactive power compensation. Reactive power, although required for creating magnetic fields, does not contribute to useful work, thereby causing energy losses, reducing efficiency, and increasing costs. Compensation systems aim to reduce reactive power flow, improve the power factor, and enhance both energy quality and system performance (Arıkan and Ermiş, 1983).

Research worldwide has shown that reactive power compensation is a key approach to improving efficiency and lowering operating costs. Especially in low-voltage facilities, compensation helps balance reactive power, reduces losses, and ensures more stable system operation. Various studies have examined the theoretical background, application methods, and devices used in reactive power compensation, while also evaluating their impacts on system performance from different perspectives. For low-voltage systems, compensation equipment such as capacitors and reactors has been defined, and practical challenges in their application have been reported (Atmaca, 2020).

Moreover, studies comparing fixed and automatic compensation systems emphasize their advantages and disadvantages depending on facility size and load profiles. While fixed systems are commonly used in small-scale facilities, automatic systems are preferred in larger plants with fluctuating loads (Balaman, 2012). Harmonics also play a critical role in low-voltage compensation practices. Capacitors and semiconductor devices can lead to harmonic distortions, which negatively affect power quality. To address this, filtering techniques have been widely proposed and applied in practice, demonstrating their effectiveness in mitigating harmonic effects (Bas, 2014).

Recent research further highlights that the integration of advanced automatic control systems, such as Supervisor Control Theory (SCT), improves compensation efficiency by providing more precise balancing of reactive power and minimizing energy losses (Gelen et al., 2020). In Türkiye, studies in industrial regions, such as İzmir-Aliağa, have revealed that compensation systems not only reduce energy costs but also improve power quality in factories and energy-intensive facilities (Koçamış, 2009).

Within this framework, the present study focuses on low-voltage reactive power compensation systems implemented in facilities of the Credit and Dormitories Institution in Muğla, Türkiye. Both contactor-switched and thyristor-switched compensation systems are analyzed through daily and monthly monitoring. The aim is to evaluate their efficiency in reducing energy consumption, lowering costs, and improving power quality. By developing detailed energy profiles, this study not only compares the performance of these systems but also provides practical insights and recommendations for enhancing energy efficiency in real-world applications.

# ELECTRICAL LOAD MODELING AND POWER COMPONENT ANALYSIS

### Fundamental Electrical Loads

Many modern devices require electrical energy to perform their functions. These devices operate either with direct current (DC) or alternating current (AC) and are generally referred to as electrical loads. Loads can be classified into three basic types: resistive, inductive, and capacitive (Figure 1). Resistive loads are denoted by R and measured in ohms ( $\Omega$ ). Inductive loads are represented by L with the unit of Henry (H), while capacitive loads are expressed by C and measured in farads (F).

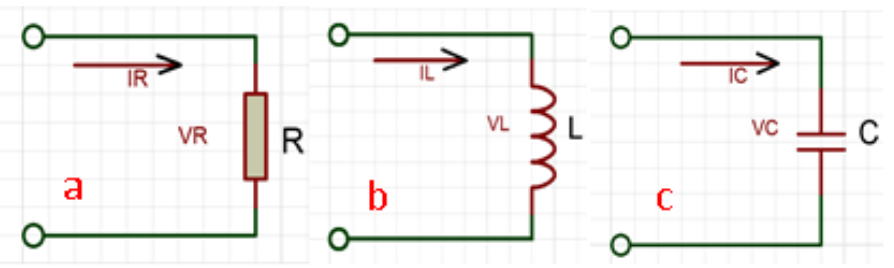


Figure 1. a) Resistive load circuit, b) Inductive load circuit, c) Capacitive load circuit

In practice, electrical circuits rarely contain purely resistive, inductive, or capacitive elements. Instead, most circuits include a combination of these components, forming RLC circuits. For example, an inductor possesses not only inductive characteristics but also a small resistance, and transmission lines exhibit both capacitance and resistance. In an ideal AC network, voltage and frequency should remain constant, harmonics should be absent, the power factor should be close to unity, and phases should be balanced to ensure a stable energy supply.

An inductor, formed by winding a conductor into a coil, generates magnetic flux proportional to the current flowing through it. This relationship is defined by the self-inductance coefficient L. The voltage-current relation is expressed as

$$V_{L}(t) = L. \frac{dI_{L}(t)}{dt}$$
 (1)

and the opposition of an inductor to alternating current is called inductive reactance, defined as

$$X_L = j\omega L \quad (\omega = 2\pi f)$$
 (2)

Consequently, in an inductive circuit the current lags the voltage by  $90^{\circ}$  (Figure 2).

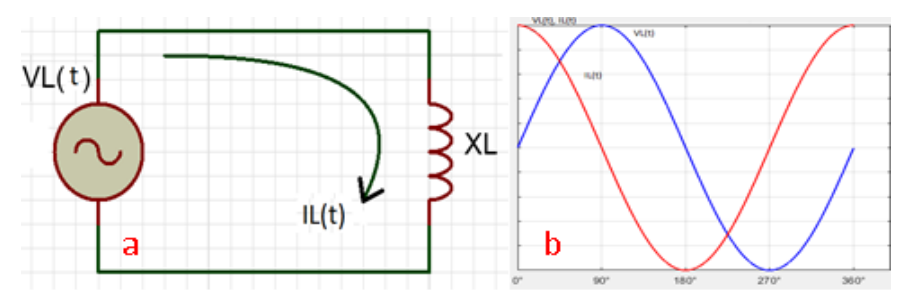


Figure 2. Inductive load circuit and current-voltage relation

A capacitor, on the other hand, consists of two conductive plates separated by a dielectric material. Its capacitance is calculated as

$$C = 0.0885 \frac{\epsilon \cdot A \cdot 10^{-12}}{d}$$
 (3)

where A is the plate area, d is the separation distance, and  $\varepsilon$  is the dielectric constant. Capacitors store electric charge, block direct current, and provide reactive power in AC circuits. Their opposition to alternating current is called capacitive reactance, given by  $X_{C} = \frac{V_{C}(t)}{I_{C}(t)} = \frac{V_{m} \cdot \sin(\omega.t)}{j.\omega.C.V_{m} \sin(\omega.t)} = \frac{1}{j.\omega.C}$ 

$$X_{C} = \frac{V_{C}(t)}{I_{C}(t)} = \frac{V_{m} \cdot \sin(\omega \cdot t)}{j.\omega.C.V_{m}\sin(\omega \cdot t)} = \frac{1}{j.\omega.C}$$
(4)

In this case, the current leads the voltage by 90° (Figure 3).

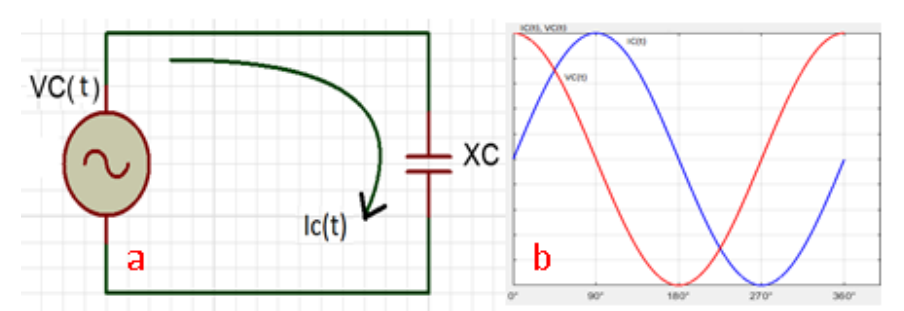


Figure 3. Capacitive load circuit and current-voltage relation

The most important common feature of inductors and capacitors is that their reactance varies with frequency. According to the relation, the reactance of an inductor increases with frequency, while the reactance of a capacitor decreases as frequency rises. Thus, in inductive elements the current lags the voltage by 90°, whereas in capacitive elements it leads by 90°. As shown in Figure 4, the two currents are 180° out of phase with each other, meaning that inductive and capacitive effects can counterbalance one another under appropriate conditions.

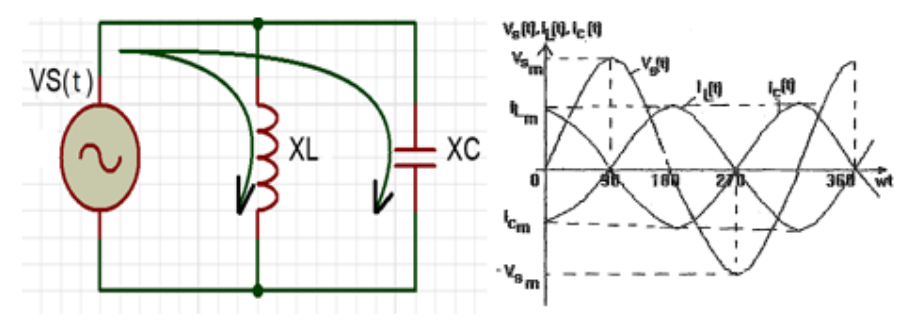


Figure 4. Comparison of inductive and capacitive loads

### Active Power, Reactive Power and Power Factor

In AC systems, the total current drawn can be decomposed into active and reactive components. Active current produces useful work (mechanical, thermal, or luminous), while reactive current sustains magnetic fields necessary for operation of devices such as generators, motors, and transformers.

The main power components are:

Active Power (P):

$$P = U.I.\cos \varphi \tag{5}$$

Measured in watts (W), it represents useful energy conversion.

Reactive Power (Q):

$$Q = U .I. \sin \varphi$$
 (6)

Measured in reactive volt-ampere (VAr), it does not perform useful work but is essential for magnetization.

Apparent Power (S):

$$S = \sqrt{P^2 + Q^2} = U.I \tag{7}$$

The power factor ( $\cos \phi$ ) expresses the efficiency of energy use. In inductive systems, current lags voltage, while in capacitive systems current leads voltage (Figure 5).

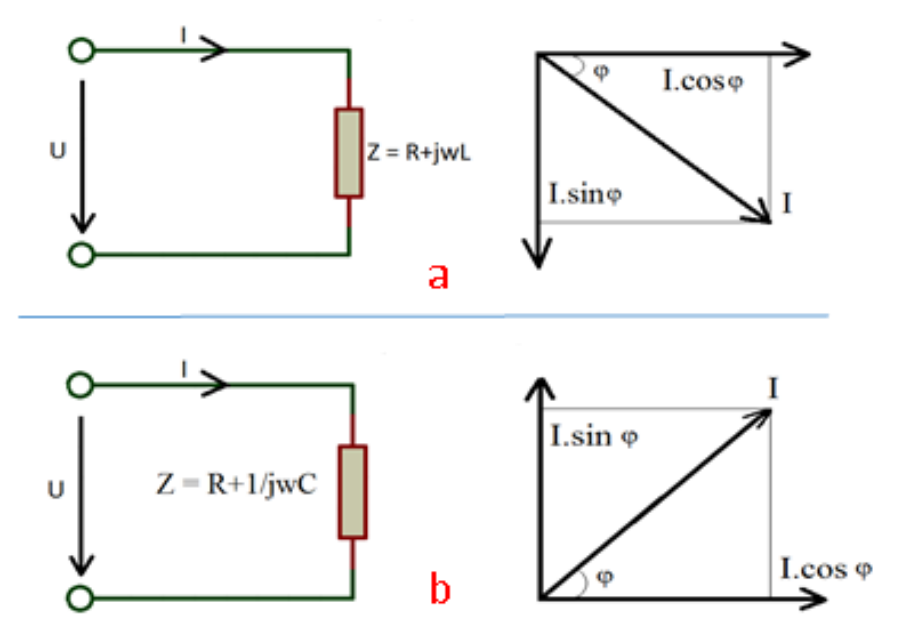


Figure 5. a) Inductive load and phasor diagram, b) Capacitive load and phasor diagram

The relationships between power components and currents are summarized as:

$$I_p = I \cdot \cos \varphi \text{ and } I_q = I \cdot \sin \varphi$$
 (8)

$$I_p = I \cdot \cos \varphi \text{ and } I_q = I \cdot \sin \varphi$$
 (8)  
 $I = \sqrt{I_p^2 + I_q^2}$  (9)

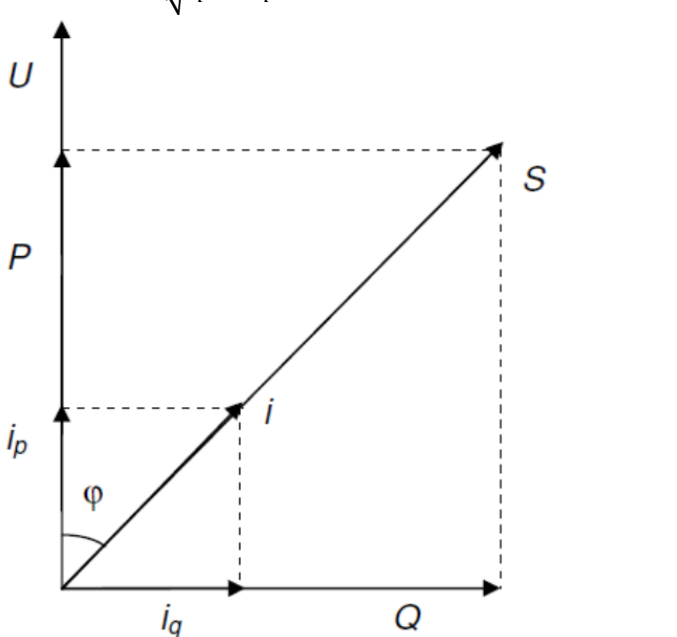


Figure 6. Active, reactive, and apparent power representation

### Loads Consuming Reactive Power

In electrical installations, devices operating with magnetic or static fields require not only active power but also reactive power. Fluorescent lamps, sodium and mercury vapor lamp ballasts, neon lamp transformers, switched-mode power supplies (SMPS), rectifiers, induction furnaces, arc furnaces, welding machines, low-excitation synchronous machines, asynchronous motors, transformers, coils, and overhead transmission lines are among the major consumers of reactive power (Kıyan, 2010). Table 1 presents typical power factor values of various electrical loads.

Table 1. Power Factor Values of Electrical Loads

Load Type	Power Factor (cos φ)
Industrial Loads	
Asynchronous motors (high efficiency)	0.85 - 0.95
Asynchronous motors (standard)	0.75 - 0.85
Belt-driven compressors	0.70 - 0.90
Fans	0.60 - 0.85
Welding machines	0.50 - 0.70
Furnaces	0.70 - 0.90
Pump motors	0.70 - 0.90
Lighting Loads	
Fluorescent lamps (without proper compensation)	0.50 - 0.70
Fluorescent lamps (with compensation)	0.90 - 0.95
LED lighting	0.90 - 0.98
Mercury vapor lamps	0.40 - 0.60
Halogen lamps	0.95 - 1.00
Household Loads	
Refrigerators	0.70 - 0.90
Air conditioners	0.85 - 0.95
Washing machines	0.70 - 0.90
Televisions (CRT)	0.60 - 0.75
Televisions (Flat-screen)	0.90 - 0.95
Computers	0.60 - 0.80
Office and Commercial Loads	
Computers	0.60 - 0.80
Photocopy machines	0.70 - 0.90
Elevators	0.60 - 0.80
UPS systems	0.60 - 0.80

### Benefits of Reactive Power Compensation

Reactive power compensation, which involves reducing the reactive power component (Q), prevents transmission lines from being unnecessarily loaded with non-productive power. Since reactive power flows

bidirectionally—towards the load during one half of the cycle and back to the source during the other—it occupies a part of line capacity and increases investment costs by requiring larger conductor cross-sections. Moreover, reactive power also flows through transformers and generators, thereby imposing additional stress and losses on these components.

For the power grid, compensation provides crucial technical advantages. By reducing the apparent power drawn from the system, it allows more active power to be delivered without exceeding system capacity. The apparent power before and after compensation can be expressed as:

$$S_1 = \sqrt{P_1^2 + Q_1^2} \tag{10}$$

$$S_2 = \sqrt{P_2^2 + Q_2^2} \tag{11}$$

$$\Delta S = S_1 - S_2 \tag{12}$$

$$\%\Delta S = \frac{\Delta S}{S_1} .100 \tag{13}$$

By lowering the reactive component, the total current drawn from the network is reduced, which directly decreases transmission losses. The power losses before and after compensation are calculated as:

$$P_{Z1} = \frac{R.P^2}{U^2 \cdot \cos \varphi_1^2} \tag{14}$$

$$P_{Z2} = \frac{R.P^2}{U^2.\cos\varphi_2^2} \tag{15}$$

$$Z = \frac{P_{Z_1} - P_{Z_2}}{P_{Z_1}} .100 = \left(\frac{\cos \varphi^2}{\cos \varphi^2} - 1\right) .100$$
 (16)

In addition, voltage drops across the grid are reduced since the current is lowered. The longitudinal voltage drop can be expressed as (Figure 7):

$$\Delta U = R.I.\cos\varphi + X.I.\sin\varphi \tag{17}$$

These improvements result in better voltage stability, mitigation of flicker, reduction of phase imbalances, and lower harmonic distortion when proper filtering devices are integrated. Ultimately, reactive power compensation enhances grid reliability, facilitates the integration of renewable sources such as wind and solar, and extends the operational lifetime of components by preventing unnecessary overloading.

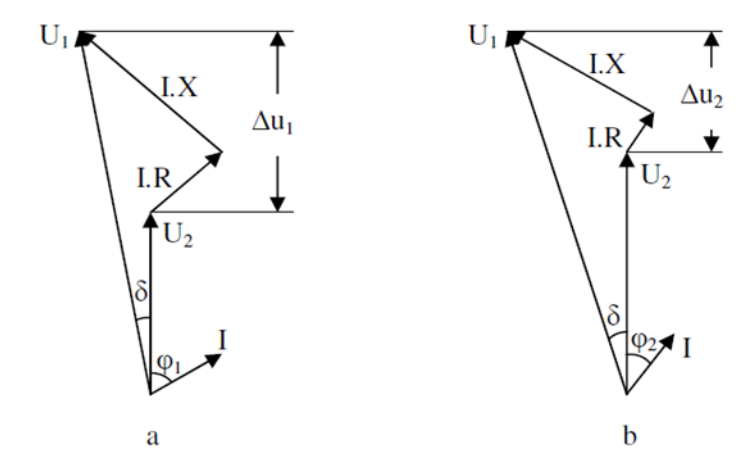


Figure 7. Effect of power factor on voltage drop

For consumers, the advantages are equally important. By optimizing the power factor, the amount of reactive energy drawn from the supply is minimized, leading to reduced energy bills and avoidance of penalty tariffs. Compensation systems also lower investment costs by improving the efficiency of existing electrical infrastructure, thereby delaying or eliminating the need for costly upgrades. More stable supply voltage decreases risks of production losses, improves operational continuity, and reduces downtime in industrial facilities.

Operating with a low power factor produces negative economic and technical impacts. Electricity bills increase due to penalty tariffs, while higher current levels lead to increased transmission and distribution losses. To handle these excessive currents, larger transformers, generators, conductors, and switching devices must be installed, resulting in higher investment and maintenance costs. Capacity utilization in power generation and transmission systems decreases, and voltage regulation becomes more difficult, causing fluctuations and instability. These effects not only reduce efficiency but also raise the overall operational costs of electrical systems.

### Reactive Power Generation and Compensation

To meet the demand for reactive power, it must be generated somewhere in the system. Power plants generate reactive power by increasing the excitation current of synchronous generators. The reactive power produced at the plant is then transferred to consumers through generators, transformers, and transmission lines. However, this process causes the facilities to be unnecessarily loaded with reactive power, reducing their capacity to transmit active power and negatively affecting their economic efficiency (Bayram, 2000).

Therefore, to prevent facilities from suffering from reactive power problems, to make full use of equipment capacity, and to ensure economic

efficiency, it is more advantageous to generate reactive power at consumption centers rather than at power plants (Önal, 1996). Two main methods are used for reactive power generation: dynamic phase shifters and static phase shifters.

Dynamic phase shifters are over-excited synchronous machines usually installed at the end of transmission lines or at the beginning of consumption centers to supply reactive power to the region. Compared to capacitors, they have higher losses, higher installation and maintenance costs, and slower response times to reactive power changes. Moreover, phase-by-phase control is not possible. Figure 8 illustrates the phasor diagram of a synchronous motor operating under no-load conditions with over-excitation. In this case, the current of the synchronous motor leads the voltage by 90°, providing capacitive reactive current (Is) to the grid, while the load current (Iy) lags behind the voltage by angle  $\varphi y$ .

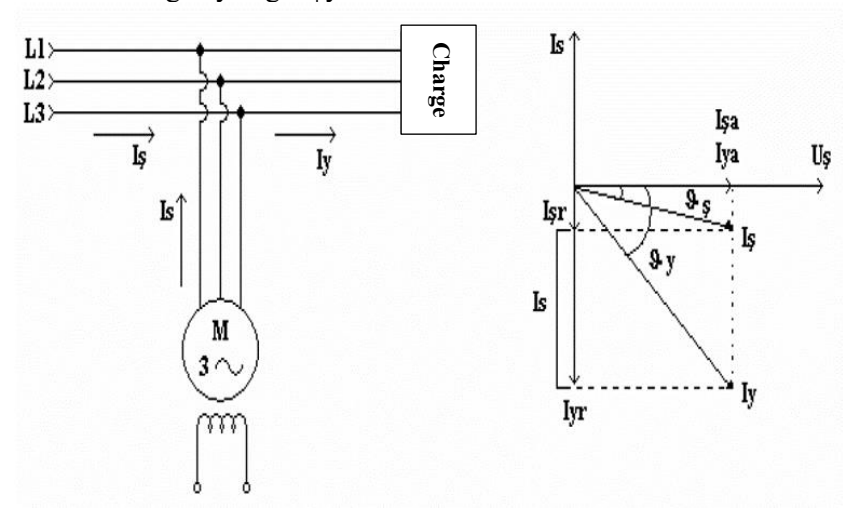


Figure 8. Correction of power factor with an over-excited synchronous motor

When the synchronous motor is not connected, the current drawn from the grid  $(I_S)$  equals the load current  $(I_V)$ . When the motor is connected, the reactive current drawn from the grid (Isr) decreases by the amount of reactive current supplied by the motor (Is). This reduces the phase angle  $\varphi s$  between the supply current and voltage, thereby improving the power factor. For example, consider a 300 kVA load connected to a 6000 V supply with a power factor of 0.7. The required synchronous motor capacity to improve the power factor to unity is calculated as follows:  $I_y = \frac{s}{\sqrt{3.0}} = \frac{300000}{\sqrt{3.6000}} = 28.86 A$ 

$$I_{y} = \frac{s}{\sqrt{3}.U_{\S}} = \frac{300000}{\sqrt{3}.6000} = 28.86 A$$
 (18)

$$I_{yr} = I_y \sin \varphi = 28.84 \, x \, 0.714 = 20.59 \, A$$
 (19)

$$S_S = \sqrt{3}x \ U_S \ x \ I_{yr} = \sqrt{3}x \ 6000 \ x \ 20.59 \approx 214 \ kVA$$
 (20)

Static phase shifters, on the other hand, are devices without moving parts, and capacitors are the most common example. They offer several advantages over synchronous machines: their losses are typically less than 1% of their rated power, they can be used at any required power level, and their compact size allows installation close to the load. By placing capacitors near the load, cable overheating is prevented, line losses are reduced, and voltage drops are minimized. Capacitors also have lower cost per kVAr compared to medium-sized synchronous machines, are easy to install and expand, and have high reliability with minimal maintenance requirements (Memis, 2007).

For loads with continuously varying reactive demand, capacitors are switched in and out using control devices. In practice, either contactors or thyristors are employed. Contactors are mechanical switches with limited operating life, while thyristors, being semiconductor devices, allow virtually unlimited switching operations.

### **Conventional Compensation Systems**

Compensation systems using electromechanical switching devices such as contactors are known as conventional systems. During switching, capacitors connected through standard contactors draw an inrush current from the grid, which may reach very high levels (Memis, 2007). While contactors can typically perform between 2000 and 5000 operations, thyristor-based systems theoretically allow unlimited switching. In this study, both mechanical and thyristor switching operations were analyzed using MATLAB/Simulink to evaluate their effects and to develop strategies for minimizing inrush currents. Related simulation analyses are presented in next chapter.

### Calculation of Capacitor Power in Reactive Compensation

When determining the required capacitor power for compensation, two approaches may be adopted:

- a) Keeping the active power (P) constant, or
- b) Keeping the apparent power (S) constant.

### a) Case 1: Constant Active Power (P = constant)

Let the initial power factor be  $\cos \varphi 1$  with apparent power S1. If the power factor is improved to cos φ2, the apparent power decreases to S2 (Figure 9).

$$Q_1 = S_1 \cdot \sin \varphi_1 \tag{21}$$

$$Q_2 = S_2 \cdot \sin \varphi_2 \tag{22}$$

$$Q_{c} = Q_{1} - Q_{2} = S_{1} \sin \varphi_{1} - S_{2} \sin \varphi_{2}$$

$$Q_{c} = P. (\tan \varphi_{1} - \tan \varphi_{2})$$
(23)
(24)

$$Q_c = P. (\tan \varphi_1 - \tan \varphi_2) \tag{24}$$

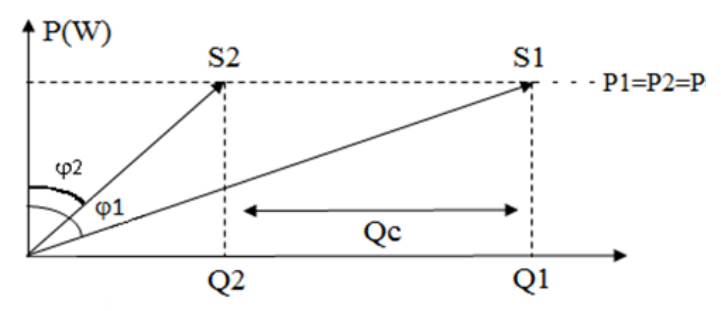


Figure 9. Phasor diagram for compensation with constant active power

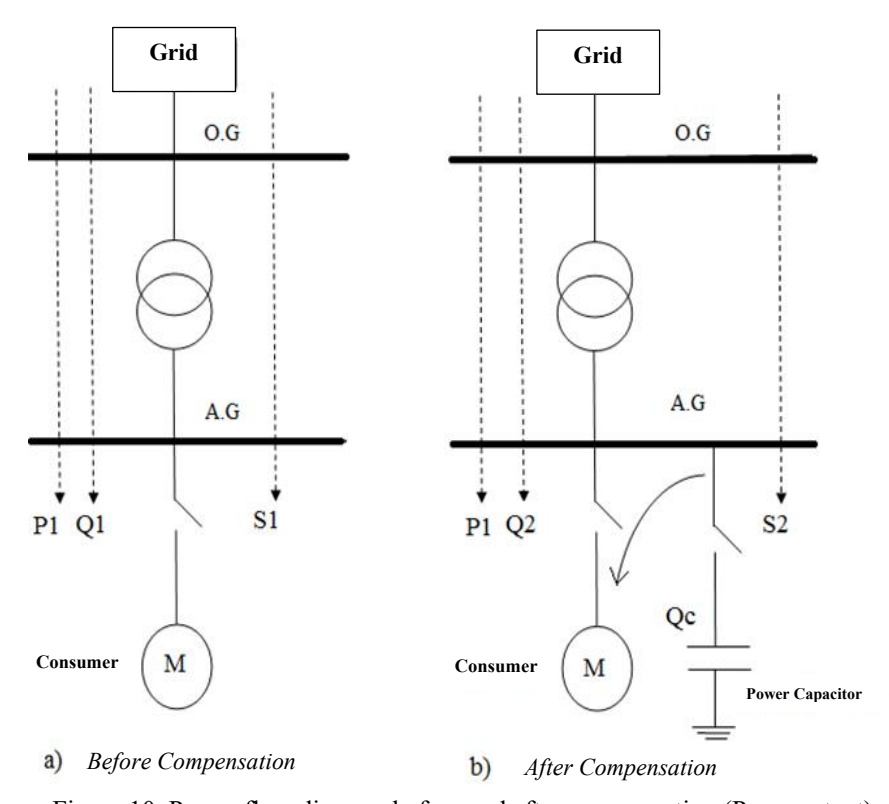


Figure 10. Power flow diagram before and after compensation (P = constant)

### Case 2: Constant Apparent Power (S = constant)

If the apparent power S is kept constant, improving the power factor from cos φ1 to cos φ2 will result in an increase in active power from P1 to P2 (Figure 2.11).

$$Q_1 = S.\sin\varphi_1\tag{25}$$

$$Q_2 = S.\sin\varphi_2 \tag{26}$$

$$Q_c = Q_1 - Q_2 = S. (\sin \varphi_1 - \sin \varphi_2)$$
 (27)

$$Q_{2} = S. \sin \varphi_{2}$$

$$Q_{c} = Q_{1} - Q_{2} = S. (\sin \varphi_{1} - \sin \varphi_{2})$$

$$Q_{c} = P_{1} \tan \varphi_{1} - P_{2} \tan \varphi_{2}$$
(26)
(27)
(28)

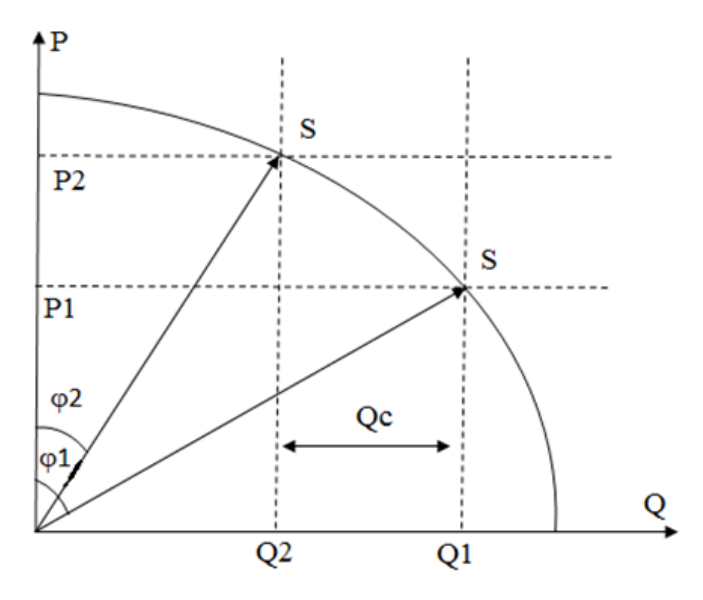


Figure 11. Phasor diagram for compensation with constant apparent power

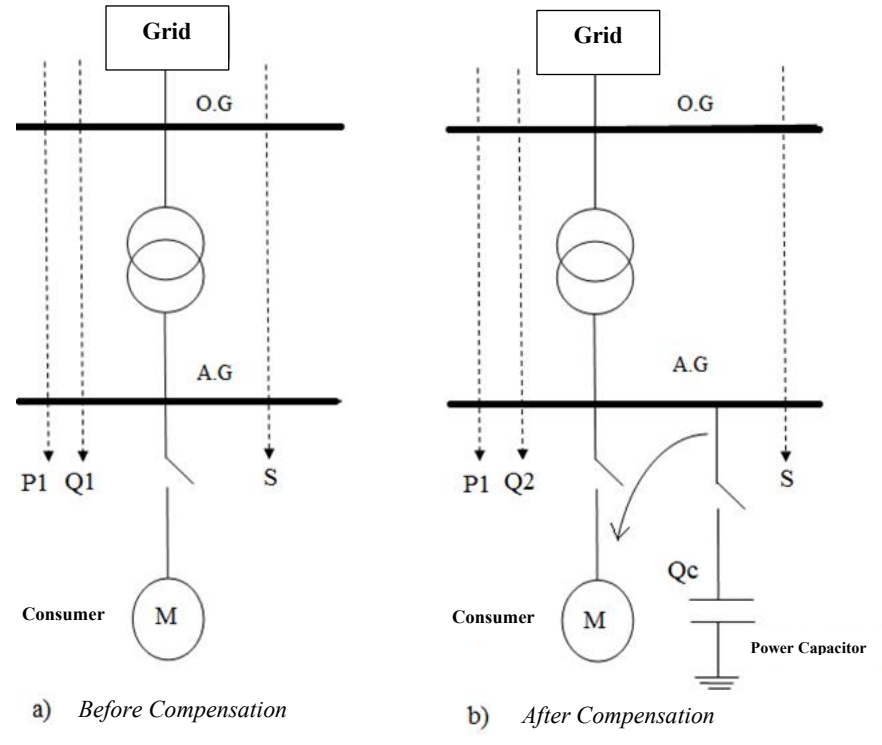


Figure 12. Power flow diagram before and after compensation (S = constant)

# ANALYSIS OF MECHANICAL (CONTACTOR) AND THYRISTOR SWITCHING STRUCTURES USING SIMULINK

In this section, a comprehensive analysis was conducted using the Simulink program to investigate and minimize the effects arising during mechanical (contactor) and thyristor switching operations. The study examined the dynamic behavior of switching structures under two conditions: when switching occurs near the zero-crossing point of the supply voltage and when it occurs at the voltage maximum. Parameters such as power factor, source voltage, source current, capacitor voltage, and capacitor current were analyzed in detail.

### Mechanical (Contactor) Switching

Figure 13 shows the simulation model of a capacitor switched through a standard contactor. Two cases were studied: switching at t = 21 ms (close to the zero-crossing of the 50 Hz supply voltage, T = 20 ms), and switching at t = 26 ms (near the maximum voltage).

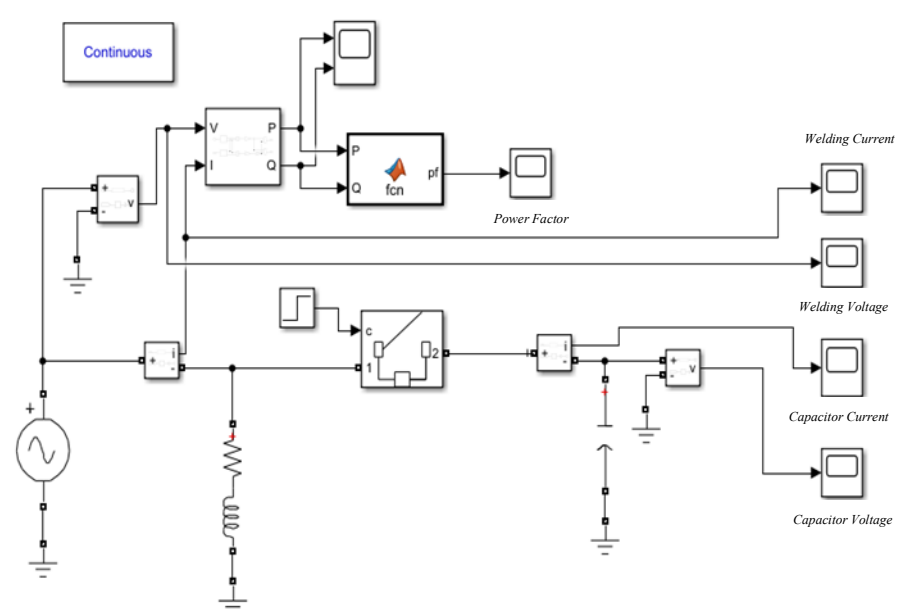


Figure 13. The simulation model of a capacitor switched through a standard contactor

As seen Figure 14, the moment the contactor is engaged, an inrush current peak of approximately 10,000 A occurs simultaneously in both the source and the capacitor current. The source voltage reaches its maximum of  $\sqrt{2.220} \text{ V} = 311 \text{ V}$  while the capacitor voltage rises from zero at the triggering instant to the same peak value.

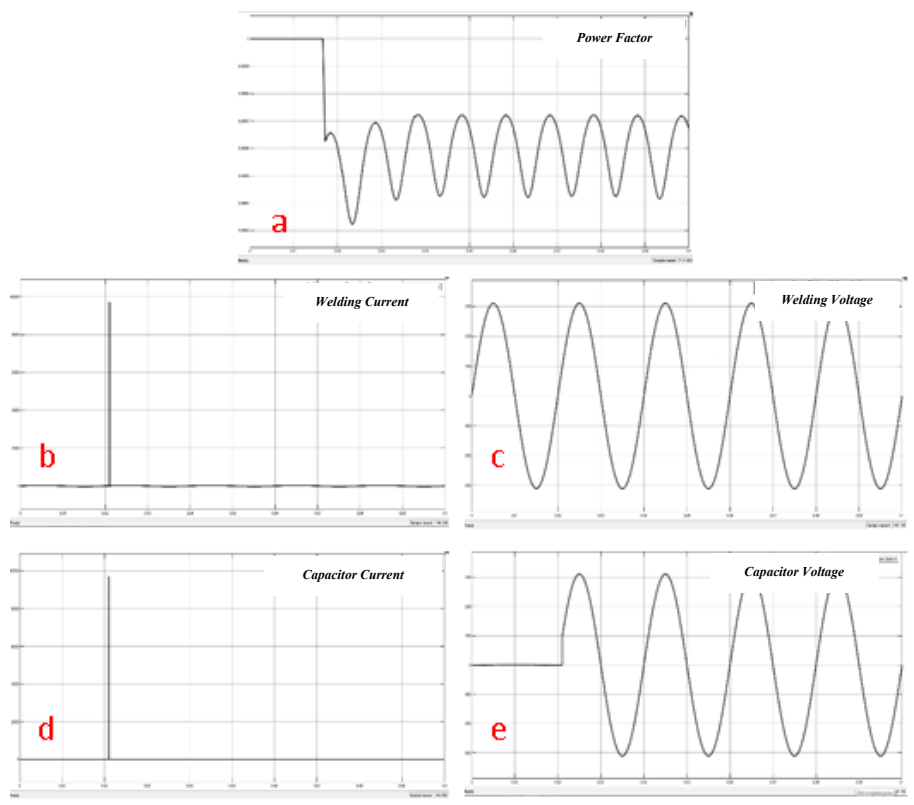


Figure 14. The current and voltage waveforms when switching occurs at t = 21 ms.

Figure 15. illustrates the case of switching at t = 26 ms (voltage maximum). Here, the source and capacitor currents reach about 30,000 A, nearly three times higher than in the zero-crossing case. This demonstrates that switching near the voltage maximum significantly amplifies the inrush current.

To mitigate this excessive current, a compensation contactor circuit including a pre-insertion resistor was implemented, as shown in Figure 16. In this configuration, the resistor is temporarily inserted into the circuit at the first switching instant and later bypassed by a secondary switch.

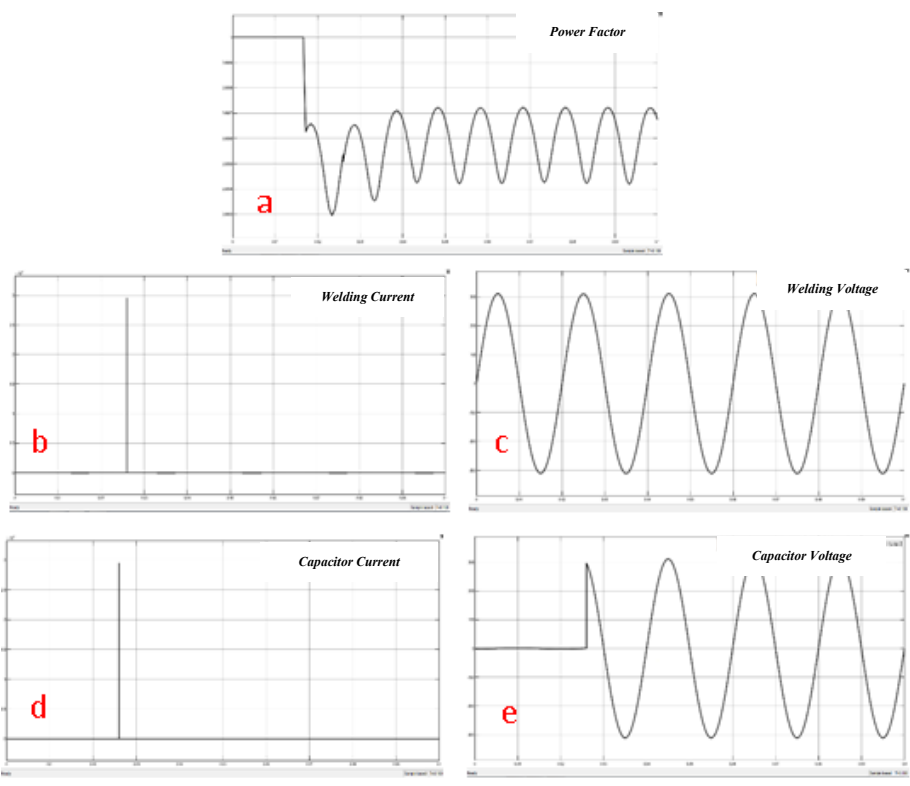


Figure 15. The current and voltage waveforms when switching occurs at t = 26 ms (voltage maximum).

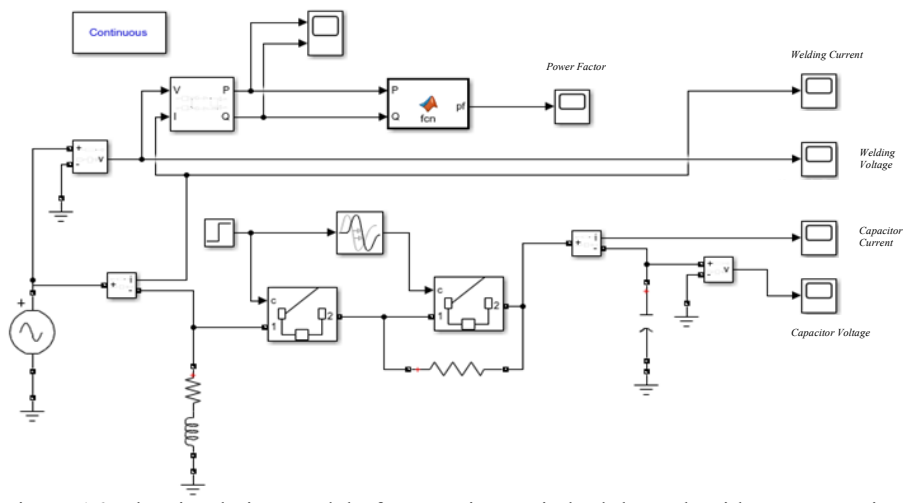


Figure 16. The simulation model of a capacitor switched through with compensation contactor

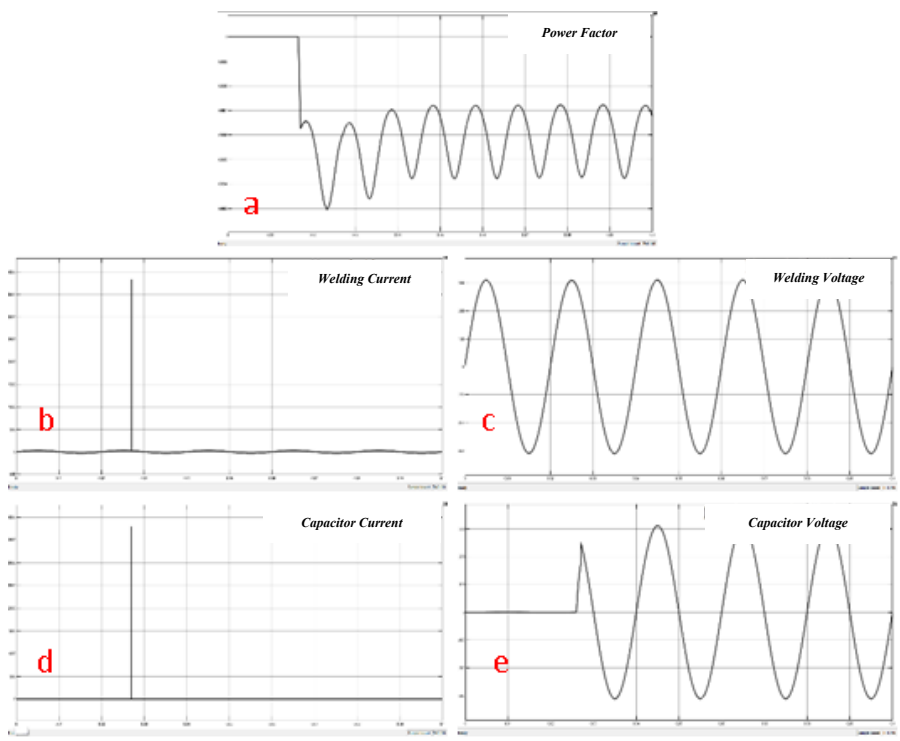


Figure 17. The current and voltage waveforms when switching occurs at t = 26 ms (voltage maximum) with compensation contactor

Figure 17 shows the improved waveforms under these conditions. The inrush current is reduced by nearly nine times, to about 3500 A, compared to the uncompensated case. Thus, the pre-insertion resistor effectively suppresses the transient current peaks while maintaining normal capacitor voltage rise to 311 V.

### Thyristor Switching

In all previously examined contactor-based circuits, high inrush currents were observed. In contrast, thyristor-switched capacitor circuits avoid this problem because thyristors can be triggered precisely at voltage zero-crossings.

Figure 18 presents the Simulink model of a thyristor-switched capacitor bank. Thanks to their controllable firing angles, thyristors can be synchronized with the zero-crossing of the supply voltage, thereby preventing inrush current.

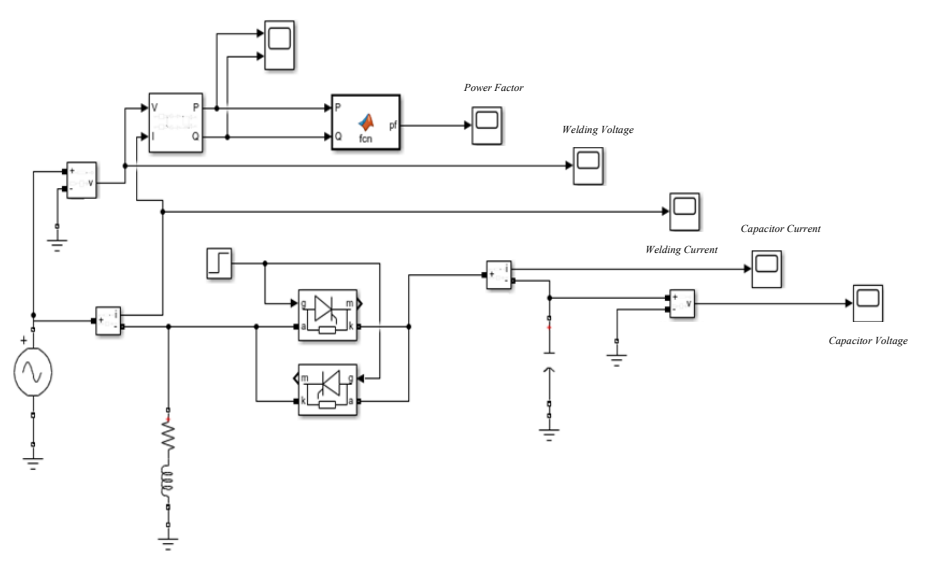


Figure 18. The Simulink model of a thyristor-switched capacitor bank

Figure 19 illustrates the resulting waveforms. The source and capacitor currents rise only to about 500 A, which is significantly lower than the contactor-based cases. This corresponds to approximately 1/20 of the inrush current observed with standard contactor switching at t = 21 ms, 1/60 at t = 26 ms, and about 1/8 of the value obtained with a compensation contactor.

These results demonstrate that while contactor switching inevitably introduces high transient currents, the use of pre-insertion resistors can mitigate their severity. However, thyristor-based switching offers the most effective solution, essentially eliminating dangerous inrush currents and ensuring smoother capacitor engagement.

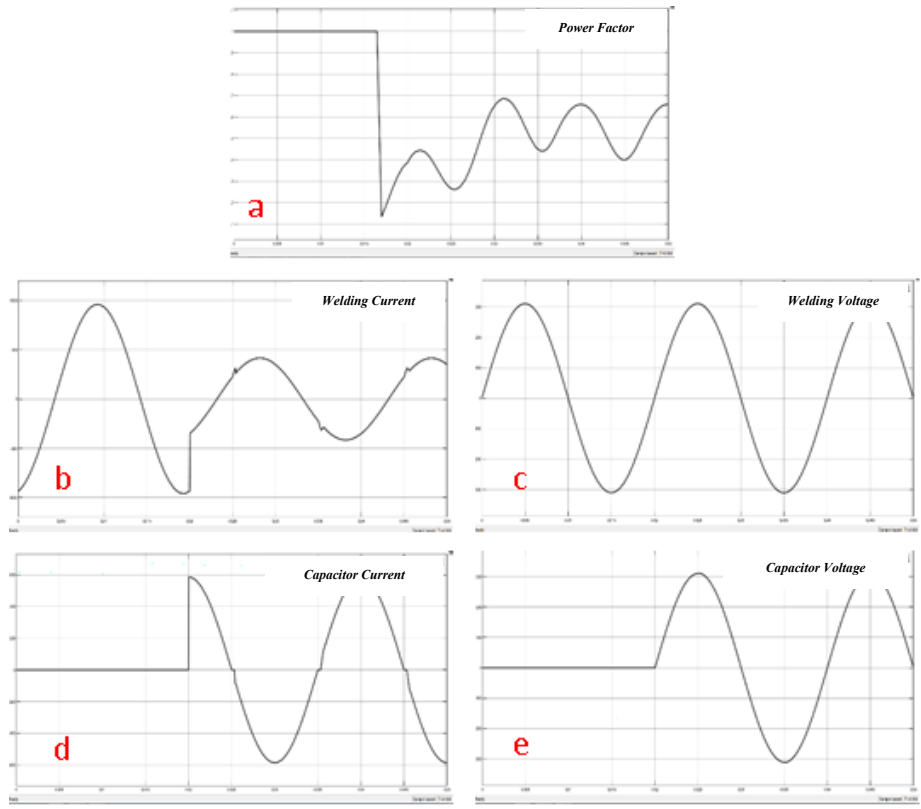


Figure 19. Current and voltage waveforms of the thyristor-switched capacitor circuit

### **DISCUSSION AND CONCLUSIONS**

This study has comprehensively analyzed the contribution of low-voltage reactive power compensation systems to energy efficiency, as well as their effects on energy consumption and operating costs, supported by both simulations and field data. The findings provide a solid foundation for evaluating the technical and economic performance of different compensation strategies.

Simulation results highlighted a critical drawback of conventional contactor-switched capacitor circuits: when switching occurs at the voltage maximum, extremely high inrush currents are generated. In some cases, such as in contactor-based systems, transient peaks reached as high as 30,000 A. These excessive current surges lead to overheating, shortened equipment lifespan, and overall reduction in system efficiency.

To overcome this challenge, thyristor-switched compensation systems were proposed and tested. By performing switching precisely at voltage zero-crossings, thyristors eliminated inrush currents, limiting them to about 500 A—approximately 1/60 of the peak value observed in contactor-based

circuits. This dramatic reduction demonstrates the effectiveness of thyristorbased solutions for enhancing system stability and extending equipment longevity, thereby ensuring economic sustainability in the long term.

In conclusion, the results of this thesis clearly demonstrate that reactive power compensation systems are indispensable for improving energy efficiency, ensuring system stability, and reducing energy costs. Beyond their immediate technical and economic benefits, these systems play a key role in advancing sustainable energy policies. The insights gained here may guide future research on the design, application, and optimization of compensation systems in modern power networks.

### REFERENCES

- Arıkan, C., & Ermiş, M. (1983). Modern methods in reactive power compensation (in Turkish). *Elektrik Mühendisliği*, 294/295, 2–3.
- Arifoğlu, U. (2002). *Computer-aided analysis of power systems* (in Turkish). Istanbul: Alfa Publications.
- Atmaca, H. (2020). *Reactive power compensation in low-voltage facilities* (Master's thesis, in Turkish). Kırklareli University, Kırklareli.
- Balaman, O. (2012). *Reactive power compensation* (Master's thesis, in Turkish). Dokuz Eylül University, İzmir.
- Baş, Z. (2014). Reactive power compensation and harmonic analysis in power systems (Master's thesis, in Turkish). Sakarya University, Sakarya.
- Bayram, M. (2000). *Reactive power compensation in high-voltage facilities* (in Turkish). Istanbul: Birsen Publishing.
- Bilki, F. (2008). *Reactive power and compensation techniques* (Master's thesis, in Turkish). Gazi University, Ankara.
- Ersamut, R. (2009). *Examination and comparison of static var compensation systems* (Master's thesis, in Turkish). Yıldız Technical University, Istanbul.
- Gelen, A., Gelen, G., & Bıçak, A. (2020). Supervisory controller design for reactive power compensation. *European Journal of Science and Technology*, 146–154.
- Kıyan, M. (2010). *Implementation of low-voltage reactive power compensation with thyristor-controlled reactors* (Master's thesis, in Turkish). Hacettepe University, Ankara.
- Kocamış, A. E. (2009). *Reactive power compensation in distribution system* (Master's thesis, in Turkish). Dokuz Eylül University, İzmir.
- Kocatape, C., Uzunoğlu, M., Yumurtacı, R., Karakaş, A., & Arıkan, O. (2003). *Harmonics in electrical installations* (in Turkish). Istanbul: Birsen Publishing.
- Memiş, R. (2007). Application of static var systems in industrial environments (Master's thesis, in Turkish). Sakarya University, Sakarya.
- Önal, H. (1996). Capacitors 1 (in Turkish). 3e Publishing.
- Sevim, Ü. (1999). *Control of reactive power using microprocessors* (Master's thesis, in Turkish). Marmara University, Istanbul.
- Şerbetçi, M. B. (2019). Design and analysis of harmonic filter-based compensation systems in facilities with harmonic problems (Master's thesis, in Turkish). Yıldız Technical University, Istanbul.

- Vardar, T., Çam, E., & Yalçın, E. (2010). Energy efficiency through reactive power compensation and applications in public institutions. *International Journal of Engineering Research and Development*, 2, 20–24.
- Yılkıran, N., & Doğan, H. (2020). Turkey's energy outlook and 2023 primary energy supply projection. *Batman University Journal of Life Sciences*, 10, 77–92.

# **An Emission Analysis Study of School Buses**

## Adem UĞURLU<sup>1</sup>

<sup>1-</sup> Assoc. Prof. Dr.; Kırklareli Üniversitesi Teknoloji Fakültesi Mekatronik Mühendisliği Bölümü. adem.ugurlu@klu.edu.tr, ORCID No: 0000-0002-9531-3944

### **ABSTRACT**

The environmental performance of school buses has emerged as a critical topic within the ongoing discourse on sustainable transportation and public mobility. These vehicles, which are integral to daily student commutes, typically operate in challenging conditions, including high passenger loads, frequent stop-and-go cycles, and extended periods of idling. Traditionally powered by diesel engines, school buses contribute significantly to greenhouse gas (GHG) emissions and local air pollution. To comprehensively evaluate the environmental impact of various propulsion technologies and fuel alternatives, a detailed Well-to-Wheel (WTW) analysis is necessary. This approach considers both upstream emissions (fuel production and distribution) and downstream emissions (vehicle operation), providing a comprehensive assessment of the total environmental footprint. This study undertakes a comparative WTW evaluation of various school bus configurations, including biodiesel blends (e.g., 20% biodiesel and 80% diesel), compressed natural gas (CNG), dimethyl ether (DME), fuel cell vehicles (FCV) utilizing compressed gaseous hydrogen, liquefied petroleum gas (LPG), low sulfur diesel (LSD), and renewable diesel II (RD2). The findings aim to support evidence-based decision-making for the transition to cleaner, more sustainable school bus fleets.

Keywords – School bus; emissions; WTW analysis.

### INTRODUCTION

School buses are specialized vehicles designed to safely transport students between their homes and educational institutions. Serving both urban and rural areas, these vehicles play a critical role in ensuring access to education while supporting the broader goals of public transportation and community mobility. As essential components of the educational infrastructure, school buses contribute to reducing traffic congestion and promoting transportation equity. However, despite their societal benefits, school buses also carry notable environmental burdens, particularly due to their frequent operation within densely populated areas and the cumulative impact of their emissions over time. Conventional school buses, particularly those powered by diesel engines, are substantial contributors to local air pollution. Diesel combustion produces harmful pollutants such as nitrogen oxides (NO<sub>x</sub>), particulate matter (PM), carbon monoxide (CO), and carbon dioxide (CO<sub>2</sub>), which are linked to adverse health effects and environmental degradation. Given their regular operation schedules and extended idling during student pick-up and drop-off, school buses consume considerable amounts of fuel, leading to elevated greenhouse gas (GHG) emissions. In response, many school districts and municipalities are exploring cleaner alternatives, including compressed natural gas (CNG), hybrid-electric systems, battery-electric school buses, and other low-emission technologies aimed at reducing the environmental footprint of school transportation services.

Air pollutants such as volatile organic compounds (VOCs), carbon monoxide (CO), nitrogen oxides (NO<sub>x</sub>), particulate matter (PM<sub>10</sub> and PM<sub>2.5</sub>), sulfur oxides (SO<sub>x</sub>), methane (CH<sub>4</sub>), and carbon dioxide (CO<sub>2</sub>) present serious risks to both environmental quality and public health. VOCs play a major role in the formation of ground-level ozone and smog (Kim et al. 2008; Sartelet et al. 2012; Schürmann et al. 2007; Palli et al. 2009; Toro et al. 2006), while CO, generated primarily through incomplete fuel combustion, poses acute health threats and contributes to climate change. NO<sub>x</sub> emissions are associated with respiratory ailments, the development of acid rain, and nutrient pollution in aquatic ecosystems (Alcantara et al. 2017). PM<sub>10</sub> and PM<sub>2.5</sub> particles are strongly linked to severe cardiovascular and respiratory conditions (Sharma and Dikshit 2016). Likewise, SO<sub>x</sub> emissions are known to exacerbate acid deposition and negatively impact human health (Aksovoglu et al. 2016; Costa et al. 2014; Viana et al. 2014). Methane (CH<sub>4</sub>), with its high global warming potential, plays a significant role in intensifying climate change (Chen et al. 2024). As a dominant greenhouse gas, CO<sub>2</sub> is a primary driver of global warming and necessitates immediate and collective action (Friedrich et al. 2016; Ozbugday and Erbas 2015; Valadkhani et al. 2019). Effectively addressing these emissions requires integrated strategies involving policy enforcement, technological advancement, and the adoption of sustainable practices across all sectors.

Biodiesel (B20), a blend of 20% biodiesel and 80% petroleum diesel, is favored for its compatibility with diesel engines and balanced performance in cost, emissions, and cold weather. It reduces particulate matter, carbon monoxide, and hydrocarbons but slightly increases nitrogen oxide (NOx) emissions. Compressed Natural Gas (CNG), primarily methane, offers up to 30% cost savings and lowers CO<sub>2</sub> emissions by 5-10% compared to diesel, but faces infrastructure and storage challenges. Dimethyl Ether (DME), a synthetic fuel with high cetane number and efficient combustion, is a clean alternative with low NOx emissions, though it has low energy density and requires pressurized storage. Fuel Cell Vehicles (FCVs) utilizing hydrogen have zero tailpipe emissions and high efficiency but face high infrastructure costs and CO<sub>2</sub> emissions during production. Liquefied Petroleum Gas (LPG), derived from natural gas or petroleum, offers reduced emissions, improved engine efficiency, and health benefits but raises storage safety concerns. Low-Sulfur Diesel (LSD) and Ultra-Low Sulfur Diesel (ULSD) reduce sulfur emissions, contributing to cleaner air and improved fuel efficiency. Renewable Diesel II (RD II), produced from renewable oils, has a lower carbon footprint than fossil diesel, with high energy density and reduced emissions, but faces raw material supply issues and cold weather operability

challenges. Each alternative fuel offers unique benefits and challenges, contributing to a transition toward more sustainable energy sources in transportation.

### METHODOLOGY

In this study, a comprehensive Well-to-Wheel (WTW) emissions analysis is conducted specifically for school buses, aiming to assess the full life-cycle environmental impact of various fuel and technology options. The analysis is performed using the Greenhouse Gases, Regulated Emissions, and Energy Use in Transportation (GREET) model developed by Argonne National Laboratory, which allows for the estimation of both upstream and operational emissions (Argonne National Laboratory 2010). The key pollutants evaluated in this study include volatile organic compounds (VOCs), carbon monoxide (CO), nitrogen oxides (NOx), particulate matter with diameters less than 10 micrometers (PM10) and 2.5 micrometers (PM2.5), sulfur oxides (SOx), methane (CH4), and carbon dioxide (CO2). These emissions are quantified and analyzed comparatively across different fuel pathways and vehicle configurations to offer insights into their relative environmental performance.

### RESULTS AND DISCUSSION

Table 1 presents a comprehensive WTW emissions inventory for school buses utilizing various fuel types across five-year intervals from 2025 to 2050. On the other hand, Fig. 1-8 illustrate the variations in emissions across different energy sources for each five-year interval. The analysis encompasses a range of fuel types, including biodiesel, compressed natural gas, dimethyl ether, fuel cell vehicles, liquefied petroleum gas, low-sulfur diesel, and renewable diesel II. The emissions are presented in kilograms per hectokilometer (kg/hkm) and encompass a comprehensive range of both regulated and unregulated pollutants, including volatile organic compounds, carbon monoxide, nitrogen oxides, particulate matter (PM<sub>10</sub> and PM<sub>2.5</sub>), sulfur oxides, methane, and carbon dioxide.

Volatile Organic Compounds (VOC) emissions remain largely constant across all years, with minor differences observed between fuels. The lowest VOC emissions are associated with RD2 and FCV, while LPG consistently exhibits the highest VOC output. Carbon Monoxide (CO) emissions show notable disparities, with CNG consistently producing significantly higher CO levels—nearly an order of magnitude greater than the other fuels—across all time points. In contrast, FCV demonstrates the lowest CO emissions, indicating conversion efficiency. Nitrogen Oxides (NOx) emissions are relatively stable across the study period for all fuels. FCVs exhibit the lowest NOx values, followed closely by CNG, while DME

and RD2 present slightly elevated levels, suggesting variations in combustion temperature or engine calibration. Particulate Matter (PM<sub>10</sub> and PM<sub>2.5</sub>) emissions are relatively low for all fuels, with DME consistently showing the lowest levels, likely due to its soot-free combustion properties. LPG demonstrates slightly higher PM values compared to other alternatives, while LSD and BD20 maintain moderate but consistent levels. Sulfur Oxides (SOx) emissions are highest in FCV, LPG, and DME pathways, which may reflect upstream sulfur content in their production chains. LSD exhibits the lowest SOx emissions, as expected given its refined composition and regulatory limitations on sulfur content. Methane (CH<sub>4</sub>) emissions are substantially elevated in CNG scenarios, reflecting the methane-rich nature of these pathways and potential leakage or incomplete combustion during operation. RD2 consistently exhibits the lowest CH<sub>4</sub> emissions, highlighting its environmental advantage in terms of greenhouse gas mitigation. Carbon Dioxide (CO<sub>2</sub>) emissions remain constant across time for each fuel type, with FCVs showing the lowest CO<sub>2</sub> output (71-72 kg/hkm), followed closely by CNG. In contrast, RD2, DME, and BD20 exhibit slightly higher CO<sub>2</sub> emissions, potentially due to their production and processing emissions, despite being renewable.

Table 1: WTW emissions by years

	School Bus	BD20	CNG	DME	FCV	LPG	LSD	RD2
Year	Emissions				WTW			
	VOC (kg/hkm)	0.014	0.017	0.016	0.012	0.023	0.012	0.011
	CO (kg/hkm)	0.078	1.468	0.088	0.037	0.561	0.077	0.079
	NO <sub>x</sub> (kg/hkm)	0.074	0.049	0.080	0.045	0.059	0.074	0.078
2025	PM <sub>10</sub> (kg/hkm)	0.003	0.002	0.001	0.002	0.003	0.003	0.003
2025	PM <sub>2.5</sub> (kg/hkm)	0.002	0.001	0.001	0.002	0.003	0.002	0.002
	SO <sub>x</sub> (kg/hkm)	0.013	0.017	0.022	0.026	0.023	0.011	0.013
	CH <sub>4</sub> (kg/hkm)	0.102	0.427	0.248	0.249	0.185	0.116	0.068
	CO <sub>2</sub> (kg/hkm)	92	76	95	72	89	91	99
	VOC (kg/hkm)	0.014	0.017	0.016	0.012	0.023	0.012	0.011
	CO (kg/hkm)	0.078	1.469	0.088	0.037	0.561	0.077	0.079
	NO <sub>x</sub> (kg/hkm)	0.072	0.049	0.080	0.045	0.058	0.073	0.075
2020	PM <sub>10</sub> (kg/hkm)	0.002	0.002	0.001	0.002	0.003	0.002	0.003
2030	PM <sub>2.5</sub> (kg/hkm)	0.002	0.001	0.001	0.002	0.003	0.002	0.002
	SO <sub>x</sub> (kg/hkm)	0.013	0.017	0.022	0.025	0.023	0.011	0.013
	CH <sub>4</sub> (kg/hkm)	0.102	0.427	0.248	0.249	0.185	0.116	0.068
	CO <sub>2</sub> (kg/hkm)	92	76	95	72	89	91	99
2035	VOC (kg/hkm)	0.014	0.017	0.016	0.012	0.023	0.012	0.011

	CO (kg/hkm)	0.078	1.468	0.088	0.037	0.561	0.077	0.079
	NO <sub>x</sub> (kg/hkm)	0.072	0.049	0.079	0.045	0.058	0.073	0.075
	PM <sub>10</sub> (kg/hkm)	0.002	0.002	0.001	0.002	0.003	0.002	0.003
	PM <sub>2.5</sub> (kg/hkm)	0.002	0.001	0.001	0.002	0.003	0.002	0.002
	SO <sub>x</sub> (kg/hkm)	0.013	0.017	0.022	0.025	0.022	0.011	0.013
	CH <sub>4</sub> (kg/hkm)	0.102	0.427	0.248	0.249	0.185	0.116	0.067
	CO <sub>2</sub> (kg/hkm)	92	76	94	72	89	91	99
	VOC (kg/hkm)	0.014	0.017	0.016	0.012	0.023	0.012	0.011
	CO (kg/hkm)	0.078	1.469	0.088	0.037	0.561	0.077	0.079
	NO <sub>x</sub> (kg/hkm)	0.072	0.049	0.079	0.045	0.058	0.073	0.075
2040	PM <sub>10</sub> (kg/hkm)	0.002	0.002	0.001	0.002	0.003	0.002	0.003
2040	PM <sub>2.5</sub> (kg/hkm)	0.002	0.001	0.001	0.002	0.003	0.002	0.002
	SO <sub>x</sub> (kg/hkm)	0.013	0.017	0.021	0.024	0.022	0.011	0.013
	CH <sub>4</sub> (kg/hkm)	0.102	0.427	0.248	0.249	0.185	0.116	0.067
	CO <sub>2</sub> (kg/hkm)	92	76	94	72	89	91	99
	VOC (kg/hkm)	0.014	0.017	0.016	0.012	0.023	0.012	0.011
	CO (kg/hkm)	0.078	1.469	0.088	0.037	0.561	0.077	0.079
	NO <sub>x</sub> (kg/hkm)	0.072	0.049	0.079	0.045	0.058	0.073	0.075
2045	PM <sub>10</sub> (kg/hkm)	0.002	0.002	0.001	0.002	0.003	0.002	0.003
2045	PM <sub>2.5</sub> (kg/hkm)	0.002	0.001	0.001	0.002	0.003	0.002	0.002
	SO <sub>x</sub> (kg/hkm)	0.013	0.017	0.021	0.024	0.022	0.011	0.013
	CH <sub>4</sub> (kg/hkm)	0.102	0.427	0.248	0.248	0.185	0.116	0.067
	CO <sub>2</sub> (kg/hkm)	92	76	94	71	89	91	99
	VOC (kg/hkm)	0.014	0.017	0.016	0.012	0.023	0.012	0.011
	CO (kg/hkm)	0.078	1.469	0.088	0.037	0.561	0.077	0.079
	NO <sub>x</sub> (kg/hkm)	0.073	0.049	0.079	0.045	0.058	0.073	0.075
3050	PM <sub>10</sub> (kg/hkm)	0.002	0.002	0.001	0.002	0.003	0.003	0.003
2050	PM <sub>2.5</sub> (kg/hkm)	0.002	0.001	0.001	0.002	0.003	0.002	0.002
	SO <sub>x</sub> (kg/hkm)	0.013	0.017	0.021	0.024	0.022	0.011	0.013
	CH <sub>4</sub> (kg/hkm)	0.102	0.427	0.248	0.248	0.185	0.116	0.067
	CO <sub>2</sub> (kg/hkm)	92	76	94	71	89	91	99

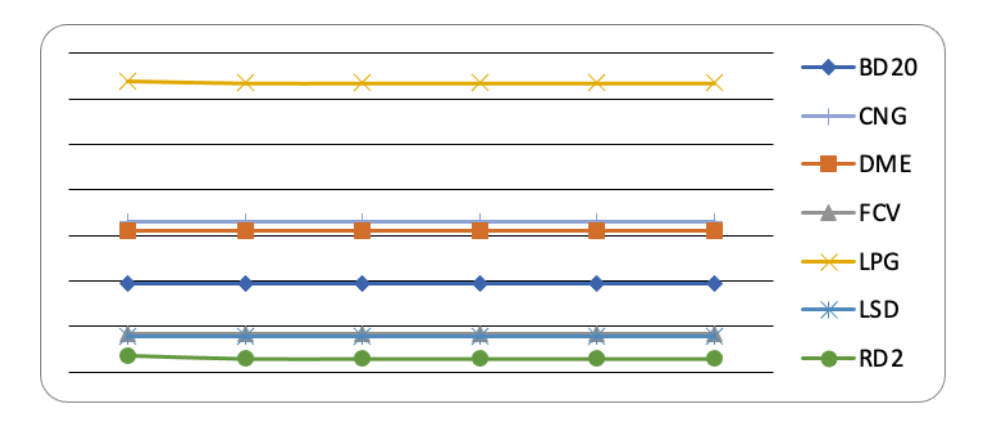


Figure 1: WTW VOC emissions by year

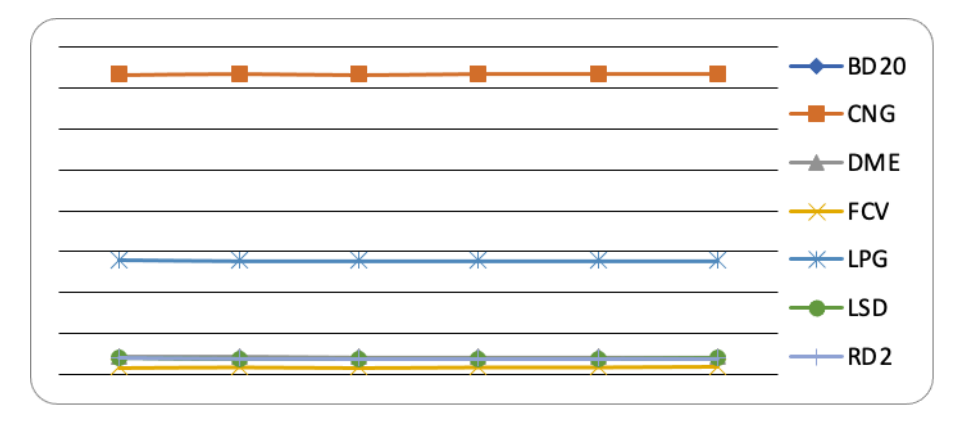


Figure 3: WTW CO emissions by year

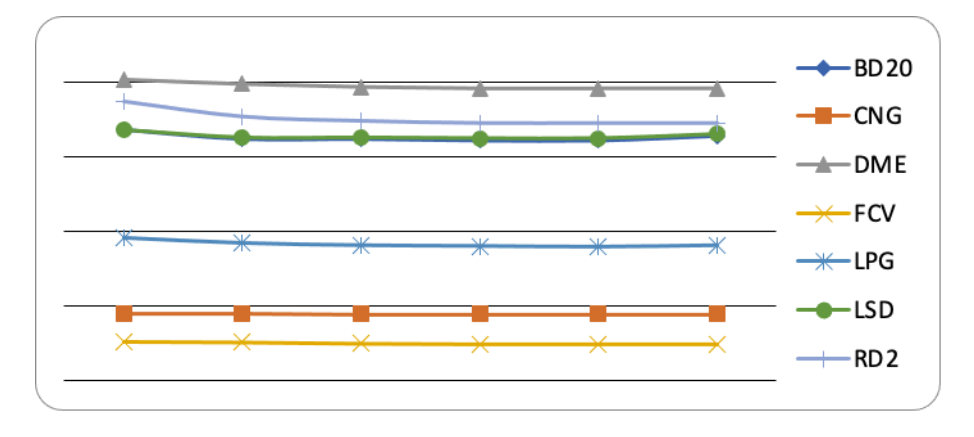


Figure 4: WTW NO<sub>x</sub> emissions by year

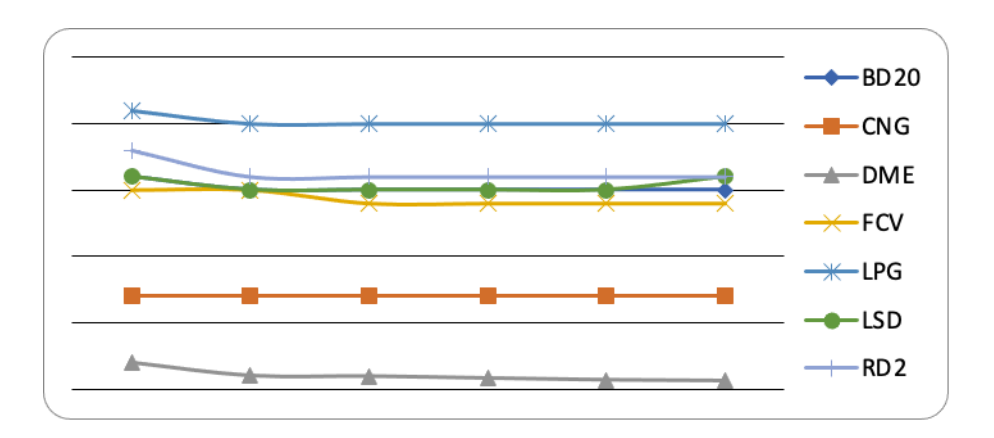


Figure 5: WTW PM<sub>10</sub> emissions by year

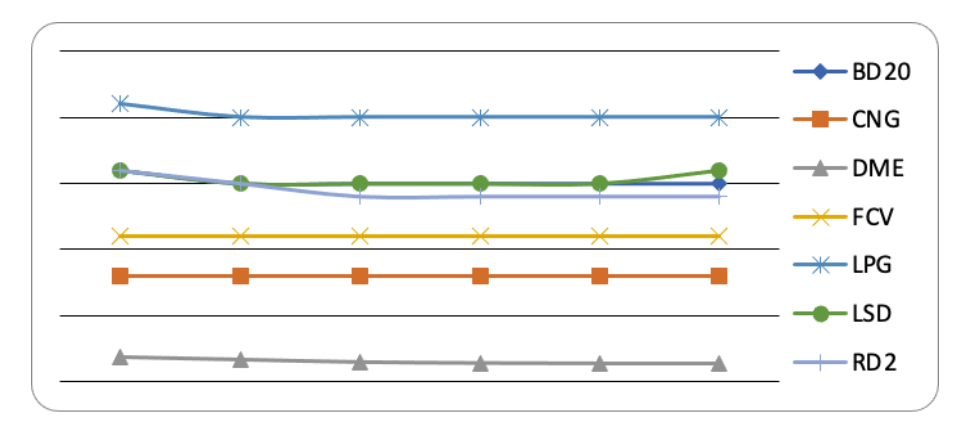


Figure 6: WTW PM<sub>2.5</sub> emissions by year

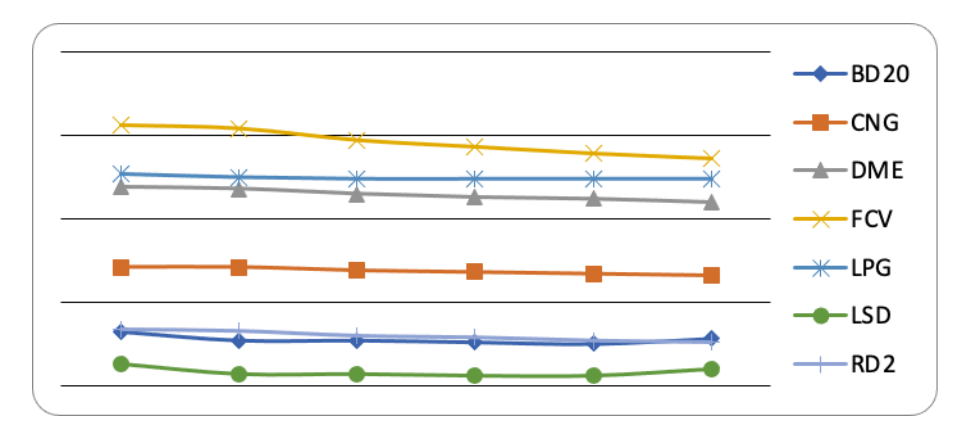


Figure 7: WTW SO<sub>x</sub> emissions by year

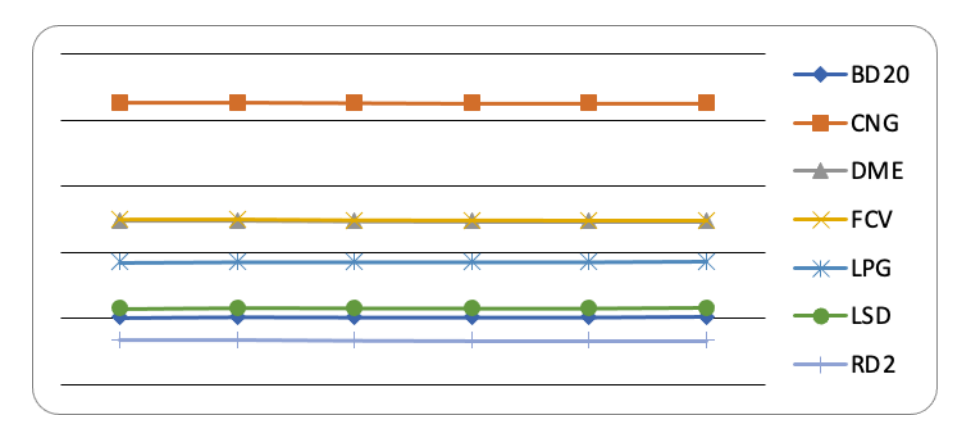


Figure 8: WTW CH<sub>4</sub> emissions by year

BD 20
CNG
DME
FCV
HCPG
HCPG
RD 2

Figure 9: WTW CO<sub>2</sub> emissions by year

Overall, FCVs and RD2 emerge as the most environmentally favorable options across multiple pollutants, particularly for CO, VOCs, NOx, and CO<sub>2</sub>. CNG, while beneficial in terms of CO<sub>2</sub> reduction, shows clear disadvantages in CO and CH<sub>4</sub> emissions. The consistency of emission values over time suggests limited changes in WTW performance assumptions or technological advancements within the modeled period. These findings underscore the importance of selecting fuel technologies not only based on CO<sub>2</sub> but also considering broader pollutant profiles to ensure holistic environmental benefits.

#### REFERENCE

Aksoyoglu S, Baltensperger U, Prévôt A (2016). Contribution of ship emissions to the concentration and deposition of air pollutants in Europe. Atmos Chem Phys 16:1895–1906.

Alcantara V, Padilla E, Piaggio M (2017). Nitrogen oxide emissions and productive structure in Spain: an input-output perspective. J. Clean. Prod 141:447–461.

- Argonne National Laboratory, (2010) GREET model available at: http://greet.es.anl.gov last access: 08/10/2024.
- Chen F, Wang L, Wang Y, Zhang H, Wang N, Ma P, Yu B (2024). Retrieval of dominant methane (CH<sub>4</sub>) emission sources, the first high-resolution (1-2 m) dataset of storage tanks of China in 2000-2021. Earth System Science Data, 16(7), 3369-3382.
- Costa S, Ferreira J, Silveira C, Costa C, Lopes D, Relvas H, Borrego C, Roebeling P, Miranda AI, Teixeira JP (2014). Integrating health on air quality assessment review report on health risks of two major European outdoor air pollutants: PM and NO2. J Toxicol Environ Health B 17:307–340.
- Friedrich T, Timmerman A, Tigchelaar M, Elison Timm O, Ganopolski A (2016). Nonlinear climate sensitivity and its implications for future greenhouse warming. Sci Adv 2:e1501923 Nov 9 1–11.
- Kim KH, Shon ZH, Kim MY, Sunwoo Y, Jeon EC, Hong JH (2008). Major aromatic VOC in the ambient air in the proximity of an urban landfill facility. J Hazard Mater 150:754–764.
- Ozbugday FC, Erbas BC (2015). How effective are energy efficiency and renewable energy in curbing CO2 emissions in the long run? A heterogeneous panel data analysis. Energy 82:734–745.
- Palli D, Sera F, Giovannelli L, Masala G, Grechi D, Bendinelli B, Caini S, Dolara P, Saieva C (2009). Environmental ozone exposure and oxidative DNA damage in adult residents of Florence, Italy. Environ Pollut 157:1521–1525.
- Sartelet KN, Couvidat F, Seigneur C, Roustan Y (2012). Impact of biogenic emissions on air quality over Europe and North America. Atmos Environ 53:131–141.
- Schürmann G, Schäfer K, Jahn C, Hoffmann H, Bauerfeind M, Fleuti E, Rappenglück B (2007). The impact of NOx, CO and VOC emissions on the air quality of Zurich airport. Atmos Environ 41:103–118.
- Sharma M, Dikshit O, (2016). Comprehensive study on air pollution and green house gases (GHGs) in Delhi. A report submitted to Government of NCT Delhi and DPCC Delhi 1-334.
- Toro MV, Cremades LV, Calbó J (2006). Relationship between VOC and NOx emissions and chemical production of tropospheric ozone in the Aburrá Valley (Colombia). Chemosphere 65:881–888.
- Valadkhani A, Smyth R, Nguyen R (2019). Effects of primary energy consumption on CO2 emissions under optimal thresholds: evidence from sixty countries over the last half century. Energy Economics 80:680–690.
- Viana M, Hammingh P, Colette A, Querol X, Degraeuwe B, Vlieger I, van Aardenn J (2014). Impact of maritime transport emissions on coastal air quality in Europe. Atmospheric Environment 90:96–105.

# A Study on Emissions of Refuse Trucks

Adem UĞURLU<sup>1</sup>

<sup>1-</sup> Assoc. Prof. Dr.; Kırklareli Üniversitesi Teknoloji Fakültesi Mekatronik Mühendisliği Bölümü. <a href="mailto:adem.ugurlu@klu.edu.tr">adem.ugurlu@klu.edu.tr</a>, ORCID No: 0000-0002-9531-3944

### **ABSTRACT**

The environmental performance of refuse trucks has become an increasingly important topic within the broader discourse on sustainable urban mobility and waste management. These heavy-duty vehicles typically operate under demanding conditions, including high payloads, frequent acceleration-deceleration cycles, and extended idling periods. Traditionally powered by diesel engines, refuse trucks are responsible for considerable levels of greenhouse gas (GHG) emissions and local air pollutants. To accurately assess the true environmental footprint of different propulsion comprehensive Well-to-Wheel technologies options. and fuel a (WTW) analysis is essential. This methodology accounts for both upstream (fuel production and distribution) and downstream (vehicle operation) emissions and energy use, offering a holistic view of the total environmental impact. This study conducts a comparative WTW assessment of various refuse truck configurations—including 20% biodiesel and 80% diesel blend (BD20), compressed natural gas (CNG), dimethyl ether (DME), electric vehicles (EVs), fuel cell vehicles (FCV) using compressed gaseous hydrogen from natural gas, liquefied natural gas (LNG), low sulfur diesel (LSD), and renewable diesel 2 (RD2)—in order to inform evidence-based decisionmaking for cleaner and more sustainable municipal fleet transitions.

Keywords – Refuse trucks; emissions; WTW analysis.

#### INTRODUCTION

Refuse trucks, also known as garbage trucks or waste collection vehicles, are specialized vehicles designed for the transportation of solid waste, recyclables, and other forms of municipal waste from residential, commercial, and industrial areas to disposal sites, recycling centers, or waste treatment facilities. These trucks are an integral component of modern urban waste management systems and play a crucial role in maintaining sanitation, public health, and environmental protection in cities and towns worldwide. While refuse trucks are necessary for maintaining urban sanitation, they also have a significant environmental footprint.

Refuse trucks, particularly those with diesel engines, are a significant source of air pollution. Diesel-powered vehicles emit pollutants such as nitrogen oxides (NOx), particulate matter (PM), carbon monoxide (CO), and carbon dioxide (CO<sub>2</sub>). These emissions contribute to urban air pollution, climate change, and health problems in urban populations. Due to their large size and the demanding nature of their operations, refuse trucks typically consume substantial amounts of fuel, contributing to higher overall greenhouse gas emissions. Efforts to reduce fuel consumption include

transitioning to alternative fuel vehicles, such as compressed natural gas (CNG) trucks, or adopting hybrid or electric refuse trucks.

Air pollutants such as volatile organic compounds (VOCs), carbon monoxide (CO), nitrogen oxides (NO<sub>x</sub>), particulate matter (PM<sub>10</sub> and PM<sub>2.5</sub>), sulfur oxides (SO<sub>x</sub>), CH<sub>4</sub>, and carbon dioxide (CO<sub>2</sub>) pose significant threats to environmental and public health. VOCs contribute to ground-level ozone and smog formation Kim et al. 2008; Sartelet et al. 2012; Schürmann et al. 2007; Palli et al. 2009; Toro et al. 2006), while CO, produced from incomplete combustion, presents immediate health hazards and exacerbates climate change. NO<sub>x</sub> emissions lead to respiratory issues, acid rain, and eutrophication (Alcantara et al. 2017), and PM pollutants are linked to serious cardiovascular and respiratory diseases (Sharma and Dikshit 2016). Similarly, SO<sub>x</sub> emissions contribute to acid rain and human health problems (Aksoyoglu et al. 2016; Costa et al. 2014; Viana et al. 2014). The presence of methane (CH<sub>4</sub>) in the atmosphere is a key factor in accelerating climate change (Chen et al. 2024). CO2, as another primary greenhouse gas, drives climate change and demands urgent global action (Friedrich et al. 2016; Ozbugday and Erbas 2015; Valadkhani et al. 2019). Mitigating these emissions requires coordinated efforts across industry, government, and society through regulatory frameworks, technological innovation, and sustainable practices.

With growing concerns about the environmental impact of diesel engines, many cities and waste management companies are transitioning to alternative fuel options for refuse trucks. Compressed natural gas (CNG), electricity, and hydrogen are emerging as cleaner alternatives that reduce the carbon footprint and decrease harmful emissions from waste collection operations. The development of electric refuse trucks marks a significant milestone in reducing the carbon emissions associated with waste collection. Electric vehicles (EVs) are quieter and produce no tailpipe emissions, which significantly reduces air pollution in urban environments. However, the adoption of electric refuse trucks is still in the early stages and depends on overcoming challenges such as battery capacity and the availability of charging infrastructure. In this study refuse trucks are analyzed for the following energy sources:

• Biodiesel (20/80) refers to a blend of 20% biodiesel and 80% petroleum diesel, commonly referred to as B20. Biodiesel itself is an alternative fuel derived from renewable biological sources such as vegetable oils, animal fats, or algae. When mixed with traditional diesel, biodiesel reduces reliance on fossil fuels and lowers carbon emissions. The 20/80 biodiesel blend strikes a balance between cost, performance, and environmental benefits, maintaining compatibility with most diesel engines while providing a reduction in greenhouse gas emissions compared to conventional diesel. The use of B20 biodiesel results in reduced carbon dioxide (CO<sub>2</sub>) emissions because biodiesel is derived from plants that absorb

CO<sub>2</sub> during growth, offsetting some of the emissions released when the fuel is burned. Additionally, biodiesel significantly contains fewer particulate matter (PM), sulfur compounds, and nitrogen oxides (NOx) than traditional diesel, improving air quality. However, biodiesel also has higher water absorption tendencies, which can lead to engine performance issues if not properly managed.

- Compressed Natural Gas (CNG) is a clean alternative fuel made by compressing natural gas to a high pressure, typically around 3,000 to 3,600 psi (pounds per square inch), to reduce its volume for storage and transportation. CNG primarily consists of methane (CH<sub>4</sub>), a carbon-based gas with a lower carbon content compared to traditional gasoline and diesel fuels. As a result, CNG combustion produces lower emissions of carbon dioxide (CO2), particulate matter (PM), nitrogen oxides (NOx), and other harmful pollutants. CNG is widely regarded as an environmentally friendly option for both passenger vehicles and heavy-duty transport. The use of CNG in transportation helps reduce urban air pollution and mitigate climate change by lowering overall greenhouse gas emissions. Furthermore, CNG is a domestically produced fuel, enhancing energy security. However, the infrastructure for CNG fueling stations is still limited, and the vehicles themselves tend to have a smaller driving range compared to gasoline or diesel-powered vehicles, primarily due to the lower energy density of compressed gas.
- Dimethyl Ether (DME) is a clean-burning, colorless gas that is chemically similar to liquefied petroleum gas (LPG) but can also be produced from a variety of feedstocks, including natural gas, coal, or biomass. As a fuel, DME is often considered a potential alternative to diesel, particularly in the context of reducing particulate matter (PM) and nitrogen oxide (NOx) emissions in diesel engines. DME can be used in compression ignition engines (such as diesel engines) but requires modifications due to its lower cetane number. When burned, DME produces very low levels of particulate matter and nitrogen oxides, which are key contributors to urban air pollution. Additionally, DME has a higher energy density compared to other alternative fuels such as natural gas, and it can be stored and transported in liquid form at relatively low pressures, similar to LPG. However, like CNG, DME still faces challenges in terms of infrastructure development and widespread adoption.
- An Electric Vehicle (EV) is a vehicle that uses electricity stored in batteries to power one or more electric motors. EVs have zero tailpipe emissions, making them an attractive option for reducing urban air pollution and mitigating climate change. The environmental benefits of electric vehicles depend largely on the source of electricity used to charge them; when powered by renewable energy sources such as solar or wind, EVs offer substantial reductions in carbon emissions compared to vehicles powered by fossil fuels. EVs are typically more energy-efficient than internal

combustion engine vehicles because electric motors convert a higher percentage of electrical energy into movement, while internal combustion engines lose more energy as heat. However, the widespread adoption of EVs faces challenges such as the need for expanded charging infrastructure, higher upfront costs, and limitations related to the range and charging time of current battery technologies. Advances in battery technology and charging infrastructure are critical to the future growth of the EV market.

- Fuel Cell Vehicles (FCVs) that use compressed gaseous hydrogen as a fuel represent a promising technology for reducing emissions in the transportation sector. Hydrogen fuel cells generate electricity through an electrochemical reaction between hydrogen gas (H2) and oxygen (O2) from the air. The only byproducts of this reaction are water vapor and heat, making FCVs one of the cleanest forms of transportation. In this particular type of FCV, hydrogen is typically produced from natural gas through a process called steam methane reforming (SMR), which extracts hydrogen from methane. The hydrogen is then compressed into high-pressure gas tanks and used in fuel cells to generate electricity for the vehicle's electric motors. Despite the clean operation of hydrogen fuel cells, the production of hydrogen from natural gas generates carbon dioxide (CO2) emissions, meaning the environmental benefits depend on how the hydrogen is produced. Fuel cell vehicles offer long driving ranges and fast refueling times, akin to conventional gasoline-powered vehicles, making them suitable for a wide range of applications, from passenger cars to heavy-duty trucks. However, challenges include the need for significant infrastructure development (hydrogen refueling stations), the cost of hydrogen production, and the energy efficiency of hydrogen production methods.
- Liquefied Natural Gas (LNG) is natural gas that has been cooled to a liquid state at approximately -162°C (-260°F) to reduce its volume by about 600 times, making it easier to store and transport over long distances. LNG is primarily composed of methane (CH4) and is used as an alternative to gasoline and diesel in various sectors, including heavy-duty transportation and marine shipping. LNG has a significantly lower carbon content compared to diesel, and its combustion produces fewer emissions of carbon dioxide (CO2), nitrogen oxides (NOx), and particulate matter (PM). Additionally, LNG-powered vehicles and ships produce less noise than their diesel counterparts, making LNG a suitable fuel for urban environments with noise pollution concerns. However, the widespread adoption of LNG faces challenges such as the need for specialized fueling infrastructure and storage facilities. Additionally, while LNG is cleaner than diesel, it still contributes to greenhouse gas emissions, particularly methane leaks during extraction, transportation, and use.
- Low-Sulfur Diesel (LSD) is a refined version of traditional diesel fuel that contains significantly lower levels of sulfur, typically less than 15 parts per million (ppm) of sulfur, compared to the higher sulfur content in

conventional diesel fuels. This reduction in sulfur content is primarily designed to enable the use of advanced emission control technologies, such as selective catalytic reduction (SCR) and diesel particulate filters (DPF), which are essential for meeting stringent air quality regulations. LSD reduces harmful emissions of sulfur dioxide (SO<sub>2</sub>) and particulate matter, both of which contribute to air pollution, acid rain, and respiratory diseases. The adoption of low-sulfur diesel has enabled cleaner combustion in diesel engines, improving air quality and reducing the environmental impact of diesel vehicles. However, while low-sulfur diesel offers significant reductions in certain pollutants, it does not eliminate other emissions, such as carbon dioxide (CO<sub>2</sub>) and nitrogen oxides (NOx), which remain a concern for further emissions reductions.

• Renewable Diesel II, often referred to as "Hydrotreated Vegetable Oil (HVO)", is a next-generation biofuel produced through the hydrotreatment of plant oils or animal fats, using hydrogen to remove impurities and create a high-quality diesel-like fuel. Unlike biodiesel, which is typically made through transesterification, renewable diesel is chemically similar to petroleum diesel and can be used in existing diesel engines without modifications. Renewable Diesel II is produced using feedstocks such as vegetable oils, waste oils, and animal fats, and it has a significantly lower carbon intensity than conventional fossil diesel. When burned, renewable diesel produces fewer particulate matter (PM), carbon monoxide (CO), and nitrogen oxides (NOx) compared to regular diesel, making it an environmentally friendly alternative for heavy-duty vehicles and other diesel-powered machinery. Additionally, renewable diesel has a higher cetane number than biodiesel, which improves combustion quality and engine performance.

### **METHODOLOGY**

In this study, a comprehensive Well-to-Wheel (WTW) emissions analysis is conducted specifically for refuse trucks, with the aim of evaluating the full life-cycle environmental impact of various fuel and technology options. The analysis is carried out using the Greenhouse Gases, Regulated Emissions, and Energy Use in Transportation (GREET) model developed by Argonne National Laboratory, which enables the estimation of both upstream and operational emissions (Argonne National Laboratory 2010). Key emission pollutants assessed in this study include volatile organic compounds (VOCs), carbon monoxide (CO), nitrogen oxides (NOx), particulate matter with diameters less than 10 micrometers (PM<sub>10</sub>) and 2.5 micrometers (PM<sub>2.5</sub>), sulfur oxides (SOx), methane (CH<sub>4</sub>), and carbon dioxide (CO<sub>2</sub>). These emissions are quantified and comparatively analyzed across different fuel pathways and vehicle configurations to provide insight into their relative environmental performance.

### RESULTS AND DISCUSSION

Fig. 1 illustrates the historical and projected share (%) of various electricity generation sources within the U.S. power mix from 1990 to 2050, categorized as non-distributed generation. The chart highlights the declining contribution of coal-fired and oil-fired power generation over time, while natural gas-fired and nuclear power generation maintain significant shares. Renewable energy sources, including wind, solar, biomass, hydroelectric, and geothermal power, exhibit a gradual increase in their proportion of the electricity mix, particularly after 2015. This trend reflects the ongoing transition toward cleaner energy technologies and a diversification of the electricity generation portfolio in response to environmental and policy drivers. All electricity-related calculations in this study were conducted based on the power generation mix presented in this figure.

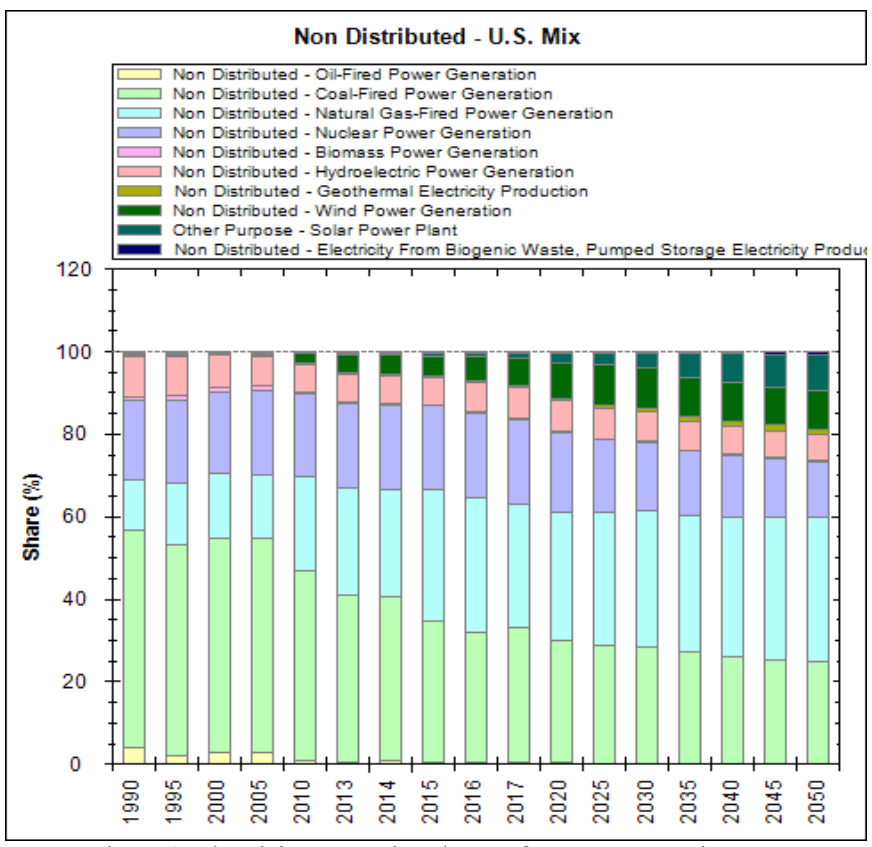


Figure 1: Electricity generation shares of energy sources in USA

Table 1 presents a comprehensive WTW emissions inventory for refuse trucks utilizing various fuel types across five-year intervals from 2025 to 2050. Figures 2–9 exclusively illustrate the variations in emission levels

across different fuel types and time periods, offering a comparative perspective on the environmental performance of each option. The fuels analyzed include biodiesel, compressed natural gas, dimethyl ether, battery-electric vehicles, fuel cell vehicles, liquefied natural gas, low sulfur diesel, and renewable diesel II. The emissions are reported in kilograms per hectokilometers (kg/hkm) and cover major regulated and unregulated pollutants, including volatile organic compounds (VOCs), carbon monoxide (CO), nitrogen oxides (NOx), particulate matter (PM10, PM2.5), sulfur oxides (SOx), methane (CH4), and carbon dioxide (CO2).

Across all fuel types, emission values remain unchanged over time, indicating that the analysis assumes static fuel pathways, technologies, and vehicle efficiencies. This suggests a scenario-based comparison rather than a predictive or dynamic modeling approach. As such, observed differences are primarily attributable to fuel and powertrain types, not temporal advancements.

EVs and FCVs clearly outperform other technologies across all emissions categories, assuming clean electricity and hydrogen production. Natural gas vehicles (CNG, LNG)—despite lower CO<sub>2</sub> than diesel—pose challenges due to high methane emissions, undermining their GHG mitigation potential. Renewable diesel (RD2) offers a moderate transitional pathway, particularly where electric or hydrogen infrastructure is lacking. The high NOx, SOx, and PM emissions from LSD and BD20 reinforce the urgency to phase out fossil diesel variants.

The WTW emissions profile of refuse trucks varies significantly by fuel type. While alternative fuels like RD2 and DME offer improvements over conventional diesel, only EVs and FCVs demonstrate consistent superiority across all environmental indicators. For municipalities aiming to decarbonize waste collection fleets and reduce urban air pollution, the results support a long-term transition toward electric or hydrogen-based refuse trucks—backed by investments in clean energy infrastructure.

R	efuse Trucks	BD20	CNG	DME	EV	FCV	LNG	LSD	RD2		
Year	Emissions		WTW								
2025	VOC (kg/hkm)	0.017	0.020	0.020	0.005	0.012	0.015	0.014	0.012		
	CO (kg/hkm)	0.057	1.483	0.071	0.015	0.038	1.459	0.056	0.059		
	NOx (kg/hkm)	0.109	0.068	0.119	0.023	0.047	0.042	0.109	0.115		
	PM10 (kg/hkm)	0.004	0.003	0.001	0.004	0.003	0.003	0.004	0.004		
	PM2.5 (kg/hkm)	0.003	0.002	0.001	0.001	0.002	0.003	0.003	0.003		
	SOx (kg/hkm)	0.018	0.023	0.030	0.062	0.027	0.020	0.016	0.018		
	CH4 (kg/hkm)	0.136	0.573	0.337	0.100	0.261	0.641	0.156	0.090		
	CO2 (kg/hkm)	125	105	129	51	75	109	125	136		
2030	VOC (kg/hkm)	0.0167	0.0204	0.020	0.005	0.012	0.015	0.014	0.012		
	CO (kg/hkm)	0.057	1.483	0.070	0.015	0.038	1.459	0.056	0.058		
	NOx (kg/hkm)	0.108	0.068	0.118	0.023	0.047	0.041	0.108	0.112		
	PM10 (kg/hkm)	0.004	0.003	0.001	0.004	0.003	0.003	0.004	0.004		

Table 1: WTW emissions by years

	PM2.5 (kg/hkm)	0.003	0.002	0.001	0.001	0.002	0.003	0.003	0.003
	SOx (kg/hkm)	0.017	0.023	0.030	0.061	0.027	0.020	0.015	0.018
	CH4 (kg/hkm)	0.137	0.573	0.337	0.101	0.261	0.641	0.156	0.090
	CO2 (kg/hkm)	125	105	129	51	75	109	125	136
2035	VOC (kg/hkm)	0.017	0.020	0.020	0.005	0.012	0.015	0.014	0.012
	CO (kg/hkm)	0.057	1.483	0.070	0.015	0.038	1.459	0.056	0.058
	NOx (kg/hkm)	0.108	0.068	0.117	0.022	0.047	0.040	0.108	0.111
	PM10 (kg/hkm)	0.004	0.003	0.001	0.004	0.002	0.003	0.004	0.004
	PM2.5 (kg/hkm)	0.003	0.002	0.001	0.001	0.002	0.003	0.003	0.003
	SOx (kg/hkm)	0.017	0.023	0.029	0.059	0.026	0.020	0.015	0.018
	CH4 (kg/hkm)	0.137	0.573	0.337	0.098	0.260	0.641	0.156	0.090
	CO2 (kg/hkm)	125	105	129	50	75	109	125	135
2040	VOC (kg/hkm)	0.017	0.020	0.020	0.005	0.012	0.015	0.014	0.012
	CO (kg/hkm)	0.057	1.483	0.070	0.015	0.038	1.459	0.056	0.058
	NOx (kg/hkm)	0.107	0.068	0.117	0.022	0.047	0.040	0.108	0.111
	PM10 (kg/hkm)	0.004	0.003	0.001	0.004	0.002	0.003	0.004	0.004
	PM2.5 (kg/hkm)	0.003	0.002	0.001	0.001	0.002	0.003	0.003	0.003
	SOx (kg/hkm)	0.017	0.023	0.029	0.057	0.025	0.020	0.015	0.018
	CH4 (kg/hkm)	0.137	0.573	0.336	0.098	0.260	0.641	0.156	0.089
	CO2 (kg/hkm)	125	105	129	49	75	109	125	135
2045	VOC (kg/hkm)	0.017	0.020	0.020	0.005	0.012	0.015	0.014	0.012
	CO (kg/hkm)	0.057	1.483	0.070	0.015	0.038	1.459	0.056	0.058
	NOx (kg/hkm)	0.107	0.068	0.117	0.021	0.047	0.040	0.108	0.111
	PM10 (kg/hkm)	0.004	0.003	0.001	0.004	0.002	0.003	0.004	0.004
	PM2.5 (kg/hkm)	0.003	0.002	0.001	0.001	0.002	0.003	0.003	0.003
	SOx (kg/hkm)	0.017	0.023	0.029	0.055	0.025	0.020	0.015	0.017
	CH4 (kg/hkm)	0.137	0.573	0.336	0.097	0.260	0.641	0.156	0.089
	CO2 (kg/hkm)	125	105	129	48	75	109	125	135
2050	VOC (kg/hkm)	0.017	0.020	0.020	0.005	0.012	0.015	0.014	0.012
	CO (kg/hkm)	0.057	1.483	0.070	0.016	0.038	1.459	0.056	0.058
	NOx (kg/hkm)	0.108	0.068	0.117	0.022	0.047	0.040	0.109	0.111
	PM10 (kg/hkm)	0.004	0.003	0.001	0.004	0.002	0.003	0.004	0.004
	PM2.5 (kg/hkm)	0.003	0.002	0.001	0.001	0.002	0.003	0.003	0.003
	SOx (kg/hkm)	0.018	0.023	0.029	0.054	0.025	0.020	0.015	0.017
	CH4 (kg/hkm)	0.137	0.573	0.336	0.097	0.260	0.641	0.157	0.089
	CO2 (kg/hkm)	125	105	129	48	75	109	125	135

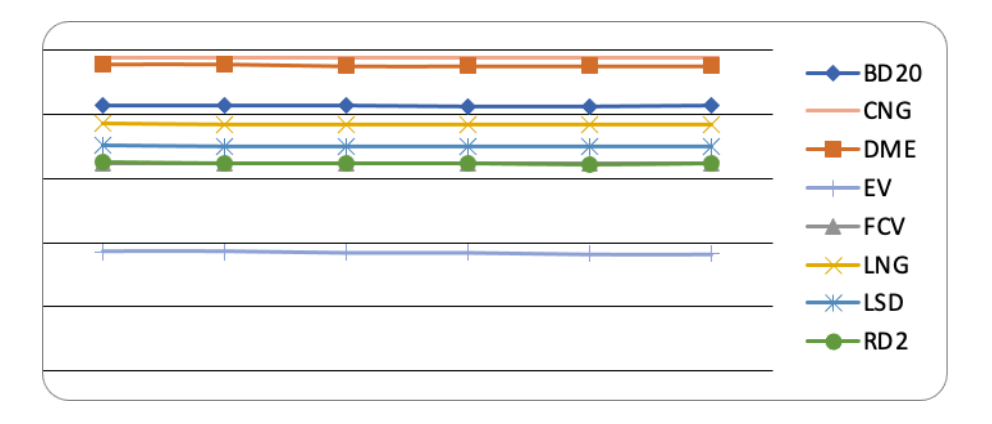


Figure 2: WTW VOC emissions by year

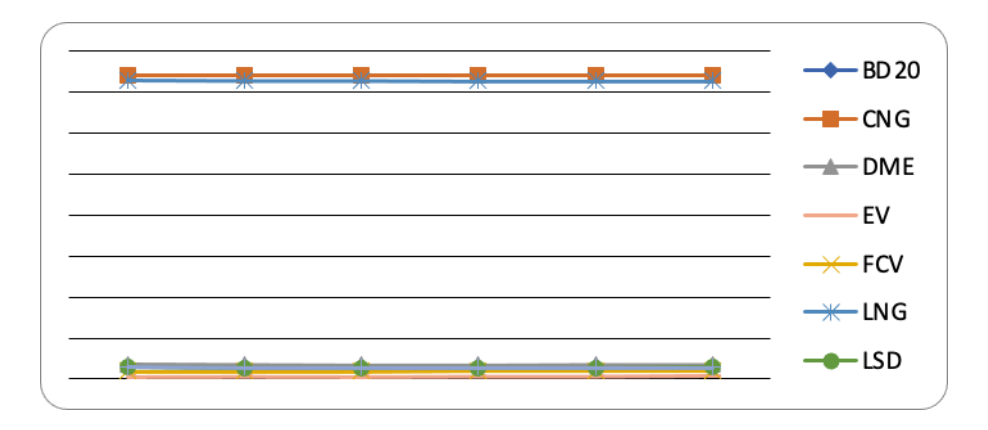


Figure 3: WTW CO emissions by year

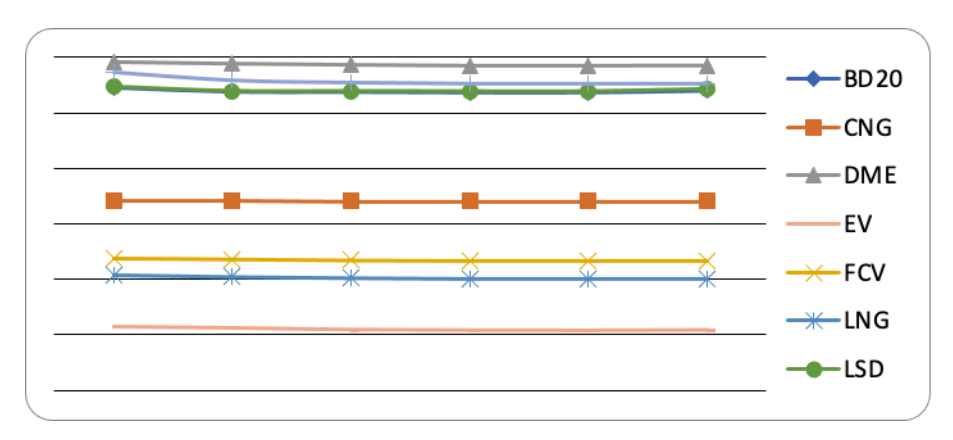


Figure 4: WTW NO<sub>x</sub> emissions by year

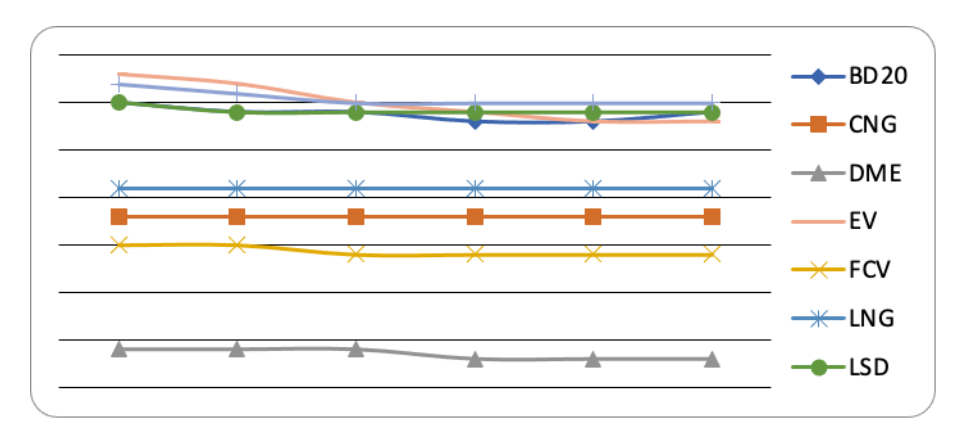


Figure 5: WTW PM<sub>10</sub> emissions by year

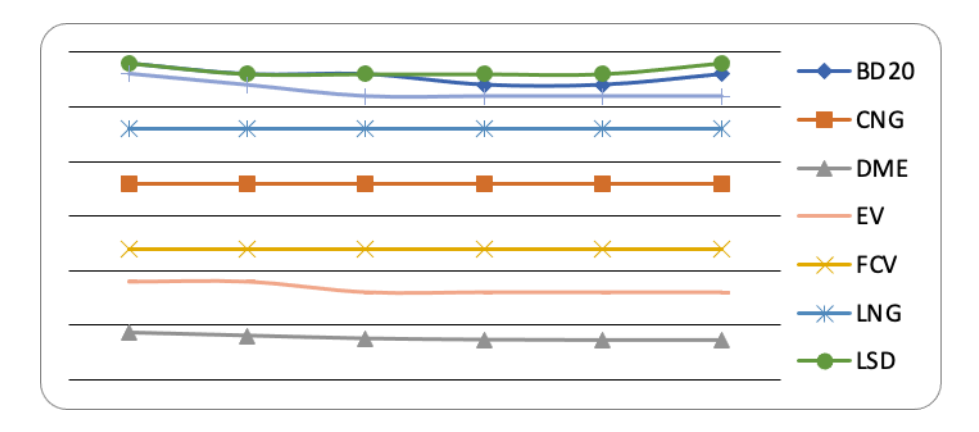


Figure 6: WTW PM<sub>2.5</sub> emissions by year

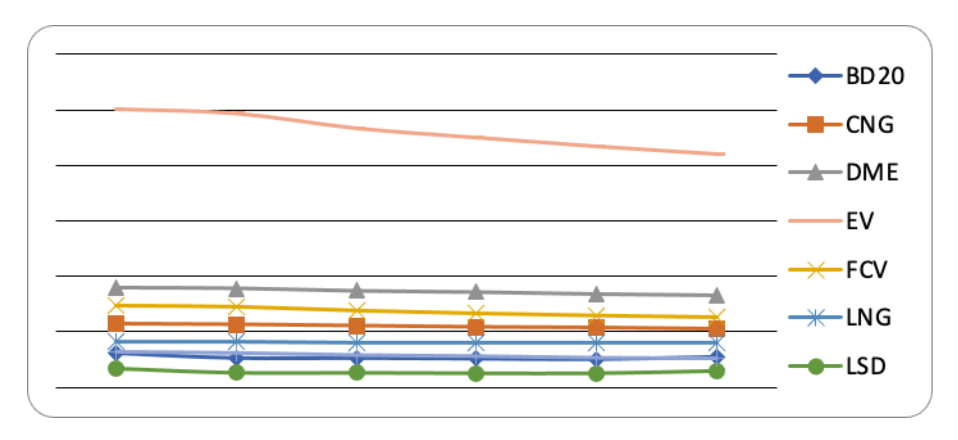


Figure 7: WTW SO<sub>x</sub> emissions by year

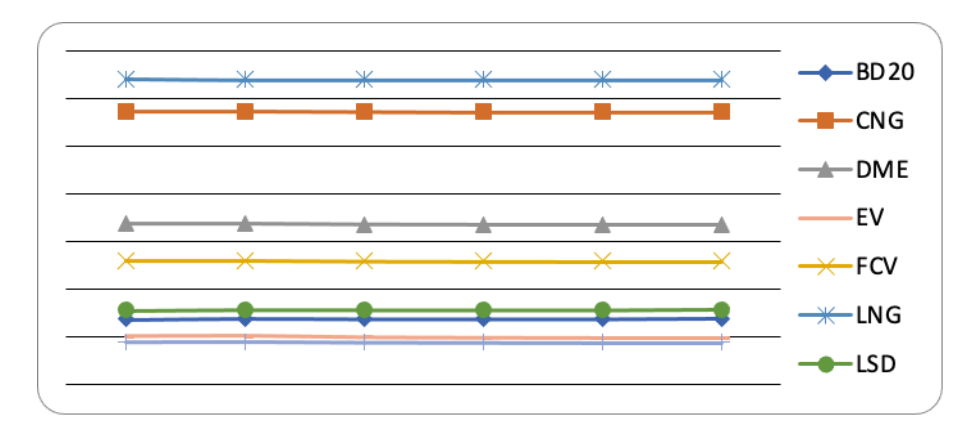


Figure 8: WTW CH<sub>4</sub> emissions by year

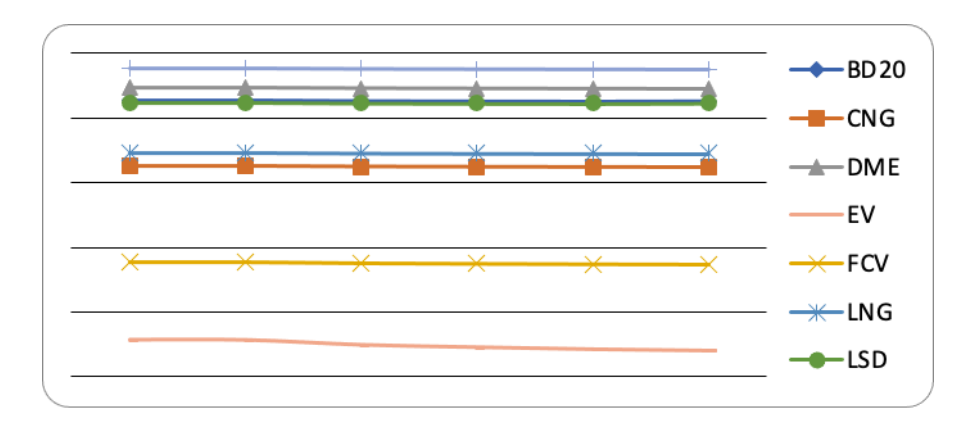


Figure 9: WTW CO<sub>2</sub> emissions by year

### REFERENCE

- Aksoyoglu S, Baltensperger U, Prévôt A (2016). Contribution of ship emissions to the concentration and deposition of air pollutants in Europe. Atmos Chem Phys 16:1895–1906.
- Alcantara V, Padilla E, Piaggio M (2017). Nitrogen oxide emissions and productive structure in Spain: an input-output perspective. J. Clean. Prod 141:447–461.
- Argonne National Laboratory, (2010) GREET model available at: http://greet.es.anl.gov last access: 08/10/2024.
- Chen F, Wang L, Wang Y, Zhang H, Wang N, Ma P, Yu B (2024). Retrieval of dominant methane (CH<sub>4</sub>) emission sources, the first high-resolution (1-2 m) dataset of storage tanks of China in 2000-2021. Earth System Science Data, 16(7), 3369-3382.
- Costa S, Ferreira J, Silveira C, Costa C, Lopes D, Relvas H, Borrego C, Roebeling P, Miranda AI, Teixeira JP (2014). Integrating health on air quality assessment review report on health risks of two major European outdoor air pollutants: PM and NO2. J Toxicol Environ Health B 17:307–340.
- Friedrich T, Timmerman A, Tigchelaar M, Elison Timm O, Ganopolski A (2016). Nonlinear climate sensitivity and its implications for future greenhouse warming. Sci Adv 2:e1501923 Nov 9 1–11.
- Kim KH, Shon ZH, Kim MY, Sunwoo Y, Jeon EC, Hong JH (2008). Major aromatic VOC in the ambient air in the proximity of an urban landfill facility. J Hazard Mater 150:754–764.
- Ozbugday FC, Erbas BC (2015). How effective are energy efficiency and renewable energy in curbing CO2 emissions in the long run? A heterogeneous panel data analysis. Energy 82:734–745.
- Palli D, Sera F, Giovannelli L, Masala G, Grechi D, Bendinelli B, Caini S, Dolara P, Saieva C (2009). Environmental ozone exposure and oxidative DNA damage in adult residents of Florence, Italy. Environ Pollut 157:1521–1525.
- Sartelet KN, Couvidat F, Seigneur C, Roustan Y (2012). Impact of biogenic emissions on air quality over Europe and North America. Atmos Environ 53:131–141.

- Schürmann G, Schäfer K, Jahn C, Hoffmann H, Bauerfeind M, Fleuti E, Rappenglück B (2007). The impact of NOx, CO and VOC emissions on the air quality of Zurich airport. Atmos Environ 41:103–118.
- Sharma M, Dikshit O, (2016). Comprehensive study on air pollution and green house gases (GHGs) in Delhi. A report submitted to Government of NCT Delhi and DPCC Delhi 1-334.
- Toro MV, Cremades LV, Calbó J (2006). Relationship between VOC and NOx emissions and chemical production of tropospheric ozone in the Aburrá Valley (Colombia). Chemosphere 65:881–888.
- Valadkhani A, Smyth R, Nguyen R (2019). Effects of primary energy consumption on CO2 emissions under optimal thresholds: evidence from sixty countries over the last half century. Energy Economics 80:680–690.
- Viana M, Hammingh P, Colette A, Querol X, Degraeuwe B, Vlieger I, van Aardenn J (2014). Impact of maritime transport emissions on coastal air quality in Europe. Atmospheric Environment 90:96–105.

# Geochemical Studies of Mangan Bearing Sediments Around Durmuştepe Village (Maden-Elazığ)

## Dicle BAL AKKOCA<sup>1</sup>

## Pelin BİNGÖL<sup>2</sup>

<sup>1-</sup> Prof. Dr.; Department of Geological Engineering Faculty of Engineering, Fırat University, Elazığ, Turkey dbal@firat.edu.tr ORCID No: 0000-0002-6567-7739

<sup>2-</sup> Senior engineer; Department of Geological Engineering Faculty of Engineering, Fırat University, Elazığ, Turkey, pelinbingol25@gmail.com. ORCID No: 0009-0000-5614-6138

### **ABSTRACT**

Some important oxides, trace elements and rare earth elements are important in revealing the source rocks of sedimentary rocks. In this study, major and trace element of the sedimentary rocks around Durmuştepe village which is located within the Maden District were obtained and compared with previous studies around the area. The investigated sediments contain manganese ore. Upper Jurassic-Lower Cretaceous Guleman Ophiolites, Maastrichtian-Lower Eocene Hazar Group, Middle Eocene Maden Group, Quaternary alluviums are present in the area. In the study area, manganese mineralizations developed in the form of lenses, heads and layers within the red mudstone of the Maden Group. The geochemical properties of these red mudstones were investigated using inductively coupled plasma (ICP). SiO<sub>2</sub>, Al<sub>2</sub>O<sub>3</sub>, MgO, Na<sub>2</sub>O, K<sub>2</sub>O, TiO<sub>2</sub>, Cr<sub>2</sub>O<sub>3</sub> is higher in the studied rocks than mining rocks. Log (SiO<sub>2</sub>/Al<sub>2</sub>O<sub>3</sub>) and log Fe<sub>2</sub>O<sub>3</sub>/K<sub>2</sub>O values shows Fe-rich shale properties, suggest that the source of the samples are Fe-rich mafic rocks. According to [Fe/(Al + Fe + Mn)], [Al/(Al + Fe + Mn)] and [(Fe + Mn)/Al] values the sediments had been affected by hydrothermal activity. Ba, V, Y, Zr, Nb is lower than Topalusağı mining rocks. The positive correlations between V and Fe, Sc, Ti, V; and Zr, Nb, Hf, Th reflects the association of these elements in silicates. Th/Sc Th/Cr, Th/Co ratios show that the source rocks is mafic rock in composition.

Keywords: Elazığ, Maden, inductively coupled plasma (ICP), Maden Group, source rocks

### INTRODUCTION

Geochemistry of sedimentary rocks is used to understand the sedimentation environments of these sediments. Geochemical studies of the sedimentary rocks are a common research method used to investigate the properties of the source rocks of the surrounding basin (Akkoca and Daş, 2018; Akkoca et al., 2019; Akkoca et al., 2024). Some important oxides, trace elements, rare earth elements are used in significant amounts because they represent source rocks.

The Eastern Taurus Mountains, which include the study area, contain many magmatic, metamorphic, and sedimentary rocks, and many researchers have studied the geology, mineralogy, and geochemistry of these rocks. The sediments under investigation are red colored sediments belonging to the Maden Group. Aktaş and Robertson (1990) named the unit as Maden Group. They stated that the unit consists of red mudstones, volcano-sediments, basaltic pillow lavas, lava flows, agglomerates, and pink-gray limestones belonging to the Maden Group in the study area. Altunbey and Sağıroğlu

(1995) studied the mineralogical and geochemical properties of manganese mineralizations in the mudstones from Maden Group. Around Topaluşağı and Katran Tepe, hydrothermal activities had an effect. Altay (2016) studied the iron manganese deposits around Hatunköy - Durmuştepe in the study area. However, geochemistry of sediments around these mineralizations did not investigated with detalied before. Geochemistry of these sediments will investigate around Durmuştepe, where manganese mineralizations are found (Figure 1). The first findings about the sediments will given with these study.

The investigated area is around Durmuştepe village which is located within the Maden District, 60 km from Elazığ city center. To the southeast of Lake Hazar, near Durmuştepe, are Hatunköy, Plajköy, and Yoncapınar, Topaluşağı, Işıktepe (Figure 1).

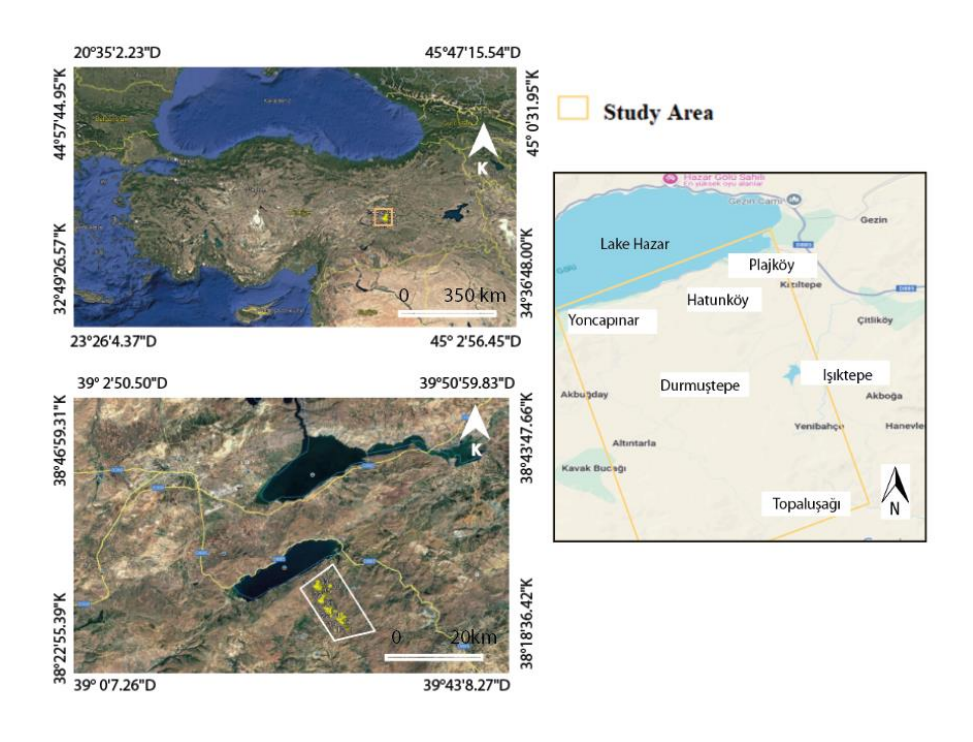


Figure 1: The study area (Google Earth)

### **GEOLOGY**

In the study area, Upper Jurassic-Lower Cretaceous Guleman Ophiolites, Maastrichtian-Lower Eocene Hazar Group, Middle Eocene Maden Group, Quaternary alluviums are located (Figure 2).

Perinçek (1979) named the Guleman Ophiolites as "Guleman Group" and Özkan (1982) named it the "Guleman Ophiolite". The unit is best observed in the Guleman (Alacakaya) district, 50 km southeast of Elazığ. A significant portion of Turkey's chromite production is obtained from the Guleman Ophiolites, which take their name from this district. In the study area, it surfaces to the east and south of Lake Hazar (Figure 2). The stratigraphic and tectonic relationships of the Guleman Ophiolites with other units in the study area are quite variable. While the unit is unconformably overlain by the mudstones of the Simaki Formation of the Hazar Group around northeast of Hatunköy. Around Elazığ lithologically, the unit is an ophiolitic succession consisting of harzburgite, dunite, wehrlite, pyroxenite, gabbro, banded gabbro and diabase dykes cutting them. In the study area, serpentinized altered ultrabasic rocks present outcrops in the form of gabbro, diorite and diabases (Figure 3a-b).

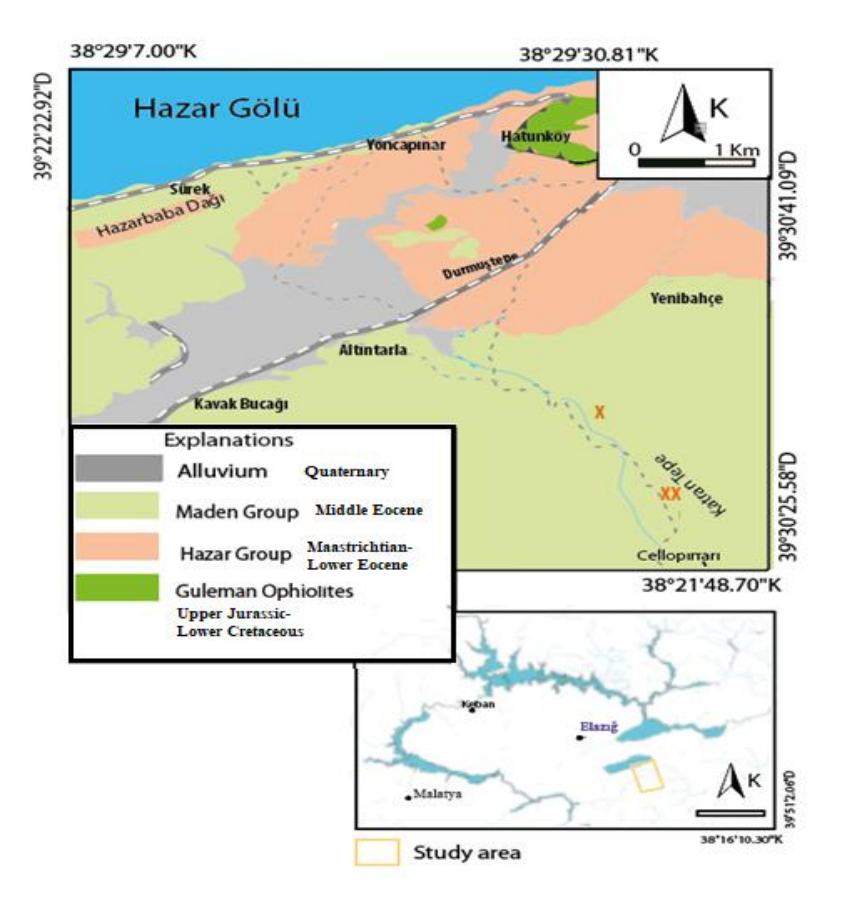


Figure 2: Geological map of the study area (modified from, Altay, 2016; Akkoca and Daş, 2018).

Hazar Group is present around Durmuştepe, Yoncapınar, Yenibahçe village. Perinçek (1979) and Tuna and Dülger (1979) named the unit as the "Hazar Complex", while Aktaş and Robertson (1984) divided the unit into three formations from bottom to top: The Ceffan Formation, the Simaki Formation and the Gehroz Formation at the top. The Simaki Formation crops out around Hatunköy, Yoncapınar and Durmuştepe. It is overlain by the Gehroz Formation, which consists of limestone and interbedded shale and sandstone (Figure 3c-d).

The Maden Group is located in the northwest and southeast of the study area. Yazgan (1983, 1984), Hempton (1984), Aktaş and Robertson (1985), Yazgan and Chessex (1991), Yiğitbaş and Yılmaz (1996) named it as "Maden Complex". The Maden Group begins with basalt. Green sandstone, silicified red chert, and red mudstone become dominant upwards in the study area (Figure 3e-f). In the study area, manganese mineralizations developed in the form of lenses, heads and layers within the red mudstone of the Maden Group (Figure 4a-b). Plio-Quaternary sediments and young alluviums are the youngest units around the area.

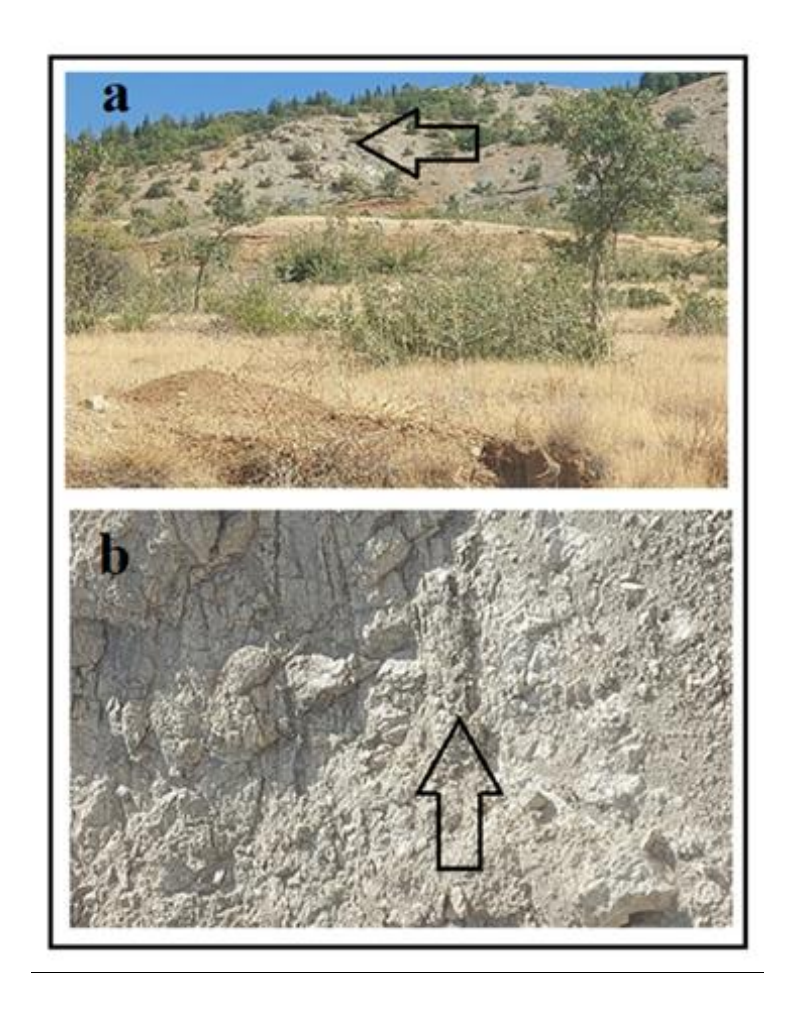


Figure 3a.b: View from altered serpentines of Guleman Ophiolites



Figure 3. c-d Interbedded shale and sandstone from Hazar Group e-f: The red mudstones of the Maden Group.

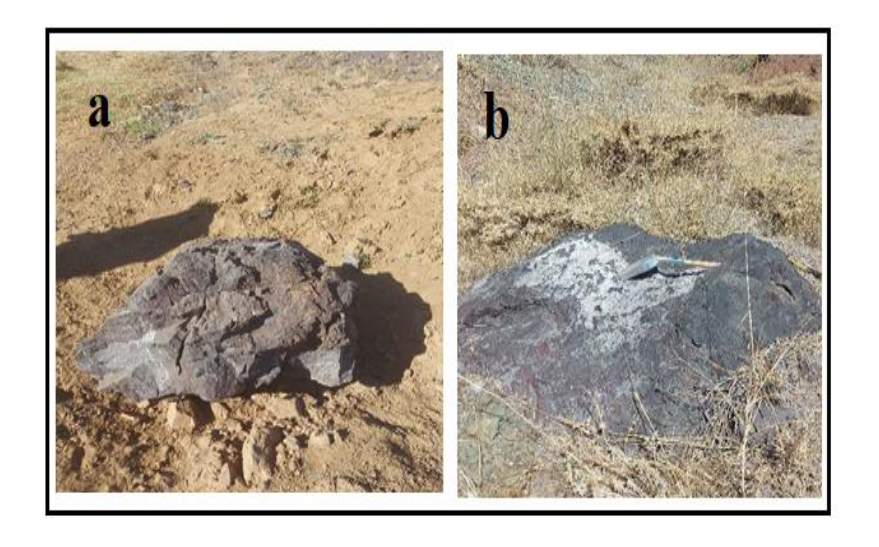


Figure 4 a-b: A view from the Durmuştepe mineralization heads

### **METHODS**

Sampling was done during field studies. Element analyzes were carried out on the samples Preparation of the samples were carried out in science and technology research and application center in the Bozok University, Yozgat Laboratories, Biltem. Major oxides (SiO<sub>2</sub>, Al<sub>2</sub>O<sub>3</sub>, Fe<sub>2</sub>O<sub>3</sub>, MgO, CaO, K<sub>2</sub>O, TiO<sub>2</sub>, P<sub>2</sub>O<sub>5</sub>) analyses were carried out on XRF on representative samples of the host rock. Trace elements Ba, Sc, V, Zr, Rb, Sr, Nb, Hf, Th were measured using inductively coupled plasma-mass spectrometry (Thermo Scientific ICAPQC, USA). This study compared previous studies which are Hatunköy wall rocks (from Akkoca and Daş, 2018), Durmuştepe wall rocks, Durmuştepe ore (Altay, 2016), Topaluşağı ore (Öztürk, 2008).

### RESULTS AND DISSCUSSIONS

### **Major Oxide Element**

The element concentrations are given in Table 1-2, Fig.5a-b.

Table 1: Table of major elements (% weight) of samples. LOI: Loss on Ignition. Ore, Topaluşağı, Ore Durmuştepe, Durmuştepe wall rock, Hatunköy wall rock. VC: Coefficient of Variation (%).

	6:0	41.0	E O	M.O	0.0	N. O	I/ O	T'O	C 0	М 0
-	SiO <sub>2</sub>	Al <sub>2</sub> O <sub>3</sub>	Fe <sub>2</sub> O <sub>3</sub>	MgO	CaO	Na <sub>2</sub> O	K <sub>2</sub> O	TiO <sub>2</sub>	Cr <sub>2</sub> O <sub>3</sub>	Mn <sub>2</sub> O <sub>3</sub>
3	43,97	19,74	6,65	14,21	2,37	2,02	1,56	0,76	0,04	0,36
7	41,82	19,36	10,09	9,39	3,32	1,60	1,10	0,95	0,05	1,85
12	44,42	21,58	10,22	6,39	2,93	1,21	1,23	0,99	0,048	0,23
22	44,79	20,82	8,83	4,38	5,88	1,41	1,44	1,04	0,02	0,12
30	45,02	18,14	14,36	4,43	3,01	3,59	0,98	1,64	0,040	1,06
35	42,90	21,04	8,32	12,18	1,79	1,35	2,85	0,96	0,02	0,68
max	45,02	21,58	14,36	14,21	5,88	3,59	2,85	1,64	0,05	1,85
min	41,82	18,14	6,65	4,38	1,79	1,21	0,98	0,76	0,02	0,12
average	43,82	20,11	9,75	8,50	3,22	1,86	1,53	1,06	0,04	0,72
St. Deviation	1,23	1,27	2,61	4,12	1,41	0,89	0,68	0,30	0,01	0,65
Variation Coefficiant	2,82	6,33	26,79	48,51	43,92	47,83	44,70	28,46	35,54	110,33
Ore Topaluşağı	23,18	3,64	64,31	1,05	11,05	0,08	0,08	0,12	0,005	
Ore Durmuştepe	22,85	4,33	33,36	0,92	10,56	0,05	0,18	0,17	0,009	
Durmuştepe hostrock	48,71	17,1	8,74	6,99	2,75	4,46	0,23	0,81	0,05	
Hatunköy hostrock	50,88	13,75	7,28	3,79	8,52	1,45	1,6	0,86	0,01	
PAAS	32,8	18,9	6,5	2,2	1,3	1,2	3,7	1	0,007	

In the samples under study, SiO<sub>2</sub> ranges from 41.82% to 45.02%, with an average value of 43.82%. SiO<sub>2</sub> is close to the Durmustepe wall rock (48.71%) and Hatunköy wall rock. According to this study, it is lower in the Topalusağı ore (23.18%) and Durmustepe ore (22.85%). This indicates that SiO<sub>2</sub> is high in the wall rock and lower in the ore (Fig. 5a). Al always represents an aluminosilicate mineral in most deposits. In the samples under study, Al<sub>2</sub>O<sub>3</sub> ranges from 18.14% to 21.58%, with an average value of 20.11%. This is close to the Durmustepe wall rock (17.1%) and Hatunköv wall rock (%13.75). It is lower in the Topaluşağı ore (3.64) and Durmuştepe ore (4.33%) according to this study. It is close to the Durmustepe wall rock (8.74%) and Hatunköy wall rock (7.28%). According to this study, it is higher in Topalusağı ore (64.31%) and Durmustepe ore (33.36%). It is richer in soils derived from mafic rocks (Kabata-Pendias, 2001). In the samples under study, Fe<sub>2</sub>O<sub>3</sub> is between 6.65% and 14.36%, with an average value of 9.75%. It is close to the Durmustepe wall rock (8.74%) and the Hatunköy wall rock (7.28%). According to the log (SiO<sub>2</sub>/Al<sub>2</sub>O<sub>3</sub>) value versus log Fe<sub>2</sub>O<sub>3</sub>/K<sub>2</sub>O (Herron, 1988) diagram, the reason why the samples fall into the Fe-rich shale area is that the samples are Fe-rich mafic rocks (Figure 5c).

Metalliferous sediments must meet the following three conditions: [Fe/(Al + Fe + Mn)] > 0.5, [Al/(Al + Fe + Mn)] < 0.3 and [(Fe + Mn)/Al] > 2.5(Boström et al., 1973). Accordingly, it has been revealed that the sediments are sediments affected by hydrothermal activity (Table 2). The average MgO element in this study is 8.50%, 1.05% in ore Topaluşağı, 0.92% in ore Durmustepe, 6.99% in Durmustepe wall rock, and 3.79 % in Hatunköy wall rock. It is low in the ore. In the samples, CaO ranges from 1.79% to 5.88%, with an average value of 3.32%. It is close to the Durmuştepe wall rock (2.75%) and Hatunköy wall rock (8.52%). It is higher in the Topaluşağı ore (11.05%) and Durmustepe ore (10.56%) according to this study. In the samples, Na<sub>2</sub>O ranges from 1.21% to 3.59%, with an average value of 1.86. It is close to the Durmuştepe wall rock (4.46%) and Hatunköy wall rock (1.45%). It is lower in the Topalusağı ore (0.08%) and Durmustepe ore (0.05%) according to this study. In the samples under study, Na<sub>2</sub>O ranges from 0.83% to 3.59%, with an average value of 1.86. It is close to the Durmuştepe wall rock (4.46%) and Hatunköy wall rock (1.45%). It is lower in the Topaluşağı ore (0.08%) and Durmuştepe ore (0.05%) according to this study. TiO<sub>2</sub> ranges from % 0.76 to %1.64, with an average value of 1.06%. It is close to the Durmuştepe wall rock (0,81%) and Hatunköy wall rock (0.86%). Cr<sub>2</sub>O<sub>3</sub> ranges from % 0.02 to 0.05%, with an average value of 0.04%. It is close to the Durmuştepe wall rock (0.05%) and Hatunköy wall rock (0.01). It is lower in the Topaluşağı ore (0.005%) and Durmuştepe ore (0.009%) according to this study.

**Table 2:** The Fe/(Al + Fe + Mn), [Al/(Al + Fe + Mn)], [(Fe + Mn)/Al] element ratios and Mn values of the sediments are given in the heavy metals section below.

Örnekler	[Fe/(Al + Fe + Mn)] > 0.5	[Al/(Al + Fe + Mn)] < 0.3	[(Fe + Mn)/Al] > 2,5
D3	0,74	0,21	3,66
D7	0,73	0,13	6,91
D12	0,87	0,10	8,53
D22	0,71	0,27	2,72
D30	0,76	0,18	4,66
D35	0,83	0,09	9,77
Average	0,78	0,18	5,74

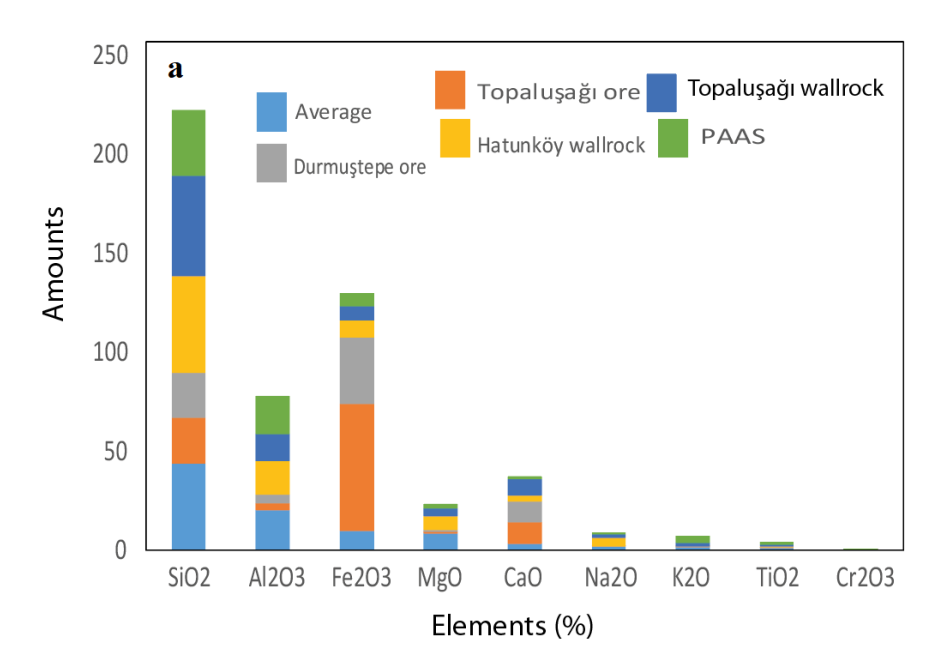


Figure 5a:Major element concentration of (% weight) of samples. Topaluşağı ore, Durmuştepe ore, Durmuştepe wall rock, Hatunköy wall rock.

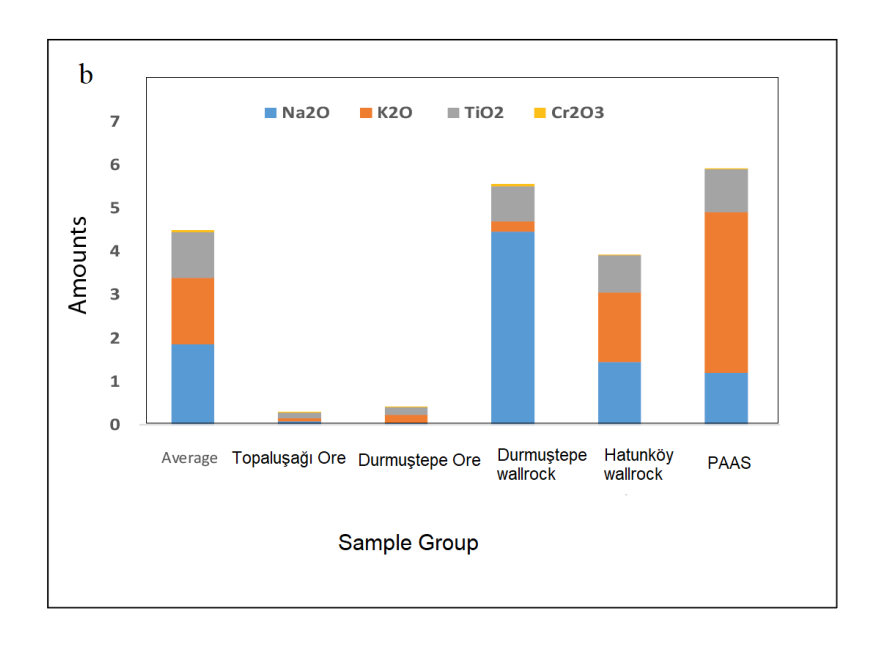


Figure 5b continue: Major element concentration of (% weight) of samples. Topaluşağı ore, Durmuştepe ore, Durmuştepe wall rock, Hatunköy wall rock.

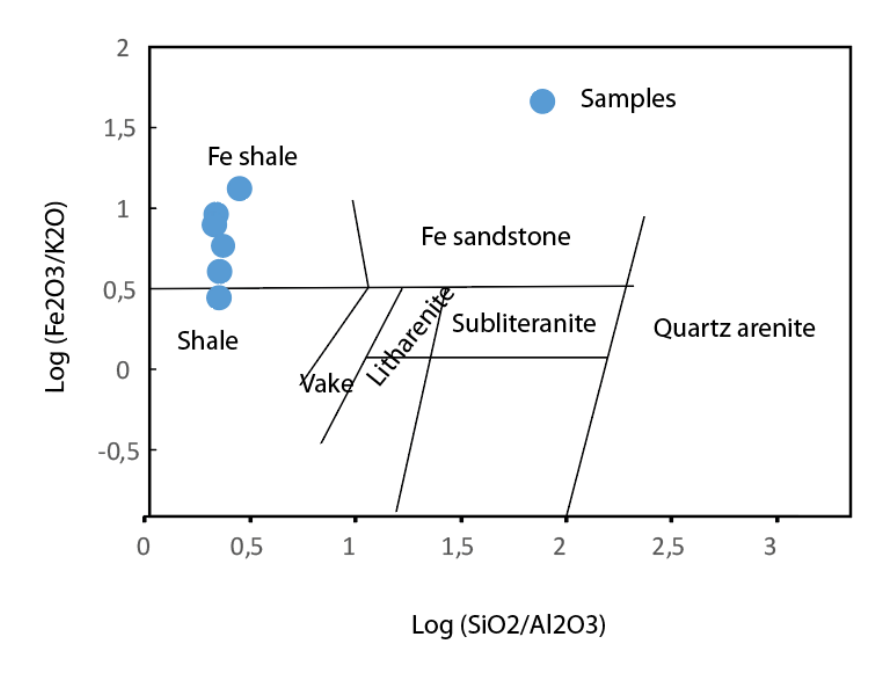


Figure 5c continue: the Log ( $SiO_2/Al_2O_3$ ) value versus Log  $Fe_2O_3/K_2O$  (Herron, 1988) diagram of samples

### **Trace Elements**

Trace element analyses of the samples are given in Table 3 and Figure 6, and correlation of trace elements were given in Tale 4. Correlation graphics of some trace elements are shown in Figure 7.

Table 3: Table of trace element (ppm) samples. Topaluşağı ore, Durmuştepe ore, Durmuştepe wall rock, Hatunköy wall rock.

Sample No:	Ba	Sc	V	Y	Zr	Rb	Sr	Nb	Hf	Th
3	190	11,53	206,78	22,43	81,61	35	55,91	4,3	1,9	3,06
7	131	5,79	208,13	32,21	78,57	87,5	197,88	3,14	1,64	3,08
12	212	9,99	218,8	18,46	68,53	36,9	91,27	3,73	1,5	3,12
22	157	11,13	155,75	36,91	74,61	14,3	114,7	4,02	1,71	3,41
30	156	27,33	253,16	61,43	109,51	13,7	131,64	8,51	2,78	3,47
35	211	6,64	209,09	11,32	40,57	72,7	139,4	2,91	0,95	3,05
max	212	27,33	253,16	61,43	109,51	87,5	197,88	8,51	2,78	3,47
min	131	5,79	155,75	11,32	40,57	13,7	55,91	2,91	0,95	3,05
average	176,17	12,07	208,62	30,46	75,57	43,35	121,80	4,44	1,75	3,20
St. Deviation	30,28	7,16	28,54	16,22	20,30	27,82	43,82	1,88	0,55	0,17
Variation Coefficiant	17,19	59,29	13,67	53,25	26,86	64,18	35,97	42,47	31,35	5,41
Ore Topaluşağı	193,7		1188	109,35	82,7			4,8	1,05	
Ore Durmuştepe	110	21,83	160	24,33	99,12	38,12	101,87	8,1	2,93	3,6
Durmuştepe hostrock	67,5		237	29,5	103		•••	3,65	2,5	
Hatunköy hostrock	114,257		623,6	127,7	66,9		449,6	3,2		1,3

In the samples under study, Ba ranges from 131 to 212 ppm, with an average value of 176,17 ppm. It is low compared to the Durmuştepe wall rock (67.5 ppm) and close to the Hatunköy wall rock (114.25 ppm). It is high in the Topaluşağı ore (193.7 ppm) and low in the Durmuştepe ore (110 ppm), according to this study. The high Ba level compared to the wall rock and ore can be explained by adsorption of Ba by manganese and hydroxides in the sediments. Because Ba is concentrated in Mn and P concretions and is primarily absorbed on oxides and hydroxides, it is not very mobile (Kabata-Pendias, 2001).

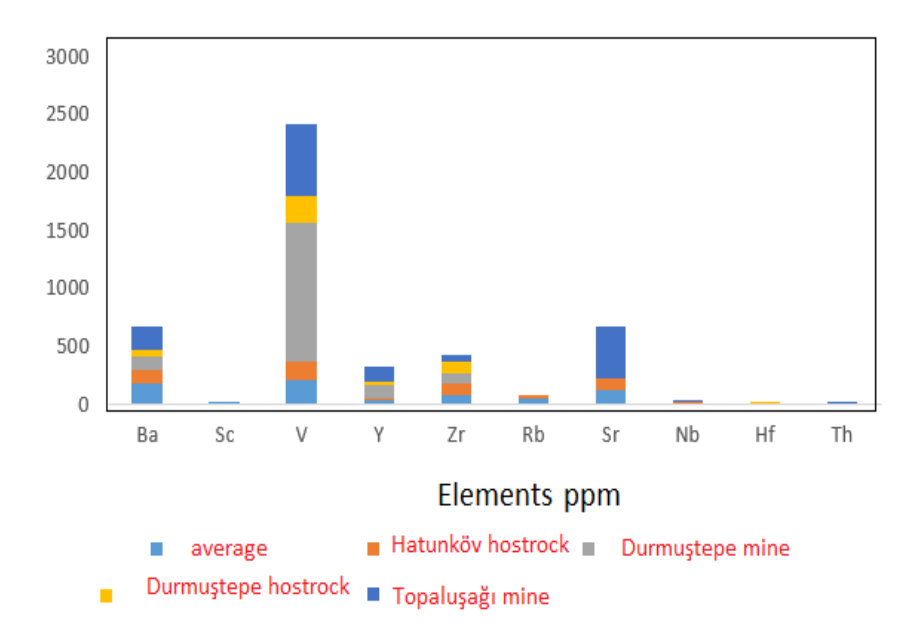


Figure 6.a.b. Trace element concentration of (ppm) of samples. Topaluşağı ore, Durmuştepe ore, Durmuştepe wall rock, Hatunköy wall rock.

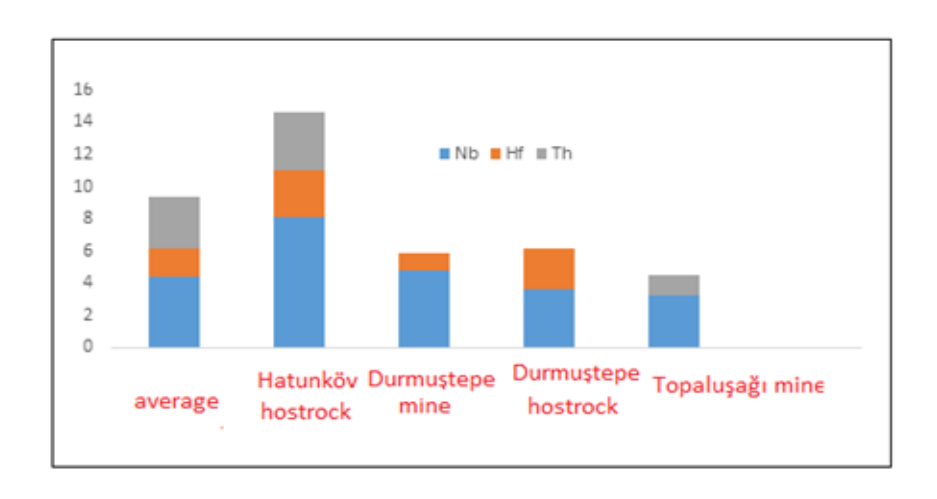


Figure 6.c. Continue. Trace element concentration of samples. Topaluşağı ore, Durmuştepe ore, Durmuştepe wall rock, Hatunköy wall rock.

Tablo 4. Correlation analysis between trace elements (P<0.05)

	Ba	Sc	V	Y	Zr	Rb	Sr	Nb	Hf	Th
Ba	1,00									
Sc	-0,21	1,00								
$\mathbf{V}$	0,10	0,58	1,00							
Y	-0,69	0,85	0,33	1,00						
Zr	-0,59	0,80	0,42	0,89	1,00					
Rb	-0,03	-0,71	0,03	-0,53	-0,55	1,00				
Sr	-0,61	-0,17	0,08	0,22	-0,04	0,62	1,00			
Nb	-0,28	1,00	0,61	0,87	0,84	-0,65	-0,10	1,00		
Hf	-0,50	0,90	0,48	0,91	0,98	-0,63	-0,10	0,93	1,00	
Th	-0,45	0,77	0,01	0,86	0,64	-0,77	0,02	0,75	0,71	1,00

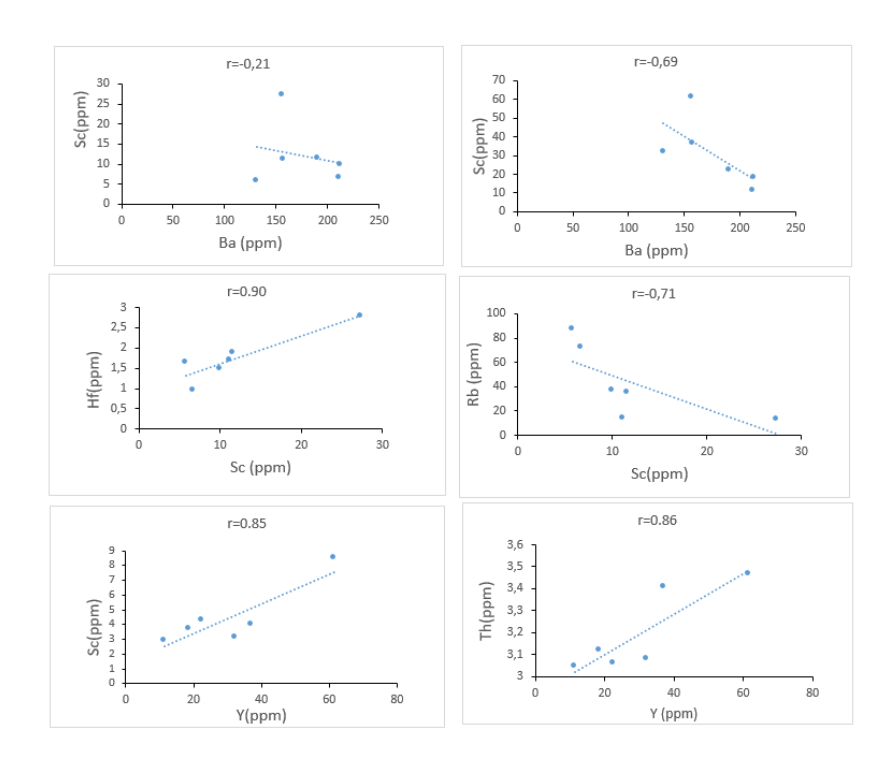


Figure 7. Correlation analysis of some trace elements

Scandium has a dispersed lithophile behavior and rarely forms minerals in which it is a significant constituent. The relatively large ionic radius of Sc<sup>3+</sup> generally precludes favorable substitution for Al and Fe in rocks, but most Sc in the lithosphere is retained in ferromagnesian minerals, particularly Fe-rich pyroxenes, where Sc<sup>3+</sup> replaces Fe<sup>3+</sup>. In contrast, Sc levels are low in olivine because Sc<sup>3+</sup> cannot substitute for Fe<sup>2+</sup>. Sc ranges from 5.79 ppm to 27.33 ppm, with an average value of 12.07 ppm. High V values are indicative of mafic rocks. Although defined as a trace element, V is relatively abundant in igneous rocks, although it rarely forms independent minerals (Kabata-Pendias, 2001). This is due to the positive correlations between V and Fe (r=0.55), V and Sc, and V and Ti. The positive correlation between V and Zr, Nb, Hf, and Th reflects the association of these elements in silicates. The highest V concentrations are found in soils developed on mafic rocks (150 to 460 mg kg<sup>-1</sup>). In the samples under study, V is between 155.75 ppm and 253.16 ppm with an average value of 208.62 ppm. It is close to the Durmuştepe wallrock (237 ppm) and the Hatunköy wallrock (160 ppm). According to this study, it is higher in the Topaluşağı ore (623.6 ppm) and Durmustepe ore (1188 ppm) (Table 3).

Yttrium enrichment has been reported in laterite and oolitic ferromanganese deposits (McLennan and Murray, 1999). The geochemical behavior of Y is most similar to that of heavy REEs. In the samples under study, Y ranges from 11.32 ppm to 61.43 ppm, with an average value of 30.46 ppm. It is close to the Durmustepe wall rock (24.33 ppm). According to this study, it is higher in the Topaluşağı ore (127.7 ppm) and Durmuştepe ore (109.35 ppm). The positive correlation of Y with Zr, Nb, Hf, and Th reflects the association of these elements in silicates. Zirconium is a lithophile metallic element, forming zirconium ZrSiO<sub>4</sub>. It can replace Ti in ilmenite and rutile and is also found at trace levels in clinopyroxene, amphibole, mica, and garnet. Felsic igneous rocks are generally rich in Zr compared to mafic lithologies. The positive correlation of Zr with Hf, Nb, and Th indicates that they are incorporated into silicates (Table 4). In the samples under study, Zr ranges from 40.57 ppm to 109.51 ppm, with an average value of 75.57 ppm. It is close to the Durmuştepe wall rock (103 ppm) and Hatunköy wall rock (99.12 ppm). The Topaluşağı ore (99.12ppm) and Durmuştepe ore (82.7 ppm) are close to those in this study (Table 3). Because Rb<sup>+</sup> has a larger ionic radius and therefore behaves incompatibly, it condenses in the late stage and differentiates in magmatic systems. In the samples under study, Rb ranges from 17.9 ppm to 87.5 ppm, with an average value of 43.35 ppm. It is at 38.2 ppm in the Hatunköy wall rock (Table 3). Strontium is a lithophile metallic element. During magmatic processes, Sr partitions into intermediate-stage fractions and therefore tends to be enriched in transitional rocks (approximately 500 mg kg<sup>-1</sup>) compared to evolved granites (<300 mg kg<sup>-1</sup>) or mafic igneous rocks (<450 mg kg<sup>-1</sup>). Mielke (1979) reported crustal Sr levels of 384 mg kg<sup>-1</sup> on average in ultramafic, basaltic, and granitic rocks. In the samples under study, Sr ranges from 55.91 ppm to 197.88 ppm, with an average value of 101.87 ppm. Sr is higher in the ore. Nb also replaces Ti in its compounds and is therefore found in above-normal concentrations in areas with mafic rocks. The Nb abundance in the crust has been estimated at 20 mg kg<sup>-1</sup> (Wedepohl 1978), based on averages of 22 mg kg<sup>-1</sup> for granitic rocks, granodiorite and diorite; 10 mg kg-1 for gabbro and basalt; 100 mg kg-1 for syenite and alkaline rocks; and 1.5 mg kg<sup>-1</sup> for peridotite. Wedepohl (1978) reported Nb value of 17 mg kg<sup>-1</sup> in clayey rocks. Mn nodules provide data and average values in the range of 32–41 mg kg<sup>-1</sup> Nb. In the samples under study, Nb ranges from 2.91 ppm to 8.51 ppm, with an average value of 4.44 ppm. It is close to the Durmuştepe wall rock (3.65 ppm) and the Hatunköy wall rock (3.2ppm). The positive correlation between Nb and Hf and Th reflects the association of these elements in silicates. Hafminium and zirconium have very similar geochemical properties because the ionic radius of Hf is almost the same as that of Zr. In general, igneous and metamorphic rocks contain very small amounts of Hf. Ultramafic rocks are typically <1 mg kg<sup>-1</sup>, mafic rocks up to 2 mg kg<sup>-1</sup>, and intermediate rock types between 2 and 4 mg kg<sup>-1</sup>. Hf content in soil varies from 1.8 to 18.7 mg kg<sup>-1</sup> depending on the host rock type

(Kabata-Pendias, 2001). This is why Hf and Zr show a very high positive correlation (r=0.97). Hf and Nb also show a positive correlation (r=0.72, Table 4). In the samples under study, Hf ranged from 0.95 ppm to 2.78 ppm, with an average value of 1.75 ppm. It is close to the Durmuştepe wall rock (2.5 ppm) and the Hatunköy wall rock (2.93 ppm). Th is generally higher in granitic than mafic igneous rocks. Because it can incorporate into some rock-forming minerals such as biotite, it is not as heavily concentrated in the discordant pegmatite phase as U. However, some Th-bearing minerals. High Th values therefore indicate the presence of felsic rocks, particularly intrusive rocks. In the samples under study, Th ranges from 3.05 to 3.47 ppm, with an average value of 3.20 ppm. The positive correlation between Hf and Th reflects the association of these elements in silicates.

Some element ratios of the samples are shown in Table 5. According to the Th/Sc Th/Cr, Th/Co ratios, it can be said that the samples have mafic rock composition.

Table 5: Comparison of some element ratios of the samples compared with Cullers (2002).

Sample	Th/Sc		Sample	Th/Cr		Sample	Th/Co	
3	0,265316	intermediate	3	0,012768	mafic	3	0,106659	mafic
7	0,531763	intermediate	7	0,015341	mafic	7	0,086314	mafic
12	0,312401	intermediate	12	0,013836	mafic	12	0,093546	mafic
30	0,126969	intermediate	30	0,095036	mafic	30	0,105599	mafic
35	0,45964	intermediate	35	0,048257	mafic	35	0,152543	mafic

Sediment Aralığı				
	Felsic rocks	Mafic rocks		
Th/Sc	0.64-20.35	0.05-0.4		
Th/Cr	0.067-4.0	0.002-0.046		
Th/Co	0.3-19.4	0.04-1.40		

According to the Zr/Sc-Th/Sc diagram of the samples, it was revealed that they were in the andesite and basalt range (Figure 8).

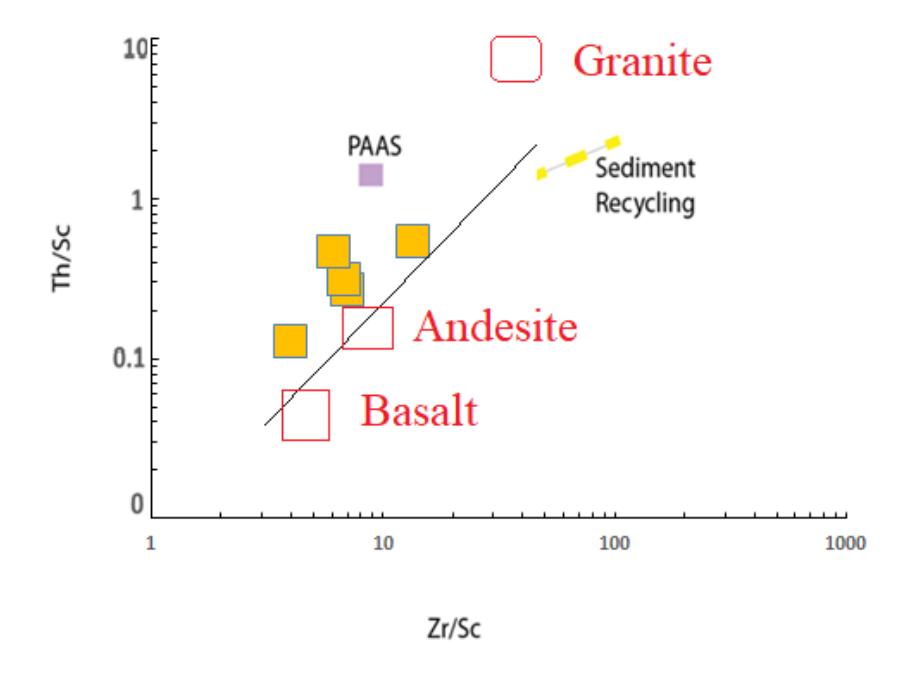


Figure 8: Distribution of samples in the Zr/Sc-Th/Sc diagram

### **CONCLUSIONS**

Geochemistry of the Mn bearing sediments around Durmuştepe village (Maden-Elazığ) were investigated in this study. For this purpose, samples were taken around the Durmuştepe village. The units cropping out in the study area, from older to younger, Upper Jurassic-Lower Cretaceous Guleman Ophiolites, Maastrichtian-Lower Eocene Hazar Group, Middle Eocene Maden Group, Quaternary alluviums.

Geochemistry of these studied rocks were compared with previous studies which are in surrounding rocks, and mining rocks.  $SiO_2$  is high in the wall rock and lower in the ore.  $Al_2O_3$  is close to the Durmuştepe wall rock and Hatunköy wall rock and is lower in the Topaluşağı ore and Durmuştepe ore.  $Fe_2O_3$  is close to the Durmuştepe wall rock and the Hatunköy wall rock. According to the log  $(SiO_2/Al_2O_3)$  value versus log  $Fe_2O_3/K_2O$  the samples fall into the Fe-rich shale area is that the samples are Fe-rich mafic rocks. Accordingly Fe/(Al + Fe + Mn), Al/(Al + Fe + Mn) and [(Fe + Mn)/Al] sediments are affected by hydrothermal activity. MgO element is low in the

ore. CaO is close to the Durmuştepe wall rock and Hatunköy wall rock and is higher in the Topaluşağı ore and Durmuştepe ore. Na<sub>2</sub>O is close to the Durmuştepe wall rock and Hatunköy wall rock and is lower in the Topaluşağı ore and Durmuştepe ore. Na<sub>2</sub>O is close to the Durmuştepe wall rock and Hatunköy wall rock and is lower in the Topaluşağı ore and Durmuştepe ore. Na<sub>2</sub>O is close to the Durmuştepe wall rock and Hatunköy wall rock and it is lower in the Topaluşağı ore and Durmuştepe ore. Cr<sub>2</sub>O<sub>3</sub> is close to the Durmuştepe wall rock and Hatunköy wall rock and is lower in the Topaluşağı ore and Durmuştepe ore.

Ba is low compared to the Durmuştepe wall rock and close to the Hatunköy wall rock. It is high in the Topaluşağı ore and low in the Durmuştepe ore. The positive correlation between V and Zr, Nb, Hf, and Th reflects the association of these elements in silicates. V is close to the Durmuştepe wall rock and is higher in the Topaluşağı ore and Durmuştepe ore. Y is close to the Durmuştepe wall rock and Hatunköy wall rock. it is higher in the Topaluşağı ore . The positive correlation of Y with Zr, Nb, Hf, and Th reflects the association of these elements in silicates. Zr is close to the all rock type. The Topaluşağı ore and Durmuştepe ore are close to those in this study. Sr is higher in the Hatunköy hostrock. Hf and Nb also show a positive correlation. The positive correlation between Hf and Th reflects the association of these elements in silicates. According to the Th/Sc Th/Cr, Th/Co ratios, it can be said that the samples have mafic rock composition. According to the Zr/Sc-Th/Sc diagram of the samples, it was revealed that they were in the andesite and basalt range.

## Acknowledgement

This study was supported by Fırat University-Scientific Research University-(FÜBAP) master's thesis research project number MF.24.84. We would like to thank FÜBAP unit

### REFERENCES

- Akkoca, D.,B. and Daş, B. (2018). Hatunköy (Hazar Gölü'nün doğusu, elazığ) civarindaki denizel sedimanter ve volkanosedimanter kayaçların jeokimyasal özellikleri. Fırat Üniversitesi Mühendislik Bilimleri Dergisi, 30(2), 49-61.
- Akkoca, D.,B., Eriş, K.K., Çağatay, M.N., and Biltekin, D. (2019). The mineralogical and geochemical composition of Holocene sediments from Lake Hazar, Elazığ, Eastern Turkey: implications for weathering, paleoclimate, redox conditions, provenance, and tectonic setting. Turkish Journal of Earth Sciences, 28 (5), 760-785.
- Akkoca, D. B., Yıldırım, I., and Al-Juboury, A. I. (2024). Parent material, weathering and heavy metal contamination in the surface soils from basin infill sediments

- in Elazığ Industrial Area, Eastern Turkey. Journal of African Earth Sciences, 212 (10),105185.
- Aktaş, G. and Robertson A. H. Y. (1984). The Maden Complex, SE Turkey; Evolution of a Neotethyan Active Margin, In: J. E. Dixon and a. H. F., Robertson (Eds.), Geol. Soc. Spec. Publ. No: 17, 375-403.
- Aktaş, G.,and Robertson, A.H.F. (1990). Tectonic evolution of the Tethys suture zone in SE Turkey: evidence from the petrology and geochemistry of Late Cretaceous and Middle Eocene extrusive, In Ophiolites oceanic crustal analogues, (Edited by Moores, E.M., Panayiotou, A and Xenophontos), Proceeding of the International Symposium "Troodos 1987", Nicosia, Cyprus, Cyprus Geological Survey Department, 311-328.
- Altay, O. (2016). Durmuştepe- Hatunköy (Maden Elazığ) Çevresindeki Demir Ve Mangan Cevherleşmesinin Jeolojik İncelenmesi Yüksek Lisans Tezi. Selçuk Üniversitesi,
- Altunbey, M. and Sağıroğlu, A., (1995). Koçkale Elazığ manganez cevherleşmelerinin özellikleri ve kökeni. Maden Tetkik ve Arama Dergisi, 117, 139-148.
- Böström K. (1973). The origin and fate of ferromanganoan activeridge sediments. Stockholm Contr. Geol. 27, 149—243.
- Cullers, R.L. (2002). The geochemistry of shales, siltstones and sandstones of Pennsylvanian-Permian age, Colorado, USA: implications for provenance and metamorphic studies. Lithos, 51, 181-203.
- Hempton, M. R. (1984). Result of Detailed Mapping near Lake Hazar (Eastern Taurus Mountains). In O. Tekeli and C. Göncüoğlu (Eds)., Geology of the Taurus Belt. Proceedins
- Herron, M.M. (1988). Geochemical classification of terrigenous sands and shales from core or log data. Journal of Sedimentary Petrology, 58, 820–829.
- Kabata-Pendias, A. and Pendias, H. (2001) Trace Elements in Soils and Plants. 3rd Edition, CRC Press, Boca Raton, 403 p.
- Köküm, M., (2019). Landsat tm görüntüleri üzerinden doğu anadolu fay sistemi'nin palu (Elazığ)-Pütürge (Malatya) arasındaki bölümünün çizgisellik analizi. Gümüşhane Üniversitesi Fen (GÜFBED/GUSTIJ), 9 (1), 119-127.
- McLennan and S.M., Murray, R.W., (1999). Geochemistry of sediments. In: Encyclopedia of geochemistry. Marshall, C.P., Fairbridge, R.W. (Eds), Kluwer Academic Publishers, Dordrecht, The Netherlands. pp. 282-292.
- Mielke, J.E. (1979). Composition of the Earth's crust and distribution of the elements. In: Review of Research on Modern Problems in Geochemistry. F.R. Siegel (Ed.), UNESCO Report, Paris, pp. 13–37.
- Özkan, Y.Z. (1982). Guleman (Elazığ) Ofiyolitinin jeolojisi ve petrolojisi: İstanbul Yerbilimleri, 3, sayı 295-312, 1-2.
- Öztürk, N. (2008). Hazar Gölü (Sivrice-Elazığ) Doğusundaki Manganez Cevherleşmelerinin Jeolojik, Mineralojik Ve Jeokimyasal Özelliklerinin İncelenmesi Yüksek Lisans Tezi Jeoloji Mühendisliği Anabilim Dalı, 54s.
- Perinçek, D., (1978). GD Anadolu'da allokton birimler: 33. TJK Bilimsel ve Teknik Kurultayı bildiri özetleri, 115-116.
- Tuna, E. and Dülger, S. (1979). Elazığ-Palu-Pertek Bölgesinin Jeolojisi. TPAO Arşivi (yayınlanmamış), Rapor No: 1363.
- Wedepohl, K.K., (1978). Handbook of geochemistry. Volume 2, Part 5. Springer-Verlag Berlin Heidelberg, 1546 p.

- Yazgan, E. (1983). A geotraverse Between the Arabian Platform and the Munzur Nappes. Geology of the Taurus Belt, Int. Symp. Guide Book for Excursion V., 17, MTA Ankara.
- Yazgan, E. (1984). Geodynamics Evolution of the Southern Taurides in the Region. In: O. Tekeli and M. C. Göncüoğlu (Eds.), Geology of the Taurus Belt, Int. Symp., Proceedings, 199-208.
- Yazgan, E., and Chessex, R. (1991). Geology and tectonic evolution of the Southeastern Taurides in the region of Malatya. TPJD. Bült., 1-41. 26.
- Yiğitbaş, E. and Yılmaz, Y. (1996). New evidence and solution to the Maden complex controversy of the the Southeast Anatolian orogenic belt (Turkey). International Geology Review, 38(9): 818-831.

# Basic Applications in Simulink Environment for Raspberry Pi Pico W

Erdem ILTEN<sup>1</sup>

<sup>1-</sup> Assoc. Prof. Dr.; Balikesir University Faculty of Engineering Department of Electrical-Electronics Engineering. erdemilten@balikesir.edu.tr ORCID No: 0000-0002-9608-2148

### **ABSTRACT**

This study describes basic applications for the Raspberry Pi Pico W board in the Simulink environment. These applications include voltage measurement with a potentiometer, ambient light intensity measurement with an LDR, distance measurement with an ultrasonic sensor, sound intensity measurement with a microphone sensor, button-LED testing, relay testing, and buzzer testing. The block diagram, prepared using the *Simulink Support Package for Arduino Hardware* library, was loaded onto the Raspberry Pi Pico W board using the Simulink *Embedded Coder* tool. System tests were conducted in real-time using Simulink External Mode. All sensor information can be viewed on the PC screen via External Mode, on digital displays and dashboard scopes. Relay positions can be adjusted. A signal of any frequency can be applied to the buzzer. When the results are examined, it is seen that the experimental studies are successful.

Keywords – Raspberry Pi, Pico, Simulink, Embedded Coder, External Mode

### INTRODUCTION

The Raspberry Pi is a small, affordable, and versatile single-board computer developed by the Raspberry Pi Foundation in the United Kingdom. Originally introduced in 2012, its primary goal was to promote computer science education and make computing accessible to people around the world. Despite its compact size, the Raspberry Pi offers powerful processing capabilities, USB and HDMI connectivity, wireless communication, and general-purpose input/output (GPIO) pins that enable interaction with sensors, motors, and other electronic components (Ilten, 2024f, 2024c, 2024b). The Raspberry Pi can run various operating systems, most commonly Raspberry Pi OS (formerly Raspbian), based on Linux. It supports programming in several languages, such as Python, C, C++, Java, and Scratch, making it an ideal platform for both beginners and experienced developers. Due to its flexibility and low cost, it has become popular in numerous applications from robotics, home automation, and Internet of Things (IoT) projects to media centers, weather stations, and even small-scale servers (Küçükdermenci, 2023b, 2023a, 2024e). The introduction of newer models, such as the Raspberry Pi 4 and Raspberry Pi 5, as well as microcontroller versions like the Raspberry Pi Pico, has expanded its use cases even further.

The Raspberry Pi Pico W is a compact and cost-effective microcontroller board developed by the Raspberry Pi Foundation, designed to provide wireless connectivity and high performance for embedded systems and IoT applications. It is built around the RP2040 microcontroller chip, a dual-core ARM Cortex-M0+ processor running at 133 MHz, featuring 264

KB of on-chip SRAM and support for up to 16 MB of external Flash memory. The key advancement of the Pico W over the original Pico is the inclusion of Wi-Fi capability, enabled by the Infineon CYW43439 wireless chip, which supports IEEE 802.11 b/g/n wireless LAN. This addition allows users to develop connected applications such as remote sensing, cloud-based monitoring, and smart automation with ease. The board offers a wide range of input/output (I/O) interfaces, including SPI, I2C, UART, PWM, and ADC, making it versatile for controlling sensors, actuators, and communication devices. It can be programmed using multiple environments such as C/C++ SDK, MicroPython, or Arduino IDE, making it accessible to both beginners and advanced developers. Due to its low power consumption, compact design, and wireless connectivity, the Raspberry Pi Pico W is well-suited for various projects in education, prototyping, and IoT development. It represents an affordable and flexible platform for exploring embedded system concepts and building real-world applications that require both processing and connectivity (Debnath, Gusain, Sharma, & Pradhan, 2024; Halfacree & Everard, 2024; Loker, 2024; Mohammed, 2024).

Simulink is a graphical programming and simulation environment developed by MathWorks, designed for modeling, simulating, and analyzing dynamic systems (Ilten, 2024). Integrated with MATLAB, it provides an intuitive block diagram interface that allows users to design and visualize complex systems without the need for extensive programming. Simulink is widely used across engineering disciplines, particularly in control systems, signal processing, communications, mechatronics, and embedded system design. The primary advantage of Simulink lies in its model-based design approach, which enables engineers to represent mathematical models and physical systems using interconnected functional blocks. These blocks correspond to system components such as gains, integrators, summation points, and transfer functions. This visual representation simplifies the process of system development, simulation, and verification. Simulink also supports automatic code generation through tools such as Simulink Coder and Embedded Coder, allowing models to be deployed directly onto hardware platforms like Arduino (Küçükdermenci, 2024c, 2025; Küçükdermenci & Ilten, 2025), Raspberry Pi, and other microcontrollers (Küçükdermenci, 2024b, 2024a). This feature bridges the gap between simulation and real-time implementation, making it a powerful tool for both research and industrial applications.

Simulink Embedded Coder, developed by MathWorks, is an advanced code generation tool that extends the capabilities of MATLAB and Simulink for producing optimized, production-quality C and C++ code from Simulink models, Stateflow charts, and MATLAB functions. It is widely used in the design and deployment of embedded systems, particularly in fields such as

automotive, aerospace, robotics, and industrial automation (Ilten, 2023b, 2024a). Embedded Coder enables engineers to implement model-based design workflows efficiently, allowing for the automatic translation of graphical models into executable code suitable for real-time hardware. The generated code is highly efficient and customizable, meeting the performance and memory constraints of embedded processors and microcontrollers. It also supports integration with various embedded development environments, compilers, and real-time operating systems (RTOS). One of the key advantages of Embedded Coder is its support for processor- and board-specific optimizations, enabling seamless deployment to hardware platforms such as Arduino (Küçükdermenci, 2024d, 2024f), Raspberry Pi, ARM Cortex-based microcontrollers, and STMicroelectronics boards. Additionally, it provides advanced configuration options for data interfaces, code structures, and naming conventions, making it suitable for both rapid prototyping and production applications.

Simulink External Mode is an advanced feature of MATLAB/Simulink that enables real-time communication between a Simulink model running on a host computer and a target hardware device, such as an Arduino, Raspberry Pi, or other embedded controller (Ilten, 2025; Ilten & Unsal, 2024). It allows engineers and researchers to monitor signals, tune parameters, and observe system behavior in real time while the model executes on the hardware. This interactive capability greatly simplifies the process of testing and refining control algorithms in practical applications. In External Mode, the Simulink model is first compiled into executable code and deployed to the target hardware. The host computer then maintains a live communication link (typically over serial (USB), Wi-Fi, or Ethernet) to exchange data with the running system. This allows users to adjust parameters such as controller gains, reference signals, or filter coefficients during execution, without the need for recompiling or restarting the program. Such real-time tuning helps in achieving rapid prototyping, system optimization, and hardware-in-the-loop (HIL) testing. For instance, when used with an Arduino board, Simulink External Mode enables real-time control experiments such as DC motor speed and position control (Ilten, 2023a, 2024d, 2024e), sensor data acquisition, and PID controller tuning. The user can visualize sensor readings, adjust control parameters, and immediately observe changes in system response. Similarly, when integrated with a Raspberry Pi, External Mode can be used to develop IoT-enabled control systems, robotics applications, or smart automation projects, where wireless communication allows for convenient monitoring and tuning over a network. One of the key advantages of Simulink External Mode is its ability to create a closed-loop connection between the simulation environment and physical hardware. This allows for accurate verification of control strategies and system dynamics under real-world operating conditions, reducing the gap between simulation and deployment. It supports modelbased design workflows by enabling iterative development (designing, simulating, testing, and refining) directly within the same environment.

The paper is organized as follows. Simulink block diagrams prepared for Raspberry Pi Pico W explained in Materials and Method section. The results of the experimental studies are given in Results and Discussion section.

### MATERIALS AND METHOD

In this study, basic applications were implemented with the Raspberry Pi Pico W. These applications are voltage measurement with a potentiometer, distance measurement with an ultrasonic sensor, light intensity measurement with a light dependent resistor (LDR), sound intensity measurement with a microphone sensor, button-LED, relay, and buzzer applications, respectively. The general block diagram of the system is presented in Figure 1.

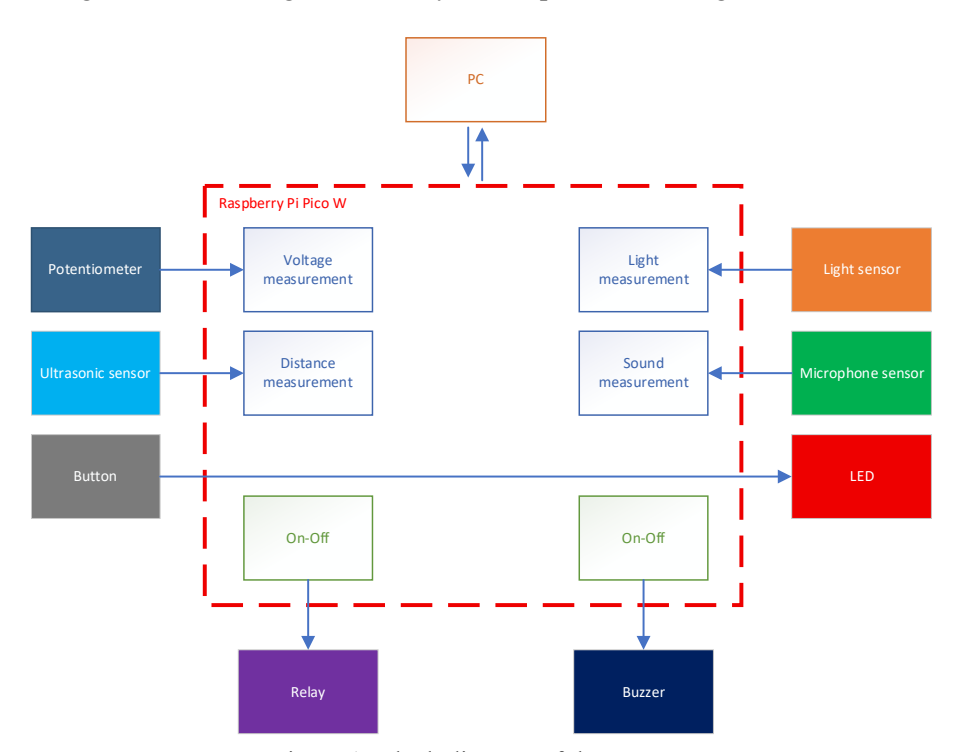


Figure 1: Block diagram of the system.

The experimental setup prepared for the system is given in Figure 2. The experimental setup consists of a Raspberry Pi Pico W board, a potentiometer, an LDR sensor, a buzzer, a push button, an LED (5mm red LED), a relay (HF46F), a microphone sensor card and an ultrasonic sensor card (HC-SR04).

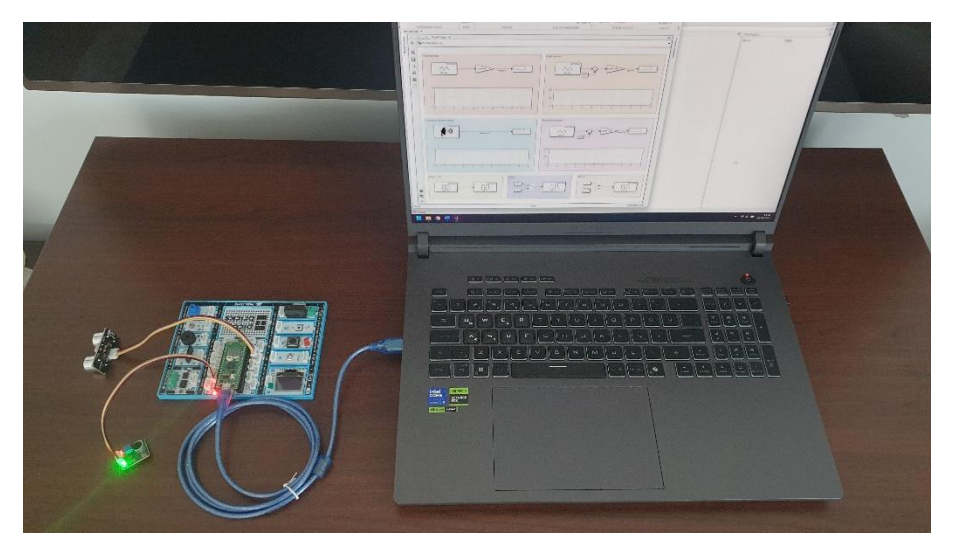


Figure 2: The experimental setup.

The potentiometer is connected to channel A0 on the Raspberry Pi Pico W board. The 3.3 Vdc supply voltage can be adjusted within the 0-3.3 Vdc range using the potentiometer. The Raspberry Pi Pico W has a 12-bit analog-to-digital converter module. It converts the 0-3.3 Vdc voltage to a value range of 0-4095. The following equation is used to convert the value read from the potentiometer back to voltage.

$$Voltage = A0 \cdot \frac{3.3}{4095} \tag{1}$$

Analog input A1 was used to measure ambient light intensity with an LDR. The digital value read via channel A1 was converted to a percentage of light intensity. The equation used for this conversion is below.

$$Light(\%) = \frac{4095 - A1}{4095} \cdot 100 \tag{2}$$

Analog input A2 was used to measure sound intensity using a microphone sensor. The measured value was converted to sound intensity as a percentage. The equations used for this conversion are given below.

Sound 
$$(\%) = \frac{4095 - A2}{4095} \cdot 100$$
 (3)

The HC-SR04 module is used as the ultrasonic sensor. Pin 15 is the trigger pin, and Pin 14 is the echo pin. The Ultrasonic Sensor block, found in the Simulink Arduino library, was used for measurement and calculation. The output of the block is in meters.

In the button-LED application, the LED lights up when the button is pressed. In the relay application, the relay position is changed by manually controlling the switch from the PC screen using the Simulink External Mode connection. In the buzzer application, control is also done with a manual switch via Simulink External Mode. When the switch is changed, a 1 kHz signal is applied to the buzzer. The Simulink Block diagram prepared for the system is presented in Figure 3.

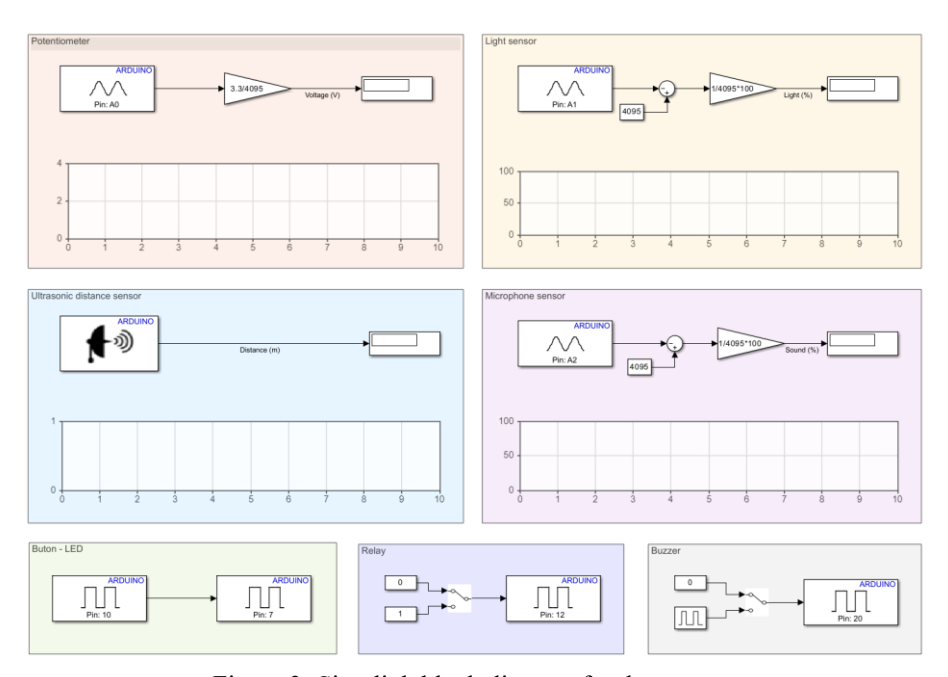


Figure 3: Simulink block diagram for the system.

In the block diagram in Figure 3, the potentiometer, LDR, and microphone are read via analog input channels A0, A1 and A2, respectively. These values are displayed on the digital display and dashboard scopes. The ultrasonic sensor is controlled via pins 15 and 16. Ultrasonic sensor information is also displayed on the digital display and dashboard scope. Pins 10 and 7 are used for the button-LED test. Pin 12 is used for the relay, and pin 20 is used for the buzzer.

### RESULTS AND DISCUSSION

Voltage measurement via potentiometer, ambient light intensity measurement with LDR, distance measurement with ultrasonic sensor, sound intensity measurement with microphone sensor, button-LED test, relay test and buzzer test were performed on the experimental setup. The block diagram prepared in the Simulink environment was compiled with *Embedded Coder* and loaded onto the Raspberry Pi Pico W board. Test data was monitored by establishing a real-time connection to the board via Simulink External Mode. Test results are presented in Figure 4.

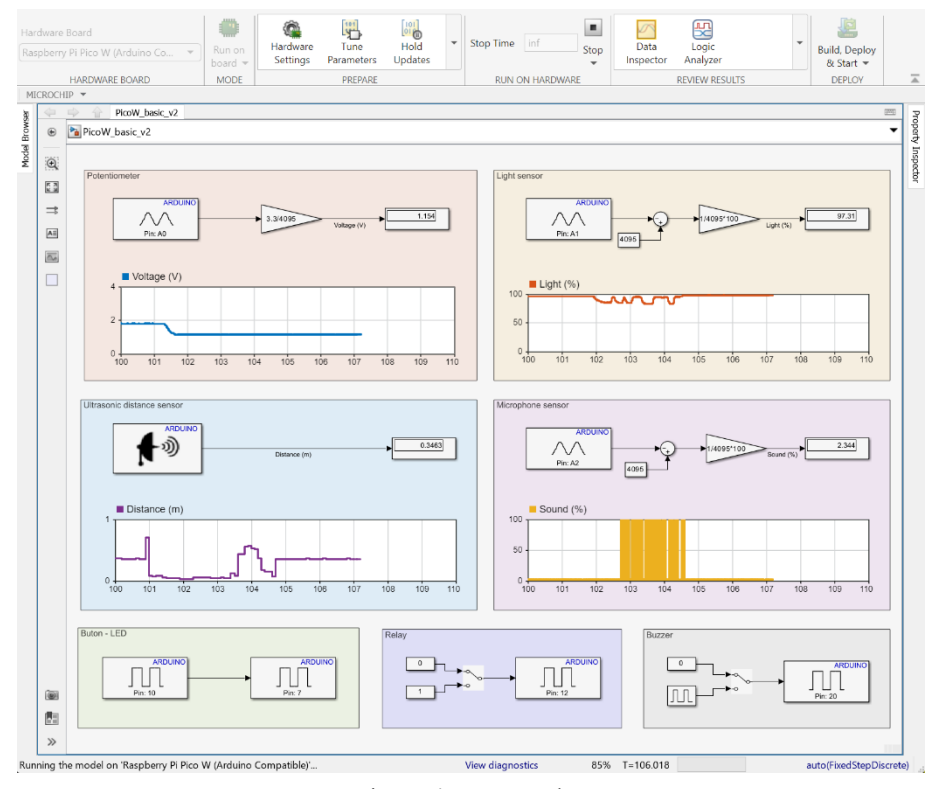


Figure 4: Test results.

Examining Figure 4, it is seen that the measured values were plotted with high accuracy and in real time. The controlled blocks (button-LED, relay, and buzzer) were observed to function correctly on the experimental setup.

### REFERENCE

Debnath, P., Gusain, A., Sharma, P., & Pradhan, P. M. (2024). MQTT Based Adaptive Estimation Over Distributed Network Using Raspberry Pi Pico W. *IEEE Embedded Systems Letters*.

- Halfacree, G., & Everard, B. (2024). Get Started with MicroPython on Raspberry Pi Pico: The Official Raspberry Pi Pico Guide. Raspberry Pi Press.
- Ilten, E. (2023a). Active Disturbance Rejection Control of a DC Motor with Raspberry Pi on Simulink External Mode. *2nd International Conference on Contemporary Academic Research*, 56–60.
- Ilten, E. (2023b). Permanent Magnet Synchronous Motor Control Interface Design and Implementation with TI F28335 DSP on Simulink External Mode. *International Conference on Applied Engineering and Natural Sciences*, *I*(1), 67–70.
- Ilten, E. (2024a). 2-DOF PID Speed Controller Application for PMSM with TI F28335 DSP and Simulink External Mode. *3rd International Conference on Scientific and Innovative Studies*, 286–291.
- Ilten, E. (2024b). Raspberry Pi Sense Hat Application on Simulink. In *New Trends and Frontiers in Engineering* (pp. 164–177). All Sciences Academy. https://doi.org/10.5281/zenodo.14016090
- Ilten, E. (2024c). Self-Excited Induction Generator Wireless Control Panel Design on Simulink External Mode with Raspberry Pi. *3rd International Conference on Engineering, Natural and Social Sciences*, 740–745.
- Ilten, E. (2024d). Sliding Mode Position Control Application for a DC Motor on Simulink External Mode with Raspberry Pi. 3rd International Conference on Frontiers in Academic Research, 74–79.
- Ilten, E. (2024e). Super-Twisting Sliding Mode Control Implementation for a DC Motor with Raspberry Pi and Simulink External Mode. *3rd International Conference on Scientific and Innovative Studies*, 280–285.
- Ilten, E. (2024f). Super-Twisting Sliding Mode Liquid Level Control Implementation for Raspberry Pi. In *Innovative Studies In Electrical, Electronic and Communication Engineering* (pp. 5–17).
- Ilten, E. (2025). 2-DOF PID Position Control Application for DC Motor with Arduino and Simulink External Mode. *4th International Conference on Trends in Advanced Research*, 166–171.
- Ilten, E. (2024). Synchronization of a 4D Hyperchaotic System with Active Disturbance Rejection Control and Its Optimization via Particle Swarm Algorithm. *Afyon Kocatepe University Journal of Sciences and Engineering*, 24(2), 465–475. https://doi.org/10.35414/akufemubid.1379669
- Ilten, E., & Unsal, M. E. (2024). Real-Time Gas Measurement System Desing and Implementation on Simulink External Mode with Arduino. *1. Bilsel International Sur Scientific Researches Congress*, 252–259. Diyarbakir.
- Küçükdermenci, S. (2023a). Raspberry Pi based braille keyboard design with audio output for the visually challenged. *Ist International Conference on Modern and Advanced Research ICMAR* 2023, 334–339. All Sciences Academy. https://doi.org/10.59287/icmar.1306
- Küçükdermenci, S. (2023b). Sign language voice convertor design using Raspberry pi for impaired individuals. *Proceeding Book of 1st International Conference on Recent and Innovative Results in Engineering and Technology ICRIRET 2023*, 160–166. All Sciences Academy. https://doi.org/10.59287/icriret.1395
- Küçükdermenci, S. (2024a). AVR mikrodenetleyicide zamanlayıcıların CTC modda programlanması. In *Innovative Studies in Engineering* (pp. 288–303). All Sciences Academy.
- Küçükdermenci, S. (2024b). AVR mikrodenetleyicide zamanlayıcıların normal

- modda programlanması. In *Innovative Studies in Engineering* (pp. 305–322). All Sciences Academy.
- Küçükdermenci, S. (2024c). Design of A Cost-Effective Weather Station with Rain Forecast. 2nd International Conference on Scientific and Innovative Studies, 909–916.
- Küçükdermenci, S. (2024d). Development of a Wireless Firefighting Robot with Obstacle Avoidance and Fire Extinguishing Modes. *3rd International Conference on Frontiers in Academic Research*, 1135–1141.
- Küçükdermenci, S. (2024e). Raspberry Pi-Based Real-time Parking Monitoring with Mobile App Integration. 5th International Conference on Engineering and Applied Natural Sciences, 1458–1464.
- Küçükdermenci, S. (2024f). Wireless Foot Pressure Monitoring System for Gait Rehabilitation. 5th International Conference on Engineering and Applied Natural Sciences, 1451–1457.
- Küçükdermenci, S. (2025). Design of a Hybrid PID-Feedforward Control System for Smart Greenhouse. 2nd International Conference on Modern and Advanced Research, 436–441.
- Küçükdermenci, S., & Ilten, E. (2025). Arduino Based Fire Extinguisher Vehicle Design and Application. *International Journal of Advanced Natural Sciences and Engineering Researches*, 9(2), 223–232. https://doi.org/10.5281/zenodo.14897860
- Loker, D. R. (2024). Data Acquisition Using the Raspberry Pi Pico W. 2024 ASEE Annual Conference & Exposition.
- Mohammed, H. J. (2024). IoT-Based Low-Cost Smart Health Monitoring System using Raspberry Pi Pico W and Blynk Application. *Journal of Engineering*, 30(07), 90–108.

# **Application of High-Entropy Perovskite Oxides in Enegy**

Fatma MEYDANERİ TEZEL

Prof. Dr.; Karabuk University, Faculty of Engineering and Natural Sciences, Department of Metallurgy and Materials Science Engineering, Karabuk/Turkey, E-mail: fatmameydaneri@karabuk.edu.tr, ORCID No: 0000-0003-1546-875X

### **ABSTRACT**

To address global challenges in the energy sector, the discovery, production, and use of new materials have gained prominence. High-entropy perovskite oxides (HEPOs), in particular, combine the advantages of perovskite oxides and high-entropy materials, offering significant potential for solving many important energetic challenges. This research highlights the potential of HEPOs in applications such as lithium-ion batteries, supercapacitors, and solid oxide fuel cells. Furthermore, a perspective on the further development and future innovations of HEPOs in energy applications is presented.

Keywords - High-entropy Perovskite Oxide, Energy, Battery, Supercapacitor

### INTRODUCTION

High-entropy perovskite oxides (HEPOs) have recently gained significant interest due to their unique structures and properties. HEPOs are formed by combining multiple primary elements within perovskite structures. Since the beginning of the Industrial Revolution, energy and environmental issues have come to the fore (Gani, 2021), and this has led to an increasing demand for renewable energy sources such as solar, geothermal, and tidal energy (Akkerman et al., 2016; Jia et al., 2019). To efficiently utilize these renewable resources, many new devices for electrochemical energy conversion and storage, including lithium-ion batteries (LIBs), supercapacitors (SCs), and solid oxide fuel cells (SOFCs), have been continuously developed.

Perovskites, characterized by their diverse element compositions, stable structures, and distinct electronic arrangements, have shown significant potential in electrochemical energy conversion and storage. This potential is evident in applications such as SCs (Da Silva et al., 2020), metalair batteries (Wang et al., 2019), and SOFCs (Abdalla et al., 2018). The term "perovskite" is named after the Russian mineralogist Lev Perovski, and its general chemical formula is ABO<sub>3</sub> (Locock and Mitchell, 2018). A-site cations, which generally have larger radii, such as rare earth elements and alkaline earth metal ions, form a dense structure with oxygen anions, resulting in the tightest packing. This plays an important role in supporting

the perovskite structure. In contrast, B-site cations, which generally have smaller radii, such as transition metals, are generally located at the centre of oxygen octahedra. These B-site cations have a wide range of oxidation states, which directly impacts their electrochemical performance (Oliveira et al., 2023). Due to their unique structure, perovskites have many advantages, such as high reversible redox capabilities, abundant oxygen vacancies, and highly tunable compositions. However, perovskites are at risk of severe degradation in adverse conditions such as high temperatures, high humidity, strong acidity or alkalinity, and high carbon dioxide levels (Trachenko et al., 2004). Two methods are commonly used to improve the stability of perovskites. The first approach involves adding a protective layer such as hydrophobic layers (Li et al., 2018) or thermal/optical/UV insulation (Wang et al., 2023-a) to protect the perovskite from these adverse conditions. An alternative strategy is to dope the perovskite with chemically neutral cations such as Zr, Nb, or Ta to increase its structural stability (Fang et al., 2011). However, both methods generally tend to increase costs and degrade performance. Therefore, there is a need to rapidly develop new methods to improve the stability of perovskites.

Since the identification of the entropy balancing effect, high-entropy materials have gained significant interest and experienced rapid development. These materials represent a new category of multicomponent materials, containing multiple elements in equimolar or near-equimolar ratios, challenging traditional material design approaches. Since the introduction of the high-entropy idea in 2004 (Yeh et al., 2004), a wide variety of high-entropy materials have been developed, such as high-entropy carbides (Jiang et al., 2020), high-entropy nitrides (Hahn et al., 2019), highentropy oxides (Berardan et al., 2016), and high-entropy sulfides (Zhang, Gucci et al., 2018). The high-entropy effect, heat conduction deterioration, slow diffusion processes, and mixed-component effects contribute to the high performance of high-entropy materials with their stable structures. High-entropy perovskite oxides (HEPOs), based on high-entropy design principles that provide increased stability compared to conventional materials, combine high configurationally entropy with the inherent multifunctionality of perovskites. Unlike older alloys, which typically consist of one or two primary elements, HEPOs incorporate at least five different elements. In particular, high-entropy perovskite oxides based on perovskite structures containing five or more cations contributing to the A or B domains have emerged. These oxides form perovskite phases driven by entropy, similar to the principles of high-entropy alloys (Chen et al., 2023). HEPOs have been shown to have improved ferroelectric relaxation (Fang et al., 2022; Guo et al., 2022-a; Shang et al., 2022; Sharma et al., 2022; Sun et al., 2022; Wang et al., 2023-b), decreased thermal conductivity (Liu et al., 2020; Liu et al., 2018; Xiong et al., 2022; Zhang et al., 2022), increased catalytic activity (Chu et al., 2022; Kante et al., 2023; Okejiri et al., 2020; Nguyen et al., 2021; Yang et al., 2022), and outstanding thermal and chemical durability (Dabrowa et al., 2020; Yang et al., 2021-a; Yang et al., 2021-b), higher proton conductivity (Gazda et al., 2020), increased oxygen permeability (Zhao et al., 2022), unique microstructures in magnetic materials (Sarkar et al., 2023), and a pronounced luminescence feature compared to conventional perovskite oxides (Corey et al., 2022). Highentropy perovskite oxides also accommodate diverse and tunable elemental compositions and stable structures of perovskite materials. This integration improves stability by increasing creep resistance, provides more active sites, and has the potential to yield unexpected results (Pikalova et al., 2022) (Figure 1).

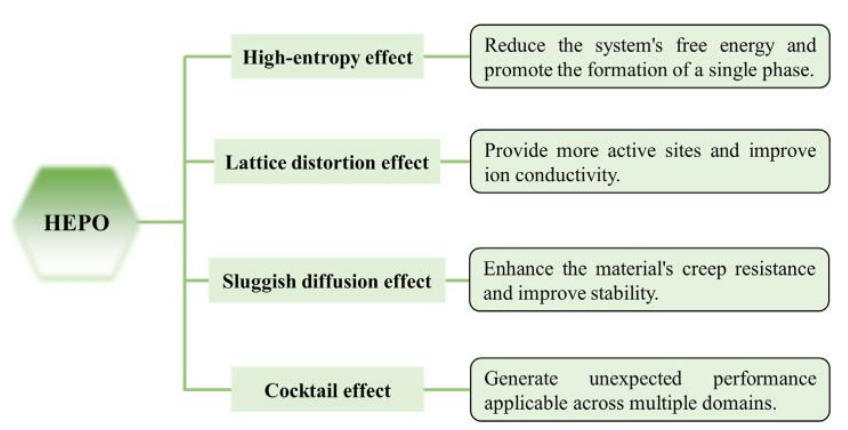


Figure 1: Four main effects of HEPOs and their possible consequences (Cao et al., 2024).

As a result, HEPOs offer potential solutions to challenges related to energy and performance; current endurance, thermal endurance. These include issues such as capacity retention and resistance after numerous charge and discharge cycles (Liu et al., 2023). These advantages led to the first use of

HEPOs in energy storage in 2020 (Yan et al., 2020). This emerging research area has the potential to overcome many barriers in electrochemical energy conversion and storage, thereby accelerating advances in the energy field.

### 2. Application of high-entropy perovskite oxides

### 2.1. Lithium-ion batteries

Among all energy storage devices, LIBs are among the most promising options due to their high efficiency (Song et al., 2020; Xiang et al., 2011; Zhao et al., 2020). A lithium battery is a rechargeable energy source that generally uses a lithium-containing material as an electrode and relies on the movement of lithium ions between the cathode and anode to provide energy. The components within the battery consist of a cathode, anode, separator, and electrolyte. LIBs are widely used in electronic and electrical products such as mobile phones, laptops, and electric vehicles (Chen et al., 2019; Jiang et al., 2020). However, the significant volume increase that occurs in LIBs during charging and discharging negatively affects their cycling performance and rapid capacity, limiting their industrial production and practical use. HEPOs, known for their high configurationally instability and staged lithium storage properties, maintain their structural integrity during cycling. This demonstrates superior lithium-ion storage performance and effective cycling stability.

Xie (Xie, 2024) produced La(Co<sub>0.2</sub>Cr<sub>0.2</sub>Fe<sub>0.2</sub>Mn<sub>0.2</sub>Ni<sub>0.2</sub>)O<sub>3</sub> and LaCoO<sub>3</sub> by solution combustion technique, and these materials were then used as negative electrode materials for lithium-ion batteries (LIB). The cycling performance of HEPOs was found to be better than that of conventional perovskites. After the first cycle, La(Co<sub>0.2</sub>Cr<sub>0.2</sub>Fe<sub>0.2</sub>Mn<sub>0.2</sub>Ni<sub>0.2</sub>)O<sub>3</sub> went through an activation phase for about 100 cycles, during which its specific capacity was higher than LaCoO<sub>3</sub>, and reached a capacity of 568 mAhg<sup>-1</sup> at the 500th cycle, which was 50 mAhg<sup>-1</sup> higher than the initial discharge capacity of LaCoO<sub>3</sub>. The improved electrochemical performance is due to the entropy-stabilized crystal structure of HEPOs, which effectively compensates for volume changes during lithium insertion and removal processes. Furthermore, the synergistic effect of multiple parent elements significantly enhances the diffusion coefficient of lithium ions and increases the pseudocapacitive contribution rate (Shao et al., 2023).

Yan and co-workers (Yan et al.. 2020) synthesized  $[(Bi,Na)_{1/5}(La,Li)_{1/5}(Ce,K)_{1/5}Ca_{1/5}Sr_{1/5}]TiO_3$  via a solid-state reaction to be used as a negative electrode and demonstrated that this material exhibited high-rate performance and cycling continuity. When the current density was gradually increased from 100 mAg<sup>-1</sup> to 3000 mAg<sup>-1</sup> and then decreased to 100 mAg<sup>-1</sup>, it was observed that the specific capacity increased from 84.3 mAg<sup>-1</sup> to 87.4 mAg<sup>-1</sup> (Figure 2-a). In addition, a remarkable recycling capacity of 120.4 mAg<sup>-1</sup> and almost 100% capacity retention were achieved after 300 cycles at a current density of 1000 mAg<sup>-1</sup>. This can be attributed to the gradual infiltration of electrolyte molecules into the electrode material and the formation of electrochemically active polymer gel membranes. This process resulted in a continuous increase in capacity (Figure 2-b).

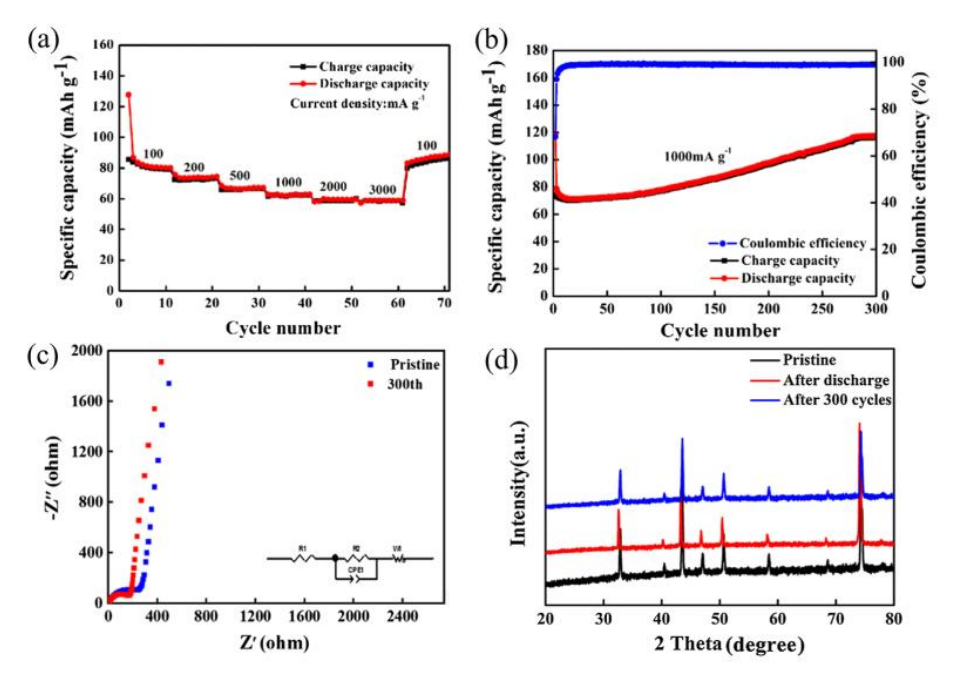


Figure 2: Electrochemical properties of [(Bi,Na)<sub>1/5</sub>(La,Li)<sub>1/5</sub>(Ce,K)1/<sub>5</sub>Ca1/5Sr<sub>1/5</sub>]TiO<sub>3</sub> HEPO: (a) Performance rate under different current densities. (b) Long-term cycling performance at 1000 mAg<sup>-1</sup> current density. (c) Nyquist plots before and after 300 cycles for 1000 mAg<sup>-1</sup> current density. (d) XRD patterns before and after 300 cycles (Yan et al., 2020).

Furthermore, the Rct value decreased significantly after 300 cycles (Figure 2-c), which may be related to the activation processes and kinetic improvements that occur during cycling. XRD analysis of the sample after 300 cycles revealed a structure similar to the initially observed crystal

structure and confirmed the excellent structural stability of HEPOs (Figure 2-d). This research demonstrates the great potential of HEPOs as negative electrode materials in lithium-ion batteries.

Lix(LiLaCaSrBa)Ti<sub>1-x</sub>Al<sub>x</sub>O<sub>3</sub>, which has a porous structure and low density, is suitable for lithium storage (Yazhou and Zhiren, 2022). As shown in Figure 3, the specific capacity, cyclic durability, and rate performance of La(Co<sub>0.2</sub>Cr<sub>0.2</sub>Fe<sub>0.2</sub>Mn0.2Ni<sub>0.2</sub>)O<sub>3</sub> are significantly superior to those of the traditional lithium storage material LaCoO<sub>3</sub>. This is due to the stabilized structure of HEPO (effectively reducing the volume changes in the lithium/delta-lithium process), the synergistic effect of a large number of main elements (increasing the Li<sup>+</sup> diffusion coefficient), and the mesoporous structure of the system (the presence of many active sites) (Jia et al., 2022).

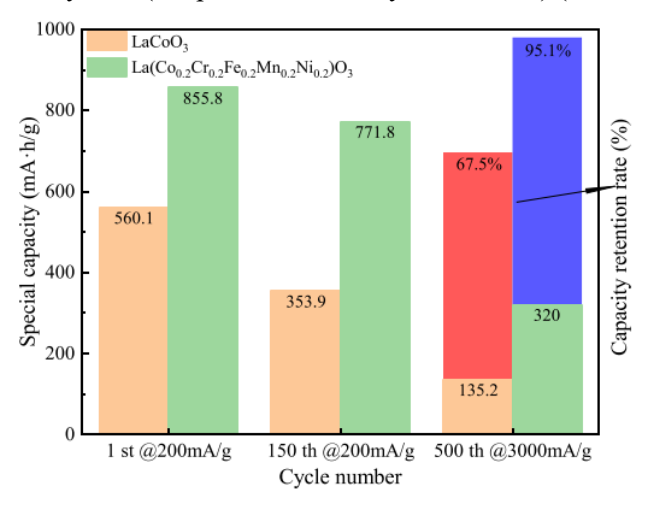


Figure 3: Extraordinary cyclic stability of La(Co<sub>0.2</sub>Cr<sub>0.2</sub>Fe<sub>0.2</sub>Mn<sub>0.2</sub>Ni<sub>0.2</sub>)O<sub>3</sub> (Jia et al., 2022).

The high-entropy effect plays a critical role in maintaining the structural strength of batteries over many cycles. Furthermore, the coexistence of heterovalent ions provides a charge-balancing mechanism that supports the high efficiency of these batteries. Therefore, the high-entropy method offers a different perspective in the design of lithium-ion batteries.

### 2.2. Supercapacitors

SCs have become a subject of great interest and research in the area of energy storage because of their many benefits including elevated energy density, quick charging capabilities, excellent cycling stability, and safe operation. These properties have placed SCs at the forefront of energy storage studies. However, their low energy density limits their development (Mefford et al., 2014; Simon and Gogotsi, 2020). HEPOs, which are characterized by stable crystal structures and oxygen vacancies that can easily participate in redox reactions in ionic solutions, theoretically offer a higher specific capacitance. Therefore, it is stated that perovskites are proposed as anode materials for supercapacitors due to the oxygen-anion-intercalation energy storage mechanism (Nan et al., 2019).

Guo and his al.. team (Guo et 2022-b) produced La(CoCrFeMnNiAl<sub>0.5</sub>)<sub>1/5.5</sub>O<sub>3</sub> component as an electrode for SCs via the codeposition method. The addition of inactive Al<sup>+3</sup> promoted superior electrochemical performance, enabling them to achieve a specific capacitance of 353.65 Fg<sup>-1</sup> at a current density of 1 Ag<sup>-1</sup>. Moreover, the electrode retained 88.61% of its initial capacitance after 2000 cycles. Meng and co-workers (Meng et al., 2023) presented an innovative method to prepare oxygen-deficient materials by using acidic carbon balls as templates that lost material over time to obtain La(CoMnFeNiCu)<sub>0.2</sub>O<sub>3</sub>. This material, with an estimated specific surface area of 28.08 m<sup>2</sup>g<sup>-1</sup> and a remarkable oxygen vacancy concentration of 37.71%, presents a high specific capacitance of 625 Fg<sup>-1</sup> at a current density of 1 Ag<sup>-1</sup> (Figure 4-a). It also exhibited an outstanding capacity retention ability, retaining 88% of its capacity after 10,000 cycles (Figure 4-b). These findings highlight the potential of HEPOs as electrodes for supercapacitors.

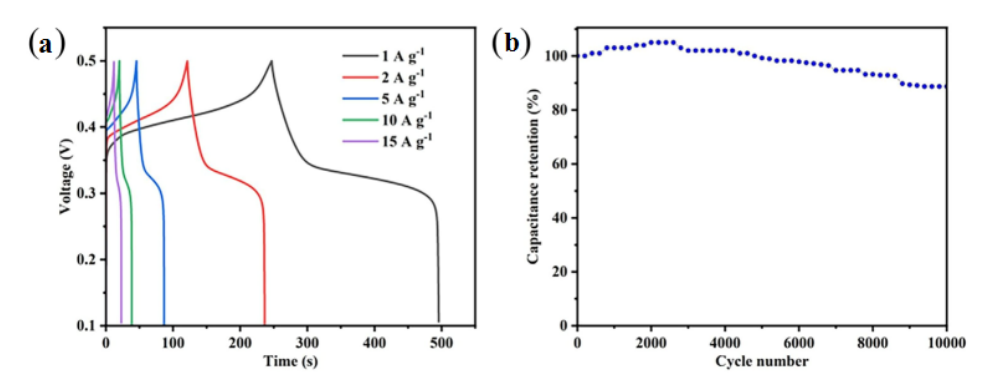


Figure 4: (a) GCD plots and (b) cycling durability of La(CoMnFeNiCu)<sub>0.2</sub>O<sub>3</sub> (Meng et al., 2023).

Recently, Nan and his team (Nan et al., 2023-a) discovered that the decrease in cycling durability of high-power battery-supercapacitor hybrid

(BSH) devices is due to irreversible phase transitions and volume expansion resulting from the mismatch between charge and discharge processes and electrochemical kinetic processes (Nan et al., 2023-b). Figure 5 illustrates the dual-ion energy storage method of water-based alkaline BSH devices. The interaction of ions with HEPOs is limited by the semi-infinite diffusion process during charging and surface adsorption during discharging. The former process occurs slower than the latter, leading to irreversible phase transitions in the material during cycling. The severely distorted surfaces of densely arranged oxygen ions hinder the diffusion and deintercalation of oxygen, causing surface and subsurface oxygen ions to intercalate with oxygen vacancies.

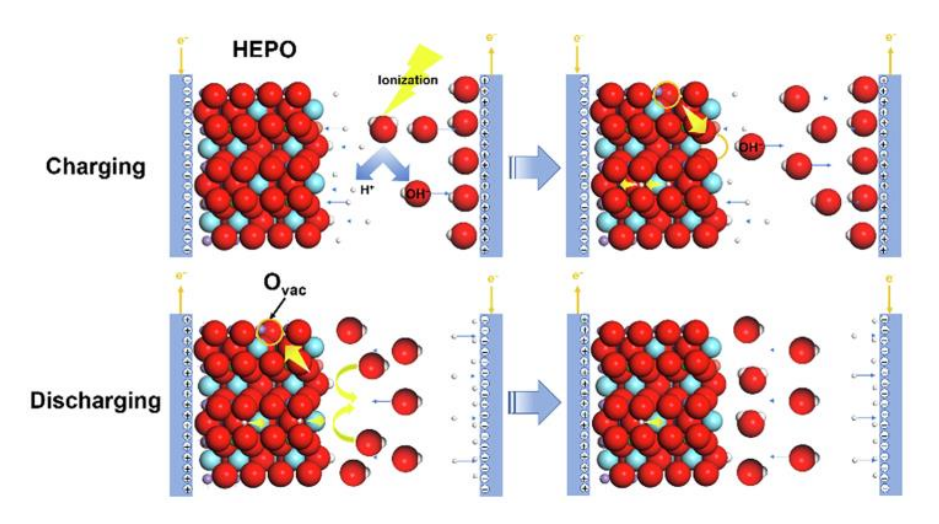


Figure 5: Double ion energy storage method in aqueous alkaline BSH systems (Nan et al., 2023-b).

This restricts the deintercalation of hydrogen and leads to an increased presence of hydrogen ions within the material. These hydrogen ions can lead to voltage build up and volume expansion, leading to collapses. Furthermore, the decrease in specific capacity is associated with the separation of cations during charge and discharge cycles. The use of ions with large ionic radii in the A-region can increase the mobility of oxygen ions and this enhances the durability of the electrode when cycling (Nan et al., 2023-a).

The high entropy influence plays a crucial role in enhancement the cycling stability of supercapacitors. Therefore, supercapacitor electrode

materials with higher performance can be obtained through doping, structure modification, and mixing effects. This suggests that HEPOs are promising electrode materials for supercapacitors.

### 2.3. Solid oxide fuel cells (SOFCs)

HEPOs, due to their outstanding electrochemical characteristics, are able to fulfill the growing need for dependable and effective energy storage solutions. SOFCs can transform the chemical energy found in fuels like hybrid fuels and ammonia straight into electrical energy. This process provides high efficiencies of up to 85% while maintaining low emissions (Cai et al., 2019; Kuai et al., 2019; Sharma et al., 2019; Thaheem et al., 2019; Vafaeenezhad et al., 2019). However, these cells must operate at high temperatures, typically between 800 and 1000 °C, to achieve optimum output performance. This leads to rapid performance degradation and reduced cycle durability (Wang et al., 2019; Xia et al., 2019). The high-temperature stability of HEPOs offers potential solutions to these problems.

In Sr-doped cathode materials, the separation of strontium is a limiting factor, significantly affecting the oxygen reduction ability and durability of the cathode.

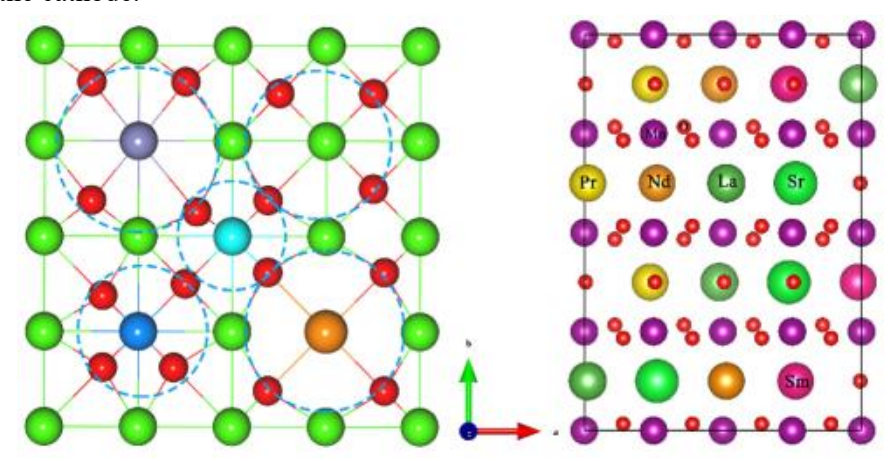


Figure 6: A diagram showing the propagation of different ions and stress fields around Sr (Yang et al., 2021-b).

Distortions in the lattice structure and interactions between various ions in HEPOs can improve the electrochemical performance by hindering the separation of Sr.  $(La_{0.2}Sr_{0.2}Pr_{0.2}Y_{0.2}Ba_{0.2})Co_{0.2}Fe_{0.8}O_3-\delta$  electrodes did not show the separation of strontium after a chromium tolerance test lasting 41

days (Li et al., 2022). Pr, Nd, and Sm, when added to the  $(La_{0.2}Pr_{0.2}Nd_{0.2}Sm_{0.2}Sr_{0.2})MnO_3-\delta$  (LSM) structure, limit the separation of strontium (Yang et al., 2021-b). Figure 6 shows the lattice distortions caused by ions homogeneously distributed around  $Sr^{2+}$  and the stress fields that restrict  $Sr^{2+}$  transport and migration (Yang et al., 2021-b).

The  $\delta(r)$  value in HE-LSM is 5.30% higher than that in LSM (2.33%), which is related to lattice distortion. However, the higher  $\delta(r)$  value does not indicate limited Sr dissociation. Shi and his team heated four samples at 800, 1000, 1100, and 1200 °C for 100 h, respectively (Shi et al., 2022). Sr dissociation was detected only on the surface of the sample with the highest  $\delta(r)$  value of 8.49%. Although the  $\delta(r)$  values of the other samples were 7.09% and 5.30% higher than those in LSM, respectively, no Sr dissociation was observed in these systems. Thus, it can be inferred that the splitting of Sr in HEPOs is influenced not just by the decline in ionic sizes but also by additional elements, including sluggish movement in high-entropy substances (Li et al., 2022).

 $Ba(Sn_{0.1}6Zr_{0.2}4Ce_{0.35}Y_{0.1}Yb_{0.1}Dy_{0.05})O_3-\delta$  is used as an electrode material in proton ceramic fuel cells (Guo and He, 2022). In addition,  $Ba(Co_{0.2}Fe_{0.2}Zr_{0.2}Sn_{0.2}Pr_{0.2})O_3$  (Sun et al., 2023) and  $(Pr_{1/6}La_{1/6}Nd_{1/6}Ba_{1/6}Sr_{1/6}Ca_{1/6})CoO_3-\delta$ , (Liu et al., 2022) have been preferred in air electrodes of reversible proton ceramic cells. HEPO electrodes exhibit strong cyclic and structural durability due to the high entropy effect. The equivalent sublattices occupied by ions of different valences provide excellent electrochemical performance by allowing ternary conductivity and hydration. Therefore, HEPOs have potential as electrode materials for SOFCs (Ma et al., 2024).

The durability of the crystal structure is improved by the high entropy effect, so the electrode structure does not change despite long-term use. Slow diffusion and lattice distortion limit ion dissociation, which allows the electrode to maintain high oxygen-reducing activity and durability. At the same time, the considerable amount of ions with different valence states has the potential to increase electrode conductivity. Overall, HEPOs have remarkable potential as electrode materials (Ma et al., 2024).

### 3. Results and discussion

HEPOs, a new category of materials, combine the benefits of highentropy materials with those of perovskite oxides. HEPOs are experiencing remarkable development in both composition design and performance improvements in terms of high entropy effects, low diffusion rates, lattice distortion, and cocktail effects. The high stability of HEPOs is associated with thermodynamic stability resulting from the high entropy effect; microstructures and defect configurations are affected by local composition fluctuations and random fields resulting from the coexistence of ions of different radii and valences. Compared to conventional materials, HEPOs exhibit high structural stability and exceptional physicochemical properties. as well as highly controllable properties. These benefits have the potential to overcome various challenges in energy applications. This process typically involves doping the B region of lanthanide perovskites, with the main dopants being Cr, Mn, Fe, Co, and Ni. These dopants demonstrate the relationship between high entropy and superior performance and the effects of high entropy on the electronic orbitals of the materials. Therefore, the use of advanced theoretical calculations and high-precision characterization methods to thoroughly investigate the relationship between high-entropy structures and their intrinsic properties is of great importance. Currently, several problems with HEPOs are emerging, including arbitrary compositional design paths, uncertainty affecting the structures of new HEPO compositions, and a lack of correlation between high configurationally entropy and high performance. Therefore, a functional compositional design method based on a clear relationship between configurationally entropy and performance, supported by accurate structure prediction, will guide the future development of HEPOs.

#### REFERENCES

- Akkerman, Q. A., Gandini, M., Di Stasio, F., Rastogi, P., Palazon, F., Bertoni, G., ... & Manna, L. (2016). Strongly emissive perovskite nanocrystal inks for high-voltage solar cells. *Nature Energy*, 2(2), 1-7.
- Abdalla, A. M., Hossain, S., Azad, A. T., Petra, P. M. I., Begum, F., Eriksson, S. G., & Azad, A. K. (2018). Nanomaterials for solid oxide fuel cells: A review. *Renewable and Sustainable Energy Reviews*, 82, 353-368.
- Bérardan, D., Franger, S., Meena, A. K., & Dragoe, N. (2016). Room temperature lithium superionic conductivity in high entropy oxides. *Journal of Materials Chemistry A*, 4(24), 9536-9541.

- Cai, H., Zhang, L., Xu, J., Huang, J., Wei, X., Wang, L., ... & Long, W. (2019). Cobalt–free La0. 5Sr0. 5Fe0. 9Mo0. 1O3–δ electrode for symmetrical SOFC running on H2 and CO fuels. *Electrochimica Acta*, 320, 134642.
- Cao, J., Wu, S., He, J., Zhou, Y., & Ma, P. (2024). Research progress of highentropy perovskite oxides in energy and environmental applications: A review. *Particuology*, 95, 62-81.
- Chen, X., He, W., Ding, L. X., Wang, S., & Wang, H. (2019). Enhancing interfacial contact in all solid state batteries with a cathode-supported solid electrolyte membrane framework. *Energy & Environmental Science*, 12(3), 938-944.
- Chen, D., Zhu, X., Yang, X., Yan, N., Cui, Y., Lei, X., ... & Li, C. (2023). A review on structure–property relationships in dielectric ceramics using high-entropy compositional strategies. *Journal of the American Ceramic Society*, 106(11), 6602-6616.
- Chu, K., Qin, J., Zhu, H., De Ras, M., Wang, C., Xiong, L., ... & Liu, T. (2022). High-entropy perovskite oxides: A versatile class of materials for nitrogen reduction reactions. *Science China Materials*, 65(10), 2711-2720.
- Corey, Z. J., Lu, P., Zhang, G., Sharma, Y., Rutherford, B. X., Dhole, S., ... & Jia, Q. (2022). Structural and optical properties of high entropy (La, Lu, Y, Gd, Ce) AlO3 perovskite thin films. *Advanced Science*, *9*(29), 2202671.
- Da Silva, L. M., Cesar, R., Moreira, C. M., Santos, J. H., De Souza, L. G., Pires, B. M., ... & Zanin, H. (2020). Reviewing the fundamentals of supercapacitors and the difficulties involving the analysis of the electrochemical findings obtained for porous electrode materials. *Energy storage materials*, 27, 555-590.
- Dąbrowa, J., Olszewska, A., Falkenstein, A., Schwab, C., Szymczak, M., Zajusz, M., ... & Świerczek, K. (2020). An innovative approach to design SOFC air electrode materials: high entropy  $La_{1-x}Sr_x$  (Co, Cr, Fe, Mn, Ni)  $O_{3-}\delta$  (x= 0, 0.1, 0.2, 0.3) perovskites synthesized by the sol–gel method.
- Fang, J., Wang, T., Li, K., Li, Y., & Gong, W. (2022). Energy storage properties of Mn-modified (Na0. 2Bi0. 2Ca0. 2Sr0. 2Ba0. 2) TiO3 high-entropy relaxorferroelectric ceramics. *Results in Physics*, 38, 105617.
- Fang, S. M., Yoo, C. Y., & Bouwmeester, H. J. (2011). Performance and stability of niobium-substituted Ba0. 5Sr0. 5Co0. 8Fe0. 2O3– δ membranes. *Solid State Ionics*, 195(1), 1-6.
- Gani, A. (2021). Fossil fuel energy and environmental performance in an extended STIRPAT model. *Journal of Cleaner Production*, 297, 126526.
- Gazda, M., Miruszewski, T., Jaworski, D., Mielewczyk-Gryń, A., Skubida, W., Wachowski, S., ... & Dzik, E. (2020). Novel class of proton conducting materials—high entropy oxides. *ACS Materials Letters*, *2*(10), 1315-1321.
- Guo, J., Xiao, W., Zhang, X., Zhang, J., Wang, J., Zhang, G., & Zhang, S. T. (2022-a). Achieving excellent energy storage properties in fine-grain high-entropy relaxor ferroelectric ceramics. *Advanced Electronic Materials*, 8(11), 2200503.
- Guo, M., Liu, Y., Zhang, F., Cheng, F., Cheng, C., Miao, Y., ... & Yu, J. (2022-b). Inactive Al3+-doped La (CoCrFeMnNiAl x) 1/(5+ x) O3 high-entropy perovskite oxides as high performance supercapacitor electrodes. *Journal of Advanced Ceramics*, 11(5), 742-753.
- Guo, R., & He, T. (2022). High-entropy perovskite electrolyte for protonic ceramic fuel cells operating below 600 C. *ACS Materials Letters*, 4(9), 1646-1652.

- Hahn, R., Kirnbauer, A., Bartosik, M., Kolozsvári, S., & Mayrhofer, P. H. (2019). Toughness of Si alloyed high-entropy nitride coatings. *Materials Letters*, 251, 238-240.
- Jia, Y.G., X. Shao, J. Cheng, P.P. Wang, A.Q. Mao, Preparation and lithium storage performance of pseudocapacitance-controlled chalcogenide high-entropy oxide LaCo0.2Cr0.2Fe0.2Mn0.2Ni0.2O3 anode materials, Chem. J. Chin. Univ. 43 (2022) 11.
- Jia, X., Ge, Y., Shao, L., Wang, C., & Wallace, G. G. (2019). Tunable conducting polymers: toward sustainable and versatile batteries. *ACS Sustainable Chemistry & Engineering*, 7(17), 14321-14340.
- Jiang, Z., Wang, S., Chen, X., Yang, W., Yao, X., Hu, X., ... & Wang, H. (2020). Lithium-Metal Batteries: Tape-Casting Li0. 34La0. 56TiO3 Ceramic Electrolyte Films Permit High Energy Density of Lithium-Metal Batteries (Adv. Mater. 6/2020). Advanced Materials, 32(6), 2070045.
- Jiang, S., Shao, L., Fan, T. W., Duan, J. M., Chen, X. T., & Tang, B. Y. (2020). Elastic and thermodynamic properties of high entropy carbide (HfTaZrTi) C and (HfTaZrNb) C from ab initio investigation. *Ceramics International*, 46(10), 15104-15112.
- Kante, M. V., Weber, M. L., Ni, S., van den Bosch, I. C., van der Minne, E., Heymann, L., ... & Baeumer, C. (2023). A high-entropy oxide as high-activity electrocatalyst for water oxidation. *ACS nano*, *17*(6), 5329-5339.
- Kuai, X., Yang, G., Chen, Y., Sun, H., Dai, J., Song, Y., ... & Shao, Z. (2019). Boosting the activity of BaCo0. 4Fe0. 4Zr0. 1Y0. 1O3– δ perovskite for oxygen reduction reactions at low-to-intermediate temperatures through tuning B-site cation deficiency. *Advanced Energy Materials*, *9*(38), 1902384.
- Li, M., Yan, X., Kang, Z., Huan, Y., Li, Y., Zhang, R., & Zhang, Y. (2018). Hydrophobic polystyrene passivation layer for simultaneously improved efficiency and stability in perovskite solar cells. *ACS applied materials & interfaces*, 10(22), 18787-18795.
- Li, Z., Guan, B., Xia, F., Nie, J., Li, W., Ma, L., ... & Liu, X. (2022). High-entropy perovskite as a high-performing chromium-tolerant cathode for solid oxide fuel cells. *ACS applied materials & interfaces*, 14(21), 24363-24373.
- Liu, Z. Y., Liu, Y., Xu, Y., Zhang, H., Shao, Z., Wang, Z., & Chen, H. (2023). Novel high-entropy oxides for energy storage and conversion: From fundamentals to practical applications. *Green Energy & Environment*, 8(5), 1341-1357.
- Liu, Y., Jia, D., Zhou, Y. U., Zhou, Y., Zhao, J., Nian, H., & Liu, B. (2020). Zn0. 1Ca0. 1Sr0. 4Ba0. 4ZrO3: A non-equimolar multicomponent perovskite ceramic with low thermal conductivity. *Journal of the European Ceramic Society*, 40(15), 6272-6277.
- Liu, Y., Zhang, W., Wang, B., Sun, L., Li, F., Xue, Z., ... & Nian, H. (2018). Theoretical and experimental investigations on high temperature mechanical and thermal properties of BaZrO3. *Ceramics international*, 44(14), 16475-16482.
- Liu, Z., Tang, Z., Song, Y., Yang, G., Qian, W., Yang, M., ... & Shao, Z. (2022). High-entropy perovskite oxide: a new opportunity for developing highly active and durable air electrode for reversible protonic ceramic electrochemical cells. *Nano-Micro Letters*, 14(1), 217.

- Locock, A. J., & Mitchell, R. H. (2018). Perovskite classification: An Excel spreadsheet to determine and depict end-member proportions for the perovskite-and vapnikite-subgroups of the perovskite supergroup. *Computers & Geosciences*, 113, 106-114.
- Ma, J., Liu, T., Ye, W., He, Q., & Chen, K. (2024). High-entropy perovskite oxides for energy materials: A review. *Journal of Energy Storage*, *90*, 111890.
- Mefford, J. T., Hardin, W. G., Dai, S., Johnston, K. P., & Stevenson, K. J. (2014). Anion charge storage through oxygen intercalation in LaMnO3 perovskite pseudocapacitor electrodes. *Nature materials*, *13*(7), 726-732.
- Meng, Z., Gong, X., Xu, J., Sun, X., Zeng, F., Du, Z., ... & Tian, H. (2023). A general strategy for preparing hollow spherical multilayer structures of Oxygen-Rich vacancy transition metal Oxides, especially high entropy perovskite oxides. *Chemical Engineering Journal*, 457, 141242.
- Nan, H. S., Hu, X. Y., & Tian, H. W. (2019). Recent advances in perovskite oxides for anion-intercalation supercapacitor: a review. *Materials Science in Semiconductor Processing*, 94, 35-50.
- Nan, H., Lv, S., Xu, Z., Feng, Y., Zhou, Y., Liu, M., ... & Tian, H. (2023-a). Inducing the cocktail effect in yolk-shell high-entropy perovskite oxides using an electronic structural design for improved electrochemical applications. *Chemical Engineering Journal*, 452, 139501.
- Nan, H., Song, K., Xu, J., Lv, S., Yu, S., Hu, X., & Tian, H. (2023-b). Dual-ion (de) intercalation into high-entropy perovskite oxides for aqueous alkaline battery-supercapacitor hybrid devices. *Acta Materialia*, 257, 119174.
- Nguyen, T. X., Liao, Y. C., Lin, C. C., Su, Y. H., & Ting, J. M. (2021). Advanced high entropy perovskite oxide electrocatalyst for oxygen evolution reaction. *Advanced Functional Materials*, *31*(27), 2101632.
- Okejiri, F., Zhang, Z., Liu, J., Liu, M., Yang, S., & Dai, S. (2020). Room-temperature synthesis of high-entropy perovskite oxide nanoparticle catalysts through ultrasonication-based method. *ChemSusChem*, *13*(1), 111-115
- Oliveira, L. C., Venâncio, R., de Azevedo, P. V., Anchieta, C. G., Nepel, T. C., Rodella, C. B., ... & Doubek, G. (2023). Reviewing perovskite oxide sites influence on electrocatalytic reactions for high energy density devices. *Journal of Energy Chemistry*, 81, 1-19.
- Pikalova, E. Y., Kalinina, E. G., Pikalova, N. S., & Filonova, E. A. (2022). High-entropy materials in SOFC technology: Theoretical foundations for their creation, features of synthesis, and recent achievements. *Materials*, *15*(24), 8783.
- Sarkar, A., Wang, D., Kante, M. V., Eiselt, L., Trouillet, V., Iankevich, G., ... & Kruk, R. (2023). High entropy approach to engineer strongly correlated functionalities in manganites. *Advanced Materials*, *35*(2), 2207436.
- Shao, X., Jia, Y., Cheng, J., Fang, D., Mao, A., & Tan, J. (2023). Preparation and electrochemical properties of perovskite-type La (Co0. 2Cr0. 2Fe0. 2Mn0. 2Ni0. 2) O3 high-entropy oxide. *The Chin J Process Eng*, 23(5), 771.
- Shang, Y., Pu, Y., Zhang, Q., Zhang, L., Zhang, X., Zhang, J., & Ning, Y. (2022). Effect of configuration entropy on dielectric relaxor, ferroelectric properties of high-entropy (NaBiBa) x (SrCa)(1-3 x)/2TiO3 ceramics. *Journal of Materials Science: Materials in Electronics*, 33(8), 5359-5369.

- Sharma, Y., Lee, M. C., Pitike, K. C., Mishra, K. K., Zheng, Q., Gao, X., ... & Ward, T. Z. (2022). High entropy oxide relaxor ferroelectrics. *ACS Applied Materials & Interfaces*, 14(9), 11962-11970.
- Sharma, R. K., Khamidy, N. I., Rapenne, L., Charlot, F., Moussaoui, H., Laurencin, J., & Djurado, E. (2019). Highly efficient architectured Pr6O11 oxygen electrode for solid oxide fuel cell. *Journal of Power Sources*, *419*, 171-180.
- Shi, Y., Ni, N., Ding, Q., & Zhao, X. (2022). Tailoring high-temperature stability and electrical conductivity of high entropy lanthanum manganite for solid oxide fuel cell cathodes. *Journal of Materials Chemistry A*, 10(5), 2256-2270.
- Simon, P., & Gogotsi, Y. (2020). Perspectives for electrochemical capacitors and related devices. *Nature materials*, 19(11), 1151-1163.
- Song, Z., Wang, H., Hou, J., Hofmann, H. F., & Sun, J. (2020). Combined state and parameter estimation of lithium-ion battery with active current injection. *IEEE Transactions on Power Electronics*, 35(4), 4439-4447.
- Sun, W., Zhang, F., Zhang, X., Shi, T., Li, J., Bai, Y., ... & Wang, Z. (2022). Enhanced electrical properties of (Bi0. 2Na0. 2Ba0. 2Ca0. 2Sr0. 2) TiO3 high-entropy ceramics prepared by hydrothermal method. *Ceramics International*, 48(13), 19492-19500.
- Sun, J., Ren, R., Yue, H., Cui, W., Wang, G., Xu, C., ... & Wang, Z. (2023). High-entropy perovskite oxide BaCo0. 2Fe0. 2Zr0. 2Sn0. 2Pr0. 2O3-δ with triple conduction for the air electrode of reversible protonic ceramic cells. *Chinese Chemical Letters*, 34(7), 107776.
- Thaheem, I., Kim, K. J., Lee, J. J., Joh, D. W., Jeong, I., & Lee, K. T. (2019). High performance Mn 1.3 Co 1.3 Cu 0.4 O 4 spinel based composite cathodes for intermediate temperature solid oxide fuel cells. *Journal of Materials Chemistry A*, 7(34), 19696-19703.
- Trachenko, K., Pruneda, M., Artacho, E., & Dove, M. T. (2004). Radiation damage effects in the perovskite Ca Ti O 3 and resistance of materials to amorphization. *Physical Review B—Condensed Matter and Materials Physics*, 70(13), 134112.
- Xia, Y., Jin, Z., Wang, H., Gong, Z., Lv, H., Peng, R., ... & Bi, L. (2019). A novel cobalt-free cathode with triple-conduction for proton-conducting solid oxide fuel cells with unprecedented performance. *Journal of Materials Chemistry A*, 7(27), 16136-16148.
- Xiang, H., Chen, J., Li, Z., & Wang, H. (2011). An inorganic membrane as a separator for lithium-ion battery. *Journal of Power Sources*, 196(20), 8651-8655.
- Xie, H. (2024). Preparation and lithium storage performance study of perovskite-type high-entropy oxides. Dissertation https://doi.org/10.27790/d.cnki.gahgy.2022.000384.
- Xiong, W., Zhang, H., Hu, Z., Reece, M. J., & Yan, H. (2022). Low thermal conductivity in A-site high entropy perovskite relaxor ferroelectric. *Applied Physics Letters*, *121*(11).
- Vafaeenezhad, S., Sandhu, N. K., Hanifi, A. R., Etsell, T. H., & Sarkar, P. (2019). Development of proton conducting fuel cells using nickel metal support. *Journal of Power Sources*, 435, 226763.
- Wang, J., Chen, X., Xie, S., Chen, L., Wang, Y., Meng, J., & Zhou, D. (2019).

  Bismuth tungstate/neodymium-doped ceria composite electrolyte for

- intermediate-temperature solid oxide fuel cell: Sintering aid and composite effect. *Journal of Power Sources*, 428, 105-114.
- Wang, C., Yu, Y., Niu, J., Liu, Y., Bridges, D., Liu, X., ... & Hu, A. (2019). Recent progress of metal–air batteries-a mini review. *Applied Sciences*, *9*(14), 2787.
- Wang, Y., Liu, J., Song, Y., Yu, J., Tian, Y., Robson, M. J., ... & Ciucci, F. (2023-a). High-entropy perovskites for energy conversion and storage: design, synthesis, and potential applications. *Small Methods*, 7(4), 2201138.
- Wang, T., Li, Y., Zhang, X., Zhang, D., & Gong, W. (2023-b). Simultaneous excellent energy storage density and efficiency under applied low electric field for high entropy relaxor ferroelectric ceramics. *Materials Research Bulletin*, 157, 112024.
- Yan, J., Wang, D., Zhang, X., Li, J., Du, Q., Liu, X., ... & Qi, X. (2020). A high-entropy perovskite titanate lithium-ion battery anode. *Journal of Materials Science*, 55(16), 6942-6951.
- Yang, X., Guo, R., Cai, R., Ouyang, Y., Yang, P., & Xiao, J. (2022). Engineering high-entropy materials for electrocatalytic water splitting. *International Journal of Hydrogen Energy*, 47(28), 13561-13578.
- Yang, Q., Wang, G., Wu, H., Beshiwork, B. A., Tian, D., Zhu, S., ... & Lin, B. (2021-a). A high-entropy perovskite cathode for solid oxide fuel cells. *Journal of Alloys and Compounds*, 872, 159633.
- Yang, Y., Bao, H., Ni, H., Ou, X., Wang, S., Lin, B., ... & Ling, Y. (2021-b). A novel facile strategy to suppress Sr segregation for high-entropy stabilized La0·8Sr0·2MnO3-δ cathode. *Journal of Power Sources*, 482, 228959.
- Yazhou, K., & Zhiren, Y. (2022). Synthesis, structure and electrochemical properties of Al doped high entropy perovskite Lix (LiLaCaSrBa) Til-xAlxO3. *Ceramics International*, 48(4), 5035-5039.
- Yeh, J. W., Chen, S. K., Lin, S. J., Gan, J. Y., Chin, T. S., Shun, T. T., ... & Chang, S. Y. (2004). Nanostructured high-entropy alloys with multiple principal elements: novel alloy design concepts and outcomes. *Advanced engineering materials*, 6(5), 299-303.
- Zhao, Z., Rehder, L., Steinbach, F., & Feldhoff, A. (2022). High-Entropy Perovskites Pr1– x Sr x (Cr, Mn, Fe, Co, Ni) O3– δ (x= 0–0.5): Synthesis and Oxygen Permeation Properties. *Membranes*, *12*(11), 1123.
- Zhao, C. X., Liu, J. N., Li, B. Q., Ren, D., Chen, X., Yu, J., & Zhang, Q. (2020). Multiscale construction of bifunctional electrocatalysts for long-lifespan rechargeable zinc–air batteries. *Advanced Functional Materials*, 30(36), 2003619.
- Zhang, P., Lou, Z., Qin, M., Xu, J., Zhu, J., Shi, Z., ... & Gao, F. (2022). High-entropy (Ca0. 2Sr0. 2Ba0. 2La0. 2Pb0. 2) TiO3 perovskite ceramics with Asite short-range disorder for thermoelectric applications. *Journal of Materials Science & Technology*, 97, 182-189.
- Zhang, R. Z., Gucci, F., Zhu, H., Chen, K., & Reece, M. J. (2018). Data-driven design of ecofriendly thermoelectric high-entropy sulfides. *Inorganic chemistry*, 57(20), 13027-13033.

# Metamaterials, applications and sustainability

Fehim FINDIK<sup>1</sup>

<sup>1-</sup> Prof. Dr. Fehim FINDIK; Sakarya University of Applied Sciences, Faculty of Technology, Metallurgy and Materials Engineering Department. <a href="mailto:findik@subu.edu.tr">findik@subu.edu.tr</a> ORCID No: 0000-0003-2537-1951

#### **ABSTRACT**

Metamaterials are artificially engineered materials that derive extraordinary properties from their precisely designed nanostructures, enabling control over electromagnetic, acoustic, and mechanical waves beyond natural limitations. They exhibit unique phenomena such as negative refraction, superlensing, with transformative cloaking, and applications telecommunications, high-resolution imaging, and seismic protection. Acoustic metamaterials also facilitate advanced noise cancellation and novel medical devices. However, sustainability presents a significant challenge. Although metamaterials offer energy efficiency benefits, their production often relies on resource-intensive processes and non-biodegradable components. Addressing lifecycle impacts and developing eco-friendly alternatives are crucial for sustainable integration. Future advancements depend on improving production scalability to move beyond lab-scale prototypes. The integration of artificial intelligence for inverse design is accelerating the discovery of optimized structures, while programmable metamaterials enable real-time property control. To maximize their positive impact, the continued evolution of metamaterials must align with sustainable design principles and circular economy models. This study reviews metamaterial functions, theoretical and practical developments, diverse applications, and sustainability challenges, offering a methodological analysis of future prospects.

Keywords – Metamaterials, Tunable materials, Applications, Sustainability, Electromagnetic manipulation

#### INTRODUCTION

Metamaterials are artificially structured materials designed to manipulate electromagnetic, acoustic, and mechanical waves that are not possible with natural materials. Their properties stem not only from their chemical composition but also from their precise nano- or micro-scale structures.

Metamaterials have three key properties: a negative refractive index, a small wavelength, and specialized electromagnetic/acoustic responses. Unlike natural materials with a positive refractive index, where light bends normally, metamaterials with a negative refractive index can bend light backwards, a phenomenon called negative refraction (Veselago, 1968:509). These materials enable super lenses that exceed the diffraction limit and invisibility effects. Furthermore, metamaterials have small wavelengths. This means that the structural properties of metamaterials are smaller than

the wavelengths of the light and sound energies they interact with. For example, a microwave metamaterial might have copper split-ring resonators repeating at the millimeter scale. Another characteristic of metamaterials is their unique electromagnetic/acoustic response. This means these materials can exhibit near-zero permeability, direction-dependent anisotropy, or nonlinear effects.

Metamaterial types can be divided into four categories: electromagnetic, acoustic, mechanical, and thermal. Example applications of metamaterials include: Electromagnetic metamaterials control electromagnetic light, radio waves, and microwaves. Invisibility cloaks and ultrathin lenses are among their applications (Table 1, Figure 1).

Acoustic metamaterials direct sound waves. Noise cancellation and seismic wave shielding are among their applications. Mechanical metamaterials exhibit exceptional hardness and flexibility. Impact-resistant armor and programmable materials are among their applications (Pendry et al., 1999:2075) (Smith et al., 2000:4184).

Thermal metamaterials control heat flow. Thermal shielding and improved heat dissipation are among the application areas of these materials.

Table 1. Types of metamaterials, functions and applications

Type	Function	<b>Example Applications</b>	
Electromagnetic	Controls light, radio waves, microwaves	Invisibility cloaks, ultra-thin lenses	
Acoustic	Manipulates sound waves	Noise cancellation, seismic wave shielding	
Mechanical	Unusual stiffness, flexibility	Impact-resistant armor, programmable materials	
Thermal	Controls heat flow	Thermal cloaking, improved heat dissipation	

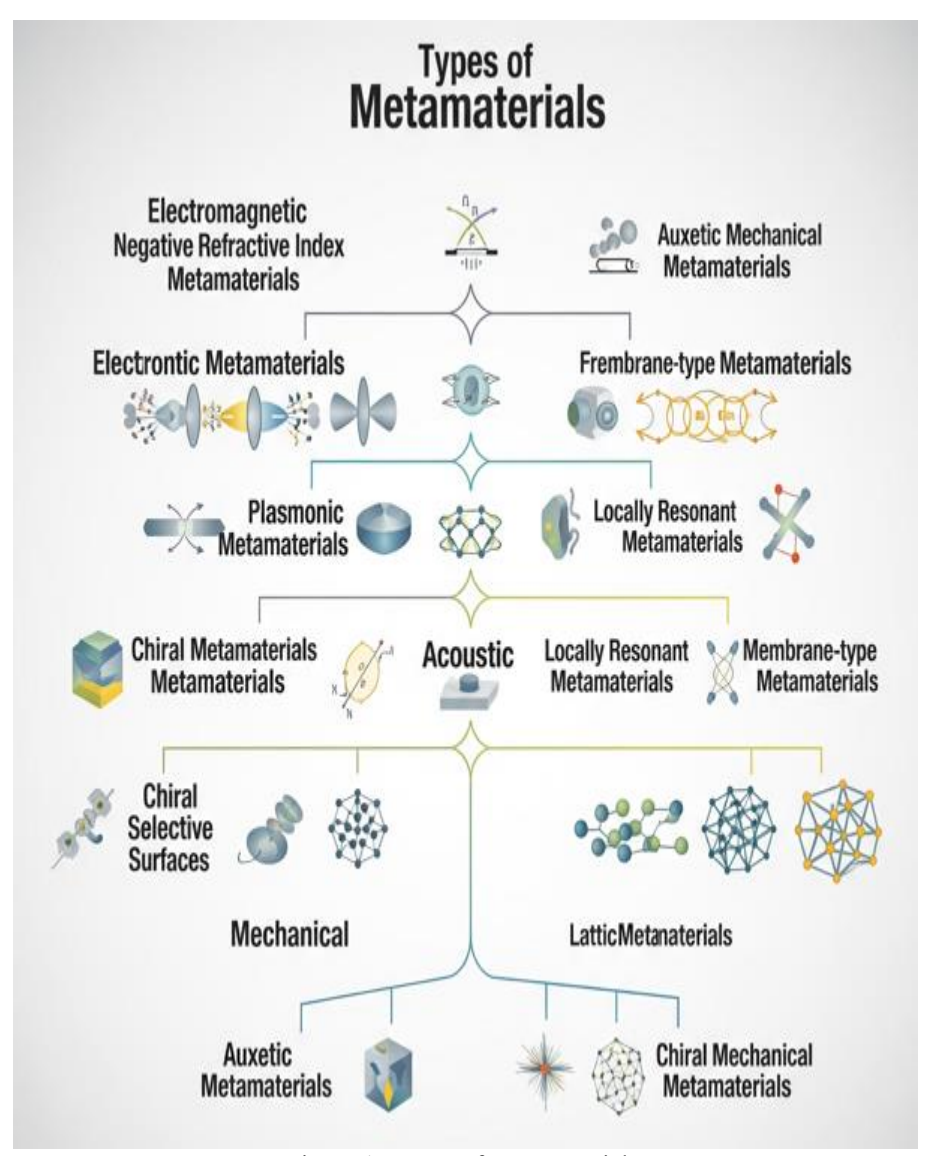


Figure 1. Types of metamaterials.

# **HISTORY**

The development of the theoretical foundations before the 2000s can be summarized as follows:

In 1967, Soviet physicist Victor Veselago published a theoretical paper on materials with a negative refractive index. No known natural material exhibited this property.

In 1987, Eli Yablonovitch and Sajeev John independently proposed photonic crystals (periodic structures that control light), the forerunners of

metamaterials. The first groundbreaking discoveries in this field of practical metamaterials occurred between 1996 and 2006.

In 1999, Sir John Pendry of Imperial College, University of London, proposed practical designs for microwave metamaterials. This "perfect lens" study demonstrated that a slab of negative-index material could focus light beyond the diffraction limit.

In 2001, David R. Smith's team at UC San Diego experimentally demonstrated negative refraction using Pendry's designs. In this study, they used copper SRRs and wires on fiberglass to bend microwaves in a non-natural way.

In 2006, Pendry & Smith at Duke University invented the first "Invisibility Cloak." In this study, a metamaterial device bent microwaves around an object, making them undetectable at certain frequencies.

Since the 2000s, studies have been conducted on expansion beyond electromagnetic fields. These studies include "silent" materials that block sound through resonant structures. Furthermore, studies have been conducted on sonic cloaking, that is, making objects invisible to sonar.

Furthermore, in the 2010s, work was conducted on mechanical and thermal metamaterials, and some progress was made on materials that expand when stretched, namely auxetics, and thermal cloaks that direct heat flow around objects.

Finally, from the 2010s to the present, various studies have been conducted on optical metamaterials. These include visible-light metamaterials (still challenging due to nanofabrication limitations) and plasmonics (light manipulation through nanostructured metals).

There are several challenges related to the work being done, such as nanofabrication, efficiency, and tunable metamaterials. Fabricating optical metamaterials requires extreme precision (e.g., electron beam lithography). Many metamaterials absorb significant amounts of energy (e.g., due to plasmonic losses in metals). Real-time control requires the incorporation of graphene, liquid crystals, or MEMS. The development of active and tunable metamaterials requires extensive and challenging work.

# **APPLICATIONS**

Metamaterials have various application areas. Some of these can be summarized as follows: cloaking and invisibility, super lenses, acoustic insulation, energy harvesting, wireless communications, medical imaging, and sensors (Figure 2).

The applications of metamaterials can be divided into three categories: electromagnetic, acoustic and mechanical, and energy and thermal metamaterials.

Applications of electromagnetic metamaterials include invisibility and camouflage, super lenses, and wireless communications (Pendry, 2000:3966) (Schuring et al., 2006:977). Developments in cloaking, camouflage, and stealth include optical cloaking and adaptive camouflage applications in military and vehicle applications. Super lenses and sub-diffraction imaging are used in nanoscale tumor detection in medical imaging, and ultra-high-resolution lithography in semiconductor inspection. In 6G and wireless communications, metamaterial antennas are used for high-gain signal transmission. Furthermore, metallurgical materials are enabling beam steering, reconfigurable antennas for satellites, and ultra-fast 6G networks.

Acoustic and mechanical metamaterials include noise cancellation, vibration shielding, and soft robotics. Related to noise cancellation and sonic cloaking, metamaterial barriers along highways can be used to reduce urban noise. Metamaterials used as earthquake and vibration shields redirect seismic waves around buildings. 3D-printed mechanical metamaterials with adjustable stiffness are used in programmable matter and soft robotics (Liu et al., 2000:1734) (Kadic et al., 2019:198).

Energy and thermal metamaterials include advanced solar absorption and thermal cloaking. Advanced solar absorption uses plasmonic metamaterials for ultrathin, high-efficiency solar cells. Thermal cloaking and thermal management utilize metamaterials to redirect heat flow in electronic devices to prevent overheating.

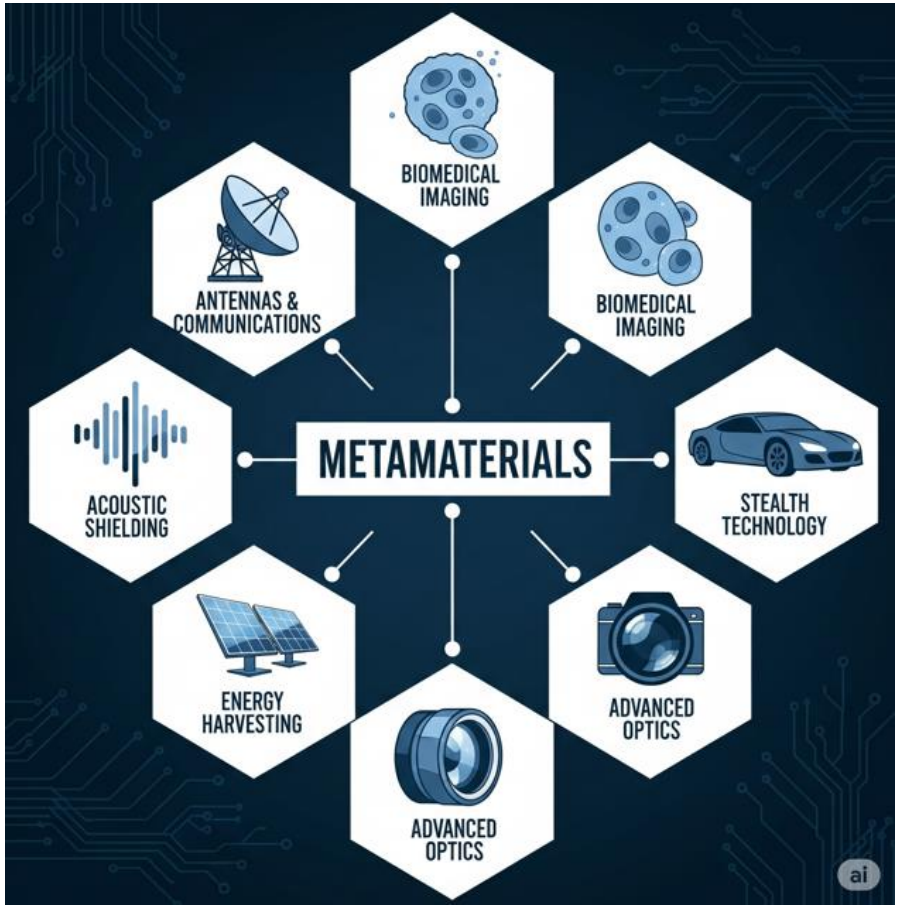


Figure 2. Applications of metamaterials.

# **SUSTAINABILITY**

Metamaterials are revolutionizing optics, acoustics, and materials science, offering groundbreaking applications ranging from invisibility to energy technology. Metamaterials can contribute to sustainability, but they can also create challenges. Metamaterials have certain advantages and disadvantages. These materials offer advantages such as energy efficiency, light weight, and reduced waste. For example, better photovoltaics have increased energy efficiency by reducing signal loss in devices. Strong but low-density lightweight structures are used in aerospace. Furthermore, the use of longer-lasting smart materials has reduced waste. Disadvantages of metamaterials include high cost, the use of rare earth elements, and difficulty in recyclability (Liu et al., 2000:1734) (Kadic et al., 2019:198).

Future research focuses on environmentally friendly, biodegradable metamaterials and scalable production methods. Sustainability challenges can be divided into environmental concerns and sustainability alternatives.

Environmental concerns include material supply and nanofabrication energy costs.

Material supply is important. This is because many metamaterial designs are based on gold, silver, or rare earth elements. This indicates unsustainable mining in design and production. Furthermore, nanofabrication has high energy costs, as the expensive and unsustainable electron beam lithography and plasma etching methods used here are energy-intensive.

Alternatively, sustainable, biodegradable metamaterials can be used (Figure 3, Table 2). Cellulose-based optical metamaterials are used here. Alternatively, recyclable and low-loss designs can be developed. Again, the use of non-metallic dielectric structures to reduce losses could be considered (Pendry, 2000:3966) (Schuring et al., 2006:977).

# Sustainability of Metamaterials: A Multidimensional Perspective

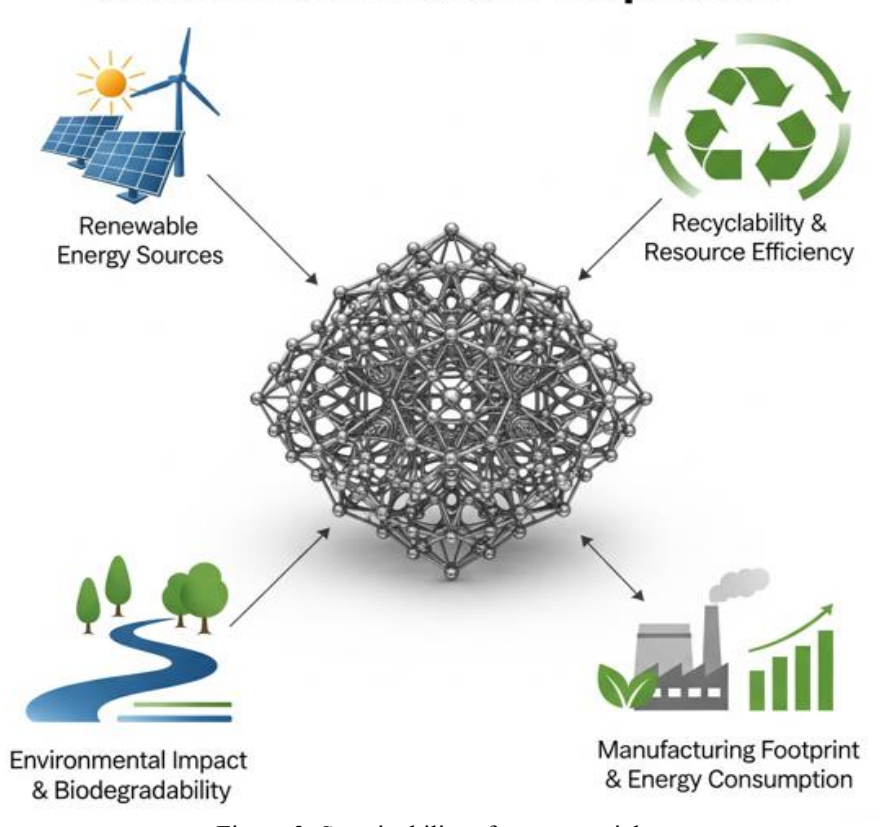


Figure 3. Sustainability of metamaterials

Table 2. A comparison table summarizing the types, applications, and sustainability of key metamaterial categories:

Type of Metamateri al	Key Applicatio ns	Sustainabi lity Pros	Sustainabilit y Cons	Future Improveme nts Needed
Electromag netic (e.g., plasmonic, dielectric metasurface s)	Invisibility cloaking  Superlenses (sub-diffraction imaging)  - 6G/THz communication antennas	- Can reduce energy loss in optical devices - Enable ultra-thin solar cells (less material use)	- Often require gold/silver (rare, expensive) - Energy- intensive nanofabricati on	- Replace noble metals with oxides/grap hene - Develop roll-to-roll manufacturi ng
Acoustic (e.g., sonic crystals, resonant structures)	- Noise-canceling barriers - Ultrasound imaging enhanceme nt - Seismic wave shielding	- Can replace heavy traditional soundproof ing materials - Passive operation (no energy input)	- Hard to scale for low- frequency sound - Some designs use non- recyclable polymers	- Bio-based sound absorbers (e.g., fungal mycelium) - 3D-printed recyclable designs
Mechanical (e.g., auxetics, origami- inspired)	- Impact- resistant armor - Lightweigh t aerospace structures - Wearable strain sensors	- Reduce material waste via optimized geometries - Potential for biodegrada ble auxetics (e.g.,	- Some rely on non- degradable elastomers - Limited load-bearing capacity	- Develop biodegradab le polymer composites - Self- healing designs

Type of Metamateri al	Key Applicatio ns	Sustainabi lity Pros	Sustainabilit y Cons	Future Improveme nts Needed
		chitosan)		
Thermal (e.g., photonic crystals, anisotropic composites)	- Heat cloaking for electronics - Enhanced thermoelect rics (energy harvesting) - Radiative cooling coatings	- Improve energy efficiency in buildings - Reduce need for active cooling systems	- Some use toxic semiconducto rs (e.g., bismuth telluride) - High-cost fabrication	- Non-toxic phase- change materials - Scalable spray-on metamateria ls
Biomedical (e.g., plasmonic biosensors, biodegradab le implants)	- Cancer hypertherm ia therapy - Glucose monitoring patches	Biodegrad able versions (e.g., cellulose, silk) - Reduce need for invasive surgeries	- Gold/nanopar ticle toxicity concerns - Sterilization challenges	- FDA- approved biocompatib le materials - AI- optimized patient- specific designs

# **FUTURE PERSPECTIVES**

It is anticipated that future research on quantum materials, AI-designed metamaterials, and space applications will continue.

Quantum metamaterials enable the control of quantum light-matter interactions for ultra-secure communication. In AI-designed metamaterials, machine learning is accelerating metamaterial discovery. In space applications, lightweight metamaterials are used for satellite antennas and radiation shielding.

In conclusion, metamaterials are leading to groundbreaking developments in cloaking, communications, energy, and medicine, but sustainability remains a challenge. Future research focuses on biodegradable

environmentally friendly materials, AI-assisted design, and space applications (Figure 4, Table 4).

Future directions in biomedical metamaterials may include biodegradable implants, AI-designed meta-surfaces, and metamaterial carriers for targeted delivery.

Sustainability tradeoffs can be summarized as follows: Most metamaterials offer energy/performance advantages but face material scarcity (gold) or manufacturing challenges. Mechanical and biomedical metamaterials are pioneers in environmentally friendly designs.

Future priorities include a circular economy, AI-assisted design, and scalable manufacturing: Metamaterials such as recyclable/biodegradable cellulose-based optics are included in the circular economy. Furthermore, AI-assisted design reduces wasteful trial and error during the development process. Finally, scalable manufacturing involves the transition from laboratory-scale to industrial methods (e.g., nanoimprint lithography) (Pendry, 2000:3966) (Schuring et al., 2006:977).

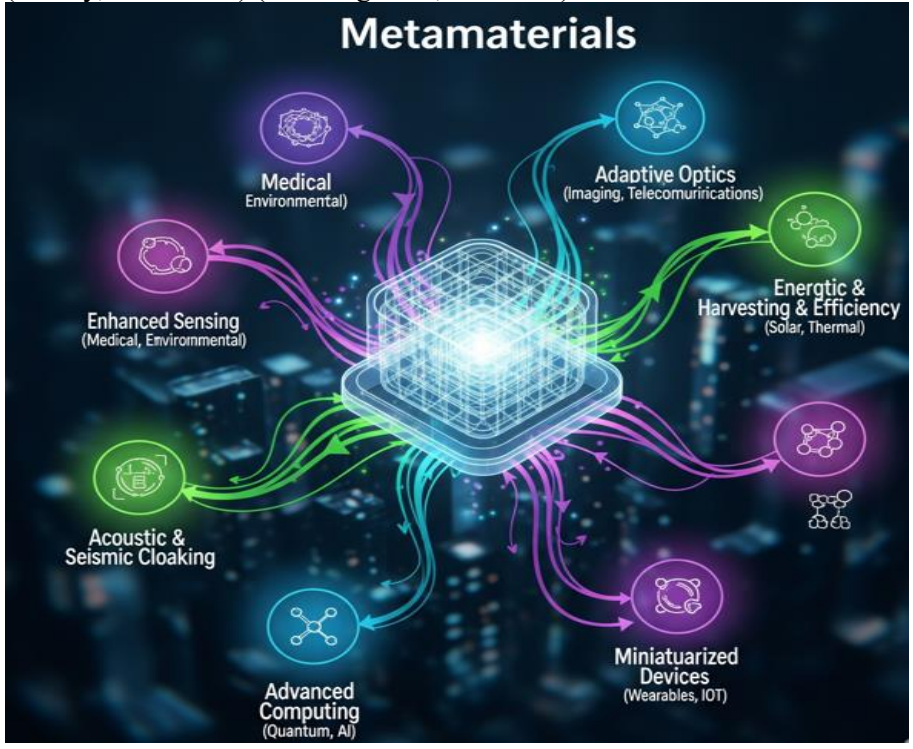


Figure 4. Future perspectives of metamaterials.

Table 4. A table about the comparison different metamaterials, their applications, sustainability and future perspectives (Shalaev, 2007:41) (Zheludev and Kivshar, 2007:917) (Soukoulis and Wegener, 2011:523).

Metamaterial Type	Key Features	Applications	Sustainabilit y	Future Outlook
Electromagneti c Metamaterials	Manipulate EM waves (e.g. negative refractive index)	Superlenses, cloaking, antennas, stealth tech	Mostly made from metals and dielectrics; can be energy- intensive to fabricate	High demand in defense, communications, and imaging; pushing 6G, quantum optics
Acoustic Metamaterials	Control sound waves, vibration isolation	Noise reduction, soundproofing , ultrasound devices	Typically low power and passive; sustainable materials possible (e.g. polymers, wood)	Growing in architectural acoustics, medical imaging, and consumer products
Mechanical Metamaterials	Unique mechanical properties auxetics, ultra- lightweight	Aerospace, biomechanics, protective gear	Can be 3D- printed with recyclable polymers; depends on material choices	Potential in soft robotics, medical devices, and lightweight structural materials
Thermal Metamaterials	Guide heat flow in unusual ways	Thermal cloaking, energy systems, electronics cooling	Potential for energy savings, especially in passive cooling; materials vary	Likely to see use in smart buildings, thermal management of electronics
Photonic Metamaterials	Manipulate light at nanoscale	Optical computing, sensors, solar cells	Energy- intensive nano- fabrication; potential for efficient light	Important in photonics, quantum computing, and advanced solar tech

Metamaterial Type	Key Features	Applications	Sustainabilit y control	Future Outlook
Chiral Metamaterials	Sensitive to polarization; asymmetric structures	Circular polarizers, sensors, biosensing	Materials and fabrication vary; often small-scale use	Biophotonics, quantum optics, and novel sensing applications growing rapidly

# CONCLUSIONS

The following conclusions can be drawn from the current investigation:

- Metamaterials are artificially structured materials designed to manipulate electromagnetic, acoustic, and mechanical waves in ways not possible with natural materials. Their properties stem not only from their chemical structure but also from their precise nano- or micro-scale structures. Metamaterials have three key properties: a negative refractive index, small wavelengths, and specific electromagnetic/acoustic responses. Types of metamaterials can be divided into four categories: electromagnetic, acoustic, mechanical, and thermal.
- The theoretical foundations of metamaterials were laid before the 2000s. For example, in 1967, Soviet physicist Victor Veselago published a theoretical paper on materials with a negative refractive index. No known natural material exhibited this property. In subsequent years, various studies on metamaterials were conducted and advancements were made. Finally, from the 2010s to the present, various studies on optical metamaterials have been conducted. These include visible-light metamaterials and plasmonic.
- Metamaterials have a variety of applications. Some of these include cloaking and invisibility, super lenses, acoustic insulation, energy harvesting, wireless communications, medical imaging, and sensors. The applications of metamaterials can be divided into three categories: electromagnetic, acoustic and mechanical, and energy and thermal metamaterials. Applications of electromagnetic metamaterials include cloaking and camouflage, super lenses, and wireless communications. Acoustic and mechanical metamaterials include noise cancellation, vibration damping, and soft robotics. Energy and thermal metamaterials include enhanced solar absorption and thermal cloaking.
- Metamaterials are revolutionizing optics, acoustics, and materials science, offering groundbreaking applications ranging from invisibility to energy technology. While metamaterials can contribute to sustainability,

they can also create challenges. Metamaterials have certain advantages and disadvantages. These materials offer advantages such as energy efficiency, light weight, and reduced waste. Strong but low-density lightweight structures are used in aerospace. Disadvantages of metamaterials include high cost, the use of rare earth elements, and difficulty in recyclability.

- Future research focuses on environmentally friendly, biodegradable metamaterials and scalable production methods. Sustainability challenges can be divided into environmental concerns and sustainability alternatives. Environmental concerns include material supply and nanofabrication energy costs. Alternatively, sustainable, biodegradable metamaterials can be used. Here, cellulose-based optical metamaterials are used. Furthermore, recyclable and low-loss designs can be developed. Again, the use of non-metallic dielectric structures can be considered to reduce losses.

- Future research on quantum materials, AI-enabled metamaterials, and space applications is expected to continue. Future research focuses on biodegradable, environmentally friendly materials, AI-enabled design, and space applications. Future trends in biomedical metamaterials may include biodegradable implants, AI-enabled meta-surfaces, and metamaterial carriers for targeted delivery.

#### REFERENCE

- Veselago, V. G. (1968). The Electrodynamics of Substances with Simultaneously Negative Values of ε and μ, *Soviet Physics Uspekhi*, 10(4), 509–514.
- Pendry, J. B. et al., (1999). Magnetism from Conductors and Enhanced Nonlinear Phenomena, *IEEE Transactions on Microwave Theory and Techniques*, 47(11), 2075–2084.
- Smith, D. R. et al., (2000). Composite Medium with Simultaneously Negative Permeability and Permittivity, *Physical Review Letters*, 84(18), 4184–4187.
- Pendry, J. B. (2000). Negative Refraction Makes a Perfect Lens, *Physical Review Letters*, 85(18), 3966–3969.
- Schurig, D. et al., (2006). Metamaterial Electromagnetic Cloak at Microwave Frequencies, *Science*, 314 (5801), 977–980.
- Liu, Z. et al., (2000). Locally Resonant Sonic Materials, *Science*, 289(5485), 1734–1736.
- Kadic, M. et al., (2019). 3D Metamaterials," *Nature Reviews Physics*, 1(3), 198–210.
- Shalaev, V. M. (2007). Optical Negative-Index Metamaterials, *Nature Photonics*, 1(1), 41–48.
- Zheludev, N. I., and Kivshar, Y. S. (2012). From Metamaterials to Metadevices, *Nature Materials*, 11(11), 917–924.
- Soukoulis, C. M., and Wegener, M. (2011). Past Achievements and Future Challenges in 3D Photonic Metamaterials, *Nature Photonics*, 5(9), 523–530.

# Wheel exploration and development

Fehim FINDIK<sup>1,2,c</sup>

<sup>1-</sup> Prof. Dr. Metallurgy and Materials Engineering Department, Faculty of Technology, Sakarya Applied Sciences University, Sakarya, Turkey. ORCID No: 0000-0003-2537-1951

<sup>2-</sup> Prof. Dr. Istanbul Aydın University, Mechanical Eng Dept, Engineering Faculty, Florya Halit Aydın Campus, Istanbul, TurkeyC: Corresponding author; e-mail: <a href="mailto:findik@subu.edu.tr">findik@subu.edu.tr</a>

#### **ABSTRACT**

In the present work, firstly, the history of the invention of the wheel, its time, place and reason for its first use are reviewed. It was first seen that the wheel was used in children's toys, but it was seen that it took a long time for the wheel to be used in transportation. It has been understood that the wheel that reduces friction makes life easier. It was first seen that horsedrawn carriages were used for transportation, and it was understood that spoked and rimmed wheels were used in these carriages. The use of these cars continued for about 200 years, before switching to steam power and then to gasoline internal combustion engines. Cars have become the center of youth culture because they provide a private space. People turned to supermarkets for shopping, which provide free parking to their customers. Electric vehicles, which used batteries that had limited range and took hours to charge, began to be used in taxi services in the USA in the early 1900s. But in a very short time, as internal combustion engines became more trustworthy, electric vehicles remained in the background. Electric car technology has made little progress since the 1920s due to batteries being heavy, large and unable to store enough energy. About 50 years later, lithium-ion batteries were developed and began to be used instead of leadbased batteries. Electrifying road vehicles that cause environmental pollution can make a significant contribution to reducing climate change by reducing emissions. It is estimated that in the future, as internal combustion engines are gradually stopped and cars, trains and other land transportation vehicles are converted to electric, exhaust emissions will decrease, and environmental problems will disappear.

Keywords - Wheel; development; history; car culture; future.

### INTRODUCTION

A wheel is a rotating piece proposed to turn an axle bearing. The wheel is one of the basic parts of the axle. Wheels make it easier to transport when supporting a load or doing work on machinery. Wheels are also utilized for another reasons, for instance ship rudders, potter's wheels and flywheels.

General models can be found in transportation functions. The wheel rolls with the use of axles, making movement easier and reducing friction. For the wheels to turn, a moment must be employed to the wheel about its axis, either through gravity or by the function of additional external force or torque. In 3500 BC, the Sumerians invented a device that used the wheel to turn it, much like a potter turning clay into the desired object.

The birth story of the automotive age can be summarized as follows:

In the 1890s, the largest towns in the Western earth were facing a growing trouble. It was impossible to miss the bad smell emitted by the manure and manure, especially from the horses pulling the horse-drawn vehicles on the streets. In the 1890s, there were 300,000 horses laboring on the roads of London and more than 150,000 in New York City. Each of these horses generated ten kilograms of dung and one liter of urine per day. It has become increasingly difficult to collect and remove thousands of tons of garbage from streets and barns.

Health representatives in Rochester, New York, computed that if the dung generated by fifteen thousand city horses each year were stacked up, it would include an acre of land up to 175 feet high and spawn 16 billion flies. All of this was harmful for municipal healthiness. According to a New York Times report in 1894, statisticians from the board of health in New York City observed higher levels of infective illness "in homes and schools within 15 feet of sheds than in more remote localities." At the turn of the century, it was reported that twenty thousand New Yorkers perished each year from "diseases floating in the grime." By the 1880s, fifteen thousand dead horses that had died from overwork were being eradicated from the roads of New York City each year.

Then, starting in the 1830s, the beginning of the steam locomotive and the building of express rail connections helped worsen the trouble. Quicker and more competent transportation among cities raised the requirement for rapid transportation of population and profits within cities, which necessitated the use of greater numbers of horse-drawn vehicles. In the 1890s, it was nearly impossible to talk on the streets of New York City due to traffic noise. Hay was occasionally spread on streets outdoor clinics and specific confidential houses to decrease noise.

Contamination, obstruction and sound were only the most evident symptoms of an extreme addiction. The equine flu epidemic that broke out in North America in October 1872 immobilized all horses and mules for numerous weeks and served as a stark notice of society's dependence on animal intensity. Concerning 1870 and 1900, the sum of horses in American towns quadrupled, although the humanoid inhabitants only multiplied. At the turn of the period, there was one horse for every ten persons in Britain and one horse for every four people in the America. Large tracts of farmland were required to provide hay and oats for horses, lowering the distance existing to increase food for humans. Horses had become both essential and untenable. Consideration began to be given to getting rid of horses and replacing them with self-propelled motor trucks.

In current years, this event has been quoted as proof of the capability of invention. However, the transition from horses to cars was not as correct a technological solution as it seemed, because cars changed the world in unexpected ways and created many other problems.

It is the motor truck rather than the horse that looks weak today. Because traffic accidents are an important reason of death and harm international. Very large districts of land are conferred to car parks, even though cars remain vacant for a typical of 95 percent; this turns cities into living spaces for people as well as dormitories for cars. But while the contamination emitted by cars is more difficult to see than horse dung, it is just as unsafe for individual healthiness as it releases toxic gases and greenhouse gases. These advanced troubles exhibit the tale of automobile acceptance in a new light. We are approaching a crossroads, as in the 1890s.

Whilst it was problematic to imagine how society would once role without horses, it is difficult to envisage how present humanity would act deprived of so many motor automobiles. As in the 1890s, there is increasing perception of the demand for alteration, led both by worries about ecological impact, protection and traffic obstruction.

Horseless carriages at the time were available in a wide collection of shapes and sizes and were diversely driven by internal combustion engines, electric motors, or steam power. Horseless carriages, like horse-drawn carriages, were assumed to be something only the wealthy could afford. But for the less wealthy, it will at least be cheaper to hail a taxi because removing the horses will reduce operating costs. One might think that electric cars are best (clean and cheap) for urban use.

Anything was achievable in the 1890s, but no one knew what the world would look like after the death of the horse, even though change seemed inevitable. Electric cars, which did not become widespread in the prompt twentieth century, are on the rise a century later. Replacing the world's cars with electric thrust would go an extended way in lowering their ecological impact, although traffic and safety points persist. Temporarily, with smartphone applications, customers can call a taxi with a few taps. Additionally, start-ups working on autonomous or driverless vehicles and flying cars that will transport people can be counted among future applications.

Reentering the antiquity of the automobile and how it altered the world can deliver a roadmap to aid seem right of these new transportation choices by screening how social, political, and technical forces interrelate to create both predictable and unpredicted consequences.

Today's car-centric traditions is the outcome of a series of selections dating back thousands of years. Many of these options could have certainly gone in a distinct direction and now they make variation complex; this is a marvel identified as route territory. Only by realizing these choices and the context in which they were made is it possible to draw lessons from past periods that can be applied to the present.

There is a five-thousand-year history journey from the wheel to the car and from there to a short past of movement. Studying the outcomes of the car can provide us with a street map for exchanging with the unexpected

effects of latest outlines of transportation. By realizing from the long-ago, we are more probable to test the right queries and make learned options in the upcoming. As we begin to separate the car from the fabric of present life, it is useful to observe where and how it is fabricated.

The aim of this study is to review the historical process regarding the invention and development of the wheel, to examine why the wheel is needed, to investigate the automobile revolution and culture, to look at electric vehicles and finally to criticize the predictions made about the future of vehicles.

#### HISTORY

The location and interval of the discovery of the wheel remain uncertain. It is believed that the Mesopotamian culture is commemorated with the innovation of the wheel (Ditkoff, 2008:15). Nonetheless, some recent resources imply that it was developed externally in both Mesopotamia and Eastern Europe (Bulliet, 2016:6). Proof of first use of wheeled carts has been located in the Middle East, Europe, Eastern Europe, India, and China. It is unknown whether the Chinese, Indians, Europeans, or even Mesopotamians devised the wheel autonomously (Standage, 2021:2).

The innovation of the solid wood disc wheel dates to the later Neolithic period. This implies that even after the innovation of farming and clay in the Pre-Pottery Neolithic period, several thousand years passed without wheels. This Ljubljana Swamp Wheel is the last wooden wheel ever unearthed, courting to the Copper Age (around 3130 BC).

The Halaf civilization of 6500-5100 BC is occasionally thought to be the first representation of a wheeled vehicle, although this is dubious due to lack of evidence (Roux and Pierre, 2009:155). Precursors to pottery wheels recognized as "turnets" or "slow wheels" were identified in the Middle East in the 5th millennium BC. One of the oldest instances was detected in Tepe Pardis, Iran, and was seen to 5200-4700 BC. These were made of stone or clay and were fixed to the position with a nail in the middle, but they needed great attempt to turn them. Real potter's wheels, with an easily rotating wheel and axle mechanism, date back to B.C. It was established in Mesopotamia (Iraq) around 4200-4000 BC (Moorey, 1999:146). The last remaining instance, found at Ur (modern-day Iraq), dates to about 1000 B.C. It is dated to 3100 (Marshall, 1996:554). Wheels of tentative date have also been obtained in the Indus Valley development, a 4th epoch BC advancement that encompassed parts of current-day India and Pakistan.

The earliest hinted proof of wheeled locomotion was obtained in the form of miniature clay wheels north of the Black Sea before 4000 BC. Descriptions of wheeled chariots obtained on clay tablet pictographs in the

Eanna territory of Uruk in the Sumerian advancement in Mesopotamia date back to B.C. Appeared 3500–3350 BC (Anthony, 2007:67).

Depiction of a chariot drawn by a wild ass on the Sumerian "War" panel of the Standard of Ur (c. 2500 BC). Representations of a wheeled van appear in Bronocice clay pottery excavated between 3631 and 3380 BC at the Funnelbeaker cultural site in southern Poland (Velušček et al., 2009:197). Existing confirmation of a wheel-axle permutation from Stare Gmajne (Ljubljana Marshes Wooden Wheel) near Ljubljana in Slovenia is dated within two normal variations to 3340–3030 BC, the axle to 3360–3045 BC (Fowler et al., 2015:109). Some historians think that wheeled vehicles spread from the Near East to Europe in the mid-4th epoch BC.

The first wheels were minimal wooden disks with a hole for the axle. Some of the initial wheels were made from parallel slices of tree trunks. Spoke wheels continued to be used without major changes till the 1870s, when spoked wheels and pneumatic tires were discovered (Jewel, 2006:722). Pneumatic tires can seriously decrease rolling confrontation and increase reassure. Wire rims are under tension rather than compression, making it feasible for the wheel to be both stiff and light. The first radial spoke wheels gave rise to tangential spoke wheels, which were broadly utilized on automobiles towards the end of the 20th epoch. Cast alloy wheels are now more generally utilized; forged alloy wheels are employed where weight is critical.

The innovation of the wheel was also significant for technology in usual; substantial efforts such as water wheel, gear wheel, revolving wheel and astrolabe. The more modern ancestry of the wheel incorporates the fan, jet engine, flywheel, and turbine.

# **NEEDS FOR WHEEL**

The people of North and South America did not utilize wheels. Before Columbus' voyages, people either brought their weights on their backs or used harnessed dogs or, in the Andes, packed llamas. Nineteen hundred years ago, a potter in southern Mexico, she receipts a slice of pale clay and turns it into a dog for her daughter to play with. This dog is a wheeled toy (Figure 1). His daughter loves him.



Figure 1. A pre-Columbian toy dog on wheels.

Wheels were used in toys to entertain children. However, it will take a long time for wheels to be used in transportation. The amount of wheeled transportation arises from the fact that the load of the load is confirmed by the wheels rather than human muscles, and the quantity of friction created when rolling somewhat rather than tugging it across the terrain is reduced. Today, when we press a grocery cart down the aisle of a superstore or haul a piece of baggage at the airfield, we choose wheels over backpacks.

Conditions outside Europe did not differ much from that inside, with four-wheeled vehicles being generally unavailable elsewhere. Two-wheeled chariots and four-wheeled chariots date back to B.C. In the Middle East, where it began to be used in the third millennium, wheeled transportation almost completely disappeared in the first five centuries AD. The reason the wheel was abandoned from Tunisia to the eastern border of Iran was the recognition that most goods could be transported more reasonably by pack camels and donkeys rather than by oxcarts.

Further east, a contrast involving China and Japan focuses the choice uncommon cultures had in adopting or not adopting the wheel. Custom holds that the Chinese rented the consumption of the chariot from nomadic families of the Eurasian steppes through the reign of Wu Ding, king of the Shang dynasty, who stayed over 1200 BC. However, horse cavalry quickly replaced chariots on the battlefield after 300 BC.

The most widespread wheeled automobile in Zhang Zeduan's painting and an even larger scroll image from the eighteenth century, intended as an update of his masterwork, features a wheelbarrow. Respectively wheelbarrow has a single greater wheel and equilibriums the weight directly on the axle of the wheel, whether in bundles or with two passengers sitting on each side of the wheel (Figure 2). The Chinese wheelbarrow thus changes importantly from the European wheelbarrow, which was a later and seemingly self-governing creation; because the worker does very slight exciting and dedicates his strength to balancing the weight and forceful the vehicle onward. The wheelbarrows we use, which come

from primitive European designs, place the load between the wheel and the handles and therefore require the operator to lift and push simultaneously. Although occasionally an animal or a second man is demonstrated simultaneously pulling the Chinese wheelbarrow, animal power anchored and forced from following operates only as a balance to human power (Bulliet, 2016:1). Wind power can also support muscle power through a modest mast and sail raised on a lone wheel. Both scroll portraits display two human porters and animals being loaded or ridden for each cart and cart. Members of the privileged travel in closed palanquins or palankeens.



Figure 2. Chinese wheelbarrows with passengers, 1910–1925 (Bulliet, 2016:1).

Traffic in pre-modern Japan seemed incredibly distinct from that in China since the Japanese utilized wheeled vehicles only in restricted roads. This is even though China and Korea greatly affected the enhancement of Japanese civilization. Equestrianism, an exercise derived from Korea, appears in promptly Japan in the form of ceramic horse models observed in Japanese tombs seeing among the third and sixth centuries. Therefore, there is no doubt about the existence of powerful native beasts in Japan, and it is unbelievable that the Japanese were ignorant that horses were used to drag chariots and chariots on the Asian continent. However, until the midnineteenth epoch, horses were rarely or never treated to tug trucks. As for the oxen used by the Japanese to drag tools, they were hardly employed to carts and never hitched to four-wheeled carts.

An anthropologist and expert, Alan Macfarlane, summarizes the evidence on Japanese rural life says (Bulliet, 2016:1): It can be said that wheeled vehicles were used in a limited way in Japan from 1600 to 1868.

However, as Japan improved in the late nineteenth epoch, wheeled vehicles became more common, but those pulled by people regained prominence. This growth of wheeled transportation in cities brought the form of rickshas. But an Englishman living in Japan throughout World War I perceived a modern form of hand-drawn carts transporting human litter from city toilets to the landscape to be exploited as manure:

A further characteristic consumption of wheels in Japan is the extravagant presents identified dashi that characteristic at fairs in numerous sections of the territory. These trucks may be two or three narrations high and have one, two or three wheels; but none of the axles rotate to permit the lift to be operated. Dashes, like rickshas and ranchers' manure carts, are usually moved not by beasts but by people pushing from behind pulling beams and ropes (Figure 3).



Figure 3. A Japanese *dashi* being pushed at a festival (Bulliet, 2016:1).

#### CARRIAGE REVOLUTION

In 1400, European aristocrats were divided along gender lines when it came to boarding wagons. If they were ancient and weak, men traveled horses and avoided wheels. However, once noble women went on a voyage, they and their companions voyaged by carriage. This division ended in the 15th and 16th centuries.

Phaetons that can be considered the pioneers of our age in any way It was not until the Middle Ages that current elegant instruments were invented or introduced; and for many years after the first launch of horse-drawn carriages, they were used only by ladies, and by them only in formal circumstances. Kings and knights contemplated all types of chariots to be exquisite machines.

Some authors thought that new equipment made sixteenth-century trucks more useful and affluent. They mentioned the "renaissance" of the rotating anterior axle, which made it easier to steer carriages in Roman

times, and the "innovative" inspiration of holding the traveler section on oblique or longitudinal groups or leather belts.

He explains the 16th century as a turning point in European transportation narration. The rare images of cars and trucks that survived from early 1500 do not show any technical similarity between horse-drawn carriages and wagons from different parts of Europe. Wheel makers, who required a great deal of skill and experience to assemble spokes, spokes, hubs and rims, produced an individual profession, but wagon producers and wagon makers did not.

But by 1600, horse-drawn carriage riding had become common throughout Europe. Nobles were as likely to benefit from these tools as their wives, mothers, and sisters (Fig. 4). Increased consolation cannot describe the new anger for travel by car, as extremely furrowed and grimy streets made cross-country travel as challenging in the 1600s as in the 1400s. They occasionally brought packs of hay to absorb mud, poles and ropes to pull transports across trenches, and extra coachmen to assist handle such foreseeable disasters (Fig. 5).

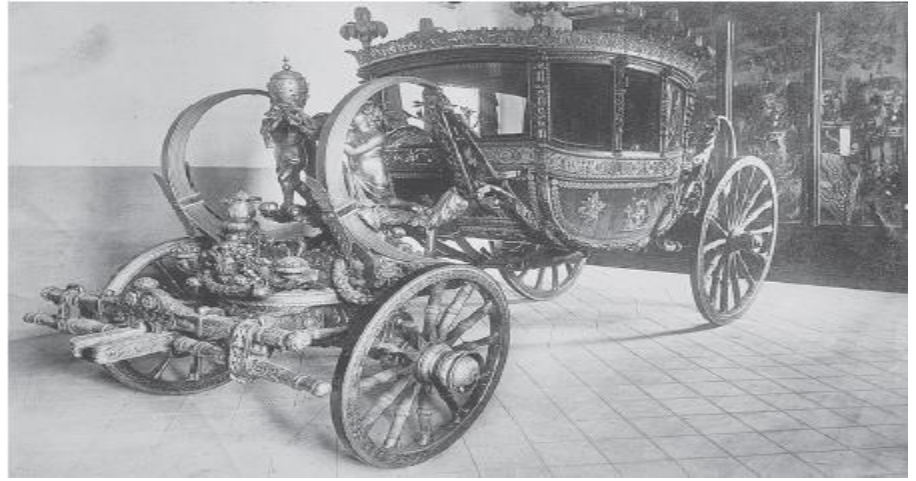


Figure 4. A papal transport with intricate interruption, nineteenth epoch (Bulliet, 2016:1).

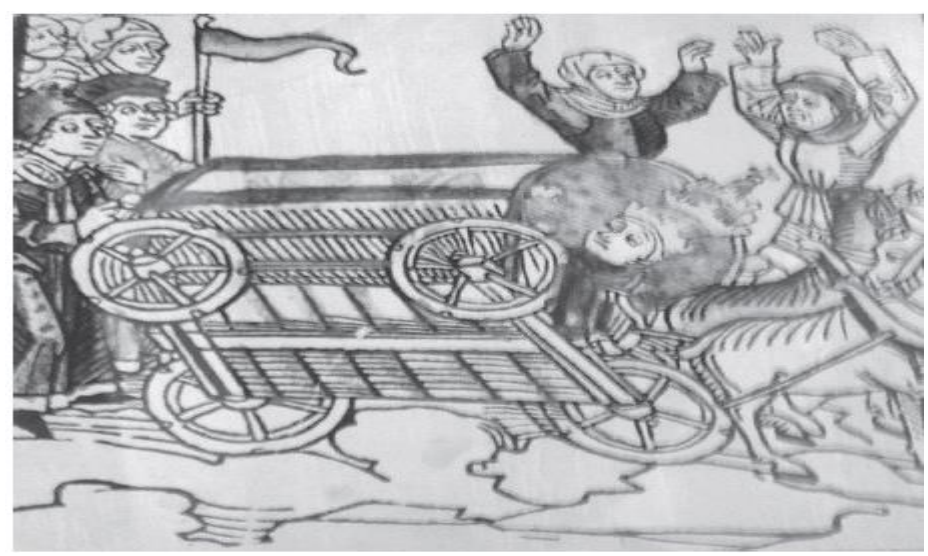


Figure 5. A toppled Hungarian transport, 1483. Note the lack of a pivot in the interior of the anterior axle (Bulliet, 2016:1).

Horse carriages also became unpopular due to government encouragement. Hungarian carriage historian László Tarr says about his hometown: It can be said that horse-drawn carriage driving in Hungary is a truly national tradition; It was so fashionable even among the lesser nobles in the 16th century that many nobles would go to war on horseback or by carriage rather than on foot for the sake of convenience (Tarr, 1969:187).

The word mentioned in this edict, Kocsi, points to Hungary as the country where high-ranking people first changed from horses to cars. Koçs was the stopping point on the route up the Danube River valley from Buda, the center of Hungary, to Vienna, the effective center of the Holy Roman Empire.

From the fifteenth to the mid-seventeenth centuries, Christian rulers and clergy ruled over the Muslim Ottoman Empire. He was his greatest adversary. The initial primitive guns began to be used in Europe in the 14th aera and were widely used in restrictions from the 15th century onwards. However, the cannons applied in the Ottoman success of Constantinople in 1453 prevailed out in terms of size and efficacy. It is said that a cannon made for the sultan was dragged some 150 miles to the town walls by two hundred men and sixty oxen. It is noteworthy that the ball creator who created this giant was a Hungarian identified Orban.

The invention of launching a gun on a couples of wheels was achieved by the Czech general Jan Žižka in 1415. Bohemia was also one of the places in Europe where development took place. The number of gunpowder guns matched that of four-wheeled trucks. Perhaps enthused by the custom of the Huns, Cumans, or other carriage wanderers who

occasionally engaged the Great Hungarian Plain, the fourth-century Roman tactician Vegetius noted that "altogether the barbarian states arranged their chariots in a circle around them" (Carlson, 2013:1).

In the 14th century, some military minds focused on the role of cannon on the battlefield. As evidence of this, "howitzer" and "pistol", two words derived from the consistent army background as the Hussite wheeled weapons, spread westward.

The Hussites famously used circular wagons as weapon platforms. Unlike the women's wagons and ornate bridal carriages that defined four-wheeled passenger transport for the elite for centuries, masculine vehicles were also developed.

Novel or progressed wheel equipment emerges while modifying conditions generate newfound demands and therefore create chances for invention. In this case, the prospects were army, but the larger effect was emotional. In outline, the transparent defines of claim are:

- 1. The folklore of relatives roaming in four-wheeled carriages is becoming widespread.
- 2. After 2000 BC, four-wheeled vehicles were replaced by two-wheeled vehicles.
- 3. Later, traveler carriages commenced to be utilized almost utterly for the transportation of high-ranking women with their woman followers.
- 4. Through the sixteenth century, European nobles steadily shed their contempt for wheeled transportation and began travelling in horse-drawn carriages.

By the immediate seventeenth epoch, the driving stage of the transport cycle was well proceeding in England. The rise in popularity of cars created further difficulties and worsened old problems: traffic, dung and muck on the roads; defeated covering gravel and booming furrows began by iron-rimmed wheels; and the social privileged who own more than one vehicle. Rural areas, where lanes were harsh and badly continued, were lengthier to be changed. On the farther progressive sideways, horse-drawn transport making became a respected profession.

Nearly two centuries later, the horse-drawn carriage revolution had reached full effect. In Europe alone and the overseas colonies of a few European countries, four-wheeled mine carts and horse-drawn carts, accompanied by the evolving iron rails and tiled streets, provided the necessary infrastructure for the change from horses and oxen to vapor power and petrol machines.

Further wheel-using civilizations around the world lasted to convince their desires for transportation with two-wheeled cars. However, lest we think that this is an indicator of backwardness, it should be remembered that cars are simpler to develop than carriages, operate with fewer friction and do not force a complex steering system.

Technically, there was not anything to stop China or India from acquiring an analogous four-wheeled structure. Equally territories adopted the chariot. What separated China and India from Europe in not improving cars was not a lack of skill, supplies or creativity. Wheeled spread transportation was a fundamental factor in this expansion, although the transport innovation that paved the way for Europe's unprecedented advancement of motorized transportation was emotional. However, the emotional momentum and imperialist support for the implementation of four-wheelers in China was lacking.

In summary, the materials used in different periods of wheel development, their areas of use and their properties are given in Table 1. In addition, the durability and performance of different materials used in different wheels are summarized in Table 2.

Table 1. Comparison of the development of the wheel in different periods.

Period	Wheel Materials	Areas of Use	Properties
Antiquity (BC 3500)	Wood	Agriculture and transportation	Simple wooden structures, low speed
Middle Age (500-1500)	Wood + Metal Circle	Horse carts, wheelbarrows	Increased durability, heavy load carrying
Industrial Revolution (1750)	Steel	Railway, industrial machinery	Strong and durable, high speed and load capacity
Modern Age (1900-)	Rubber + Metal Body	Automobiles, aircraft, heavy machinery	Improved road holding and safety

Table 2. Material and usage table according to wheel types.

Wheel Types	Used Materials	Used Area	Durability and Performance
Wood Wheels	All wood	First agricultural vehicles, horse-drawn carts	Low
Metal Wheels	Iron, steel	Railway, industrial machinery	High
Rubber Coated	Rubber + Metal Body	Car, bicycle	Medium-High
Radial/Pneumatic Rubbers	Rubber + Reinforced Steel Cord	Modern vehicles, airplanes	Very High

### **CAR CULTURE**

Cultural tropes that emerged in the 1940s and 1950s, when cars changed the way people socialized, ate, and shopped, spread throughout the world and reshaped Western popular culture.

One of the factors of the emergence of young people was the car. The minimum driving age in most American states was sixteen, and second-hand vehicles were cheap and readily available. "Hanging out with friends, riding in cars, football players and cheerleaders, school proms, etc." played an important role in the emergence of youth culture. Cars were central to this new youth culture because they provided independence from parents and a private space beyond prying eyes (Figure 6).

Cars accelerated the change in courtship.

Tradition in the middle class, it was common for young women to invite young men into their homes. The couple would then sit in the living room to chat with the young woman's parents, which sometimes led to the whole family being invited to dinner. Dating, which became common among middle-class families from the 1920s onwards, often involved the young man inviting the woman to go out with him. He was expected to pay for some form of entertainment, while she was expected to simply accompany him. By the outbreak of World War II, flirting had completely replaced calling.

Young male car owners had a distinct advantage in this new model. Since they have their own transportation, they can potentially date a larger group of girls and take them to a wider range of places. Anyone with a car or access to a family car will have no shortage of friends. It was found that by the 1930s, the average urban teenager spent four nights a week out with friends, in groups or in pairs.

Cars provided greater sexual freedom and excited young people. Advice on dating etiquette abounded in magazine columns. But the war changed attitudes. After the war, living regularly with a single partner became an established part of youth culture.

Drive-in theaters first appeared in the 1910s but became more common in the 1930s. Hollingshead, who worked as a salesman for his family's auto parts company, tested the concept by putting a movie projector on the hood of his car in the driveway, hanging a sheet from some trees as a curtain and inviting his neighbors over. He patented his idea and opened his first drive-in near Camden, New Jersey, in June 1933. Tickets were twenty-five cents per person and per car. He declared that his invention "transforms an ordinary motor car almost into a private movie theater."

This idea was slow to come to fruition. There were only fifteen drive-ins in America. The number of drive-in cinemas increased to two thousand in 1950 and to over four thousand in 1958. Unlike indoor cinemas, drive-in theaters could only operate when it was dark, because otherwise it

was difficult to see the projected image. But this, combined with the privacy that cars provide, has made drive-in venues ideal date venues for obvious reasons. Hollywood studios saw drive-ins as a threat.

As cars changed the way people courted, they also changed the way they ate. Drivers in a hurry wanted to eat quickly, and the automobile industry provided a model for rapid production of standardized products. Drive-in restaurants quickly appeared on American highways, catering to time-strapped drivers, giving rise to the modern fast-food concept.

A Pig Stand franchise in California in 1931 appears to have been the first fast-food restaurant to allow customers to order by driving up to the window rather than parking and waiting for the car. Drive-in restaurants raced to serve customers as quickly as possible, equipping drive-thrus with roller skates and experimenting with various ordering systems.

The McDonald brothers opened a drive-thru restaurant in Pasadena. California sold mostly hot dogs in 1937. This being successful, they opened the McDonald Brothers Burger Bar Drive-In in 1940, selling mostly hamburgers as the name suggests. This new restaurant performed better in part because it was close to a high school. Its popularity enabled the brothers to buy a large house with a swimming pool and tennis court. But its success also led to problems. Cars were backed up in front of the restaurant during peak hours, as each order took an average of twenty minutes to deliver. They eventually closed their restaurant in 1948 to overhaul it. When it reopened three months later, it was still selling burgers. But everything about him had changed. McDonald's got rid of drive-thrust and required customers to get out of their cars and place their orders at the window. They also reduced their menu from twenty-five items to nine, realizing that burgers accounted for more than 80 percent of food sales. They eliminated trays, plates, glassware and cutlery that could be broken or stolen, and replaced them with disposable paper bags, wrapping paper and cups (Carlson, 2013:1).

The brothers called the result the Speedee Service System with fewer staff and a more efficient production process, they can offer hamburgers for fifteen cents and cheeseburgers for nineteen cents, about half the price of the same order at a sit-down restaurant. Queues formed outside their restaurant, but they moved quickly because the small, standard menu meant that burgers and fries could be produced constantly, rather than each item being cooked to order. The brothers appeared on the cover of American Restaurant magazine in 1952 and were inundated with letters from other restaurateurs asking about their system. McDonalds realized that their new approach had great potential and began licensing it to franchisees.

Kroc came to see McDonalds after purchasing two in 1954.

After making a deal with the brothers, Kroc began opening dealerships across America, focusing on fast-growing suburbs, initially in California, due to high rates of car ownership. By 1960 there were 228 franchises and Kroc planned to open 100 more each year. But aggression

overly competitive tactics alienated the brothers, and he bought them out in 1961.

After opening more than a thousand McDonald's restaurants, in the United States, Kroc began expanding internationally in 1967. Today, it has more than thirty-seven thousand branches in more than a hundred countries, creating McDonald's the subsequent biggest fast-food corporation in the creation.

The largest chain with more than forty-two thousand sales points worldwide is Subway, and Starbucks, KFC and Burger King are in the top five. All the world's fifteen largest fast-food chains, ranked by number of branches, are American. Surprisingly, McDonald's adopted the drive-thru model relatively late, opening its first drive-thru in Arizona in 1975. But drive-thru sales soon accounted for 70 percent of its sales in America.

Roadside restaurants weren't the only way cars changed the way people bought food. An even bigger change was the rise of supermarkets. The idea of customers serving themselves, rather than asking a store owner to prepare their orders for them, first emerged with the opening of the Piggly Wiggly grocery store in Memphis, Tennessee, in September 1916. It was an instant success and spawned many imitators. However, while Clarence Saunders, the founder of Piggly Wiggly, pioneered the idea of self-service in grocery stores, it was another entrepreneur, Michael J. Cullen, who designed the supermarket concept. In 1930, Cullen, who had worked for many years at Kroger, a chain of self-service grocery stores, came up with the idea of a much larger store, forty times the size of a traditional grocery store.

Supermarkets combined Piggy Wiggly's self-service model with curbside retail pioneered by drive-through filling stations, the first of which opened in 1913. National Supply Stations, which opened a chain of filling stations in California that year, claimed to offer drivers fuel of more equal quality and at a lower price under a brand that promised consistency. Independent retailers have responded to the rise of gas station chains by opening "super service stations" that sell gas and oil from retail spaces arranged along the side of a street, as well as offering other auto supplies, repair services, and cleaning services. off-street forecourt. The ease of hitting the road to access these various services has led to the adoption of this model by food and other goods retailers. To spread markets with off-street parking proliferated in Southern California in the 1920s, located along major thoroughfares in affluent areas and away from the congestion of downtown commercial districts. Mix it with self-service and scale everything and the result is late nights (Carlson, 2013:1).

It was the 1930s suburban supermarket; It was a generally windowless building located in a parking lot two or three times the size of the store. This new approach was only possible with the widespread use of car ownership. Placing supermarkets next to main roads on the city edges rather than in city center shopping areas meant lower rents.

Stores can be much larger and offer plenty of free parking to their customers. Supermarkets can offer lower prices by purchasing larger quantities of products from suppliers. Customers arriving by car could purchase large quantities of products at discounted prices; enough coffee, flour or sugar to last several weeks at a time. Supermarkets also acted as their own warehouses, unlike small grocery stores that could not keep large amounts of stock. This allowed for further price reductions by reducing distribution costs. The first true supermarket, King Kullen, opened in Jamaica, Queens, New York City, in August 1930. His motto was: "Raise. Sell at a low price." In Depression-era America, this was a winning formula. By the mid-1930s, Kullen had opened seventeen stores, and other retailers such as Big Bear, Handy Andy, and Giant Tiger were following suit. By 1941 there were more than ten thousand supermarkets in America.

"Possibly no stage of marketing dissemination has depicted the vision of the American community more than the superstore," declared the Journal of Marketing that year. "In less than a decade, nearly 50% of American consumers have altered their food shopping preferences." When supermarkets first emerged, the appeal of these food discounts was so great that consumers drove from as far as 75 and 100 miles away. This factor became possible only thanks to the huge development of the vehicle. No prolonged does the housewife depend on her own strength to shop for groceries or feel the need to stay within a limited comfort radius to do the folks spending. His vehicle made him separate from a specific region; and if he has a convenient parking space, he can drive almost any distance he wishes to purchase groceries if the price appeal is great enough.

This new model has changed not only how people shop, but also where they shop. "The relocation of the major food marketplace from the center or main road of a city to the borders of the city or to different housing areas further than the commercial midpoint is altering the corporeal feature of metropolises and urban preparation," the Journal of Marketing notes. "This also means we may see communities becoming more dispersed and rural and urban populations merging more." In other words, suburbia. Supermarkets have shown that suburban car owners are willing to travel to get better prices. Larger, formally planned shopping malls, often located around department stores, had existed since at least the 1920s.

Building shopping malls was particularly lucrative. New tax rules, along with rising real estate prices, allowed developers to build one mall, exhaust the tax benefits, sell it for more than it cost to build it, and then start building another.

The 1954 rule change also spurred the development of America's first nationwide motel chains, such as Holiday Inn and Howard Johnson's. It also contributed to the decline of drive-in cinemas.

His plan placed a shopping center at the heart of a 463-acre site. His design would be extremely effective. Developers ignored his proposals for

housing, schools and outdoor space and built the shopping center surrounded by a large parking lot. This new type of space, now known as a shopping mall, has been welcomed by many. Southdale became the template for shopping malls in America and beyond for the rest of the twentieth century. It was arguably the most influential building of the post-war period.

Gruen envisioned Southdale as the antidote to car-based suburbs because it would force shoppers to abandon their cars and wander around the common area. As he said while announcing his ideas at an architecture conference in 1964, "We were stunned by a technological phenomenon. This is the advent of the rubber-tyred vehicle. Private cars, trucks and trailers as public transportation vehicles. And their threat to human life and health is as great as open sewage." But the new shopping malls were only accessible by car, and their proliferation on the edges of cities both solidified America's car dependency and helped spread it to other countries. By 1970, when the 1954 tax loophole began to be closed, there were more than thirteen thousand shopping malls (including indoor malls) in America; almost all of these had been built in suburban areas in the previous fifteen years, accelerating the decline of traditional city centers. Fortune magazine said, "Downtown Has Escaped to the Suburbs."

With the emergence of cars, fast food intersections, and shopping malls, cars remodeled the natural and artistic scenery of America, and subsequently several another nation. However, all car-centered institutions of the twentieth epoch are now in decrease. The limited continuing drive-ins have revived interest in movie theaters through coronavirus quarantines, and in a systematic swap of antiquity, 160 Walmart space groups were converted into provisional drive-ins in the summer of 2020. Drive-ins and parking lots surrounding the globe have also hosted publicly detached cathedral provisions. Fast food chains have also seen that consumers have become more health conscious in recent years and demand has slowed down.

Overall, the car's prominence in American popular culture seems to have peaked in the 1970s and 1980s, just as the first generation. A large proportion of post-war American teenagers found themselves in control of the world's entertainment industry. In all these cases, cars are symbols of freedom, glory, and power, at least for white men; They are shown driving on open, empty roads and never find themselves stuck in traffic, unable to find parking, or subjected to unwarranted police stop.

But cars are no longer associated with freedom in the same way. Instead, it is the smartphone that now gives users previously unimaginable freedom to socialize, shop, and transport themselves to exciting new areas, out of their parents' line of sight. Just as the young people of the 1940s never knew a world without cars, today's young people have never known a world without the Internet and are creating their own cultural norms around smartphones and online communication. As with cars, the first generation to

grow up with a new technology may define its social and cultural impact, or new technologies may simply take a generation to catch on.

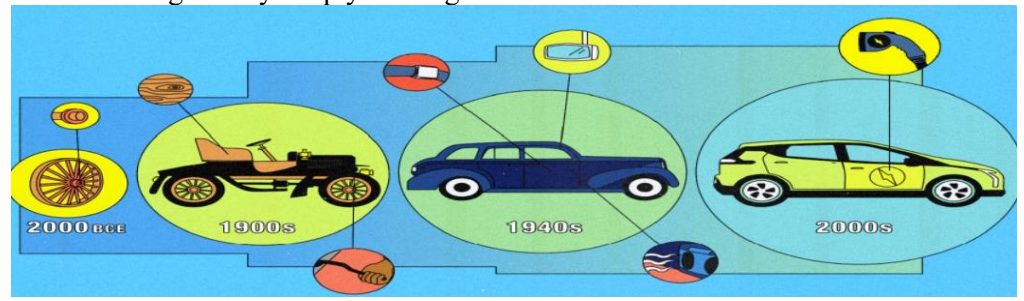


Figure 6. Car culture is changing

# **CONCLUSIONS**

The ensuing inferences can be drawn from the presented investigation:

- a. Although the time and place of the invention of the wheel remain uncertain, it has been suggested that the wheel was invented independently in both Mesopotamia and Eastern Europe. Evidence of the earliest use of wheeled chariots has been found in India, China, the Middle East, and Eastern Europe.
- b. Wheels were first used in toys to entertain children. It took a long time for wheels to be used in transportation. Wheels were needed because they reduced friction and made life easier.
- c. In 1400, horse-drawn carriages and wheeled carts with spoked rims were used. There were deep potholes, mud and manure problems in the streets. This problem continued until the 1600s. About two centuries later, animal power was replaced by steam power and 100 years later by gasoline engines.
- d. Cars became central to youth culture because they provided independence from parents and a private space beyond prying eyes.
- e. With the opening of supermarkets next to main roads on the edges of cities, customers arriving by car could purchase large quantities of products at discounted prices from supermarkets that offered free parking to their customers.
- f. With the advent of cars, fast food joints, and shopping malls, cars reshaped the physical and cultural landscape of America and subsequently many countries.
- g. Globally, 24 percent of transportation-related carbon dioxide emissions come from burning fossil fuels. Approximately one-third of these emissions come from diesel-powered vehicles, and two-thirds come from light-duty, mostly gasoline-powered vehicles. Therefore, electrifying road vehicles can make a significant contribution to mitigating climate change.
- h. Automobiles kill about sixty thousand people a year and injure more than 4 million, pollute the environment more than any other industrial source, and

destroy cities. For these and similar reasons, it can be said that the automobile increase rate has decreased. It can be said that the fact that people turn to Uber also plays a role in this.

i. As internal combustion engines are phased out and cars, trains, and other ground transportation vehicles become electric, direct exhaust products will not be a problem. Additionally, using e-scooters in places where vehicles should not be used will contribute to keeping the environment clean.

#### REFERENCES

- Ditkoff, M. L. (2008). Awake at the Wheel: Getting Your Great Ideas Rolling (in an Uphill World). New York: Morgan James Publishing. p. 15, May 1.
- Bulliet, Richard W. (2016). *The Wheel: Inventions and Reinventions*. New York: Columbia University Press. 6, 51–70.
- Standage, Tom (2021). A Brief History of Motion: From the Wheel to the Car, to What Comes Next. New York: Bloomsbury Publishing, August 17, 2–5.
- Roux, Valentine; de Miroschedji, Pierre (2009). Revisiting the History of the Potter's Wheel in the Southern Levant. Levant. 41 (2): 155–173.
- Moorey, Peter Roger Stuart (1999). Ancient Mesopotamian Materials and Industries: The Archaeological Evidence. Winona Lake, IN: Eisenbrauns. p. 146.
- John Marshall (1996). Mohenjo-Daro and the Indus Civilization: Being an Official Account of Archaeological Excavations at Mohenjo-Daro Carried Out by the Government of India Between the Years 1922 and 1927, Volume 1. Asian Education Services, 1: 554-560.
- Anthony, David A. (2007). The horse, the wheel, and language: how Bronze-Age riders from the Eurasian steppes shaped the modern world. Princeton, NJ: Princeton University Press. p. 67.
- Velušček, A.; Čufar, K. and Zupančič, M. (2009). *Prazgodovinsko leseno kolo z osjo s kolišča Stare gmajne na Ljubljanskem barju*, p. 197–222 in A. Velušček (ed.). Koliščarska naselbina Stare gmajne in njen as. Ljubljansko barje v 2. polovici 4. tisočletja pr. Kr. Opera Instituti Archaeologici Sloveniae 16. Ljubljana.
- Fowler, Chris; Harding, Jan and Hofmann, Daniela (eds.) (2015). *The Oxford Handbook of Neolithic Europe*. Archived 29 December 2016 at the Wayback Machine OUP Oxford. p. 109.
- Jewel, Elizabeth (2006). *The Pocket Oxford Dictionary and Thesaurus*. Oxford University Press. p. 722.
- Bulliet, R. W. The Wheel, Colombia University Press, New York, 2016.
- László Tarr (1969). The History of the Carriage, New York: Arco, 187.
- Carlson, W. B. (2013). *Understanding the Inventions That Changed the World*, The Teaching Company, p. 1-273.
- Standage, T. (2021). A brief history of motion, Bloomsbury Publishing, London.

# An Economic Production Quantity Model with Defectives and Backordering under Non-Synchronized Production and Screening Activities

Harun SULAK<sup>1</sup>

Abdullah EROĞLU<sup>2</sup>

<sup>1</sup> Süleyman Demirel University, Faculty of Economics and Administrative Sciences Department of Econometrics, <a href="https://harunsulak@sdu.edu.tr">harunsulak@sdu.edu.tr</a>, Isparta, Türkiye. ORCID No: 0000-0001-8286-1813

<sup>2</sup> Süleyman Demirel University, Faculty of Engineering and Natural Sciences, Department of Industrial Engineering, <a href="mailto:abdullaheroglu@sdu.edu.tr">abdullaheroglu@sdu.edu.tr</a>, Isparta, Türkiye. ORCID No: 0000-0002-3035-8682 Corresponding author: <a href="mailto:harunsulak@sdu.edu.tr">harunsulak@sdu.edu.tr</a>

#### **ABSTRACT**

Studies on the production of a certain percentage of defective products in production have a significant and extensive place in literature. Studies on Economic Order/Production Quantity (EOQ/EPQ) models have made prominent assumptions one of them is the existence of a certain percentage of imperfect (defective) production; the proportion of defective production conforming to a certain probability distribution; and the classification of defective products as scrap, repairable, or defective. Studies on EPQ models, which are based on whether the screening speed during the process of separating defective products from good products during production is greater or less than the production speed, have been published in literature. Moussawi-Haidar et al. (2016) assume that during the production period, only the inspection activity (low inspection speed) ensures that only enough good products are available to meet demand; the normal inspection activity is performed after production is completed. Their model does not allow backordering. Wee et al. (2014) proposed two different EPO models, addressing situations where the production time is greater and less than the time required to met backordered demand. In their model, production, inspection, and elimination activities of backordering begin when the maximum backordering is reached. This study, unlike previous studies, assumes that the production and inspection processes are discrete. In other words, the inspection of manufactured products and the fulfillment of backordering begin after the completion of the production activity. Therefore, since there is no inspection process in the production process, demand cannot be met, and demand is delayed, allowing for backordering. In the developed model, the inspection or screening time is assumed to be shorter than the elimination time of backordering. Numerical examples are given to show the model's operation. In order to investigate the impact of changing parameters on optimal results, sensitivity analyses are performed.

Keywords: Rework, Defective Items, Economic Production Quantity Model, Backordering, Inspection Time

#### INTRODUCTION

One of the fundamental assumptions in classical EPQ models is a certain percentage of defective products will be produced during production. During the production process, defective products can be reworked or repaired to make them perfect, sold as defective at a lower price, or scrapped if they become completely unusable. In most studies on this topic, finding the optimal economic production quantity is considered in conjunction with optimal process monitoring and maintenance planning. In economic production quantity models, defective products that emerge during production are identified through a specific inspection process. The time spent during this

process, whether shorter or longer than the production time, has led to development of different models.

Rosenblatt and Lee (1986) studied on an EPQ model under the assumption that a production system produces perfect products for a randomly variable period but then begins producing defective products at a certain rate, and defective products are reworked while production continues at a certain cost. Schwaller (1988) derived an economic order quantity model under the assumption that the defective rate in the ordered batch is known and that there are fixed and variable inspection and screening costs for these products. Salameh and Jaber (2000) proposed an EOQ model for defective products and that the defective rate follows a random and uniform distribution. In the model, a 100% inspection process is performed, and detected defective products are sold at a lower price.

The Salameh and Jaber (2000) model has received considerable attention in literature and has been revisited and developed in many studies. Goval and Cardenes-Baron (2002) studied Salameh and Jaber's model and developed a new, simpler and easier-to-implement approach to finding the optimal order quantity. Papachristos and Konstantaras (2006) revised Salameh and Jaber's model and established the necessary and sufficient conditions to prevent shortages in the resulting models. Maddah and Jaber (2008) corrected the shortcomings and errors in Salameh and Jaber's model. Khan et al. (2011) stated the extensions of the EOQ model to include defective products in Salameh and Jaber's (2000) model. Havek and Salameh (2001) examined the case of defective production, assuming a uniform distribution of defective product rates and that defective products are reworked to make them good. The model they developed allows for subsequent demand fulfillment and shortages. Chan et al. (2003) proposed three different economic production quantity models for defective production. In their model, products are subject to 100% inspection and are categorized as perfect, imperfect and defective products. Konstantaras et al. (2007) studied an inventory model that examines lot size and inspection policies. In the model, the ordered lot contains a random proportion of defective products that cannot be used to meet demand. These products can be reworked for sale to meet demand or sold at as a single lot with discounted price. Taleizadeh et al. (2014) examined the defective production process for scrap and reworkable products. Inventory models allow for both backordering and shortages. Ouyang et al. (2002), Eroğlu and Özdemir (2007) and Cárdenas-Barrón (2009) examined EOQ models under shortages. Sarkar et al. (2014) developed inventory models for defective products under rework and backordering conditions. In their models, the defective rate of production is a random variable with uniform, triangular, and beta probability distributions. Moussawi-Haidar et al. (2016) developed different economic production models in which backordering is not allowed and defective products are sold at lower prices after the inspection process or

reworked to became good quality items. In the model where shortages are not allowed, they considered the availability of only perfect products to meet demand during the production period under a low inspection rate, assuming that normal inspection activities are performed after production is completed. Nobil et al. (2020) developed a model that allows for the subsequent fulfillment of demand for defective products. They classified good products as high or low quality, and defective products as reworkable or scrap. Karagül and Eroğlu (2022) proposed an inventory control model for reworkable defective products. The model allows for backordering and all defective items can be reworked and transformed into perfect products after rework.

A review of the literature displays that all studies on defective product inspection and rework processes assume that, under allowable shortages, the inspection time required to separate good and defective products is sufficiently longer than the time passed to eliminate backorder. Wee et al. (2014) proposed two different EPQ models, addressing situations where the production time is greater and less than the time passed to eliminate backorder. In their model, production, inspection, and elimination of backordering begin when the maximum shortage is reached. Unlike previous studies, this study assumes that the production process and inspection processes are discrete. That is, shortages occur until the production activity is completed, and the inspection of manufactured products and elimination of backordering activities begin after the production activity is completed. It is assumed that the inspection time is less than the elimination time of backordering.

#### MATHEMATICAL FORMULATION OF THE MODEL

In production process one item is produced with a rate of  $\alpha$ . The products are inspected at the end of the production process with a rate of x, thus defective and good quality items are separated. Inspection time is shorter than the elimination time of backordering,  $(t_3 < t_3 + t_4)$ . When production activity is completed, the maximum shortage is reached and inspection and backorder elimination activities begin. In developed model, following notations and assumptions are used:

#### **Notations**

The following notations are used in the proposed model:

- q Production quantity in a cycle
- w Maximum allowable backorder level
- $\beta$  Demand rate
- α Production rate
- $\alpha_1$  Rework rate
- x Inspection rate
- p Defective rate

- h Holding cost for good quality inventory
- $h_1$  Holding cost for defective products
- b Backorder cost
- c Production cost
- d Inspection cost
- c<sub>r</sub> Rework cost
- K Setup cost
- *E*[.] Expected value operator
- $t_1 + t_2$  Time to allow backordering
- $t_2$  Production time to produce quantity of q
- $t_3$  Inspection time to screen quantity of q
- $t_3 + t_4$  Time to eliminate backorders
- $t_4 + t_5$  Time to rework defective items
- $t_6$  Time required to meet demand with  $z_1$  quantity of perfect items
- z<sub>1</sub> Inventory level of perfect items at the time the rework process is completed
- $z_2$  Backorder level at the time the inspection process is finished
- z<sub>3</sub> Inventory level of defective items at the time the inspection process is finished

# Assumptions

Assumptions of proposed model are as follows:

- Demand, rework rate and inspection rate are constant and known.
- During production, a proportion of defective items occur at a rate of p. The rate of defective products, p, is a random variable which has a probability function f(p).
- After production process is completed, all products are screened by 100% inspection process with an inspection rate of x per unit of time. When the inspection process finishes, defective items are reworked with a constant rework rate of  $\alpha_1$ . All defective items become good quality items after rework process.
- Shortages are allowed. Allowable shortages are completely backordered with perfect quality items while defective items are reworked after inspection process.
- Inspection process time is smaller than the time taken to eliminate the backorder level. Therefore, after the inspection process finished, some backordering levels still not eliminated. Uneliminated backorder is fulfilled by the reworked items.

The inventory level according to the time for good quality and defective items is shown in Figure 1 and 2 respectively.

inventory level

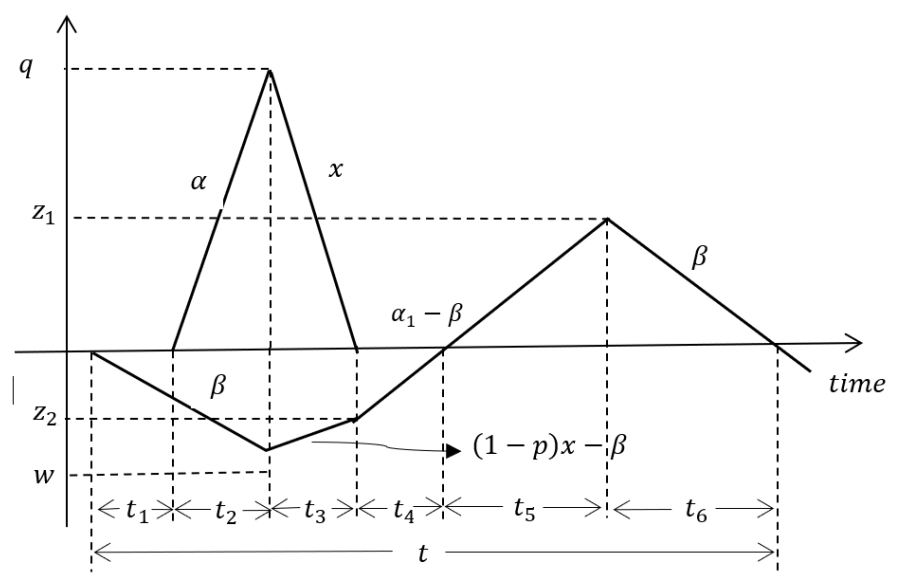


Figure 1: The inventory level for good quality items

inventory level

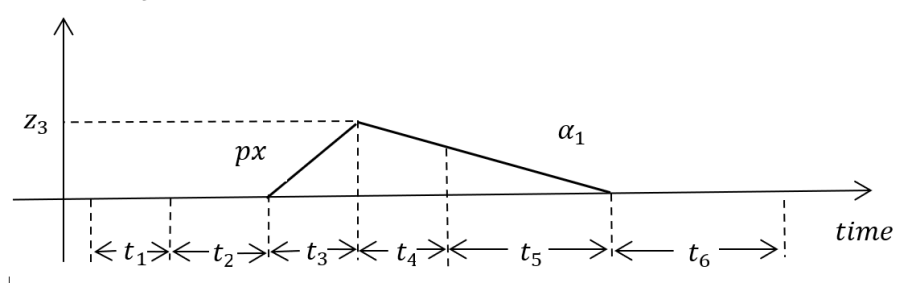


Figure 2: The inventory level for defective items

The equations to be used throughout the model are obtained according to Figure 1 and 2 as follows:

During  $t_1 + t_2$ , with demand rate  $\beta$ , w quantity of backorder occurs and during the production process,  $t_2$ , q amount of products are produced with rate of  $\alpha$ . Then following equations can be written:

$$t_1 + t_2 = \frac{w}{\beta} \tag{1}$$

$$t_2 = \frac{q}{\alpha} \tag{2}$$

$$t_1 = \frac{w}{\beta} - t_2 = \frac{w}{\beta} - \frac{q}{\alpha} \tag{3}$$

During  $t_3$ , good and defective items in production process are separated with inspection rate x. The rate of good quality and defective items in inspection process are (1-p)x and px respectively. During this inspection process, demand is fulfilled from good quality items with rate of  $\beta$ , part of backordering  $(w-z_2)$  is eliminated with rate of  $[(1-p)x-\beta]$  and inventory stock of defective items occurred with rate of px. Thus, following equations are obtained:

$$t_3 = \frac{w - z_2}{(1 - p)x - \beta} = \frac{q}{x} \tag{4}$$

$$z_2 = w - [(1 - p)x - \beta]q = w - Aq$$
 (5)

$$A = (1 - p - \beta/x) \tag{6}$$

$$z_3 = pq \tag{7}$$

During  $t_4 + t_5$  defective items are reworked with a rate of  $\alpha_1$ . All defective items become good quality after rework process. In this period, demand is met with rate of  $\beta$ . During  $t_4$ , the backorder level that can't be eliminated in period  $t_3$ , is fulfilled and during  $t_5$ , inventory level of  $z_1$  is cumulated with rate of  $\alpha_1 - \beta$ . Based on these explanations, the following equations can be written from Figures 1 and 2:

$$t_4 + t_5 = \frac{z_3}{\alpha_1} = \frac{pq}{\alpha_1} = \frac{z_1 + z_2}{\alpha_1 - \beta} \tag{8}$$

$$z_1 = (1 - \beta/\alpha_1)pq - z_2 = \left[1 - \beta\left(\frac{1}{x} + \frac{p}{\alpha_1}\right)\right]q - w \tag{9}$$

$$t_4 = \frac{z_2}{\alpha_1 - \beta} = \frac{w - Aq}{\alpha_1 - \beta} \tag{10}$$

$$t_5 = \frac{z_2}{\alpha_1} - t_4 = \left[ \left( \frac{1}{\alpha_1} - \frac{1}{\alpha_1 - \beta} \right) p + \frac{1 - \beta/x}{\alpha_1 - \beta} \right] q - \frac{w}{\alpha_1 - \beta}$$

$$\tag{11}$$

During  $t_6$ , demand is met from good quality items of  $z_1$  with rate of  $\beta$ . So;

$$t_6 = \frac{z_1}{\beta} = \left(\frac{1}{\beta} - \frac{1}{x} - \frac{p}{\alpha_1}\right)q - \frac{w}{\beta} \tag{12}$$

$$t = \sum_{i=1}^{6} t_i = \frac{q}{\beta} \tag{13}$$

Then, in a cycle TC is written as follows:

$$TC = cq + dq + c_r pq + K + h \left[ \frac{(t_2 + t_3)q}{2} + \frac{(t_5 + t_6)z_1}{2} \right] + h_1 \left[ \frac{(t_3 + t_4 + t_5)z_3}{2} \right] + b \left[ \frac{(t_1 + t_2)w}{2} + \frac{t_3(w + z_2)}{2} + \frac{t_4 z_2}{2} \right]$$

$$(14)$$

When the previously obtained t and z values are substituted into equation (14) and the expected value is taken, the expected value of the total cost per cycle, ETC, is obtained as follows:

$$ETC = \{c + d + c_r E[p]\} q + K + \left[ \frac{(h-h_1)\beta + (h_1+b)\alpha_1}{2\alpha_1(\alpha_1-\beta)} E[p^2] + \left( \frac{h_1+\beta}{2x} - \frac{(h+b)(1-\beta/x)}{\alpha_1-\beta} \right) E[p] + \left( \frac{(1-\beta/x)^2(h\alpha_1+b\beta)}{2\beta(\alpha_1-\beta)} + \frac{h-b(1-\beta/x)}{2x} + \frac{h}{2\alpha} \right) q^2 - \left[ \frac{(1-\beta/x)}{\alpha_1-\beta} \left( \frac{h\alpha_1}{\beta} + b \right) - \frac{(h+b)E[p]}{\alpha_1-\beta} - \frac{b}{x} \right] qw + \left[ \frac{(h+b)\alpha_1}{2\beta(\alpha_1-\beta)} - \frac{1-\beta/x}{\alpha_1-\beta} \left( \frac{h\alpha_1}{\beta} + b \right) \right] w^2$$
(15)

Here, to smaller the equation (15), by defining:

$$\begin{split} n_1 &= c + d + c_r E[p] \\ m_1 &= \frac{(h - h_1)\beta + (h_1 + b)\alpha_1}{2\alpha_1(\alpha_1 - \beta)} \\ m_2 &= \frac{h_1 + \beta}{2x} - \frac{(h + b)(1 - \beta/x)}{\alpha_1 - \beta} \\ m_3 &= \frac{(1 - \beta/x)^2(h\alpha_1 + b\beta)}{2\beta(\alpha_1 - \beta)} + \frac{h - b(1 - \beta/x)}{2x} + \frac{h}{2\alpha} \\ n_2 &= m_1 E[p^2] + m_2 E[p] + m_3 \\ n_3 &= \frac{(1 - \beta/x)}{\alpha_1 - \beta} \Big(\frac{h\alpha_1}{\beta} + b\Big) - \frac{(h + b)E[p]}{\alpha_1 - \beta} - \frac{b}{x} \\ n_4 &= \frac{(h + b)\alpha_1}{2\beta(\alpha_1 - \beta)} - \frac{1 - \beta/x}{\alpha_1 - \beta} \Big(\frac{h\alpha_1}{\beta} + b\Big) \end{split}$$

The expected value of total cost, ETC, can be written more compactly as:

$$ETC = n_1 q + K + n_2 q^2 - n_3 q w + n_4 w^2 (16)$$

The expected total cost, ETC in Equation (16) is divided by the expected cycle length, E[T], expected value of the total cost per unit time, ETCU is obtained as:

$$ETCU = \frac{ETC}{t} = \frac{\beta(ETC)}{q} = n_1 \beta + \frac{\kappa \beta}{q} + n_2 \beta q - n_3 \beta w + \frac{\beta n_4 w^2}{q}$$
 (17)

By taking the partial derivatives of the *ETCU* function according to the production and backorder quantity and setting them equal to zero optimal values of proposed model obtained.

$$\frac{\partial ETCU}{\partial w} = -n_3 \beta + \frac{2\beta n_4 w}{q} = 0$$

$$\frac{\partial ETCU}{\partial a} = -\frac{K\beta}{a^2} + n_2\beta - \frac{\beta n_4 w^2}{a^2} = 0$$

From these equations, the following optimal production and maximum backorder quantities are obtained:

$$q = \sqrt{\frac{4n_4K}{4n_2n_4 - n_3^2}} \tag{18}$$

$$w = \sqrt{\frac{n_3^2 K}{n_4 (4n_2 n_4 - n_3^2)}} \tag{19}$$

Since the defective product rate (p) is a random variable, the following equations can be written:

$$E[z_1] = \left\{1 - \beta \left(\frac{E[p]}{\alpha_1} + \frac{1}{x}\right)\right\} q - w \tag{20}$$

$$E[z_2] = w - \{1 - E[p] - \beta/x\}q \tag{21}$$

$$E[z_3] = qE[p] \tag{22}$$

$$E[t_1] = \frac{w}{\beta} - \frac{q}{\alpha} \tag{23}$$

$$E[t_2] = \frac{q}{\alpha} \tag{24}$$

$$E[t_3] = \frac{q}{x} \tag{25}$$

$$E[t_4] = \frac{w - \{1 - E[p] - \beta/x\}q}{\alpha_1 - \beta}$$
 (26)

$$E[t_5] = \left\{ \left( \frac{1}{\alpha_1} - \frac{1}{\alpha_1 - \beta} \right) E[p] + \frac{1 - \beta/x}{\alpha_1 - \beta} \right\} q - \frac{w}{\alpha_1 - \beta}$$

$$(27)$$

$$E[t_6] = \frac{1}{\beta} E[z_1] \tag{28}$$

# Numerical Example 1

The monthly demand for a product is 800 units and the monthly production capacity is 9000 units. It is known that the defective rate in production follows a continuous uniform distribution. The probability density function is as follows:

$$f(p) = \begin{cases} 12.5, & 0.28 \le p \le 0.36 \\ 0, & otherwise \end{cases}$$

Monthly inspection and repair capacities are 4000 units and 2000 units, respectively. Unit production and inspection costs are 50 TL and 2 TL, respectively. Unit repair cost is 8 TL, and unit backorder cost is 1.5 TL. Unit

inventory costs for defective and good quality items are 2.5 TL and 4.5 TL, respectively. Preparation to production cost is 10,000 TL. So, the parameters used in the numerical example are as follows:

$$\beta = 800, \alpha = 9000, x = 4000, \alpha_1 = 2000, c = 50, d = 2, c_r = 8, b = 1.5,$$
  
 $h_1 = 2.5, h = 4.5, K = 10000$ 

First, the expected values in the model can be found by taking into account the above parameters.

$$E[p] = \int_{0.28}^{0.36} pf(p)dp = 0.32$$
$$E[p^2] = 0.102933$$

Then from equations (17), (18) and (19), optimal production quantity maximum allowable backorder level and total cost per unit time are obtained as:

$$q = 2630.36$$
 unit

w = 1373.05 unit

ETCU = 49730.82 TL

From Equations (20)-(28), following values are obtained:

$$E[z_1] = 394.55$$
  $E[t_1] = 1.424046$   $E[z_2] = 110.47$   $E[t_2] = 0.292262$   $E[z_3] = 841.71$   $E[t_3] = 0.657589$   $E[t_4] = 0.092062$   $E[t_5] = 0.328795$   $E(t) = 3.287947$  day  $E[t_6] = 0.493192$ 

#### Numerical Example 2

Defective rate is normally distributed with mean of 0.27 and variance of 0.0009The other parameters are the same as in Numerical Example 1. In this case, the data are as follows:

$$E(p) = 0.27, V(p) = 0.0009, E[p^2] = 0.0738, \beta = 800, \alpha = 9000,$$
  
 $x = 4000, \alpha_1 = 2000, c = 50, d = 2, c_r = 8, b = 1.5, h_1 = 2.5,$   
 $h = 4.5, K = 10000$ 

Then from equations (17), (18) and (19), optimal production quantity maximum allowable backorder level and total cost per unit time are obtained as:

q = 2645.29 unit

w = 1433,75 unit

ETCU = 49376.50 TL

From Equations (20)-(28), following values are obtained:

$E[z_1] = 396.79$	$E[t_1] = 1.498260$
$E[z_2] = 31.74$	$E[t_2] = 0.293921$
$E[z_3] = 714.23$	$E[t_3] = 0.661321$
	$E[t_4] = 0.026453$
	$E[t_5] = 0.330661$
E(t) = 3.306606  day	$E[t_6] = 0.495991$

#### Sensitivity Analysis

Sensitivity analysis will be used to examine how and in what direction the optimal values in the developed model change with changes in relevant parameters. This will analyze the effects of changes in inventory holding, backorder, setup costs and the expected value of the defective rate on optimal production quantity, maximum allowable backorder level and total cost.

Table 1: The effect of changes in the holding cost of good quality items on optimal values

h	ETCU	q	W	Reason for infeasibility	Solution
0.5	47009.96	4759.13	1056.53	$E[t_4], E[z_2] < 0$	
1.5	48066.97	3620.76	1346.92	$E[t_4], E[z_2] < 0$	Infeasible
2.5	48742.29	3140.77	1403.93	$E[t_4], E[z_2] < 0$	
3.5	49274.39	2843.74	1399.12		
4.5	49730.82	2630.36	1373.05		
7	50692.20	2271.37	1285.86		Feasible
10	51657.82	1997.55	1186.02		reasible
20	54196.74	1516.77	955.78		
50	59478.22	1010.72	661.54		

As unit inventory holding cost of good quality items, (h) increases, the expected total cost per unit time (ETCU) increases, optimal economic production quantity (q) decreases and maximum allowable backorder level (w) exhibits a concave structure.

Table 2: The effect of changes in the holding cost of defective items on optimal values

$h_1$	ETCU	q	W
1.5	49590.89	2692.29	1405.38
2.5	49730.82	2630.36	1373.05
7	50324.32	2396.53	1250.99
15	51266.10	2100.26	1096.34
30	52773.62	1753.30	915.23
60	55213.48	1383.43	722.15

As the unit inventory holding cost of defective products  $(h_1)$  increases, the expected total cost per unit time (ETCU) increases, while optimal economic production quantity (q) and maximum allowable backorder level (w) decrease.

Table 3: The effect of changes in the backorder cost on optimal values

b	ETCU	q	W	Reason for infeasibility	Solution
0.5	49100.68	2934.34	1795.81		
1.5	49730.82	2630.36	1373.05		Feasible
2.0	49963.66	2533.38	1234.73		
2.5	50160.94	2456.65	1124.44	$E[z_2], E[t_4] < 0$	
3.5	50480.19	2341.85	958.99	$E[z_2], E[t_4] < 0$	Infeasible
5.0	50838.22	2225.24	792.66	$E[z_2], E[t_4] < 0$	inteasible

As the unit backorder cost (b) increases, the expected total cost per unit time (ETCU) increases, while the economic production quantity (q) and maximum allowable backorder level (w) decrease.

Table 4: The effect of changes in the setup cost on optimal values

K	ETCU	q	W
1000	45571.56	831.79	434.20
3000	46979.70	1440.71	752.05
5000	47949.21	1859.94	970.89
10000	49730.82	2630.36	1373.05
20000	52250.41	3719.89	1941.78
40000	55813.65	5260.71	2746.09
70000	59741.64	6959.27	3632.74

As setup cost (K) increases, the expected total cost per unit time (ETCU), economic production quantity (q) and maximum allowable backorder level (w) increases.

Table 5: The effects of changes in expected value of defective rate on optimal values

f	g	<i>E</i> [ <i>p</i> ]	ETCU	q	w	Reason for infeasibility	Solution
0.04	0.12	0.08	48118.59	2663.74	1646.19	$E[t_4], E[z_2] < 0$	
0.10	0.18	0.14	48498.75	2665.44	1583.27	$E[t_4], E[z_2] < 0$	Infesasible
0.16	0.24	0.20	48894.26	2660.34	1516.40	$E[t_4], E[z_2] < 0$	
0.22	0.30	0.26	49305.02	2648.56	1446.11		
0.28	0.36	0.32	49730.82	2630.36	1373.05		
0.34	0.42	0.38	50171.38	2606.13	1297.85		Feasible
0.46	0.54	0.50	51095.02	2541.69	1143.76		reasible
0.70	0.78	0.74	53096.91	2366.55	837.76		

For a continuous uniform distribution, as the expected value of defective rate (E[p]) increases, with the condition that the defective rate range (g-f=.08) remains constant, the expected total cost per unit time (ETCU) increases, the economic production quantity (q) exhibits a concave structure, and maximum allowable backorder level (w) decreases.

#### **CONCLUSION**

Numerous studies have been conducted on defective items, imperfect production, backordering and rework in EOQ/EPQ models. In economic production quantity models, defective products that arise during production are identified through a specific inspection process. The time taken during this process, whether shorter or longer than the production time or the time to eliminate the backordering, has led to the development of different models. In this study, an economic production quantity model is developed for the situation backordering where the demand is allowed to be fulfilled later and all defective products are converted into good quality items after the rework process. To distinguish defective and non-defective products, all products are inspected and scanned after the production process is completed. After the inspection process is completed, defective products are reworked at a fixed rate. In the proposed model, the inspection time required to separate defective and good quality products is assumed to be shorter than the time to eliminate the backorder. A numerical example is given to illustrate the model's operation, and optimal values are obtained. The effects of changes in stock holding, backorder, setup costs and the expected value of the defective product rate on the optimal values are analyzed with sensitivity analysis. As inventory holding costs and the expected value of the defective product rate increase, total costs increase, while optimal production and backorder level decrease. Conversely, as setup costs increase, total costs, optimal production rates, and maximum backorder level increase. Future studies could develop new models that allow for payment delays, partial backordering and learning effects.

# Appendix 1: Proof of Convexity of ETCU Function

Consider following Hessian matrix:

$$H = \begin{bmatrix} \frac{\partial^2 ETCU}{\partial q^2} & \frac{\partial^2 ETCU}{\partial q \partial w} \\ \frac{\partial^2 ETCU}{\partial w \partial q} & \frac{\partial^2 ETCU}{\partial w^2} \end{bmatrix}$$

If.

$$\begin{bmatrix} q & w \end{bmatrix} \times H \times \begin{bmatrix} q \\ w \end{bmatrix} > 0, \ q, w \neq 0$$

then the function of ETCU is strictly convex.

$$H = \begin{bmatrix} \frac{2K\beta + 2\beta n_4 w^2}{q^3} & -\frac{2\beta n_4 w}{q^2} \\ -\frac{2\beta n_4 w}{q^2} & \frac{2\beta n_4}{q} \end{bmatrix} \text{ and } \begin{bmatrix} q & w \end{bmatrix} \times H \times \begin{bmatrix} q \\ w \end{bmatrix} = \frac{2K\beta}{q} > 0.$$

Since the value is positive, the function of ETCU is strictly convex. Thus, optimum values of q and w which make ETCU minimum have single values

# Appendix 2.

Expected values for 
$$f(p) = \begin{cases} \frac{1}{g-f}, & f \le p \le g \\ 0, & otherwise \end{cases}$$

$$E[p] = \frac{f+g}{2}$$

$$E[p^2] = \frac{f^2 + g^2 + fg}{3}$$

#### REFERENCES

- Cardenas-Barron, L. E. (2009). Economic production quantity with rework process at a single-stage manufacturing system with planned backorders. *Computers and Industrial Engineering*, 57, 1105-1113.
- Chan, W. M., Ibrahim, R.N. and Lochert, P.B. (2003). A new EPQ model: integrating lower pricing, rework and reject situations. *Production Planning and Control*, 14(7), 588-595.
- Eroğlu, A. and Özdemir, G. (2007). An economic order quantity model with defective items and shortages. *International Journal of Production Economics*, 106 (2), 544-549.
- Goyal, S. K. and Cardenes-Barron, L. E. (2002). Note on: economic production quantity model for items with imperfect quality-a practical approach. *International Journal of Production Economics*, 77, 85-87.
- Hayek, P. A. and Salameh, M. K., (2001). Production lot sizing with the reworking of imperfect quality items produced. *Production Planning and Control*, 12 (6), 584-590.

- Karagül N. and Eroğlu A. (2022). Production lot sizing with quality screening, rework and shortages backordered. *Pamukkale University Journal of Engineering Sciences*, 28(4), 604-612.
- Khan, M., Jaber, M. Y. and Bonney, M. (2011). An economic order quantity (EOQ) for items with imperfect quality and inspection errors. *International Journal of Production Economics*, 133(1), 113–118.
- Konstantaras, I., Goyal, S. K. and Papachristos, S. (2007). Economic ordering policy for an item with imperfect quality subject to the in-house inspection. *International Journal of Systems Science*, 38(6), 473–482.
- Maddah, B. and Jaber, M. Y. (2008). Economic order quantity for items with imperfect quality: revisited. *International Journal of Production Economics*, 112 (2), 808–815.
- Moussawi-Haidar L., Salameh M. and Nasr W. (2016). Production lot sizing with quality screening and rework. *Applied Mathematical Modelling*, 40, 3242-3256.
- Nobil A., Afshar-Sedigh A. and Afshar-Nadjafi B. (2020). Lot-sizing problem for a defective processing system with categorized items, backordering and pricing policy. *Journal of Revenue Pricing Management*, 19, 255-265.
- Ouyang, L. Y., Chen, C. K. and Chang, H. C. (2002). Quality improvement, setup cost and lead-time reductions in lot size reorder point models with an imperfect production process. *Computer and Operations Research*, 29, 1701-1717.
- Papachristos, S. and Konstantaras, I., (2006). Economic ordering quantity models for items with imperfect quality. *International Journal of Production Economics*, 100(1), 148-156.
- Rosenblatt, M. J. and Lee, H. L., (1986). Economic production cycles with imperfect production process. *IIE Transactions*, 18, 48-55.
- Salameh, M. K. and Jaber, M. Y. (2000). Economic production quantity model for items with imperfect quality. *International Journal of Production Economics*, 64, 59-64.
- Sarkar B., Cardenas-Barron L.E., Sarkar M. and Singgih M.L. (2014). An economic production quantity model with random defective rate, rework process and backorders for a single stage production system. *Journal of Manufacturing Systems*, 33, 423-435.
- Schwaller, R. L., (1988). EOQ under inspection costs. *Production and Inventory Management*, 29, 22-35.
- Taleizadeh, A. A., Cárdenas-Barrón, L. E. and Mohammadi, B. (2014). A deterministic multi product single machine EPQ model with backordering, scraped products, rework and interruption in manufacturing process. *International Journal of Production Economics*, 150, 9-27.
- Wee H.M., Wang W.T., Kuo T.C., Cheng Y.L. and Huang Y.D., (2014), An Economic Production Quantity Model with non-synchronized screening and rework, Applied Mathematics and Computation, 233, 127-138

# Roof Systems in Agricultural Buildings; Literature Review

# Israfil KOCAMAN

Tekirdag Namik Kemal University Agricultural Faculty Biosystems Engineering Department, TR-59030 Tekirdag Turkey.

#### ABSTRACT

In agricultural production structures, maximizing the use of the third dimension of the structure is closely linked to the planning and design of roof systems. Studies on roof systems have presented different approaches across various perspectives, including structural strength, energy efficiency, intended use, and environmental sustainability. The literature in this area focuses on the performance and design criteria of roof systems in both traditional and modern agricultural structures. In the vast majority of agricultural structures, roof systems are designed using traditional methods or empirical practice rather than engineering analysis. This situation results in the use of excessive or insufficient materials in load-bearing systems, which can lead to economic and structural problems. The primary objective of this study is to establish, through a literature review, the fundamental principles of planning roof systems used in agricultural buildings.

Keywords: Agricultural structures, Roof systems, Truss elements, Purlin elements

#### 1. Introduction

Agricultural production is an economic and social activity whose strategic importance is increasing due to the increasing global population, changing consumption habits and increasingly limited natural resources. The agricultural sector is one of the main actors at both national and international levels, especially in ensuring food security, supporting rural development, keeping input-output markets alive and disseminating sustainable production methods. This requires meticulous design of the structures that form the spatial infrastructure of agricultural production. In agricultural enterprises where activities such as animal husbandry, crop production, and product storage are carried out, the quality of the structural infrastructure plays a decisive role in product productivity, operating costs, food safety, and production continuity.

Within building systems, roof elements play a significant role not only in providing a top cover but also in overall stability, thermal and moisture insulation, energy efficiency, and operating costs. Mohammadzadeh (2016) emphasized that roof systems are a decisive factor in optimizing energy, environmental impact, and cost, and emphasized the need to develop holistic models for the performance analysis of multifunctional systems, particularly steel roofs. Other studies have shown that metal roofs, in particular, stand out for their durability, longevity, and low maintenance costs.

Moran (1980), in his full-scale experimental study, demonstrated that roof geometry, slope ratio, and span have significant effects on structural load

distribution, and that external factors, particularly wind loads, significantly influence roof pressure distribution. Field-based studies in developing countries have demonstrated that traditional practices lacking engineering principles lead to structural inadequacies, material waste, and increased costs (Olukunle, 2014). Walters and Midden (2018) emphasize that roofs play a strategic role not only in physical protection but also in energy management and functionality in agricultural structures.

In the vast majority of agricultural structures, roof systems are designed using traditional methods or empirical practices rather than engineering analysis. This results in the use of excessive or insufficient materials in structural systems and can lead to economic and structural problems. The primary objective of this study is to explore, through a literature review, the fundamental principles for planning roof systems used in agricultural structures.

# 2. The Concept of Agricultural Structure

The concept of agricultural structures refers to the physical and technical infrastructures that enable agricultural activities. The primary purpose of these structures is to create areas capable of fulfilling the protection, storage, processing, and management functions required in agricultural production processes. Agricultural structures consist of structural elements designed in accordance with the type of agricultural production, geographical conditions, and climatic requirements. These structures are planned in a specialized manner for different agricultural activities, such as animal husbandry, crop production, product storage, and processing (Maraveas and Bartzanas, 2021). Agricultural structures span a wide area. They include various types of structures, such as barns, poultry houses, greenhouses, warehouses, grain silos, irrigation facilities, and product processing centers. The design of these structures is determined by the nature and needs of agricultural activities. For example, barns and shelters for animal production are constructed with special features to protect the health and well-being of animals. Greenhouses used for crop production, on the other hand, are designed to control environmental conditions (Gabriela et al., 2017). They also differ in their structural designs and materials used. While structures constructed using traditional methods are generally comprised of local materials, modern agricultural structures are designed with more durable and efficient materials. Materials such as steel, concrete, and wood are among the frequently preferred options for agricultural

structures. Material selection varies depending on the structure's function, environmental conditions, and economic factors (Mohammadzadeh, 2016).

The planning and design processes of agricultural structures are optimized to increase the efficiency of agricultural activities and meet their needs. Structures are generally designed according to the principles of functionality, durability, and longevity. Furthermore, agricultural structures are supported by engineering calculations and technical analyses and constructed in accordance with relevant standards. For example, roofs are carefully designed with waterproofing and insulation features to protect the interior spaces of the structures (Pernisova, 2016). It also plays a crucial role in storage and logistics processes. Structures such as grain silos and cold storage facilities are designed to ensure the proper preservation of agricultural products. Such structures allow for the preservation of product quality and increased transportability. Furthermore, structures integrated into irrigation systems support the efficient use of water resources (Coma et al., 2016). The concept of agricultural structures is not limited to physical structures; it also encompasses many disciplines, including structural design, engineering processes, and technological integration. For example, modern agricultural structures utilize innovative technologies such as digital sensors and automation systems. These technologies contribute to monitoring structural performance, energy savings, and increased efficiency (Maraveas and Bartzanas, 2021).

# 3. The Importance of Agricultural Structures

The importance of agricultural structures stems from their direct impact on the economic and environmental dimensions of agricultural production. Modern agricultural practices are effectively managed and optimized through agricultural structures. For example, greenhouses protect the production process from climate impacts by providing controlled environmental conditions for plant production (Grigorenko, 2017). The function of these structures is not limited to increasing production; they also improve product quality and ensure the sustainability of agricultural production. Furthermore, agricultural structures increase the resilience of agricultural activities against climate change and natural disasters (Maraveas and Bartzanas, 2021).

Agricultural structures are considered a critical element contributing to the sustainable growth of the agricultural economy. For example, animal production facilities are being modernized to meet high demand and maintain the quality standards of animal products. These facilities provide favorable

environmental conditions to improve animal health and welfare, while also enabling the mechanization of production processes (Szabolcs et al., 2017). Mechanization reduces labor requirements, lowers costs, and increases production capacity (Bahorka et al., 2024).

The environmental aspects of agricultural structures are also crucial. Modern building technologies, such as steel construction systems, increase energy efficiency by using environmentally friendly materials. Steel is a frequently preferred material in agricultural structures due to its recyclability and light weight. These structures contribute to environmental sustainability by enabling more efficient use of natural resources (Hodbod et al., 2016). Furthermore, the technology used in agricultural structures offers innovative solutions in areas such as waste management and water conservation (Gupta et al., 2022).

The strategic importance of agricultural structures is not limited to production processes. These structures also play a significant role in rural development and employment creation. Particularly in developing countries, agricultural structures contribute to the revitalization of local economies and the improvement of living standards in rural areas (Divanbeigi et al., 2016). Agricultural structures support social well-being by increasing food security in rural areas (Stoycheva, 2023). They are an integral part of modern agricultural systems and play a critical role in economic, environmental, and social aspects. These structures are indispensable for ensuring the sustainability of agricultural production, preserving natural resources, and addressing the challenges facing the agricultural sector.

# 4. Roof Systems and Their Importance

Roof systems, as one of the fundamental components of a building, play a crucial role in ensuring structural integrity and meeting aesthetic and functional requirements. Roofs act as a barrier protecting buildings from external factors, providing protection against environmental factors such as rain, snow, sunlight, and wind. Furthermore, roofs contribute to the longevity of buildings by fulfilling various functions such as energy conservation, insulation, aesthetics, and security (Gabriela et al., 2017).

The primary function of roof systems is to protect the interior spaces of buildings from external factors. Roofs provide resistance to environmental conditions through key features such as waterproofing, thermal insulation, and wind resistance. Waterproofing is critical, particularly in protecting interior elements from moisture and water. Thermal insulation, in turn, saves energy

and optimizes comfort in interior spaces (Abu Awwad and Suliman, 2018). Wind resistance is another important factor affecting the stability of roof systems. The durability of roof systems is particularly crucial in regions exposed to high wind speeds (Baha and Osman, 2017).

Roof systems also contribute to the energy efficiency of buildings. Properly designed roof systems reduce energy costs and support environmental sustainability goals. For example, green roof systems reduce the heat island effect and reduce a building's energy consumption by using vegetation. These types of roofs also provide benefits for rainwater management. Roof systems integrated with solar panels enable renewable energy production and reduce carbon footprints (Guerrero-Cuasapaz et al., 2021).

The aesthetic dimension of roofs contributes significantly to the overall appearance of a building. Roof design reflects the building's architectural style and enhances its aesthetic value. Different roof types, such as pitched roofs, flat roofs, and domed roofs, are used to meet various architectural requirements. For example, pitched roofs reflect traditional architectural styles, while flat roofs are frequently preferred in modern architecture (Gabriela et al., 2017). Therefore, roof systems are considered not only as structural components but also as tools of aesthetic expression.

The safety function of roof systems enhances the overall safety performance of a building. Roofs are designed to protect against fire, earthquakes, and other natural disasters. Fire resistance is critical, especially in high-risk areas such as industrial facilities. The fireproof properties of roofing materials reduce fire risk and increase safety. Earthquake-resistant roof systems, on the other hand, maintain the stability of the structure and ensure the safety of building occupants (Lebed et al., 2018).

Roof systems also play a crucial role in water management. Roof drainage systems ensure the efficient drainage of rainwater, preventing it from damaging the structure. A properly designed drainage system prevents water accumulation and extends the life of the roof (Misar and Novotny, 2017). Furthermore, water collection systems allow for the storage and reuse of rainwater accumulated on roofs. Such systems save water and promote environmental sustainability.

Modern roof systems are becoming more functional with developing technologies. Smart roof systems optimize energy efficiency by sensing environmental conditions. For example, thermal sensors and automatic ventilation systems regulate indoor temperatures and reduce energy

consumption (Chesnokov et al., 2022). Furthermore, innovative materials such as steel roof systems offer significant advantages in terms of both durability and aesthetics (Gabriela et al., 2017).

The economics of roof systems are considered a significant factor for both building owners and the public. Properly designed and constructed with high-quality materials, roof systems reduce maintenance and repair costs and provide long-term economic benefits. Furthermore, energy-efficient roof systems reduce energy costs and provide savings (Huberman et al., 2015).

Roof systems are categorized based on their design and construction materials. Types such as pitched roofs, flat roofs, domed roofs, and hybrid roofs address a variety of architectural and engineering needs. Pitched roofs are preferred for their rapid drainage of rain and snow water. These types of roofs offer aesthetic and functional advantages (Awwad et al., 2018).

Flat roof systems are often used in modern architecture and offer a minimalist aesthetic. These types of roofs offer the advantages of easy maintenance and ample usable space. They provide a suitable base for applications such as roof gardens or solar panels and contribute to energy efficiency (Abu Awwad and Suliman, 2018). However, flat roofs require careful design and implementation of waterproofing, otherwise they can lead to problems such as water accumulation (Misar and Novotny, 2017).

Domed roofs are frequently used in the roof systems of large-scale buildings. These systems can support large spans and add aesthetic value to the structure. Domed roofs offer a lightweight and durable structure, particularly through the use of geodesic designs (Lebed et al., 2018). Furthermore, domed roofs are also preferred for improving acoustic performance and optimizing energy efficiency.

Hybrid roof systems combine different design and construction materials to provide both aesthetic and structural durability. Hybrid roofs support sustainability goals by using recyclable materials (Chesnokov et al., 2022). Furthermore, hybrid roofs offer an effective solution for covering large openings and can be integrated with energy storage systems (Huberman et al., 2015). Another factor to consider when designing roof systems is their energy efficiency. Composite energy-efficient roof systems reduce energy costs by providing thermal insulation in summer and thermal retention in winter. Such systems offer an effective solution for improving building energy performance.

# 4.1. Wooden roof systems

Timber roof systems are an important structural element in structural engineering, distinguished by their aesthetic, functional, and environmental advantages. These systems are frequently preferred in both traditional and modern architecture thanks to wood's lightness, durability, and aesthetic appeal. Timber roof systems are widely used, particularly in residential buildings, historical buildings, and projects focused on environmental sustainability (Dutkiewicz et al., 2021). Timber roof systems fulfill many functions by forming the upper portion of a structure. These systems serve key functions such as protecting against environmental influences, providing structural support, and adding aesthetic value. Furthermore, thanks to their natural material structure, timber roof systems offer thermal comfort and high insulation capacity in interior spaces (Kain et al., 2020).

The fundamental elements used in the design and implementation of wood roof systems include beams, purlins, rafters, and roofing materials. These elements are used in various combinations to increase the roof system's load-bearing capacity and ensure durability. For example, in modern wood roof systems, advanced materials such as glued laminated wood beams are used to cover large openings and increase load-bearing capacity. One of the most significant advantages of wood roof systems is their sustainability and environmental friendliness. Wood, being a renewable material and with a low carbon footprint, contributes to environmental sustainability goals. Furthermore, wood is recyclable and biodegradable, minimizing environmental impact. Wood roof systems can be manufactured with low energy consumption, contributing to the reduction of energy costs.

Wooden roof systems also offer advantages in terms of durability and longevity. With appropriate protection methods and regular maintenance, wood can maintain its structural integrity for many years. Furthermore, wood can be made fire-resistant with fire-retardant coatings and special treatments (Abramyan and Ishmametov, 2016). Wooden roof systems also offer an effective solution for earthquake resistance. Their lightweight structure minimizes the impact of seismic loads on the structure and increases its overall stability (Dutkiewicz et al., 2021).

The aesthetic aspect of wooden roof systems plays a significant role in architectural projects. The natural texture and warm appearance of wood add aesthetic value to a building and create a natural atmosphere in interior spaces. For example, sloping wooden roofs are used as an aesthetic element in

traditional architecture and are preferred in the restoration of historic buildings (Secka, 2015). Wooden roof systems also offer an ideal solution for geometric and minimalist designs in modern architecture.

The assembly and installation processes for wooden roof systems are faster and easier than those for other materials. Thanks to their easy workability, wooden elements can be adapted to different design and structural requirements. The use of prefabricated wooden elements speeds up construction processes and reduces labor costs. Furthermore, the lightweight structure of wooden roof systems saves energy during transportation and installation.

Maintenance and repair of wooden roof systems should be carried out at regular intervals. The natural properties of wood require protection against moisture, pests, and UV rays. Therefore, regular protective coating applications extend the life of wooden roof systems (Giuriani et al., 2016). Furthermore, the easy replacement of wooden roof elements when necessary increases the economic efficiency of these systems.

# 4.2. Reinforced concrete roof systems

Reinforced concrete roof systems are among the structural elements that stand out with the durability, flexibility, and design advantages offered by modern construction technology. These systems fulfill various functions by covering the upper portions of buildings and offer solutions suitable for various architectural requirements. Reinforced concrete roofs are particularly important for covering large openings, providing fire resistance, and protection against environmental factors (Gilodo and Arsiriy, 2023).

The primary function of reinforced concrete roof systems is to protect buildings from environmental factors. These systems offer high resistance to environmental factors such as rain, snow, and wind. Reinforced concrete roofs protect the interior of the building with their watertight properties, preventing moisture-related damage. Furthermore, thanks to their resistance to snow and wind loads, they maintain their structural integrity even in harsh climatic conditions (Degtyarev et al., 2021).

Reinforced concrete roof systems offer great flexibility in architectural design. They offer a wide range of applications with different design options, such as flat, sloped, vaulted, or domed roofs. For example, vaulted reinforced concrete roofs offer an effective solution for covering large openings and providing an aesthetically pleasing appearance. These types of roofs are frequently

preferred, especially in large spaces such as sports halls, concert halls, and industrial facilities (Kvaraia and Giorgobiani, 2023).

Reinforced concrete roofs also offer significant advantages in terms of energy efficiency. A well-insulated reinforced concrete roof minimizes heat loss, resulting in energy savings. Furthermore, reinforced concrete roofs integrated with solar panels provide a suitable environment for renewable energy production (Huberman et al., 2015). The insulation materials used in reinforced concrete roofs maintain a balanced indoor temperature in both summer and winter, optimizing comfort.

Reinforced concrete roof systems offer numerous advantages in terms of durability. Thanks to its high compressive strength and long-lasting structure, reinforced concrete maintains structural stability and minimizes maintenance requirements. For example, reinforced concrete roofs reinforced with steel plates both increase load-bearing capacity and optimize durability. Fire resistance is another key advantage of reinforced concrete roofs. Reinforced concrete, with its high-temperature resistance, provides reliable protection in the event of a fire.

The use of prefabricated elements in the construction of reinforced concrete roofs speeds up assembly processes and reduces labor costs. Prefabricated reinforced concrete roof panels are designed with high precision during production, saving time during installation (Parskiy et al., 2017). These systems play a significant role in economic efficiency, especially in large-scale projects.

Reinforced concrete roofs are a suitable option not only for industrial and commercial buildings but also for residential projects. Particularly in residential projects requiring large openings, reinforced concrete roof systems offer significant value in terms of functionality and aesthetics (Jawalgi et al., 2020). Furthermore, reinforced concrete roofs offer advantages in terms of noise insulation and increased indoor comfort.

# 4.3. Steel roof systems

Steel roof systems are among the structural elements that stand out in the modern construction industry for their durability, lightness, and flexibility. These systems offer a wide range of applications, meeting various architectural and engineering requirements. Steel materials offer significant advantages in the design and implementation of roof systems thanks to their high strength, ease of workability, and longevity (Gabriela et al., 2017).

The most distinctive features of steel roof systems are their high strength and light weight. Steel has a high load-bearing capacity, making it an ideal material for supporting large spans. This makes steel roof systems a preferred choice for projects requiring large openings, such as sports halls, industrial facilities, and large-scale commercial buildings. For example, steel trusses are a frequently preferred structural element for covering large openings (Diao et al., 2019).

Steel roofing systems stand out with their wide range of applications. From industrial facilities to residential projects, sports complexes to shopping malls, steel roofs are preferred in many areas. The durability, aesthetics, and sustainability advantages offered by steel materials make steel roofing systems an indispensable structural element in modern construction projects.

Steel roof systems offer high durability and strength. Due to its high load-bearing capacity, steel is particularly preferred in areas exposed to harsh environmental conditions such as heavy snow loads or wind. Consequently, steel roof systems have a longer lifespan than traditional materials and maintain structural stability. For example, a study on the durability of steel roof systems exposed to snow loads found that these structures, when properly designed, meet high safety standards (Kozak and Liel, 2015).

Steel roof systems also offer advantages in terms of sustainability. Steel is a fully recyclable material, contributing to the achievement of environmental sustainability goals. Steel structural elements do not lose any properties during the recycling process and can be reused. Furthermore, the light weight of steel roof systems saves energy during transportation and installation (Huberman et al., 2015). This contributes to reducing the carbon footprint and makes steel roof systems an environmentally friendly option.

Steel roofs can be optimized for insulation and energy management. For example, in energy-efficient roof systems, the combination of steel and insulation materials provides both thermal insulation and reduces energy costs (Liang et al., 2015). Steel roof systems that can be integrated with solar panels support renewable energy production and increase energy efficiency.

Steel roof systems also offer numerous security advantages. Steel roofs, which are resistant to earthquakes, fires, and other natural disasters, increase user safety. For example, when combined with fire-resistant coatings, steel materials provide a high level of fire protection (Lebed et al., 2018). Furthermore, steel roof systems offer an ideal solution for earthquake-resistant structures and increase the structure's overall stability.

# 4.2.1. Materials and Elements Used in Steel Roof Systems

The primary material used in steel roof systems is structural steel. Steel, with its high strength-to-weight ratio, enables the covering of large openings and increases the load-carrying capacity of structures. Structural steel elements include steel beams, columns, trusses, purlins, rafters, and tie elements (Diao et al., 2019). Fasteners are critical to ensuring the structural integrity of steel roof systems. Connection methods such as screws, bolts, and welding are used to assemble steel elements. Bolted connections offer the advantage of rapid assembly and disassembly, while welded connections provide a stronger and more permanent joint. The selection of fasteners varies depending on the structure's function, design requirements, and environmental conditions.

In steel roof systems, cladding materials play a crucial role in protecting the structure against external factors. Metal sheets, composite panels, and steel cladding are commonly used in cladding steel roofs. These materials offer properties such as waterproofing, thermal insulation, and aesthetic appeal. For example, galvanized steel sheets provide high corrosion resistance and offer a long-lasting cladding solution (Parskiy et al., 2017).

Insulation materials are used in steel roof systems to increase energy efficiency and ensure indoor comfort. Materials such as glass wool, rock wool, polyurethane foam, and polystyrene are preferred for thermal insulation in steel roofs. Insulation materials help maintain indoor temperatures in both summer and winter, reducing energy costs. In addition, insulation materials provide sound insulation and improve acoustic performance (Huberman et al., 2015).

Another important element used in steel roof systems is load-bearing beams. These elements are critical for increasing the structure's load-bearing capacity and ensuring its stability. Steel load-bearing beams are generally designed in the form of I- or H-profiles and offer high strength. Furthermore, their lightweight construction simplifies the installation process and reduces the structure's overall weight (Lebed et al., 2018).

Coatings and paints used to protect steel roof systems against corrosion extend the life of the material. Methods such as zinc coating, epoxy paint, and polyurethane coating increase the corrosion resistance of steel elements and reduce maintenance requirements. Such protective coatings increase the durability of steel roof systems, especially in humid or salty environments (Shimada et al., 2020).

#### **4.2.1.1.** Trusses

Trusses are structural elements widely used in modern engineering, providing high durability and efficiency. These elements consist of a series of triangular-shaped components and are often preferred in the construction of roof systems, bridges, towers, and various industrial structures. The design and application of trusses are optimized in terms of material usage, structural stability, and cost, meeting various engineering requirements. One of the key characteristics of trusses is their triangular geometry, which increases their load-carrying capacity and promotes structural stability. These triangular forms allow for even load distribution and the ability of the elements to undergo axial tension or compression. This structure reduces weight while increasing durability, providing an ideal solution for supporting large spans (Kaveh and Ghazaan, 2018).

The design of trusses involves processes such as dimensioning, shape optimization, and topology optimization. Dimensioning involves determining the correct cross-sectional dimensions of each element, while shape optimization determines the overall geometry of the structure. Topology optimization, on the other hand, aims to increase material utilization and efficiency of the structure by eliminating unnecessary elements (Zhang, 2024). For example, different types of truss designs, such as Pratt, Howe, and Warren, are selected to meet specific structural requirements.

Trusses are among the indispensable structural elements of steel roof systems, providing economical and durable coverage of wide openings. Steel trusses, with their triangular geometry, increase structural stability by distributing loads evenly and are widely used in various engineering projects. These elements, with their lightweight, high strength, and design flexibility, are preferred in projects requiring wide openings, such as industrial buildings, sports complexes, and commercial buildings (Kaveh and Ghazaan, 2018).

The fundamental design principle of trusses is to effectively support axial loads. These structures are typically constructed with a triangular array of compression and tension members, distributing external forces in a way that enhances the structure's overall stability. The high strength and flexibility of steel allow trusses to carry heavy loads and support large spans.

The steel profiles used in the structure of lattice girders are generally designed as I-, H-, T-, or tubular-section elements. These profiles both reduce weight and increase load-carrying capacity. Furthermore, steel lattice girders are

often protected against corrosion by galvanizing or painting, thus providing a long-lasting solution (Yan et al., 2019).

The fasteners of steel trusses are critical to ensuring the structure's durability and stability. Connection methods such as bolting, welding, and riveting ensure the secure assembly of truss elements. Bolted connections, in particular, offer both an economical and practical solution by facilitating easy assembly and disassembly (Javanmiri and Mäkinen, 2022).

Trusses also offer significant economic advantages. These elements optimize material usage and reduce costs when covering large openings. Furthermore, prefabricated steel trusses shorten installation time and reduce labor costs. Trusses play a significant role in steel roof systems, both in terms of aesthetics and functionality. Their high durability, light weight, and design flexibility make these structural elements an indispensable solution for modern engineering projects.

# 4.2.1.2. Roof purlin elements

Purlins, one of the most critical elements of roof systems, are used to support roof coverings, transfer loads to the supporting elements, and ensure structural stability. These elements are typically manufactured from materials such as steel, aluminum, or wood and are widely used in a wide range of roof types.

Purlins, one of the most critical elements of roof systems, are used to support roof coverings, transfer loads to load-bearing elements, and ensure structural stability. These elements are typically manufactured from materials such as steel, aluminum, or wood and have a wide range of applications in different roof types. The design and implementation of purlins in roof systems play a significant role in terms of structural safety, cost, and aesthetics (Torabian, 2023). The primary function of purlins is to support the roof covering materials and transfer loads to the main load-bearing elements. These loads are caused by environmental factors such as the weight of the roof coverings, snow, and wind. Proper design of purlins ensures even distribution of these loads and maintains structural integrityFor example, thin-walled Z-profile purlins are widely used, especially in wide-span steel roofs. These profiles stand out for their lightweight and high-strength structures. The design of purlin systems is generally based on factors such as load-bearing capacity, stability, and cost. Purlin sizing directly affects the overall performance of the roof system. Furthermore, purlins are often used in conjunction with beams to increase rigidity and durability (Aydoğdu et al., 2018). The materials used in purlin systems are generally selected according to the requirements of the

application. Steel purlins have a wide range of applications due to their high strength and corrosion resistance properties. Furthermore, wooden purlins are preferred in projects that meet environmental sustainability goals. Hybrid purlin systems offer both durability and cost advantages by combining different materials, such as steel and wood (Garcia et al., 2018).

Bracing elements used to increase purlin stability limit deformations under wind loads and other environmental influences. For example, cross-bracing added to purlin systems reduces the risk of buckling and increases load-carrying capacity. These bracing elements are particularly critical in regions with high wind loads (Tang et al., 2018).

Optimizing purlin systems for energy efficiency and sustainability is a key component of modern roof designs. Purlins, working in conjunction with roof coverings and insulation materials, reduce heat loss and energy costs. Furthermore, purlin systems integrated with renewable energy sources such as solar panels contribute to environmental sustainability goals (Shifferaw et al., 2016).

#### **4.2.1.3.** Fasteners

In roof systems, fasteners are critical for assembling structural components and safely transferring loads. These elements increase structural stability and safety by connecting roof beams, purlins, cladding materials, and load-bearing elements. In modern construction projects, the selection and design of fasteners are optimized based on factors such as material properties, load-bearing capacity, and ease of installation. The primary function of fasteners is to ensure the safe transfer of loads and the transfer of forces between structural elements. Fasteners such as screws, bolts, welds, and rivets are used to meet various structural requirements. For example, bolted connections used in steel roofs are widely preferred due to their ease of installation and high strength (Liu et al., 2015).

The materials used in the design of fasteners are generally durable and long-lasting materials such as steel, aluminum, and polymer. Steel fasteners offer high strength and corrosion resistance, while aluminum elements stand out for their light weight and workability. Additionally, polymer materials are used to provide insulation and chemical resistance in certain applications (Dowswell, 2016).

Another important factor to consider in the design of fasteners is the stiffness and durability of the connection. The stiffness of the fasteners increases the stability of the structural elements and minimizes deformations. For example, steel angle connections used in prefabricated roof systems ensure safe load transfer and speed up the installation process (Dal Lago et al., 2017).

#### 5. Conclusion

Roof systems play a crucial role in the planning and design of agricultural structures. The ability to maximize the third dimension of a structure, particularly in plant and animal production structures, product storage, and hangars, is closely related to the design of roof systems. Furthermore, as a fundamental component of a structure, roof systems play a crucial role in ensuring structural integrity and optimally meeting aesthetic and functional requirements. Furthermore, roofs protect buildings from external factors, contributing to their longevity.

#### 6. References

- Abramyan, S. G., & Ishmametov, R. K. (2016). Strengthening timber roof trusses during building construction and reconstruction. *Procedia Engineering*, 150, 2133-2137.
- Awwad, B. A., & Suliman, M. O. (2018). Study on Flat Roofing Systems. *Journal of Advanced Sciences and Engineering Technologies*, 1(2), 45-59.
- Aydoğdu, M. H., Cançelik, M., Yenigün, K., Küçük, N. & Yenikale, A. (2021). Are you happy to be a farmer? Understanding indicators related to agricultural production and influencing factors: GAP-Şanlıurfa, Turkey. *Sustainability*, 13(22), 12663.
- Baha, N. Z., & Osman, S. A. (2017). Extreme wind effects on roof structures of low rise buildings. *Hip*, *1*.
- Bahorka, M., Abramovych, I., & Kravets, O. (2024). The implementation of marketing management solutions in agricultural enterprises.
- Chesnokov, A., Mikhailov, V., & Dolmatov, I. (2022, May). Mastering Hybrid Roof Structures via Students' Research Activity. In 2022 2nd International Conference on Technology Enhanced Learning in Higher Education (TELE) (pp. 175-180). IEEE.
- Coma, J., Pérez, G., Solé, C., Castell, A., & Cabeza, L. F. (2016). Thermal assessment of extensive green roofs as passive tool for energy savings in buildings. *Renewable energy*, 85, 1106-1115.
- Dal Lago, B., Toniolo, G., Felicetti, R., & Lamperti Tornaghi, M. (2017). End support connection of precast roof elements by bolted steel angles. *Structural Concrete*, 18(5), 755-767.
- Degtyarev, G. V., Saida, S. K., & Al Hajal, A. (2021, February). Comparative analysis of typical and reinforced support parts' design parameters for reinforced concrete roof beams. In *IOP Conference Series: Materials Science and Engineering*, Vol. 1083, No: 1.
- Diao, M. Z., Li, Y., Lu, X. Z., Guan, H., & Sun, Y. L. (2019). The structural and construction performances of a large-span half steel-plate-reinforced concrete hollow roof. *Advanced Steel Construction*, *15*(1), 16-22.

- Divanbeigi, R., Paustian, N., & Loayza, N. (2016). Structural transformation of the agricultural sector: a primer. *World Bank Research and Policy Briefs*, (104231).
- Dowswell, B. (2016). Stability of Rectangular Connection Elements. *Engineering Journal*, 53(4), 171-202.
- Dutkiewicz, M., Hajyalikhani, P., Lamparski, T., Whitman, L., & Covarrubias, J. (2021, November). Structural bracing of wooden roofs under the extreme winds. In *IOP Conference Series: Materials Science and Engineering* (Vol. 1203, No. 2, p. 022024). IOP Publishing.
- Gabriela, D., Maican, A. M., & Rotaru, V. D. (2017). Roof structures. Comparisons between traditional roof structures and industrialized ones. *Ovidius University Annals of Constanta-Series Civil Engineering*, 19(1), 79-85.
- García, H., Zubizarreta, M., Cuadrado, J., & Osa, J. L. (2018). Sustainability improvement in the design of lightweight roofs: A new prototype of hybrid steel and wood purlins. *Sustainability*, *11*(1), 39.
- Gilodo, A. Y., & Arsiriy, A. M. (2023). Strengthening of reinforced concrete roof with steel frame.
- Giuriani, E. P., Marini, A., & Preti, M. (2016). Thin-folded shell for the renewal of existing wooden roofs. *International Journal of Architectural Heritage*, 10(6), 797-816.
- Grigorenko, Y. (2017). Agricultural potential role in ensuring economic security. *European Cooperation*, 12(19), 34-47.
- Guerrero, D., Figueroa, M. B. G., Guallpa, J. L. P., Redrovan, C. D. P., & López, N. (2022). Analysis of the structural behavior of flat and circular self-supporting roof using finite elements. *Revista de la Universidad del Zulia*, *13*(36), 222-240.
- Gupta, A., Singh, U. B., Sahu, P. K., Paul, S., Kumar, A., Malviya, D., ... & Saxena, A. K. (2022). Linking soil microbial diversity to modern agriculture practices: a review. *International Journal of Environmental Research and Public Health*, 19(5), 3141.
- Hodbod, J., Barreteau, O., Allen, C., & Magda, D. (2016). Managing adaptively for multifunctionality in agricultural systems. *Journal of environmental management*, 183, 379-388.
- Huberman, N., Pearlmutter, D., Gal, E., & Meir, I. A. (2015). Optimizing structural roof form for life-cycle energy efficiency. *Energy and Buildings*, *104*, 336-349.
- Javanmiri, A., & Mäkinen, J. (2022). Weight optimization of truss structures by using genetic algorithms. *Rakenteiden Mekaniikka*, 55(2), 42-54.
- Jawalgi, A. S., Renukadevi, M. V., Jagadish, K. S., & Basutkar, S. M. (2020). Composite T-beam Roof: An Alternate Affordable Roofing System. *Journal of The Institution of Engineers (India): Series A*, 101, 259-264.
- Kain, G., Idam, F., Federspiel, F., Réh, R., & KriSťák, Ľ. (2020). Suitability of wooden shingles for ventilated roofs: An evaluation of ventilation efficiency. *Applied Sciences*, *10*(18), 6499.
- Kaveh, A., Ilchi Ghazaan, M., Kaveh, A., & Ilchi Ghazaan, M. (2018). Optimal Design of Large-Scale Special Truss Structures. *Meta-heuristic Algorithms for Optimal Design of Real-Size Structures*, 45-63.
- Kozak, D. L., & Liel, A. B. (2015). Reliability of steel roof structures under snow loads. *Structural Safety*, *54*, 46-56.

- Kvaraia, I., & Giorgobiani, I. (2023). Simplification of the reinforced concrete arched roofing construction. *Architecture and Engineering*, 8(2), 58-62.
- Lebed, E. V., & Alukaev, A. U. (2018). Large-span metal dome roofs and their construction. *Structural Mechanics of Engineering Constructions and Buildings*, 14(1), 4-16.
- Liang, H., Roy, K., Fang, Z., & Lim, J. B. (2022). A critical review on optimization of cold-formed steel members for better structural and thermal performances. *Buildings*, *12*(1), 34.
- Liu, Q., Yang, J., & Wang, F. (2015). Numerical simulation of sleeve connections for cold formed steel sigma sections. *Engineering Structures*, 100, 686-695.
- Maraveas, C., & Bartzanas, T. (2021). Sensors for structural health monitoring of agricultural structures. *Sensors*, 21(1), 314.
- Misar, I., & Novotný, M. (2017). Defects and behaviour of inverted flat roof from the point of building physics. In *MATEC Web of Conferences* (Vol. 93, p. 02002). EDP Sciences.
- Mohammadzadeh, N. (2016, May). An Optimization Approach for Integrating Different Roof Functions with Environmental Impacts Constraint. In *Innovation: Shifting Ground*. EDRA.
- Moran, P. (1980). Full-scale experiments to acquire wind loading data for use in the design of agricultural buildings. *Journal of Agricultural Engineering Research*, 25(3), 287-297.
- Olukunle, A. J. (2014). Improving the quality of roofing system of traditional buildings in rural area of Nigeria.
- Parskiy, N. D., Molodtsov, M. V., & Molodtsova, V. E. (2017, November). Cost effectiveness of precast reinforced concrete roof slabs. In *IOP Conference Series: Materials Science and Engineering* (Vol. 262, No. 1, p. 012036). IOP Publishing.
- Pernisova, A. (2016). Drainage systems for sloping roofs and possibilities of rain water use. *Applied Mechanics and Materials*, 820, 63-68.
- Secka, L. (2015). Criteria for defining the architectural form of wooden structures. *Selected Scientific Papers-Journal of Civil Engineering*, 10(1), 19-26.
- Shifferaw, Y., Woldeyes, K., & Bitsuamlak, G. (2016). Stability and strength behavior of thin-walled roof-panel-purlin system under wind loading. In *Proc., Annual Stability Conf. Structural Stability Research Council* (pp. 650-668).
- Shimada, Y., Yamada, S., Kishiki, S., Hasegawa, T., & Takeuchi, T. (2020). Method of reinforcement for joints between steel roofs and RC columns in existing buildings. *Engineering Structures*, 209, 110255.
- Stoycheva, I. (2023). Place and role of the agricultural sector in the national and regional economic structure. In *SHS Web of Conferences* (Vol. 176, p. 03007). EDP Sciences.
- Szabolcs, B., Janos, S., & Potori, N. (2017, June). Economic Importance of the Common Agricultural Policy in Terms of Agricultural Production in Hungary and Its Implications after 2020. In *Proceeding of the International Scientific Conference*" Strategies for the Agri-Food Sector and Rural Areas-Dilemmas of Development (pp. 19-21).
- Tang, Y., Tong, G., & Zhang, L. (2018). Buckling of parallel purlins in standing seam or screw-fastened roofs. *Thin-Walled Structures*, *132*, 136-150.

- Torabian, S. (2023). Effect of System Reliability on Design of Metal Building Roof Purlins. *Civil Engineering Research Journal*.
- Walters, S. A., & Stoelzle Midden, K. (2018). Sustainability of urban agriculture: Vegetable production on green roofs. *Agriculture*, 8(11), 168.
- Yan, S., Rasmussen, K. J., Liu, X., Dai, L., & Zhao, X. (2019). Behaviour of H-section purlin connections in resisting progressive collapse of roofs. *Engineering Structures*, 201, 109849.
- Zhang, Y., Song, X., & Zhang, Q. (2016). Dynamic characteristics and wind-induced vibration coefficients of purlin-sheet roofs. *Steel Compos Struct*, 22(5), 1039-1054.

# **Electrical Energy Efficiency, Smart Systems** and Artificial Intelligence

Metin DEMİRTAS<sup>1</sup>

<sup>1-</sup> Res. Prof. Dr.; Balikesir University, Engineering Faculty, Electrical and Electronics Engineering Deartment. mdtas@balikesir.edu.tr ORCID No:0000-0003-2622-5286

#### **ABSTRACT**

Rising electricity demand and the increasing complexity of modern power systems necessitate analytics and artificial intelligence approaches for energy management efficiency and sustainability. This study examines the integration of electrical energy efficiency strategies with smart systems and artificial intelligence (AI) technologies, as well as previous studies in the literature. The use of smart systems, such as metering infrastructure, demand response mechanisms, and smart controllers in electrical energy systems, enables real-time monitoring of energy consumption and optimized energy consumption. AI techniques, including machine learning, predictive analysis, and optimization algorithms, facilitate accurate load forecasting, fault detection, and efficient energy distribution.

The combination of these technologies not only reduces energy waste and operating costs, but also improves grid reliability and supports the integration of renewable energy sources. This study highlights recent advances, challenges, and future prospects in the convergence of energy efficiency, optimization algorithms, smart systems, and AI, highlighting their critical roles in achieving sustainable and resilient electricity grids..

Keywords – Electrical energy, Power system, Optimization, Artificial İntelligence, Smart system.

#### 1. INTRODUCTION

Global energy demand is increasing annually due to industrialization, urbanization, and digitalization; in parallel, electrical energy consumption is becoming the most dynamic component of energy systems. This creates significant pressures for both energy supply security and environmental sustainability. According to data from the International Energy Agency (IEA, 2024), the improvement in global energy intensity was only 1.2% in 2024, well short of the pace required for an energy transition aligned with the Paris Agreement goals. Therefore, energy efficiency is defined by many countries as the "first fuel of the clean energy transition" (International Energy Agency [IEA], 2024).

Electrical energy efficiency refers to reducing the amount of electricity consumed per unit of production or service and is one of the most effective tools for energy management. The Energy Efficiency Strategy Document (2023–2030), currently in effect in Turkey, targets a 15% reduction in energy intensity by 2030; within this scope, smart system-based

solutions in the industrial, building, and transportation sectors have been identified as priority areas (Ministry of Energy and Natural Resources [ETKB], 2024). Achieving these goals requires not only equipment-based efficiency but also critical measures such as digital energy management, data analytics, artificial intelligence-assisted forecasting, and smart grid applications (Khalid et al., 2024). According to current research, electrical energy demand forecasting is now increasingly performed using the advantages of hybrid models. For example, the Electricity Demand Forecasting Methodologies and Applications (2025) study highlights the increasing prevalence of models consisting of statistical methods, machine learning/artificial intelligence techniques, and their combinations; hybrid models, in particular, are noted to demonstrate superior performance in terms of accuracy, flexibility, and stability. Furthermore, the article, "A state-of-the-art comparative review of load forecasting," compares traditional methods (ARIMA, regression, time series models) with modern deep learning-based models and demonstrates that advanced techniques can significantly reduce errors, particularly in medium- and long-term forecasts. Similar trends are observed in studies conducted specifically for Turkey: A study conducted in the provinces of Aydın, Denizli, and Muğla compared CatBoost and BiLSTM models, and found that both methods performed well (especially in capturing seasonality and variable patterns), according to Proceedings. In another example, Turkey's electricity consumption, along with economic and demographic variables such as GDP, population, and inflation, was modeled using MNN (Medium Neural Network), Whale Optimization Algorithm (WAO), and Support Vector Machine (SVM).

Additionally, new approaches such as tensor-factor models that better capture seasonal patterns in multidimensional data are also emerging in the literature; such models attempt to capture both spatial and temporal correlations by disaggregating hourly consumption data into day, week, and hour modes. Furthermore, hybrid models such as CNN-LSTM + Multi-Head Attention + Particle Swarm Optimization (PSO) also provide successful error reduction results in short-term forecastsPE  $\approx 1.94\%$ ) (Quan et al.,2023).

Smart systems are integrated energy management structures consisting of sensors, data collection units, communication infrastructure, and decisionsupport algorithms. These systems allow for monitoring, measuring, and optimizing the entire energy chain from production to consumption. Smart grids, in particular, provide two-way data flow between energy producers and consumers, enabling real-time adjustment of the supply-demand balance (IEEE Power & Energy Society, 2024). This facilitates the integration of renewable energy resources into the grid, reduces losses, and increases system reliability (Khalid et al., 2024).

Figure 1 illustrates the components and operational processes of a smart grid. The image shows various energy production facilities (hydroelectric, nuclear, thermal, wind. and solar power interconnected and managed by smart systems and devices. The image shows that electrical energy generated from various sources is transmitted to consumption points such as cities, factories, electric vehicle charging stations, and smart homes through energy production, transmission, and distribution systems. The "Smart Grid," shown in the center of the grid, securely and sustainably controls production and consumption processes using digital technologies, smart devices, SCADA systems, automation, communication, and two-way communication. Electric vehicles used in smart grids, smart measurement systems and devices such as meters, and renewable energy sources constitute important components of this grid. Thanks to smart grids, energy is managed in a more efficient, high-quality, environmentally friendly, sustainable secure. and manner.

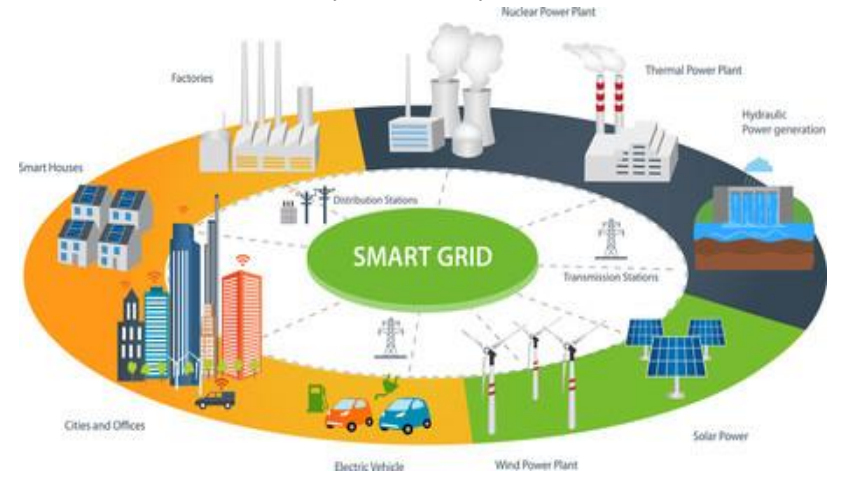


Figure 1. Smart Grid Structure (Vasudeyan, 2023)

Developing technologies, particularly artificial intelligence (AI) and machine learning (ML), have ushered in a new era in energy management. AI algorithms analyze large data sets to perform optimization processes in the energy sector, such as demand forecasting, fault detection and preventative measures, balanced load distribution, and electrical energy storage (Ejiyi et al., 2025). These methods, unlike traditional methods, offer proactive grid management capabilities as systems that continuously learn and adapt to new conditions.

The internationally recognized ISO 50001:2018 Energy Management System Standard provides a framework for nations and organizations to systematically improve their systems to improve their performance (International Organization for Standardization [ISO], 2018). This standard not only reduces energy costs but also helps organizations reduce their carbon footprint and achieve their sustainability goals. Consequently, it is anticipated that the need for smart grids will continue to grow, and in this context, the efficiency of electrical energy and the integrated operation of smart systems will be crucial for both economic and environmental sustainability.

#### 2. THE CONCEPT OF ELECTRICAL ENERGY EFFICIENCY

Electrical energy efficiency is defined as minimizing input costs to provide a specific service or production volume. This concept addresses the system's energy production process, starting with minimizing transmission, distribution, and consumption losses. Increased efficiency allows the same outputs to be achieved with fewer inputs, resulting in economic returns and less environmental damage. Energy efficiency policies have become increasingly dominant worldwide, particularly due to rising energy prices that fuel inflation, reducing carbon emissions that harm the environment, and sustainability pressures. For example, Bera and colleagues reported in a study that energy efficiency technologies (especially smart metering infrastructures, advanced control systems, and digitalization solutions) could save between 10% and 30% of electricity consumption (Bera et al., 2025). Furthermore, the IEA's "Energy Efficiency 2023" report highlighted the slow pace of improving global energy intensity, highlighting the need for aggressive efficiency policies (IEA, 2023).

#### 3. FUNDAMENTALS OF INTELLIGENT SYSTEMS

Electrical energy is easier and more economical to transport and use than other energy systems. Systems used to increase electrical energy efficiency are integrated systems that combine sensors, smart measurement devices and software, communication infrastructure, various control algorithms, and artificial intelligence. These systems enable real-time measurement and monitoring of energy flow between producers and consumers, rapid fault detection and maintenance, load balancing, and energy optimization. Smart metering infrastructures (Advanced Metering Infrastructure (AMI), in particular, enable the implementation of demand-side management and flexible consumption strategies by recording detailed consumer energy use (Khalid, Rahman, & Tanveer, 2024). These infrastructures not only collect electricity consumption data but also provide the necessary database to improve system efficiency and reduce energy losses (International Energy Agency [IEA], 2024).

Another key component of smart systems is data analytics and AI-enabled energy management. Big data analytics and machine learning algorithms analyze production and consumption data, enabling energy demand forecasting, optimizing the production-consumption balance, and early detection of faults (Ejiyi, Khan, & Kumar, 2025). This allows energy efficiency to be maximized not only at the device and system level, but also at the grid and corporate level. Furthermore, energy management systems such as the ISO 50001 standard provide a framework for continuous energy performance improvement by integrating smart systems with enterprise applications (International Organization for Standardization [ISO], 2018). The figure illustrates the data collection, processing, and resource optimization process in smart electricity grids.

Figure 2 shows IoT sensors and devices continuously collect data on the grid, such as energy consumption, production, voltage, and current. During data collection, data from these sensors is brought together in a centralized collection system. During preprocessing, raw data is cleaned, filtered, and made suitable for analysis. The communication network securely transfers data to the cloud and edge systems. Cloud platforms and edge computing provide rapid analysis close to where the data is generated (e.g., transformers or local control units). The cloud platform performs more

comprehensive analysis and long-term storage. A deep learning model performs prediction, classification, or optimization on this data. During resource allocation, the obtained results are used to efficiently allocate energy resources (e.g., solar, wind, batteries). With optimized resource allocation, the grid is managed efficiently, balancedly and sustainably in real time.

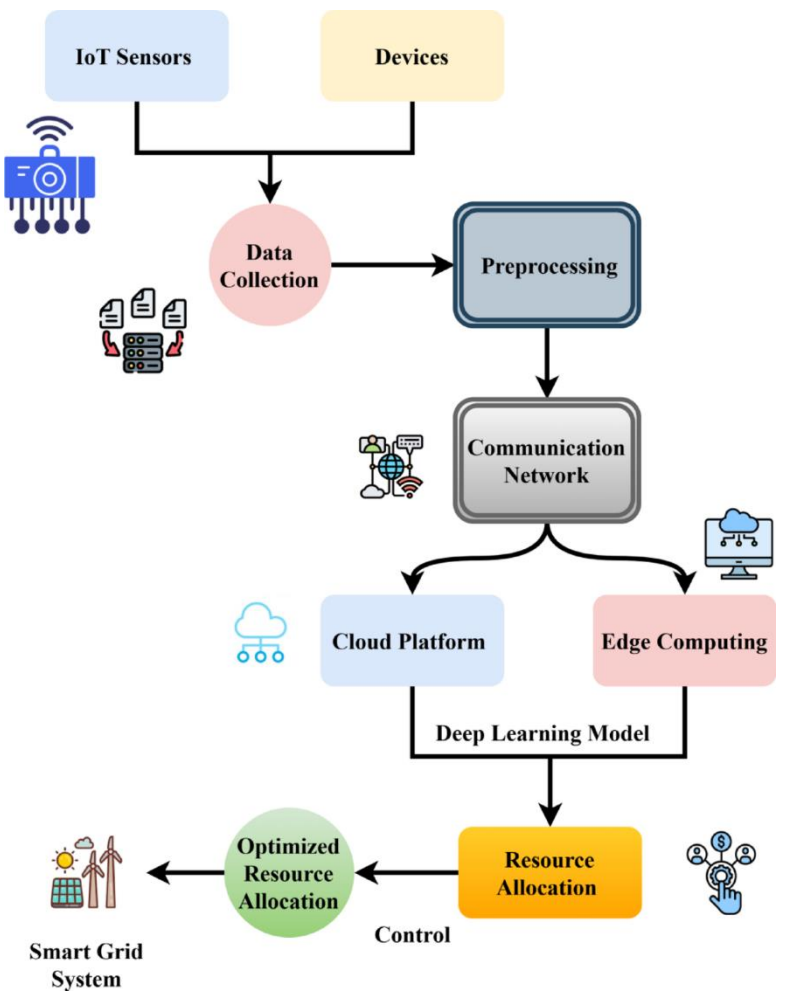


Figure 2. Data collection, processing and resource optimization process (Singh, 2025)

#### 4. SMART GRID AND ENERGY MANAGEMENT SYSTEMS

Smart grids are modern energy infrastructures that monitor the entire energy flow from electricity generation to consumption, provide two-way data communication, and optimize the demand-consumption balance. These systems facilitate the integration of distributed energy resources (solar, wind, biogas), reduce energy losses, and increase grid reliability (Khalid, Rahman, & Tanveer, 2024). Advanced metering infrastructure (AMI) and SCADA systems, critical components of smart grids, collect consumer-side data in real time and transmit it to energy management systems, enabling demand-side management and load balancing strategies to be implemented (International Energy Agency [IEA], 2024).

Energy management systems (EMS) are software and hardware-based solutions that integrate with the smart grid to optimize energy production, distribution, and consumption. EMS predicts energy demand using machine learning and artificial intelligence algorithms, enables the integration of renewable energy sources into the grid, and optimizes the use of energy storage units (Ejiyi, Khan, & Kumar, 2025). Furthermore, EMS applications within the framework of the ISO 50001 standard allow organizations to continuously monitor and improve their energy performance, resulting in significant reductions in energy costs (International Organization for Standardization [ISO], 2018). This integrated approach plays a critical role in increasing energy efficiency from both economic and environmental perspectives. The energy information flow map, which includes generation, transmission, distribution, customer-side, and feedback paths within the grid, is shown in Figure 3.

AI has become a cornerstone in enhancing energy efficiency and management in modern smart systems. In smart buildings, AI algorithms such as machine learning and deep learning optimize energy consumption by enabling predictive maintenance, real-time load forecasting, and efficient HVAC system management (Aghili, 2025). Similarly, in smart grids, AI facilitates the integration of renewable energy sources, improves load balancing, and supports predictive maintenance to reduce energy waste and enhance operational efficiency (Balamurugan, 2025). Moreover, ensuring cyber security in smart grids is critical, and AI-driven solutions help detect and mitigate cyber threats to devices such as smart meters and remote terminal units, safeguarding both efficiency and reliability (Ishfaq & Zhou, 2025). In residential settings, AI-based energy management models further

enhance sustainability by optimizing energy consumption patterns in smart homes, highlighting the significant potential of AI for future energy systems (Rehman, Faria, & Vale, 2025). Collectively, these studies demonstrate that AI not only improves operational efficiency but also supports the secure, sustainable, and intelligent management of modern energy systems.

Figure 3 shows the holistic architecture of the smart grid structure. The diagram explains the energy journey from production to consumption, as well as the information and control infrastructure in this process, in a layered manner. This figure holistically illustrates the general structure of smart grids and their interaction with energy management systems. The system consists of three main sections: energy production, transmission and distribution, and consumption (residential/industrial). On the production side, renewable energy sources (wind, solar, hydroelectric) are integrated with traditional generation facilities (nuclear, thermal).

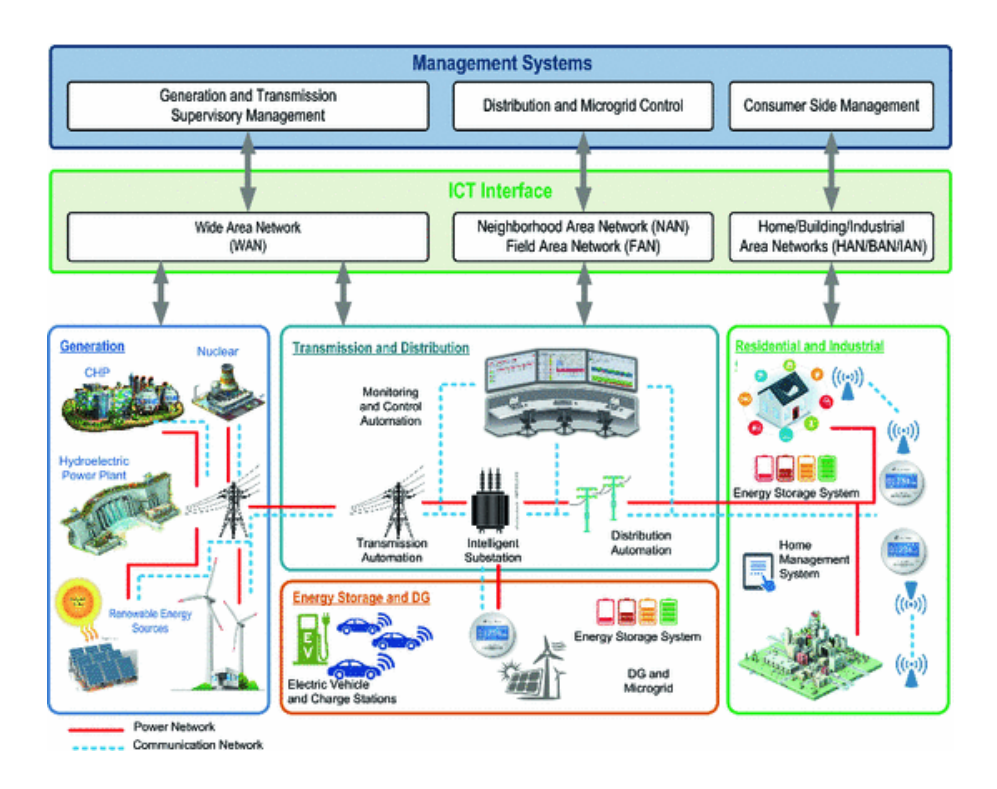


Figure 3. Energy Management System (Martin, 2025)

The transmission and distribution side features smart transformer centers, monitoring and control automation, and distribution automation based on communication infrastructure. This structure is supported by WAN, NAN, FAN, and HAN networks via information and communication technologies (ICT). This allows data to be transferred in real time from generation to consumption. Energy storage systems, electric vehicles, and microgrids optimize the balance between energy supply and demand, while home and building energy management systems increase efficiency on the consumer side. Management systems at the upper level (generation-transmission control, microgrid control, and consumer management) coordinate this entire structure, ensuring safe, flexible, and sustainable operation. This integrated structure forms the foundation of the future's smart energy infrastructure, based on digitalization, automation, and data analysis.

This structure is supported by WAN, NAN, FAN, and HAN networks through information and communication technologies (ICT). This allows data to be transferred from generation to consumption in real time. Energy storage systems, electric vehicles, and microgrids optimize the balance between energy supply and demand, while home and building energy management systems increase efficiency on the consumer side. Higher-level management systems (generation-transmission control, microgrid control, and consumer management) coordinate this structure, ensuring a safe, flexible, and sustainable operation. This integrated structure forms the basis of the future's smart energy infrastructure based on digitalization, automation, and data analysis.

Some of the algorithm types commonly used in today's literature in the field of smart grid and energy management systems (EMS) are given in Table 1.

Table 1: The algorithm types

Category	Method / Algorithm	Description / Application Area
Metaheuristic Optimization	PSO (Particle Swarm Optimization), GA (Genetic Algorithm), GWO (Grey Wolf Optimization)	Used for solving multi-variable optimization problems such as minimizing energy cost, load allocation, and resource optimization.
Hybrid / Multi- criteria Optimization	ANFIS-based multi- objective optimization models	Studies that simultaneously address demand response, energy storage, and cost optimization.
Deep Learning & Machine Learning	LSTM, GRU, CNN-LSTM, autoregressive neural networks	Applied in time series—based consumption forecasting, load prediction, and demand response applications.
Deep Reinforcement Learning	Multi-agent RL, hierarchical RL structures	Used in real-time decision-making systems such as grid control, power flow optimization, and reactive power control.
Combination / Hybrid Approaches	Integration of optimization and learning models	For example, tuning the parameters of a metaheuristic algorithm using deep learning or reinforcement learning methods. arXiv+2MDPI+2

#### 5. ENERGY EFFICIENCY IN INDUSTRIAL APPLICATIONS

The industrial sector accounts for approximately 40% of global electricity consumption and is therefore a critical area for energy efficiency applications (International Energy Agency [IEA], 2024). Key approaches to achieving energy efficiency in industrial facilities include high-efficiency motors, variable speed drives (VFDs), optimized compressed air systems, and energy-efficient lighting solutions. Implementing these technologies not only reduces energy consumption, lowers production costs, and shrinks the carbon footprint (Bera, Kumar, & Singh, 2025).

Additionally, industrial energy management systems (EMS) and smart sensor infrastructures monitor energy usage across the facility in real time, enabling optimization. Artificial intelligence and machine learning algorithms analyze the efficiency status of equipment, enabling predictive maintenance and energy optimization strategies (Ejiyi, Khan, & Kumar, 2025). The adoption of the ISO 50001 standard provides a framework for continuously improving energy performance in industrial facilities, potentially resulting in savings of up to 10–30% in energy costs (International Organization for Standardization [ISO], 2018). This integrated approach is critical for improving energy efficiency in industrial applications and supporting sustainable manufacturing processes.

Energy efficiency in industrial applications can be achieved not only through technological improvements but also through process optimization, maintenance and repair strategies, and employee behavioral modifications. Energy efficiency in industrial applications plays a critical role in reducing operational costs, minimizing environmental impact, and improving overall productivity. It involves the systematic use of technologies, processes, and management strategies to optimize energy consumption compromising the quality of output. For instance, in a steel manufacturing plant, installing variable frequency drives (VFDs) on electric motors allows the motor speed to match real-time process demands rather than running at full speed continuously, leading to substantial reductions in electricity use. Similarly, in the chemical industry, heat recovery systems capture excess thermal energy from one part of the process and reuse it in another, significantly lowering the need for additional heating and reducing energy waste. Furthermore, the integration of smart sensors, real-time monitoring, and predictive maintenance powered by artificial intelligence enables industrial facilities to detect equipment inefficiencies or impending failures before they occur, preventing unplanned downtime and energy losses. Advanced automation and control systems, such as AI-driven process optimization, can further fine-tune operational parameters to minimize energy consumption across multiple production lines simultaneously. By adopting these measures, industries not only achieve cost savings but also contribute to environmental sustainability through reduced carbon emissions, better resource utilization, and compliance with increasingly stringent energy regulations. Overall, energy efficiency in industrial settings is a multifaceted approach that combines technology, data analytics, and strategic planning to create more sustainable and economically viable operations.

These visuals demonstrate that achieving energy efficiency requires first collecting and measuring data, then analyzing it (extracting characteristics/identifying losses), and then pursuing optimization or technological improvements. These steps include critical factors such as "where energy losses are concentrated," "which machines are operating inefficiently," "the status of maintenance cycles," "process temperature and pressure control," and "load balancing." In industrial facilities, these methods not only save costs but also reduce greenhouse gas emissions.

Figure 4 comprehensively illustrates the overall operation of an industrial energy efficiency system and the main components involved in this process. The image clearly illustrates how energy resources (electricity, heat, compressed air, steam, etc.) used in production facilities are distributed across production lines, where energy losses occur throughout the process, and how these losses are monitored and optimized.

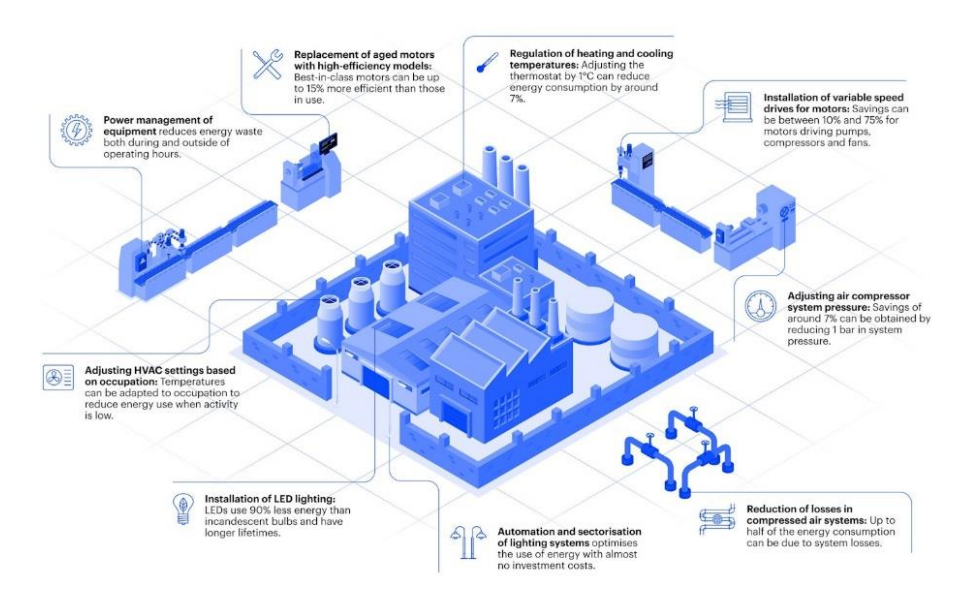


Figure 4. Energy Efficiency in Industrial Applications (IEA,2025)

At the heart of the system, the "Smart Grid," or Energy Management Platform, aggregates data from sensors, meters, and control systems, balancing energy consumption and increasing efficiency through data analysis and AI-based optimization algorithms. On the industrial side, energy losses are minimized by using automation, variable speed drives (VSDs), and monitoring systems on high-consumption equipment such as motors, pumps, furnaces, and compressed air systems.

# 6. ENERGY OPTIMIZATION WITH ARTIFICIAL INTELLIGENCE AND DATA ANALYTICS

AI and data analytics play a critical role in improving energy efficiency. Big data and machine learning algorithms analyze energy production and consumption data to perform functions such as demand forecasting, load balancing, and energy storage optimization (Ejiyi, Khan, & Kumar, 2025). These methods offer significant advantages, particularly in the integration of renewable energy sources and the management of variable demand conditions. For example, unpredictable fluctuations in solar and wind energy production can be more accurately managed and grid stability enhanced by AI-powered forecasting algorithms (Khalid, Rahman, & Tanveer, 2024).

AI and data analytics integrated with enterprise-level and industrial-level energy management systems (EMS) offer significant energy savings potential. Sensor data is analyzed in real time to optimize equipment efficiency, maintenance scheduling, and production processes (International Energy Agency [IEA], 2024). Implementing these systems within the scope of the ISO 50001 standard allows organizations to continuously improve energy performance and achieve energy cost savings of up to 10–30% (International Organization for Standardization [ISO], 2018). Thus, AI and data analytics are becoming essential tools for energy optimization, both economically and environmentally.

Table 2: Energy Optimization with artificial intelligence and data analytics

Feature / Aspect	Artificial Intelligence (AI)	Data Analytics
Purpose	Enables predictive, adaptive, and	Provides insights, trends, and
	autonomous energy management	correlations in energy usage to
	through learning from data and	support decision-making.
	interactions.	
Techniques /	Machine Learning (LSTM, GRU,	Statistical analysis, regression,
Methods	CNN), Deep Reinforcement	clustering, time-series analysis,
	Learning, Hybrid AI-Optimization	anomaly detection.
	models.	
Decision	Can make autonomous decisions	Supports decision-making but
Capability	and optimize in real-time.	requires human interpretation.
Prediction	High accuracy for complex, non-	Good for historical trends and
Accuracy	linear, and dynamic energy	patterns but limited for complex,
	systems.	dynamic forecasting.
Application	Smart grid management, load	Energy consumption reporting,
Areas	forecasting, demand response,	trend analysis, peak demand
	energy cost optimization,	identification, efficiency
	microgrid control.	benchmarking.
Scalability	Scales well with large, multi-	Effective for medium-sized
	source, and high-dimensional data.	datasets; may require more
		processing for very large datasets.
Adaptability	Learns and adapts over time to	Mostly static; relies on periodic
	changing energy patterns.	analysis updates.
Implementation	Higher complexity due to model	Lower complexity; often simpler
Complexity	training, tuning, and deployment.	to implement and interpret.
<b>Cost Efficiency</b>	Can reduce operational costs in the	Helps identify cost-saving
	long term through optimized	opportunities but cannot
	decisions.	autonomously optimize.
Real-time	High; can make decisions in real-	Moderate; mostly post-hoc
Capability	time for energy dispatch or load	analysis, not suitable for
	balancing.	immediate actions.
Data	Requires large, high-quality	Can work with smaller datasets;
Requirements	datasets for training robust models.	quality improves insight but not
		model "learning."
Error Handling /	Can be robust to noise and missing	Sensitive to missing data or
Robustness	data if properly trained.	outliers; may require
		preprocessing and cleaning.
Integration with	Excellent; can be embedded into	Good for monitoring and
IoT / Smart	IoT-enabled energy systems for	reporting; can feed data into AI
Systems	autonomous control.	models but less suitable for
		control.

A comparison of AI and data analytics from different perspectives in terms of energy management and optimization is given in Table 2. According to this table, AI and data analytics play complementary but distinct roles in energy management. AI provides predictive, adaptive, and autonomous decision-making capabilities in large, multi-source, and dynamic energy systems. Using methods such as LSTM, GRU, or deep reinforcement learning, AI can perform real-time load forecasting, demand response, and energy cost optimization. Data analytics, on the other hand, primarily extracts trends, anomalies, and cost-saving opportunities from historical data to guide human decision-makers. Techniques like regression, statistical analysis, or time-series analysis are used for energy consumption reporting and performance evaluation. While AI offers high accuracy, scalability, and adaptability, Data analytics is relatively simpler and faster to implement but is generally less suitable for real-time automated decisionmaking. Moreover, AI can be integrated with IoT-based smart systems to achieve operational cost savings and performance optimization, whereas Data analytics is mostly used for monitoring and reporting. In summary, in energy management, Data analytics provides the foundational data, while AI leverages this data to deliver predictions and automated optimization, significantly enhancing the efficiency and effectiveness of energy systems. Smart grid energy management algorithm is given in Figure 5.

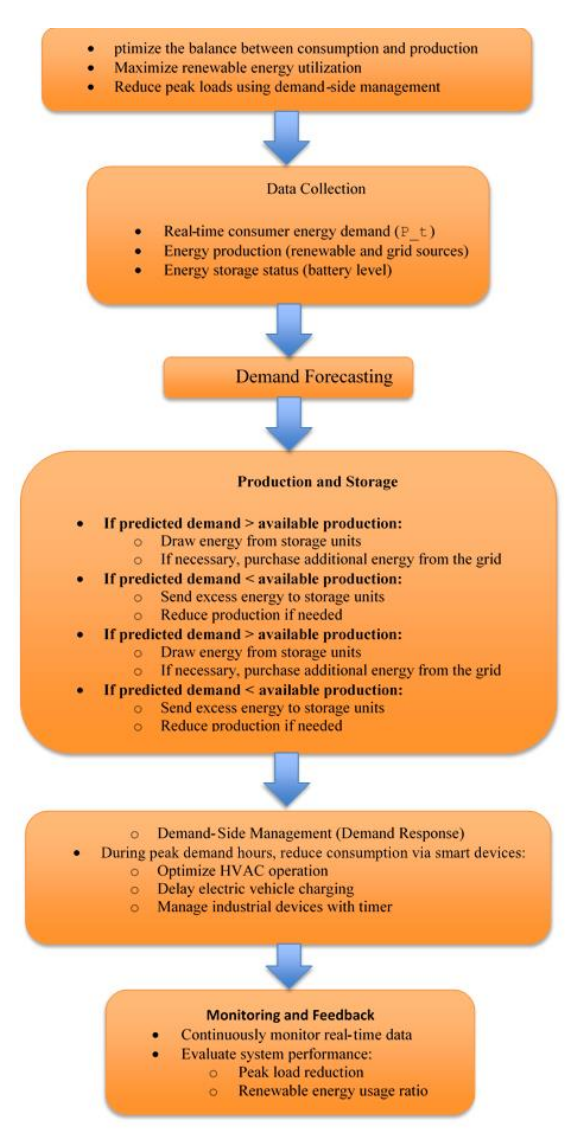


Figure 5. Smart grid energy management algorithm

### 7. RESULTS AND DISCUSSION

Electrical energy efficiency is critical to the sustainability of modern energy systems. Increasing energy demand and limited energy resources necessitate optimizing energy production and consumption. Integrating smart systems and devices into energy management systems yields positive results in reducing energy losses and ensuring grid reliability and resilience. Consumption in industrial factories, buildings, and distributed energy systems can be monitored in real time with smart meters, sensors, and control algorithms. Furthermore, energy production and consumption are optimized, ensuring both economic efficiency and environmental impact.

One of the greatest advantages of smart systems is the ability to collect, monitor, and analyze energy production and consumption data in real time for both producers and consumers. Using this data from these systems provides significant benefits in areas such as demand forecasting and control, balanced load distribution, energy storage, and pre-failure response, leading to successful optimization processes. Energy management systems, used in corporate, industrial, or small-scale individual applications, enable continuous, real-time monitoring of energy performance and power quality, and enable power quality improvement. Furthermore, the use of smart systems supported by well-defined policies and regulatory tools facilitates the achievement of desired goals.

In the near future, increasing energy demand, coupled with the digitalization of systems, the use of smart devices, and the widespread adoption of artificial intelligence-based optimization methods, will lead to significant increases in energy efficiency. The increasing number of microgrids, the integration of vehicle charging stations into the grid, and the emergence of innovative energy trading mechanisms will make energy transmission, production, distribution, and consumption processes more flexible, secure, and transparent. The use of artificial intelligence and data analytics in energy system management will increase energy efficiency and savings by more accurately managing the energy production of renewable energy sources and fossil fuels, ensuring more stable system operation.

Consequently, reducing losses during the production, transmission, distribution, and consumption of electricity, and utilizing it more efficiently, necessitates the combined use of smart grids and modern energy infrastructure. This will significantly contribute to facilitating the sustainable, reliable, and economical operation of energy. The combination of technological innovations, digitalization, the use of smart systems and devices, and continuous monitoring methods such as SCADA (Systems and Systems Management System) will provide significant benefits at both the national and international levels. As demand for electrical energy continues to grow, the widespread adoption and use of smart and integrated systems, along with continuous improvement in power quality, will play a key role in energy security and environmental sustainability.

#### REFERENCE

- Aghili, S. A., Haji Mohammad Rezaei, A., Tafazzoli, M., Khanzadi, M., & Rahbar, M. (2025). Artificial intelligence approaches to energy management in HVAC systems: A systematic review. Buildings, 15(7), 1008.
- Balamurugan, M. (2025). Role of artificial intelligence in smart grid a mini review. National Center for Biotechnology Information.
- Bera, M., Kumar, S., & Singh, R. (2025). Advancing energy efficiency: Innovative technologies and strategic measures for achieving net-zero emissions. Energy Efficiency Journal, 18(4), 123-145.
- Enerji ve Tabii Kaynaklar Bakanlığı (ETKB). (2024). Türkiye'nin Enerji Verimliliği 2030 Stratejisi ve II. Ulusal Enerji Verimliliği Eylem Planı. Ankara: ETKB Yayınları.
- Ejiyi, C. J., Khan, M. A., & Kumar, R. (2025). Comprehensive review of artificial intelligence applications in renewable energy systems. Journal of Big Data, 12(4), 1–28.
- IEEE Power & Energy Society. (2024). Smart grids and intelligent energy systems overview. IEEE Transactions on Smart Grid, 15(2), 123–135.
- International Organization for Standardization (ISO). (2018). ISO 50001:2018 Energy management systems Requirements with guidance for use. Geneva: ISO.
- International Energy Agency (IEA). (2023). Energy Efficiency 2023: Analysis and key findings.
- International Energy Agency (IEA). (2024). Energy Efficiency 2024 Report. Paris: IEA.
- International Energy Agency. (2025). Gaining an edge. IEA.
- Ishfaq, H., & Zhou, W. (2025). Enhancing smart grid security and efficiency: AI, energy management, and cybersecurity..
- Khalid, M., Rahman, H., & Tanveer, S. (2024). Smart grids and renewable energy systems: Perspectives and review. Renewable Energy Reports, 11, 245–260.
- Martin, M. J. (2025, Haziran 21). Integrating distributed energy resources into the smart grid: A technical overview.
- Ocak, M. A., ve Akdemir, O. (2008). An investigation of primary school science teachers' use of computer applications. The Turkish Online Journal of Educational Technology, 7(4), 54-60.
- Ocak, M.A. (2005). Mathematics teachers' attitudes toward the computers. The Turkish Online Journal of Educational Technology, 4(3), 82-88.
- Quansah, P. K., & Tenkorang, E. K. A. (2023). Short-term load forecasting using a particle-swarm optimized multi-head attention-augmented CNN-LSTM network. Applied Energy, 330, 120935.
- Rehman, U., Faria, P., & Vale, Z. (2025). Future of energy management models in smart homes: A systematic literature review of research trends, gaps, and future directions.
- Scahill, E. M., Melican, C., ve Walstad, W. (2005). The preparation and experience of advanced placement in economics instructors. Journal of Economic Education, 36(1), 93-98.

- Singh, A. R., Sujatha, M. S., Kadu, A. D., & others. (2025). A deep learning and IoT-driven framework for real-time adaptive resource allocation and grid optimization in smart energy systems. Scientific Reports, 15, 19309.
- Vasudevan, N., Venkatraman, V., Ramkumar, A., Muthukumar, T., Sheela, A. et al. (2023). Design and Development of an Intelligent Energy Management System for a Smart Grid to Enhance the Power Quality. Energy Engineering, 120(8), 1747–1761.

# **Examination of an Off-Grid Solar Energy System for a Rural Residence**

Muhammed Arslan OMAR<sup>1</sup>

<sup>&</sup>lt;sup>1</sup>Kafkas University, Faculty of Engineering and Architecture, Department of Mechanical Engineering. m.arslanomar@gmail.com ORCID No: 0000-0003-4258-8634

#### **ABSTRACT**

The environmental impacts of fossil fuels, the risk of depletion, and transportation costs have increased the importance of alternative energy sources. In this context, renewable energy sources, particularly solar and wind energy, offer sustainable and economical solutions. Like many countries, Turkey is also investing in this field; for example, the Kızören Solar Power Plant in Konya Karatay is noteworthy.

This study examines the feasibility of an off-grid photovoltaic solar energy system in a rural home without an electrical grid. Photovoltaic systems consist of modules, batteries, charge controllers, inverters, and various electronic components. These systems can meet basic electricity needs in rural areas, reduce energy costs, and enable energy production without harming nature.

In off-grid photovoltaic systems, selecting batteries with appropriate capacity and controlling charging and discharging are crucial for energy continuity. Additionally, an inverter is necessary to meet the alternating current requirements of the system. Consequently, photovoltaic systems offer a sustainable, economical, and environmentally friendly solution in rural areas; when properly designed, they reliably meet the energy needs of homes.

Keywords: Solar Energy, Photovoltaics, Off-Grid Systems, Renewable Energy.

#### 1. Introduction

The fact that fossil-based energy sources pose a major risk to the global ecological system, the risk of depletion of these sources in the future, and the increase in transportation costs make it important to find and develop alternative sources for energy production [1-5]. In this regard, renewable energy sources are among the most attractive alternative energy sources due to their infinite nature and the absence of depletion and transportation problems [6]. For this reason, many countries today are making significant investments to develop and widely use this technology [7]. An example of this is the Les Mées solar power station system, shown in Figure 1, which was built on the hills of the Provence region in France.



Figure 1. Solar energy system installed on the hills [8, 9]

In recent years, interest in alternative energy sources (solar and wind energy) has increased in our country, and significant investments have been made [10]. One of these is the Kızören Solar Power Plant located in Konya Karatay, shown in Figure 2. This plant has an installed capacity of 17.82 MW. Our country ranks second after the People's Republic of China in terms of the highest capacity in solar thermal systems [11].



Figure 2. Kızören Solar Power Plant[12]

Within this scope, the government provides support for alternative energy sources and guarantees the purchase of electricity generated from alternative energy types. There are many types of alternative energy sources used in practice, including wind energy, thermal solar energy, photovoltaic solar energy, hydraulic energy, geothermal energy, wave energy, biomass energy, biogas energy, and biodiesel energy. Among these types, wind energy, thermal solar energy, and photovoltaic solar energy are the most commonly used methods, depending on the location.

One of the places where the use of alternative energy sources is undoubtedly mandatory is rural areas. This is because in these areas, where there is no electricity grid, electricity generation using different methods, such as generators, is difficult and not continuous. Therefore, the use of alternative energy sources is inevitable, especially in rural areas where there is no electrical infrastructure. Figure 3 shows a photovoltaic solar energy system applied to a residence. This study examines an off-grid photovoltaic system to meet the electricity needs of a residence in a rural area.



Figure 3. A photovoltaic solar energy system used in a residential building [13]

Solar energy has been a type of energy source used by humankind since ancient times, and there are many sources in the literature related to this. This energy source is used in the simplest sense for purposes such as heating, drying, and obtaining hot water in many areas, while today, with developing technologies, it has also become widespread in areas such as electricity generation with photovoltaic systems [14]. Hydrogen is even produced using electrolysis methods with solar energy [15].

Abdalaziz [16] investigated the efficiency of photovoltaic systems under hot climate conditions. To this end, he numerically examined the efficiency of photovoltaic panels under Kuwaiti conditions using specialized software. As a result, he found that efficiency decreased by 14% at high temperatures, depending on both panel temperature and cell temperature. At low temperatures, he found a 2.11% increase in efficiency based on panel temperature and a 0.79% increase based on cell temperature.

Duyan and Bayrakdarlar [17] evaluated the use of photovoltaic solar panels for buildings as structural elements in architectural design, specifically for parapets, shaded roofs, and facades. This study examined and evaluated photovoltaic panels used on roofs, facades, shades, and outside buildings in terms of shape, size, efficiency, and product variety. They determined that it is possible to use photovoltaic panels in appropriate ways within the framework of sustainable design without compromising aesthetic and stylish appearance.

Rizal [18] simulated the economic analysis of an off-grid solar energy system for residential applications using Homer software. In the study, he determined that there was a decrease in energy consumption per kWh by using methods such as Net Present Cost and Energy Cost methods for the simulation of the Off-Grid system.

Akgül et al. [19] examined an off-grid solar energy system for rural applications. In the study, they focused on the design, modeling, and technical simulation of a small-scale off-grid solar energy system for the province of Şanlıurfa, conducting a cost-benefit analysis and examining energy production, service life, and battery performance. They performed numerical modeling and simulation using Matlab software in their analyses.

#### 2. Photovoltaic Panels

Photovoltaic solar energy systems are systems that convert solar energy into electrical energy. These systems currently hold the most important position among energy sources used as alternatives to fossil fuels. Since these systems are used in modules, they can meet the electricity needs of a small residence as well as large and massive structures. Thus, while several modules can be used together for small homes, they can also be installed in large areas called solar energy farms to meet large energy needs. Figure 4 shows photovoltaic solar panels.



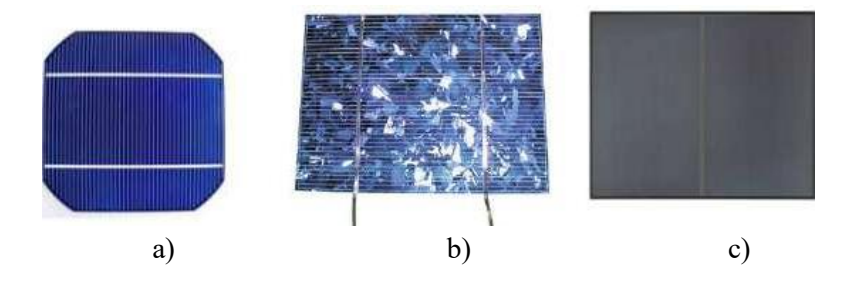
Figure 4. Photovoltaic solar panels [20]

In homes with high electricity demand, photovoltaic solar energy systems can be installed to reduce electricity costs to zero through grid-independent or grid-connected systems. In fact, grid-connected systems can even generate additional income by exporting electricity to the grid. These systems offer significant advantages, particularly in rural areas where there is no electricity grid.

There are many types of photovoltaic solar energy systems depending on the material they are made of, these are [21];

- Single Crystal Solar Panel
- Multi Crystal Solar Panel
- Thin Film (Amorphous) Solar Panel
- Flexible Solar Panel
- Transparent Solar Panel

The efficiency of photovoltaic solar panels varies depending on the panel type, ranging between 15-20% [22], and the panel types are shown in Figure 5.



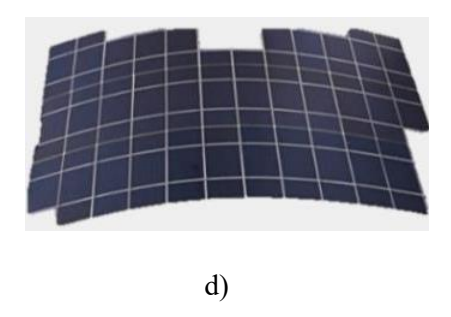


Figure 5. a) Single Crystal, b) Polycrystalline, c) Thin Film (Amorphous) [23], d) Flexible Solar Cell [21]

# 3. Off-Grid Systems

Off-grid photovoltaic solar energy systems are the most ideal systems for providing energy in rural areas with grid connection problems. This study investigates a system to meet the electricity needs of a rural residence. Figure 6 shows the schematic of an off-grid photovoltaic solar energy system. In this research, off-grid system components were selected considering the electricity needs of a residence.

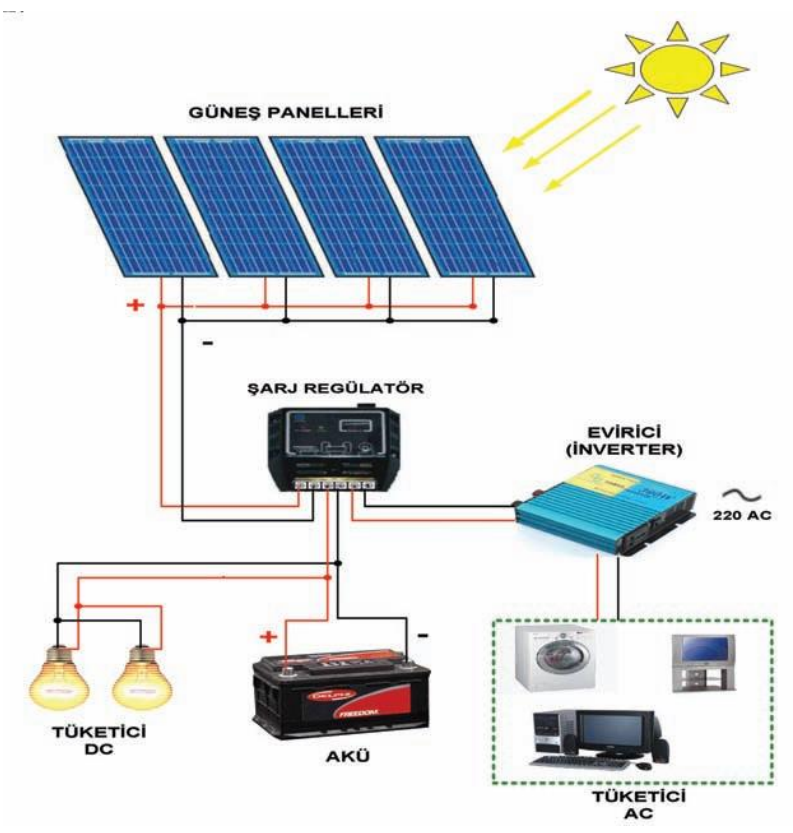


Figure 6. Schematic diagram of an off-grid photovoltaic solar energy system [24]

The application areas of off-grid systems are very broad. These systems can be used in meeting the electricity needs of mountain huts, protecting metal bridges and towers from corrosion, cathodic protection of oil pipelines, electricity and water distribution systems, forest observation towers, and earthquake monitoring stations. In addition, the most common applications of off-grid systems are listed below [25].

- Agricultural irrigation
- Lighthouses
- Communication stations,
- Radio and telephone systems
- Weather observation stations
- Indoor or outdoor lighting

#### 3.1. System Components

The components that make up photovoltaic solar energy systems generally consist of the following units, depending on the application [16],

- Photovoltaic Modules
- Batteries
- Charge Controller
- Inverter
- Battery Charge Monitoring Devices
- Various Electronic Circuits and Construction

#### 3.1.1. Photovoltaic Modules

Photovoltaic modules constitute a significant portion of the cost of a photovoltaic solar energy system. Photovoltaic module prices vary depending on the type of panel. The most commonly used type on the market for commercial purposes is 250 W photovoltaic module panels. A sufficient number of photovoltaic panels must be used in an off-grid photovoltaic solar energy system. A photovoltaic solar energy panel is shown in Figure 4.

# 3.1.2. Battery System

Photovoltaic modules generate electrical energy throughout the day, and the electrical energy produced is stored in batteries. Batteries are used to store electrical energy by converting it into chemical energy. It is essential to have a battery system in place as an ideal solution to meet the electricity needs of the home during cloudy times when there is no sun or when the sun is insufficient. Battery banks may not be necessary in grid-connected systems, but they are essential in off-grid systems.

The most important factor in determining the number and capacity of batteries to be used in the system is the general weather conditions of the region. If the region generally has rainy and cloudy weather, the battery capacity must be selected accordingly. To determine the energy storage load of the system, it is necessary to calculate the number of days and hours when the region will not see sunlight.

# 3.1.3. Charge Controller

Since batteries are mandatory in photovoltaic solar energy systems, the safe use of the battery bank is of great importance. The charge controller is a device that prevents damage to the battery during overcharging and over-discharging,

thereby preventing a decrease in efficiency and a shortening of the operating life. Since batteries are expensive components of the system, they must be charged correctly and safely. Photovoltaic solar energy systems continuously generate electricity when the sun is shining, so the batteries are constantly supplied with energy. To ensure a long battery life, the energy supply must be cut off after charging, which is why the use of a charge regulator is important.

#### 3.1.4. Inverter

Inverters are devices that convert direct current to alternating current. Photovoltaic solar energy systems produce direct current electrical energy. In situations where there are devices operating on alternating current in the home, an inverter is added to the system to convert the direct current from the battery to alternating current. When selecting an inverter, the total power consumption of the devices that will be operating simultaneously in the home where the system will be used should be taken into account.

#### 3.1.5. Various Electronic Circuits and Construction

In addition to the elements mentioned above, other elements that must be used in the system are cables and fuses. In order to safely transmit the electrical energy produced by solar panels, cables of the appropriate size for the system's power must be selected. Furthermore, fuses with appropriate capacity must be used to prevent the system from encountering situations such as short circuits and overload. In some cases, other electronic systems can also be used optionally in the system to instantly monitor the charge status of the batteries and to monitor the energy produced by the solar panels.

Since photovoltaic solar energy panels are systems installed outside the home, the panels must be secured. Photovoltaic solar panels are usually mounted on the roofs of homes, but when roofs are not suitable for mounting photovoltaic solar energy panels, they can also be mounted in the garden. To prevent solar panels from being affected by outdoor conditions (wind, storms, snow, rain, etc.), they must be secured with a sturdy metal construction that is resistant to corrosion.

#### 4. Conclusion

This study examines an off-grid photovoltaic solar energy system designed to meet the electricity needs of a residential building located in a rural area without grid connection. The system's main components; photovoltaic panels, batteries, charge controller, inverter, and other electronic equipment were analyzed, and the function, importance within the system, and selection criteria for each component were discussed.

Photovoltaic systems offer a sustainable and economical solution, especially in rural areas where the electricity grid infrastructure is inadequate. In this context, it is critically important for the continuity of energy that the system is designed with a sufficient number of panels and a battery bank of appropriate capacity to meet the basic electricity needs of the residence. Furthermore, it was found that for the system to operate efficiently and have a long service life, a charge regulator that ensures a safe charge-discharge cycle for the batteries and an inverter with appropriate capacity must be integrated into the system.

In conclusion, when planned with the right engineering approach, the offgrid system proposed in this study has the potential to reliably meet the daily energy needs of a rural residence. This system contributes to reducing fossil fuel consumption, frees users from energy costs, and enables energy production without harming nature.

#### References

- 1. Omar, M.A., *Investigation Of Burners Used In Wall-Hung Combi-Boilers:* A Comparative And Cfd Study. Environmental Engineering & Management Journal (Eemj), 2022. **21**(12).
- 2. Terhan, M., E. Özağdaş, and M.A. Omar, Energy and economic assessments of waste heat recovery by designs of economizer, condensing economizer and air preheater. Journal of the Faculty of Engineering and Architecture of Gazi University, 2023. **38**(4): p. 2521-2536.
- 3. Othan, O. and M.A. Omar, *Thermo-economic study of two different combined heat-power system for a hospital*. Journal of the Faculty of Engineering and Architecture of Gazi University, 2023. **38**(3): p. 1467-1480.
- 4. Omar, M.A., Comparison of central and individual heating systems used for heating housings. Türk Doğa ve Fen Dergisi, 2023. **12**(2): p. 8-16.
- 5. Omar, M.A., et al., Economic analysis of required heat energy for a residence by using condensing and conventional combi boiler. Mugla Journal of Science and Technology, 2016. **2**(1): p. 38-42.
- 6. Omar, M.A. and G. Saltan, *A Techno-Economic Analysis On The Selection Of Wind Turbines*. Environmental Engineering & Management Journal (Eemj), 2024. **23**(9).
- 7. Özşimşek, A.O. and M.A. Omar, A numerical study on the effect of employing porous medium on thermal performance of a PV/T system. Renewable Energy, 2024. **226**: p. 120327.

- 8. Ozdamar, Y., *Güneş Enerjisi Çiftlikleri: Dünyanın En Başarılı Tasarımları.* www.teknoloji.org, 2021.
- 9. Uslu, M.E., Energy Poverty In The World And Challenges And Opportunities Of The Solar Pv Technology. İim ve Medeniyet https://www.ilimvemedeniyet.com/energy-poverty-in-the-world-and-challenges-and-opportunities-of-the-solar-pv-technology, 2018.
- 10. Hamdemir, V. and M.A. Omar, *Güneş Kollektörlerinde Elips Kesitli Boru Kullanımının İncelenmesi*. Karadeniz Fen Bilimleri Dergisi, 2024. **14**(1): p. 1-13.
- 11. Sarıkaya, S., *Güneş Enerjisi Sektör Raporu*. Doğu Anadolu Kalkınma Ajansı.
- 12. URL, *Konya Kızören GES Projesi*. Tarım Kütüphanem https://tarimkutuphanem.wordpress.com/2018/05/24/konya-kizoren-gesprojesi/.
- 13. Kıncay, O., Güneş enerji.
- 14. Omar, M., Providing The Energy Required For The Heating Of Hospitals By The Solar Energy (Hastanelerin Isitilması İçin Gereken Enerjinin Güneş Enerjisi İle Karşılanması). 2019.
- 15. Omar, M.A. and K. Altinişik, Simulation of hydrogen production system with hybrid solar collector. International Journal of Hydrogen Energy, 2016. **41**(30): p. 12836-12841.
- 16. Shehada, A.Z.H., *Numerical Analysis Of Photovoltaic Panel Efficiency In The Arid Climate Of Kuwait.* Master's Thesis, Altinbaş University Institute of Graduate Studies Mechanical Engineering, 2025.
- 17. Duyan, F. and K.P. Bayrakdarlar, *Enerji Etkin Bina Tasarımında Yapı Elemanı olarak Fotovoltaik Sistemler*. Mimarlık ve Yaşam, 2022. 7(3): p. 965-980.
- 18. Rizal, R.F., Economic analysis of off-grid simulation of PV array installation for 900 VA home scale based on homer software. Jurnal Sistem Telekomunikasi Elektronika Sistem Kontrol Power Sistem dan Komputer, 2023. **3**(1): p. 33-40.
- 19. Akgül, B.A., et al., *Kırsal alanlarda elektrik temini için şebekeden bağımsız mobilite güneş enerjisi üretimi analizi: Şanlıurfa Türkiye'de bir uygulama çalışması.* Pamukkale Üniversitesi Mühendislik Bilimleri Dergisi. **29**(5): p. 458-467.
- 20. URL, Güneş Paneli. https://www.atonenerji.com/gunes-paneli/.
- 21. Benli, F., *Fotovoltaik (PV) ve Fotovoltaik Termal (PV-T) kolektörlerinin deneysel olarak karşılaştırılması.* 2018, Yüksek Lisans Tezi, Osmaniye Korkut Ata Üniversitesi Fen Bilimleri Enstitüsü ....
- 22. URL, Güneş Enerjisi Elektrik Üretim Sisteminin Tasarlanması ve Maliyet Hesabı. https://enerji-danismanlik.blogspot.com/2015/09/gunes-enerjisi-elektrik-uretim.html, 2025.

- 23. Ghann, W., et al., Fabrication, optimization and characterization of natural dye sensitized solar cell. Scientific reports, 2017. 7(1): p. 41470.
- 24. Tahsin Köroğlu, A.T., K Çağatay Bayındır, Mehmet Tümay, *Güneş Paneli Sistemlerinin Tasarımı*. Elektrik Mühendisliği, 2010. **439**.
- 25. Güneş Enerjisi ve Teknolojileri. Yenilenebilir Enerji Genel Müdürlüğü.

# **Geopolymer Concrete For Sustainable Infrastructure: A Chemical Review**

 $\ddot{O}mer\;LA \dot{C}\dot{I}N^{1*}$ 

Fatih DEMİR<sup>2</sup>

Fatih SEVİM<sup>3</sup>

<sup>1- \*</sup>Corresponding Author, Prof. Dr.; Atatürk University Eng. Fac. Chem. Eng. Dep. olacin@atauni.edu.tr ORCID No: 0000-0002-5276-3056

Prof. Dr.; Atatürk University Eng. Fac. Chem. Eng. Dep. fatihdemir@atauni.edu.tr ORCID No: 0000-0002-0264-1074

<sup>3-</sup> Prof. Dr.; Atatürk University Eng. Fac. Chem. Eng. Dep. fsevim@atauni.edu.tr ORCID No: 0000-0002-0805-8499

#### **ABSTRACT**

The urgent need to reduce carbon emissions and improve the sustainability of construction materials has driven increasing interest in geopolymer concrete as a viable alternative to Ordinary Portland Cement (OPC). Responsible for nearly 8% of global CO<sub>2</sub> emissions, OPC production has motivated the search for low-carbon binders since the 1970s. Geopolymer concrete, first introduced by Joseph Davidovits in 1978, is an inorganic polymer binder system produced by the alkali activation of aluminosilicate sources such as fly ash, metakaolin, blast furnace slag, and volcanic tuff. Through the polycondensation of dissolved silicate and aluminate species in highly alkaline environments, a three-dimensional sodium or calcium aluminosilicate hydrate (N-A-S-H or C-A-S-H) network is formed, resulting in a dense, durable matrix with superior mechanical and chemical performance.

This chapter provides a detailed chemical review of geopolymer concrete, covering its raw materials, reaction mechanisms, and curing geopolymerization process-comprising dissolution. processes. The activation, condensation, and structure formation elucidated through balanced reaction equations and structural schematics. The influence of curing temperature and duration on gel formation and strength development is also discussed. Moreover, the role of chemical admixtures such as superplasticizers (notably polycarboxylate ethers), nano-additives (e.g., SiO<sub>2</sub>, TiO<sub>2</sub>, graphene oxide), fibers, and shrinkage reducers is evaluated in enhancing rheology, durability, and microstructure. Ultimately, geopolymer concrete offers a sustainable, high-performance alternative that reduces CO2 emissions and utilizes industrial by-products, making it a cornerstone material for next-generation green infrastructure.

Keywords – Geopolymerization; Alkali-activated materials; Sustainable binders; Reaction mechanism; Supplementary cementitious materials

#### INTRODUCTION

In today's construction industry, concepts such as sustainability, energy efficiency, high mechanical strength, chemical resistance, fire resistance, and reducing carbon footprint are encountered quite frequently.

In the 1970s, it was stated that this amount needed to be reduced because the traditional Portland cement (OPC) industry caused annual CO<sub>2</sub> emissions of approximately 3 billion tons worldwide (about 8% of total CO<sub>2</sub> emissions).

In this context, inorganic polymer-based geopolymer concrete was developed for the first time in 1978 by French chemist Joseph Davidovits, both as an alternative to Portland cement and for the purpose of evaluating industrial wastes.

Initially produced for low carbon emissions, this concrete has evolved over time into a building material with high strength, superior chemical resistance, improved thermal stability, and environmentally friendly properties through the application of different design recipes [1-3].

With the decrease in the cement clinker ratio, CO<sub>2</sub> emissions and water/cement ratios decreased by 60–80%, and less porous and more durable concretes were produced. Additionally, the evaluation of industrial byproducts with pozzolanic properties, which it contains, has provided significant advantages both environmentally and economically; despite the high initial investment cost, its low long-term cost has made this material extremely valuable [4–5].

# 1. Geopolymer Concrete

Geopolymer concrete production relies entirely on alternative binder systems, unlike traditional Portland cement. The materials used in this system are designed in different combinations to reduce environmental impact, increase durability, and obtain long-lasting building materials [6]. The basic components of the geopolymer system are: aluminosilicate sources, alkali activators, water, special additives, and aggregates. [7].

# a) Sources of Alumina Silicate

These materials contain high levels of  $SiO_2$  and  $Al_2O_3$  and are the main components of geopolymerization. The main sources are given in Table 1, and it is generally obtained from industrial waste, making their evaluation environmentally friendly.

Table 1: Major Sources of Aluminosilicate

Material	Properties	
Fly Ash (Class F)	Low calcium, high glass phase, fine particle structure, economical and abundant.	
Blast Furnace Slag (GGBFS)	High calcium content, effective for early resistance.	
Metakaolin	Pure and reactive, it provides high performance based on the laboratory.	

Volcanic Tuff / Zeolite Naturally sourced, sustainable in terms of environmental impact.

The most commonly used aluminosilicate sources are combinations of fly ash and blast furnace slag; these materials offer advantages in terms of workability and strength balance.

#### b) Alkaline Activators

These are the basic components that initiate the geopolymer reaction. By providing a high pH, they enable the dissolution of aluminosilicates and the formation of a three-dimensional network structure. Commonly used activators are listed in Table 2.

Table 2. Commonly Used Activators

Activator	Function
NaOH (Sodium Hydroxide)	Provides solubility, increases reactivity.
Na <sub>2</sub> SiO <sub>3</sub> (Sodium Silicate)	It offers a source of silicates for the polymer chain.
KOH (Potassium Hydroxide)	Alternative base medium, but more expensive.
Na <sub>2</sub> CO <sub>3</sub> / NaAlO <sub>2</sub>	It is used in alternating systems for slow reactions.

# c) Special Additives

Chemical admixtures are used to improve the properties of concrete during the mixing, placing, and curing stages. To improve the rheological properties of GPC and optimize the mix design, many studies are being conducted and continue to be conducted by adding different chemical admixtures to the mix. These contributions affect the workability, setting time, strength development, durability, and other performance aspects of concrete. Some commonly used special additives are listed as follows [8-9]:

# Superplasticizers

Superplasticizers are used to reduce viscosity, thereby increasing the workability, strength, and durability of GPC, and also to reduce water content. Commonly used superplasticizers include polycarboxylates, polycarboxylate ether (PCE), naphthalene, lignosulfonates, melamine, sulfonated melamine formaldehyde (SMF), and sulfonated naphthalene formaldehyde (SNF). When choosing a superplasticizer, it is necessary to pay attention to criteria such as compatibility with alkaline environments, solubility, and reactive surface interaction. Although it is stated that the selection and dosage of superplasticizers depend on the specific concrete mix design and compatibility with environmental conditions, it is mentioned that PCE is the most compatible. PCE superplasticizers contribute to improved workability and durability by reducing the amount of water needed to produce a liquid mixture, and thus permeability. It has been stated that slump values up to 25 cm can be achieved with the addition of PCE [10-14]. With the use of superplasticizers, high-strength concrete, self-compacting concrete, precast concrete, and ready-mix concrete in the construction industry have achieved good workability and high strength [15-20]. This improved workability allows for better dispersion of the geopolymers and aggregates, resulting in improved interfacial adhesion and increased strength. Additionally, denser and less permeable concrete is obtained due to the reduced water content, which increases durability by reducing porosity and permeability [21].

#### • Nano Admixtures

It strengthens the microstructure by accelerating gel formation, increases density and strength by tightening the pore structure, and prevents cracks (eg., SiO<sub>2</sub>, TiO<sub>2</sub>, GO (graphene oxide)).

#### • Fiber Admixtures

Geopolymer concretes can exhibit a brittle structure. Therefore, ductility, impact resistance, and crack control can be achieved with fiber additives such as steel, basalt, and propylene. They provide up to a 30% increase in flexural strength.

- Setting Retarders or Accelerators (for Compliance with Curing Conditions)
  - Sodium Citrate / Sodium Tartrate: Extends the setting time in alkaline systems in a controlled manner.
  - O Calcium Formate (as a setting accelerator): Accelerates gelation and setting. It shows synergy with Ca(OH)<sub>2</sub>.
- Crack Remover / Shrinkage Reducing Additive
  - Polyethylene glycol (PEG-400 / PEG-600): It has a waterretaining effect, reduces internal stress.
  - o Hydrophobic additives (e.g., silicone emulsion): Limits microcrack formation by reducing surface water absorption.
  - Swelling clay minerals (extra bentonite, vermiculite):
     Provides shrinkage compensation.
  - Sodium borate (Borax): Improves ductility and controls microcracking.
  - o Polyvinyl alcohol (PVA): It is a capillary crack control and adhesion enhancer.

# d) Aggregates

Similar to conventional concrete, sand and crushed stone are directly used as aggregates. However, a high proportion of fine aggregates is preferable for workability, and reactive aggregates should be avoided. Geopolymer concrete is obtained by mixing these elements gradually and molding and curing the gel obtained as a result of the chemical reaction that occurs during this process.

# 2. Geopolymer Chemistry and Curing

# 2.1. Polycondensation (Polymerization) Reaction in Geopolymer Concrete Production

This process is completely different from traditional cement hydration and is based on polycondensation reactions at the molecular level. Geopolymer concrete is an inorganic polymeric binder system with an amorphous or partially crystalline structure, formed as a result of the exothermic reaction of alumina silicates containing high levels of silica (SiO<sub>2</sub>) and alumina (Al<sub>2</sub>O<sub>3</sub>) with strong alkaline activator solutions [22-25].

The three-dimensional chain structures formed as a result of these reactions, although similar to traditional cement concretes, provide far superior performance [26-28].

The reaction process takes place in four main stages: dissolution, activation, condensation, and structure formation, which are explained below. The production process ends with curing [5,29-30].

## a) Dissolution

Amorphous/reactive alumina silicates in the solid phase dissolve in a highly alkaline environment (pH > 13.5, high OH<sup>-</sup> excess) to form the species in Equation 1:

$$Al_2O_3 \cdot SiO_2(s) + 2OH^- + 5H_2O \rightarrow 2Al(OH)_4^- + Si(OH)_4$$
 (1)

Here, Si(OH)<sub>4</sub> (monomeric silicic acid) and Al(OH)<sub>4</sub><sup>-</sup> (aluminate anion) are formed by OH<sup>-</sup> ions breaking the Si–O–Si and Si–O–Al bonds (pH decreases as OH<sup>-</sup> begins to deplete as Si/Al dissolves).

## b) Activation

Each Al(OH)<sub>4</sub><sup>-</sup> ion binds to the structure with four oxygens to be tetrahedral, and each Al ion maintains charge balance with an alkaline cation (Na<sup>+</sup> or K<sup>+</sup>) ion. Si(OH)<sub>4</sub> is neutral, and in an environment of sufficient [OH<sup>-</sup>] and temperature, these species approach each other, becoming ready for polycondensation.

#### c) Condensation

At this stage, the condensation reactions of the monomeric silicic acid and aluminum hydroxide (Al(OH)<sub>4</sub><sup>-</sup>) complex in, Eq. 2-4 take place (pH decreases rapidly to 10-11 as OH<sup>-</sup> is rapidly depleted). As the steps here are repeated, low molecular weight oligomers are formed, followed by a geopolymer gel with a cross-linked 3D network structure. The pores inside the gel trap water and ions.

$$2Si(OH)_4 \rightarrow (OH)_3Si-O-Si(OH)_3 + H_2O$$
 (2)

$$Si(OH)_4 + Al(OH)_4 \rightarrow (OH)_3Si-O-Al(OH)_3 + H_2O$$
 (3)

$$Al(OH)_4^- + Si(OH)_4 \rightarrow (OH)_3Si-O-Al(OH)_3^- + H_2O$$
 (4)

The reaction in Eq. 2 is a polycondensation reaction of silicates, a process in which two monomeric silicic acid molecules form a dimeric siloxane (Si–O–Si) bond (the backbone of the network structure), releasing

water. The reactions in equations 3 and 4 are processes in which a complex of a monomeric silicic acid molecule and an aluminum hydroxide (Al(OH)<sub>4</sub>) form a Si–O–Al bridge (which provides the charge balance of the network) and release water, which usually determines the reaction step. From the sum of these three condensation reactions, Equation 5 is obtained, in which 3 moles of water are released.

$$4Si(OH)_4+2Al(OH)_4\xrightarrow{-}(OH)_3Si-O-Si(OH)_3+2(OH)_3Si-O-Al(OH)_3\xrightarrow{-}$$

$$3H_2O$$
(5)

#### d) Structure Formation

At this stage, as a result of polycondensation (polymerization) formed by the repetition of the steps, the geopolymer gel is formed, the general reaction of which is given in Eq. 6. The gel hardens over time to form a glass-like, durable structure, and as in Figure 1, Na<sup>+</sup> and/or K<sup>+</sup> ions settle in the cavities to balance the negative charges of the structure, forming sodium alumina silicate hydrate (N-A-S-H) and/or calcium alumina silicate hydrate (C-A-S-H) gels if calcium is present in the environment.

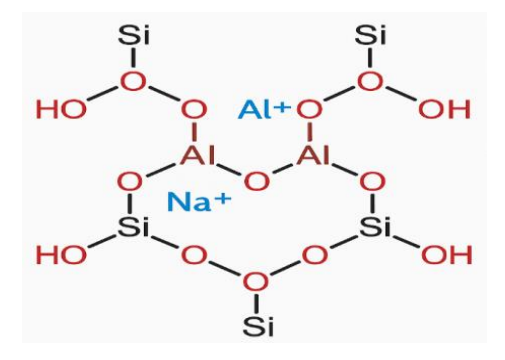


Figure 1. Neutral Geopolymer Gel Structure

These stages can be summarized with the verbal diagram as follows and schematized with Figure 2:

Geopolymer gel general reaction,

$$4nSi(OH)_4+2nAl(OH)_4^-+nNa^+ \rightarrow nNa(OH)_3Si-O-Si(OH)_3+2n(OH)_3Si-O-Al(OH)_3^-+3nH_2O$$
 (6)

# Verbal Diagram

- Alumina silicate
  - ↓ Soluble with OH-
- → Si(OH)<sub>4</sub>, Al(OH)<sub>4</sub> species \ Condenses
- → Oligomers: Si–O–Si, Si–O–Al 3D construction
- $\rightarrow$  Hardened geopolymer gel + embedded Na<sup>+</sup>/K<sup>+</sup> + water outlet

#### Schematization of the stages

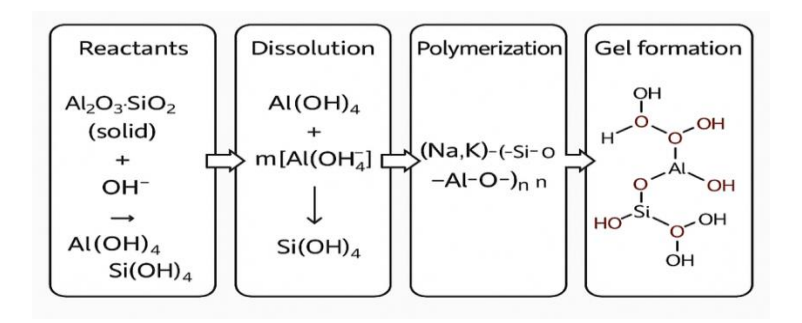


Figure 2. Schematic Form

The activation of high-calcium aluminosilicates (e.g., slag) produces calcium aluminosilicate hydrate (C-A-S-H) gels, while the activation of low-calcium aluminosilicates (eg., fly ash) produces sodium aluminosilicate hydrate (N-A-S-H) gels, and calcium-sodium aluminosilicate hydrate (N, C-A-S-H) gels are formed by the combination of the two [20]. The microstructure obtained by curing these binder phases binds the aggregates and other unreacted components of the concrete together to form geopolymer concrete (GPC) (Figure 3).

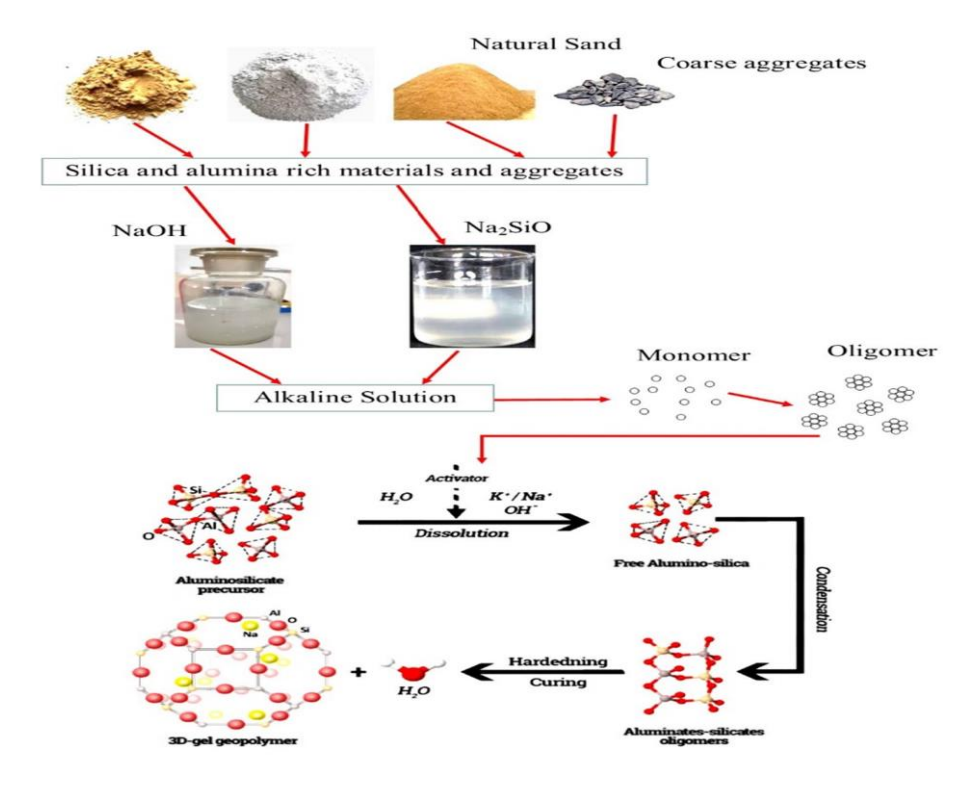


Figure 3. Geopolymer Concrete Production Process [31].

# 2.2. Curing

Since polycondensation reactions, not hydration, dominate the strength development and microstructure formation of geopolymer concrete during production, the curing conditions applied are also the most important external factor affecting the geopolymerization kinetics. Curing process: By preventing water evaporation, it aims to complete gelation, prevent crack formation, and optimize strength development. Curing temperature and duration play a critical role in the early age and final strength development of geopolymer concrete. Commonly used curing methods are heat curing, ambient curing, and steam curing [6,7,32]. These cures are briefly summarized as follows:

#### Thermal Cure

• Temperature: 40–90 °C (usually 60–75 °C)

• Duration: 6–24 hours

• Advantage: Rapid strength development

Use: In fly ash-based systems

Thermal curing accelerates the process of dissolution and formation of polymer chains, increasing early-age strength. Therefore, it is frequently used in the production of prefabricated elements.

# Curing at Ambient Temperature

- Temperature: 20–30 °C
- Advantage: Economical, sustainable
- Disadvantage: Slow strength development
- Use: In slag-based or hybrid systems (fly ash + slag)

New generation geopolymer mixtures (high calcium systems) can gain strength with this method.

#### Steam Cure

- High temperature and humid environment
- Applied in precast elements
- Accelerates strength increase

#### References

- [1] Rafi, M. M., Nadjai, A., Ali, F., & Talamona, D. (2008). Aspects of behaviour of CFRP reinforced concrete beams in bending. Construction and Building Materials, 22(3), 277-285. https://doi.org/10.1016/j.conbuildmat.2006.08.014
- [2] Naik, T. R. (2008). Sustainability of concrete construction. Practice Periodical on Structural Design and Construction, 13(2), 98–103. https://doi.org/10.1061/(ASCE)1084-0680(2008)13:2(98)
- [3] Shi, C., Meyer, C., & Behnood, A. (2008). Utilization of copper slag in cement and concrete. Resources, Conservation and Recycling, 52(10), 1115–1120. https://doi.org/10.1016/j.resconrec.2007.11.003
- [4] Van Deventer, J. S. J., Provis, J. L., & Duxson, P. (2012). Technical and commercial progress in the adoption of geopolymer cement. Minerals Engineering, 29, 89–104. <a href="https://doi.org/10.1016/j.mineng.2011.09.009">https://doi.org/10.1016/j.mineng.2011.09.009</a>
- [5] Davidovits, J. (2013). Geopolymer chemistry and applications (4th ed.). Saint-Quentin: Institut Géopolymère.
- [6] Provis, J. L., & van Deventer, J. S. J. (Eds.). (2014). Alkali activated materials: State-of-the-art report, RILEM TC 224-AAM. Vol(13). Springer. https://doi.org/10.1007/978-94-007-7672-2.
- [7] Temuujin, J., Minjigmaa, A., Lee, M., Chen-Tan, N., & Van Riessen, A. (2011). Characterisation of class F fly ash geopolymer pastes immersed in acid and alkaline solutions. Cement and concrete composites, *33*(10), 1086-1091.
- [8] de Hita, M. J., & Criado, M. (2023). Influence of superplasticizers on the workability and mechanical development of binary and ternary blended cement and alkali-activated cement. Construction and Building Materials, 366, 130272.

- [9] Bakharev, T., Sanjayan, J. G., & Cheng, Y. B. (2000). Effect of admixtures on properties of alkali-activated slag concrete. Cement and Concrete Research, 30(9), 1367–1374. https://doi.org/10.1016/S0008-8846(00)00349-5
- [10] Paul, E. (2022). Influence of superplasticizer on workability and strength of ambient cured alkali activated mortar. Cleaner Materials, 6, 100152. https://doi.org/10.1016/j.clema.2022.100152
- [11] Lloyd, N. A., & Rangan, B. V. (2010, June). Geopolymer concrete with fly ash. In Second international conference on sustainable construction materials and technologies (Vol. 3, pp. 1493-1504). Sustainable Construction Materials and Technologies, Coventry, England.
- [12] Kandagaddala, R. K., Dhanapal, S. V., & Nanthagopalan, P. (2023). Rheological characterization of limestone calcined clay cement pastes with various generations of superplasticizers for pumping applications. Journal of Building Engineering, 76, 107410. <a href="https://doi.org/10.1016/j.jobe.2023.107410">https://doi.org/10.1016/j.jobe.2023.107410</a>
- [13] Sha, S., Mantellato, S., Weckwerth, S. A., Zhang, Z., Shi, C., & Flatt, R. J. (2023). Do superplasticizers work the way we think? New insights from their effect on the percolation threshold of limestone pastes. Cement and Concrete Research, 172, 107235. https://doi.org/10.1016/j.cemconres.2023.107235
- [14] Vora, P. R., & Dave, U. V. (2013). Parametric studies on compressive strength of geopolymer concrete. Procedia Engineering, 51, 210–219. https://doi.org/10.1016/j.proeng.2013.01.030
- [15] Sherwani, A. F. H., Younis, K. H., Arndt, R. W., & Pilakoutas, K. (2022). Performance of self-compacted geopolymer concrete containing fly ash and slag as binders. Sustainability, *14*(22), 15063.
- [16] Rajendran, R., Kumar, D. S., Megan, K., Muneswaren, P., Senthilvel, D., Shri, B., et al. (2021). Strength analysis of geopolymer concrete based on fly ash and P-sand. Materials Today: Proceedings, 47, 5489–5492.
- [17] Almutairi, A. L., Tayeh, B. A., Adesina, A., Isleem, H. F., & Zeyad, A. M. (2021). Potential applications of geopolymer concrete in construction: A review. Case Studies in Construction Materials, 15, e00733. https://doi.org/10.1016/j.cscm.2021.e00733
- [18] Mahmood, A. H., Foster, S. J., & Castel, A. (2021). Effects of mixing duration on engineering properties of geopolymer concrete. Construction and Building Materials, 303, 124449. https://doi.org/10.1016/j.conbuildmat.2021.124449
- [19] Negahban, E., Bagheri, A., & Sanjayan, J. (2023). Pore structure profile of ambient temperature-cured geopolymer concrete and its effect on engineering properties. Construction and Building Materials, 406, 133311. https://doi.org/10.1016/j.conbuildmat.2023.133311
- [20] Kugler, F., Karrer, J., Krcmar, W., & Teipel, U. (2022). Setting behavior and mechanical properties of concrete rubble fly ash geopolymers. Open Ceramics, 11, 100286. https://doi.org/10.1016/j.oceram.2022.100286
- [21] Triwulan, M., Wigestika, P., & Ekaputri, J. J. (2016). Addition of superplasticizer on geopolymer concrete. ARPN Journal of Engineering and Applied Sciences, 11(24), 14456–14462.
- [22] Alharbi, Y. R., Abadel, A. A., Salah, A. A., Mayhoub, O. A., & Kohail, M. (2021). Engineering properties of alkali activated materials reactive powder concrete. Construction and Building Materials, 271, 121550. <a href="https://doi.org/10.1016/j.conbuildmat.2020.121550">https://doi.org/10.1016/j.conbuildmat.2020.121550</a>

- [23] Bajgain, S. K., & Mookherjee, M. (2021). Carbon bearing aluminosilicate melt at high pressure. Geochimica et Cosmochimica Acta, 312, 106–123.
- [24] Abdullah, M. N. I., Mustapha, F., Ahmad, K. A., Mustapha, M., Khan, T., Singh, B., et al. (2022). Effect of different pre-treatment on the microstructure and intumescent properties of rice husk ash-based geopolymer hybrid coating. Polymers, 14(11), 2252. https://doi.org/10.3390/polym14112252
- [25] Çelik, A. İ., Tunç, U., Bahrami, A., Karalar, M., Mydin, M. A. O., Alomayri, T., & Özkılıç, Y. O. (2023). Use of waste glass powder toward more sustainable geopolymer concrete. Journal of materials research and technology, 24, 8533-8546.
- [26] Nath, P., Sarker, P. K., & Rangan, V. B. (2015). Early age properties of low-calcium fly ash geopolymer concrete suitable for ambient curing. Procedia Engineering, 125, 601–607.
- [27] Chand, G. (2021). Microstructural study of sustainable cements produced from industrial by-products, natural minerals and agricultural wastes: A critical review on engineering properties. Cleaner Engineering and Technology, 4, 100224. https://doi.org/10.1016/j.clet.2021.100224
- [28] Kishore, K., Pandey, A., Wagri, N. K., Saxena, A., Patel, J., & Al-Fakih, A. (2023). Technological challenges in nanoparticle-modified geopolymer concrete: A comprehensive review on nanomaterial dispersion, characterization techniques and its mechanical properties. Case Studies in Construction Materials, 19, e02265. https://doi.org/10.1016/j.cscm.2023.e02265
- [29] Duxson, P., Fernández-Jiménez, A., Provis, J. L., Lukey, G. C., Palomo, A., & van Deventer, J. S. J. (2007). Geopolymer technology: The current state of the art. Journal of Materials Science, 42(9), 2917–2933. <a href="https://doi.org/10.1007/s10853-006-0637-z">https://doi.org/10.1007/s10853-006-0637-z</a>
- [30] Provis, J. L., & van Deventer, J. S. J. (2009). Geopolymers: Structures, processing, properties and industrial applications. Elsevier.
- [31] Mabroum, S., Moukannaa, S., El Machi, A., Taha, Y., Benzaazoua, M., & Hakkou, R. (2020). Mine wastes based geopolymers: A critical review. Cleaner Engineering and Technology, 1, 100014. https://doi.org/10.1016/j.clet.2020.100014
- [32] Duxson, P., Lukey, G. C., & van Deventer, J. S. (2006). Thermal evolution of metakaolin geopolymers: Part 1–Physical evolution. *Journal of Non-Crystalline Solids*, 352(52-54), 5541-5555.

# Geopolymer Concrete for Sustainable Infrastructure: Functional Role of Components and Optimum Design Parameters

Ömer LAÇİN<sup>1\*</sup>

Fatih DEMİR<sup>2</sup>

Fatih SEVİM<sup>3</sup>

<sup>1- \*</sup>Corresponding Author, Prof. Dr.; Atatürk University Eng. Fac. Chem. Eng. Dep. olacin@atauni.edu.tr ORCID No: 0000-0002-5276-3056

<sup>2-</sup> Prof. Dr.; Atatürk University Eng. Fac. Chem. Eng. Dep. fatihdemir@atauni.edu.tr ORCID No: 0000-0002-0264-1074

<sup>3-</sup> Prof. Dr.; Atatürk University Eng. Fac. Chem. Eng. Dep. fsevim@atauni.edu.tr ORCID No: 0000-0002-0805-8499

#### **ABSTRACT**

Geopolymer concrete (GPC) has emerged as a next-generation sustainable construction material that can significantly reduce the environmental impact associated with Ordinary Portland Cement (OPC). This chapter presents a comprehensive review and design-based evaluation of geopolymer concrete systems, highlighting the functional role of each component and optimizing key parameters for enhanced performance. Aluminosilicate sources (e.g., metakaolin, fly ash, volcanic tuff) react with alkali activators such as NaOH and Na<sub>2</sub>SiO<sub>3</sub> through dissolution and polycondensation, forming N-A-S-H and C-A-S-H gels that constitute a dense, durable binder matrix. The integration of nano-silica, graphene oxide, and fibers (steel, basalt) further enhances microstructural compactness, ductility, and resistance to cracking. Polycarboxylate ethers improve workability under high alkalinity, while polyethylene glycol ensures moisture stability during curing.

Optimal design parameters such as Si/Al (2-4), SiO<sub>2</sub>/Na<sup>+</sup> (2.0-2.5), solid/activator (2.0-2.5), and W/B (0.3-0.35) are identified to balance workability, polymerization efficiency, and mechanical strength. Thermal curing at  $60 \pm 2$  °C for 24-48 h accelerates gel transformation and yields >90% of final strength. Experimental findings and literature data indicate that GPC exhibits superior resistance to sulfate and acid attack, chloride ion penetration, high temperatures (≤ 800 °C), and freeze-thaw cycles, with minimal strength loss compared to OPC. Furthermore, boron-modified formulations demonstrate potential as radiation and heavy metal barriers. Although the initial material cost of GPC is higher, its lower lifetime maintenance and replacement frequency render it economically advantageous. Overall, multi-component geopolymer concretes represent a technically and environmentally sustainable alternative for long-lasting infrastructure, marine, and high-temperature applications.

Keywords — Geopolymerization; Alkali-activated materials; Sustainable binders; Reaction mechanism; Supplementary cementitious materials

#### INTRODUCTION

When reviewing the literature on geopolymer concrete (GPC) production, most studies focus on: the type, content, and quantity of mixture components used; the compatibility of additives; setting time; sulfate and acid resistance; chloride ion permeability; high temperature resistance, volume change and cracking behavior, workability, the occupational health and safety risks of alkali solutions, carbonation and efflorescence due to

ambient humidity and CO<sub>2</sub> effects and its reduction of the compressive strength of concrete, the disadvantages caused by the inappropriate selection of thermal curing methods and the lack of standards. Due to the variety of usage areas of GPC and the different effects of each parameter, the design recipes of the concrete to be produced also differ. Therefore, every current and future study in the literature is of great importance for the development of geopolymer concrete [1,2].

# 1. Geopolymer Concrete Design Example

A summary design recipe example about the components to be used in GPC production and their functions is presented in Table 1.

Table 1. Design Prescription Example				
Material	Function			
	It improves mechanical strength, gelling speed, and microstructure quality			
Alumina	by dissolving Al and Si components. The small pore structure improves			
silicate	impermeability and ensures good bonding. It imparts high chlorine/sulfate			
	resistance, viscosity, and thermal stability.			
	It accelerates dissolution, increases early-age mechanical strength by			
NaOH	forming Na-A-S-H gel. It provides pH stability, has a low carbon			
	footprint, strengthens polycondensation with its reactivity, improves			
	processability, and controls setting time. Reduces porosity and prevents			
	cracking, contributes to increased chlorine/sulfate resistance, and can			
	achieve low temperature curing.			
	It enables rapid construction of the Si-O-Al network, accelerates nucleation, and improves microstructure by increasing density. However,			
Nano silicate	adding a large amount increases viscosity, and adding a small amount			
	reduces the reaction rate and reduces early age. strength.			
Steel fiber	Increases tensile strength and ductility, limits the formation of			
Steel Hoel	microcracks.			
Basalt fiber	It increases thermal and impact resistance, limits microcrack formation,			
	and contributes to increasing chlorine/sulfate resistance.			
Graphene oxide	It improves thermal strength, limits the formation of microcracks, and			
Graphene oxide	strengthens the microstructure.			
Polyethylene	It reduces water loss, stabilizes curing moisture, delays setting time, and			
glycol	prolongs workability.			
Water	Regulates the water/solid ratio (approximate ratio 0.28)			
Polycarboxylate ether	Superplasticizer, anti-slump, increase workability, reduce water			
	requirement. It should be added last so that it does not deteriorate in an			
C 1 :	alkaline environment.			
Gel conversion	The mixture obtained from the design is cured in accordance with the			

rate and heat desired gel transformation rate.

# 2. Geopolymer Concrete Production stages according to the design example

The reaction mechanism between alumina silicate source, sodium hydroxide (NaOH), and sodium silicate (Na<sub>2</sub>SiO<sub>3</sub>) solution involves a complex process of ionic dissolution and polycondensation through alkaline activation, resulting in the formation of C-A-S-H gels in the presence of N-A-S-H and Ca<sup>2+</sup>. During this process;

NaOH dissolves to form Na<sup>+</sup> and OH<sup>-</sup> ions (Eq. 1).

$$NaOH \rightarrow Na^{+} + OH^{-} \tag{1}$$

Basic substances in the environment increase the alkalinity (pH ~11-13) and dissolution rate, and the surfaces of alumina silicate sources are surrounded by OH<sup>-</sup> ions and dissolved. From the dissolution reaction, Si(OH)<sub>4</sub> and Al(OH)<sub>4</sub> species are formed (Eq. 2).

$$Al_2O_3 \cdot SiO_2(s) + 2OH^- + 5H2O \rightarrow 2Al(OH)_4^- + Si(OH)_4$$
 (2)

After the condensation reaction, sodium-aluminosilicate-hydrate (N-A-S-H) gel and calcium-aluminosilicate-hydrate (C-A-S-H) colloidal particle gels are formed due to possible Ca<sup>2+</sup> ions in the environment, while polymerization continues simultaneously (Eq. 3).

$$4nSi(OH)_4+2nAl(OH)_4^-+nNa^+ \rightarrow nNa(OH)_3Si-O-Si(OH)_3+2n(OH)_3Si-O-Al(OH)_3^-+3nH_2O \eqno(3)$$

As polymerization progresses, the gels dry and harden, the pores shrink, and the mechanical strength increases (70-80% strength can be achieved within 48 hours). Different additives can be added to the mixture according to the usage area. For example, the addition of additives such as nano silica and graphene oxide improves homogeneity and density in the gel's microstructure. The addition of fiber increases the physical strength rather than chemical resistance, controlling micro-cracks during the drying of the gel. This creates a durable, microporous, binding gel matrix

composed of reactive Si-Al-Na components. Gel porosity decreases to about 40% initially and to about 10-15% in 24-72 hours. After 7 days and beyond, stable crystalline phases (zeolite-like) are formed, bringing the strength to a level close to the maximum.

#### 2.1 Materials and Methods

#### Devices:

- Planetary mixer or laboratory mixer (300-1200 rpm)
- Temperature-controlled mixing bowl (temperature must be monitored)
- pH and, if possible, viscosity measuring devices (pH and viscosity should be monitored (0, 10 min, 1 h, 4 h, 24 h, 72 h, and 168 h)
- Precision balance (0.1 g accuracy)
- Molds (40x40x160 mm or 50x50x50 mm)
- Curing cabinet or humid media box

#### Solid Materials:

- Alumina silicate welding
- Nano fiber
- Steel fiber
- Basalt fiber

#### Liquid Ingredients:

- Sodium hydroxide
- Sodium silicate
- Polycarboxylate ether
- PEG-400
- Water

## 2.2 Mixing

Preparation of activator solution: Sodium silicate, dissolved sodium hydroxide, and water are dissolved by mixing them in a controlled manner in the proportions specified in the recipe. To ensure gel formation and viscosity stabilization, the pH > should be 12 and the temperature < 45 °C. After obtaining a homogeneous mixture, it is recommended to let the solution rest for 12–24 hours.

Preparation of dry ingredients: Alumina silicate source and nano silica are homogenized by mixing homogeneously at low speed for 5 minutes. The prepared activator solution is carefully added to the dry mixture and mixed at high speed for 3 minutes after 5 minutes of medium speed. Fibers are added to the mixture at this stage to protect them from the degrading effect of the alkaline environment.

Adding additives to the liquid: PCE, PVA, and Polyethylene glycol (PEG-400) are added and mixed first with a 5-minute low speed and then 2 minutes with high speed. Then, since it may decompose in the addition of alkaline solution, graphene oxide is added to the mixture in a controlled manner and mixed at a low speed for 10 minutes to ensure homogeneous distribution.

Fine-tuning: The mixture is mixed at high speed for 2 minutes at a speed of 900–1200 rpm, and the consistency is adjusted, as a result of which viscosity and workability can be optimized. The mixture is carefully poured into molds, air is removed by vibration, and an appropriate curing process is carried out to achieve the desired gel transformation rate.

#### 2.3 Curing

Curing is critical for completing polycondensation, accelerating microstructure development, and maximizing final mechanical properties [3-8]. Although it is possible to achieve this goal with ambient curing, considering that the curing time will increase to 28 days, 90-100% relative humidity will have to be maintained in the mixture continuously, the samples will have to be stored in the curing cabinet wrapped with a wet cloth after the molds are opened, and the dissolution time will be longer; in addition, considering the scientific justifications presented in Table 2, heat curing is recommended as the most common method [9-11].

Table 2. Thermal Cure Application and Justifications

Parameters	Recommended Condition	Scientific Rationale
Temperature	$60 \pm 2$ °C	It accelerates the diffusion of the activator

	solution and the dissolution-polymerization-	
	gelling kinetics by 3-5 times.	
24-48 hours (heat cure)	Over 90% gel transformation can be	
	achieved.	
90-100% RH (or closed system)	Since gel formation will stop if water is lost,	
	a humid environment is mandatory for the	
	continuation of gelation.	
Oven (oven) or steam curing	Homogeneous distribution of heat and a	
cabinet	controlled steam environment are provided.	
	90-100% RH (or closed system)  Oven (oven) or steam curing	

## Curing Steps:

- 1. After the samples are molded, they are kept in the environment for 2 hours for pre-setting.
- 2. Samples are wrapped with a polyethylene bag or taken to a steam curing cabinet.
- 3. Curing is carried out for 24–48 hours at a temperature of  $60 \pm 2$  °C.
- 4. It is then taken to ambient temperature and stored in a humid environment (95% RH) for 7-28 days.

# 3. Ideal Parameter Ranges in Geopolymer Concrete Production

GPCs prepared according to different design recipes; they show superior features such as superior microstructure, high strength, low water permeability, superior chemical resistance, high thermal stability, and environmental friendliness. To ensure this performance, appropriate material selection and correct mixing ratios are critical. Ideal parameter ranges frequently used in the literature are given below [10, 12-24]:

- pH:12-13 increases solubility and reaction speed. pH: <10.5 reduces both gelation and strength. pH>13.5 is undesirable as it increases viscosity and reduces workability. In addition, the highly alkaline environment expands and cracks silica gels.
- The temperature is less than 45 °C before thermal cure (excessive temperature may cause sudden gelation), and 60-80 °C in thermal curing increases the reaction rate.

- Si/Al ratio: 2-4% provides high strength and density. If the ratio is low, no gel will form; if it is high, the strength decreases because the structure is brittle.
- SiO2/Na<sup>+</sup> equivalent ratio: 2.0-2.5% increases polymerization rate and processability. If the ratio is low, full polymerization will not occur, and it should be known that as the ratio increases, even if the strength and viscosity increase, the workability will decrease, and the microcrack will increase. In addition, it should be known that excessive Na<sup>+</sup> will form a carbonate component with CO<sub>2</sub> and cause efflorescence, and the concrete surface may deteriorate.
- Fiber additive ratio: 0.5-1.5% by volume provides micro-crack control, ductility, as well as an increase of up to 30% in bending strength.
- Superplasticizer ratio: 0.5-1.0% lowers viscosity, improving workability and reducing water requirements.
- The solid/activator ratio should be 2:1-2.5:1. More than this rate results in poor binding of the liquid gel, while less results in insufficient dissolution.
- Water/solid binder ratio (W/B): ~0.3-0.35 makes fluidity and microstructure control more ideal.
- When the slag content is above 40%, the strength increases in the ambient cure.
- Aggregate gradation: Being in the 0-4 mm fraction, it reduces voids and increases workability.
- The Nano-SiO<sub>2</sub>/Nano-Al<sub>2</sub>O<sub>3</sub> additive tightens the microstructure and reduces microcracks.

- Graphene oxide additive provides fluidity and microcrack control.
- Homogeneous dispersion with intelligent robotic mixers reduces the amount of water.
- During sample molding, air bubbles should be removed by vibration/agitation or ultrasonic pretreatment.
- Post-cure stabilization should be monitored for 28 days without the sample being exposed to outdoor conditions.
- If steel fiber is used, it should be added to the dry phase, not the liquid phase, to avoid lumping in the mixture.
- Basalt fiber increases tensile strength at an early age, but the mixing time should be carefully adjusted, as it may break if mixed for too long.
- Since excessive use of PEG-400 may slow down gelation, the ideal dose of 1% should not be exceeded.

In addition, considering the findings of the studies in the literature, it is seen that GB exhibits significant advantages compared to traditional concrete in terms of its resistance to sulfate and acid environments, chloride ion permeability, high temperature resistance, and performance in freeze-thaw cycles [25-30]:

• Sulfate resistance: It shows high resistance to expansion and cracking caused by sulfate ions. The main reason for this situation is the low amount of calcium in hydration products and the suppression of ettringite formation. For example, when geopolymer concrete samples are soaked in a 5% Na<sub>2</sub>SO<sub>4</sub> solution for 6 months, the strength loss is less than 10%, while OPC concretes have reported over 30% loss under the same conditions. Fly ash–slag

hybrid systems are among the most resistant variants to sulfate action.

- Acid resistance: Even in strongly acidic environments, such as pH ≤4, it maintains its stability against dissolution and degradation thanks to its polymeric bond structure. While the mass loss ≤ in geopolymer concretes exposed to 5% H<sub>2</sub>SO<sub>4</sub> solution for 28 days is 2%, this rate is ≥ 10% in Portland cement samples. The N-A-S-H gel structure is much less prone to dissolving in acid.
- Chloride ion permeability: The RCPT value (ASTM C1202) of <1000 coulombs and the chloride diffusion coefficient of approximately -2 × 10<sup>-12</sup> m<sup>2</sup>/s is a critical advantage for preventing reinforcement corrosion, especially in marine structures and bridges.
- *High temperature resistance:* Geopolymer concretes can maintain their structural integrity up to 800 °C, whereas OPC concretes begin to decompose above 400 °C. Due to these features, it is preferred in fire-resistant panels. Additionally, the basalt fiber additive further enhances thermal strength and microcrack resistance.
- Freeze-thaw resistance: It is highly resistant to freeze-thaw cycles due to its low water content and dense microstructure. However, this strength is highly sensitive to mixing ratios and curing conditions. In systems supported by air-entraining additives, the strength loss is less than 10% at the end of 300 cycles. Fiber supplementation limits the formation of microcracks more effectively.
- Carbonation: Since it maintains a high pH level for a long time, it
  has a greater carbonation depth compared to OPC concretes.
  Therefore, surface coating and curing methods should be applied
  carefully in reinforced applications.
- Heavy metal and radiation barrier: Boron-added geopolymer concretes can be used as radiation armor in nuclear facilities. This

type of concrete has a high capacity to bind heavy metals (especially arsenic, lead, and zinc).

Therefore, geopolymer concrete stands out not only with its high mechanical strength but also with its superior durability performance against harsh environmental conditions. Due to these features, it is widely preferred in aggressive environmental conditions such as infrastructure projects, nuclear energy facilities, sewage systems, and chemical industry applications.

# 4. OPC and Geopolymer Concrete Cost Analysis

Although the initial investment cost is higher in geopolymer concrete, the total cost is lower when the lifetime cost is taken into account. This situation can be explained as in Table 3 [25, 31-33].

Table 3. Performance / Cost Ratio (Over 50 Years)

	OPC Concrete	<b>Geopolymer Concrete</b>
Connector Cost	Miscarriage	Middle
Contribution Cost (activator)	None/less	Medium/High
Curing Energy	Few	Medium (thermal cure)
Labor and maintenance	High	Miscarriage
Lifetime Cost	High	Miscarriage
Demolition/backup	1-2 times (every 25-30	1 time (≥50 years)
frequency	years)	1 time (≥30 years)
Annual cost per m <sup>3</sup>	More expensive	Cheaper

As a result, multi-component geopolymer concrete systems with low environmental impact, optimum cost, and high performance can be developed. Thanks to different design variations, it can be used in critical areas such as marine structures, high temperature environments, and nuclear/chemical waste barriers; sustainable, long-lasting, low CO<sub>2</sub> emissions, pH stable, high thermal stability, high acid and sulfate resistance, fiber-reinforced, and high impermeability concretes can be produced.

#### REFERENCES

- [1] De Hita, M. J., & Criado, M. (2023). Influence of superplasticizers on the workability and mechanical development of binary and ternary blended cement and alkali-activated cement. Construction and Building Materials, 366, 130272.
- [2] Bakharev, T., Sanjayan, J. G., & Cheng, Y. B. (2000). Effect of admixtures on properties of alkali-activated slag concrete. Cement and Concrete Research, 30(9), 1367–1374. https://doi.org/10.1016/S0008-8846(00)00349-5
- [3] Provis, J. L., & van Deventer, J. S. J. (Eds.). (2014). Alkali activated materials: State-of-the-art report, RILEM TC 224-AAM. Vol(13). Springer. https://doi.org/10.1007/978-94-007-7672-2.
- [4] Duxson, P., Lukey, G. C., & van Deventer, J. S. (2006). Thermal evolution of metakaolin geopolymers: Part 1–Physical evolution. *Journal of Non-Crystalline Solids*, 352(52-54), 5541-5555.
- [5] Komnitsas, K., & Zaharaki, D. (2007). Geopolymerisation: A review and prospects for the minerals industry. Minerals Engineering, 20(14), 1261–1277. <u>https://doi.org/10.1016/j.mineng.2007.07.011</u>
- [6] Kumar, S., Kumar, R., & Mehrotra, S. P. (2010). Influence of granulated blast furnace slag on the reaction, structure and properties of fly ash based geopolymer. *Journal of materials science*, 45(3), 607-615.
- [7] Sofi, M., van Deventer, J. S. J., Mendis, P. A., & Lukey, G. C. (2007). Engineering properties of inorganic polymer concretes (IPCs). Cement and Concrete Research, 37(2), 251–257. https://doi.org/10.1016/j.cemconres.2006.10.008
- [8] Zuhua, Z., Xiao, Y., Huajun, Z., & Yue, C. (2009). Role of water in the synthesis of calcined kaolin-based geopolymer. Applied Clay Science, 43(2), 218–223. <a href="https://doi.org/10.1016/j.clay.2008.09.003">https://doi.org/10.1016/j.clay.2008.09.003</a>
- [9] Kishore, K., Pandey, A., Wagri, N. K., Saxena, A., Patel, J., & Al-Fakih, A. (2023). Technological challenges in nanoparticle-modified geopolymer concrete: A comprehensive review on nanomaterial dispersion, characterization techniques and its mechanical properties. Case Studies in Construction Materials, 19, e02265. https://doi.org/10.1016/j.cscm.2023.e02265
- [10] Duxson, P., Fernández-Jiménez, A., Provis, J. L., Lukey, G. C., Palomo, A., & van Deventer, J. S. J. (2007). Geopolymer technology: The current state of the art. Journal of Materials Science, 42(9), 2917–2933. <a href="https://doi.org/10.1007/s10853-006-0637-z">https://doi.org/10.1007/s10853-006-0637-z</a>
- [11] Fernández-Jiménez, A., & Palomo, Á. (2005). Composition and microstructure of alkali activated fly ash binder: Effect of the activator. *Cement and concrete research*, 35(10), 1984-1992.
- [12] Temuujin, J., van Riessen, A., & Williams, R. (2010). Influence of calcium compounds on the mechanical properties of fly ash geopolymer pastes. Journal of Hazardous Materials, 167(1–3), 82–88. <a href="https://doi.org/10.1016/j.jhazmat.2008.12.121">https://doi.org/10.1016/j.jhazmat.2008.12.121</a>
- [13] Rajan, M. S., & AnuPriya, A. (2024). Development and properties of low-calcium fly ash-based geo polymer concrete. *Int J Innov Res Adv Eng*, 11, 465-9.
- [14] Thunuguntla, C. S., & Gunneswara Rao, T. D. (2018). Mix design procedure for alkali-activated slag concrete using particle packing theory. *Journal of Materials in Civil Engineering*, 30(6), 04018113. https://doi.org/10.1061/(ASCE)MT.1943-5533.0002296

- [15] Bakharev, T., Sanjayan, J. G., & Cheng, Y. B. (2001). Resistance of alkaliactivated slag concrete to carbonation. *Cement and Concrete Research*, 31(9), 1277-1283. https://doi.org/10.1016/S0008-8846(01)00574-9
- [16] Lee, W. K. W., & van Deventer, J. S. J. (2002). The effect of ionic contaminants on the early-age properties of alkali-activated fly ash-based geopolymers. Cement and Concrete Research, 32(4), 577–584.
- [17] Kou, S. C., & Poon, C. S. (2009). Properties of concrete prepared with crushed fine stone, furnace bottom ash and fine recycled aggregate as fine aggregates. Construction and Building Materials, 23(8), 2877–2886.
- [18] Frayyeh, Q. J., & Kamil, M. H. (2021). The effect of adding fibers on dry shrinkage of geopolymer concrete. Civil Engineering Journal, 7(12), 2099-2108. https://doi.org/10.28991/cej-2021-03091780
- [19] Matalkah, F., Salem, T., Shaafaey, M., & Soroushian, P. (2019). Drying shrinkage of alkali-activated binders cured at room temperature. Construction and Building Materials, 201, 563–570. <a href="https://doi.org/10.1016/j.conbuildmat.2018.12.223">https://doi.org/10.1016/j.conbuildmat.2018.12.223</a>
- [20] Adjei, S., Elkatatny, S., & Ayranci, K. (2022). Effect of elevated temperature on the microstructure of metakaolin-based geopolymer. *ACS omega*, 7(12), 10268-10276.
- [21] Ali, H. K., Abid, S. R., & Tayşi, N. (2023). Thermal behaviour and microstructure of self-cured high-strength plain and fibrous geopolymer concrete exposed to various fire scenarios. *Buildings*, *13*(10), 2444. <a href="https://doi.org/10.3390/buildings13102444">https://doi.org/10.3390/buildings13102444</a>
- [22] Durak, M. (2022). Effect of short-term elevated temperature curing on the mechanical performance of fly ash-based geopolymer mortar. Arabian Journal of Geosciences, 15, 1091. https://doi.org/10.1007/s12517-022-10050-4
- [23] Ping-hua, Z., Li-yuan, Y., Hua-jian, C., et al. (2003). The permeability and strength of green high performance concrete. Journal of Wuhan University of Technology Materials Science Edition, 18, 99–101. <a href="https://doi.org/10.1007/BF02838473">https://doi.org/10.1007/BF02838473</a>
- [24] Reddy, D. V., Edouard, J.-B., & Sobhan, K. (2013). Durability of fly ash-based geopolymer structural concrete in the marine environment. Journal of Materials in Civil Engineering, 25(6), 803–811. https://doi.org/10.1061/(ASCE)MT.1943-5533.0000632
- [25] Van Deventer, J. S. J., Provis, J. L., & Duxson, P. (2012). Technical and commercial progress in the adoption of geopolymer cement. Minerals Engineering, 29, 89–104. <a href="https://doi.org/10.1016/j.mineng.2011.09.009">https://doi.org/10.1016/j.mineng.2011.09.009</a>
- [26] Temuujin, J., Minjigmaa, A., Lee, M., Chen-Tan, N., & Van Riessen, A. (2011). Characterisation of class F fly ash geopolymer pastes immersed in acid and alkaline solutions. *Cement and concrete composites*, 33(10), 1086-1091.
- [27] Zhang, Z., Yao, X., & Zhu, H. (2010). Potential application of geopolymers as protection coatings for marine concrete: I. Basic properties. *Applied clay science*, 49(1-2), 1-6.
- [28] Wallah, S. E., & Rangan, B. V. (2006). Low-calcium fly ash-based geopolymer concrete: Long-term properties. Curtin University of Technology, 108.
- [29] Komnitsas, K., & Zaharaki, D. (2007). Geopolymerisation: A review and prospects for the minerals industry. Minerals Engineering, 20(14), 1261–1277. https://doi.org/10.1016/j.mineng.2007.07.011

- [30] Wasim, M., Ngo, T. D., & Law, D. (2021). A state-of-the-art review on the durability of geopolymer concrete for sustainable structures and infrastructure. *Construction and Building Materials*, 291, 123381... <a href="https://doi.org/10.1016/j.conbuildmat.2021.123381">https://doi.org/10.1016/j.conbuildmat.2021.123381</a>
- [31] Hardjito, D., Wallah, S. E., Sumajouw, D. M. J., & Rangan, B. V. (2004). On the development of fly ash-based geopolymer concrete. ACI Materials Journal, 101(6), 467–472.
- [32] Habert, G., d'Espinose de Lacaillerie, J. B., & Roussel, N. (2011). An environmental evaluation of geopolymer based concrete production: Reviewing current research trends. Journal of Cleaner Production, 19(11), 1229–1238. https://doi.org/10.1016/j.jclepro.2011.03.012
- [33] Akhtar, N., Ahmad, T., Husain, D., Majdi, A., Alam, M. T., Husain, N., & Wayal, A. K. S. (2022). Ecological footprint and economic assessment of conventional and geopolymer concrete for sustainable construction. *Journal of Cleaner Production*, 380, 134910.

# Magnetic-depth estimation and geophysical investigations of Timor Island and surrounding area, eastern Indonesia

Sercan KAYIN<sup>1</sup>

M. Nuri DOLMAZ<sup>2</sup>

Ezgi ERBEK-KIRAN<sup>3</sup>

<sup>1-</sup> Assist. Prof. Dr.: Gümüşhane University, Gümüşhane Vocational School, Department of Mining and Mine Extraction, Gümüşhane, <u>sercankayin@gumushane.edu.tr</u> ORCID No: 0000-0003-2279-0579

<sup>2-</sup> Prof. Dr.; Süleyman Demirel University, Engineering and Natural Sciences Faculty, Department of Geophysical Engineering, Isparta. nuridolmaz@sdu.edu.tr ORCID No: 0000-0002-9185-9835

<sup>3-</sup> Assoc. Prof. Dr.: Süleyman Demirel University, Engineering and Natural Sciences Faculty, Department of Geophysical Engineering, Isparta <a href="mailto:ezgierbek@gmail.com">ezgierbek@gmail.com</a> ORCID No: 0000-0003-4627-8932

#### ABSTRACT

The study aims to reveal the relationship between the magnetic data and depth in Timor Island and its surrounding area, which is located in the collision zone between the Banda Arc and the Australian continent, a region that is tectonically complex. Timor Island is situated on an accretionary prism formed by the collision between the Indo-Australian and Eurasian plates, and it hosts rock assemblages spanning a wide age range from the Permian to the Quaternary. The region's tectonic evolution has been influenced by dynamic processes, including the rapid forearc migration of Sumba Island. This study helps to better understand the depth and the subsurface structure in the region. For this purpose, EMAG2-v3 magnetic model's magnetic data were analyzed using several geophysical techniques, including reduction to the equator, analytic signal, first vertical derivative, and depth estimation. After applying the reduction to the equator (RTE), the first vertical derivative method was used to highlight shallow features, and an anomaly map was created. The magnetic data were processed using reduction to the equator to correct for low-latitude distortions. Elevated magnetic anomalies, most of the severe first derivative anomalies are predominantly concentrated along the suture zone and the northern margin of Timor Island, suggesting the presence of strongly magnetized structures likely associated with tectonic complexities and crustal heterogeneities in the collision zone. We detected these magnetic effects on the map derived from the application of the analytical signal technique. In the three-dimensional map we obtained as a result of the depth-to-basement contact of the region applied to the magnetic data, we found that the deepest magnetic anomalies extend up to 24.3 km in the study area. These anomalies are interpreted to be associated with volcanic products and deformation resulting from plate collision, indicating a significant relationship with subduction-related volcanism and tectonic activity.

Keywords - Magnetic, Depth, Timor island, Indonesia.

#### INTRODUCTION

Timor Island and its surrounding region in eastern Indonesia are located within a complex tectonic setting shaped by the ongoing convergence of the Indo-Australian and Eurasian plates (Fig. 1). This region is located in the convergence zone between the Australian continental margin and the Banda Arc, resulting in intense deformation and the development of an accretionary prism. The geological formations on Timor Island include rock units ranging in age from the Permian to the Quaternary, reflecting a long and dynamic tectonic history.

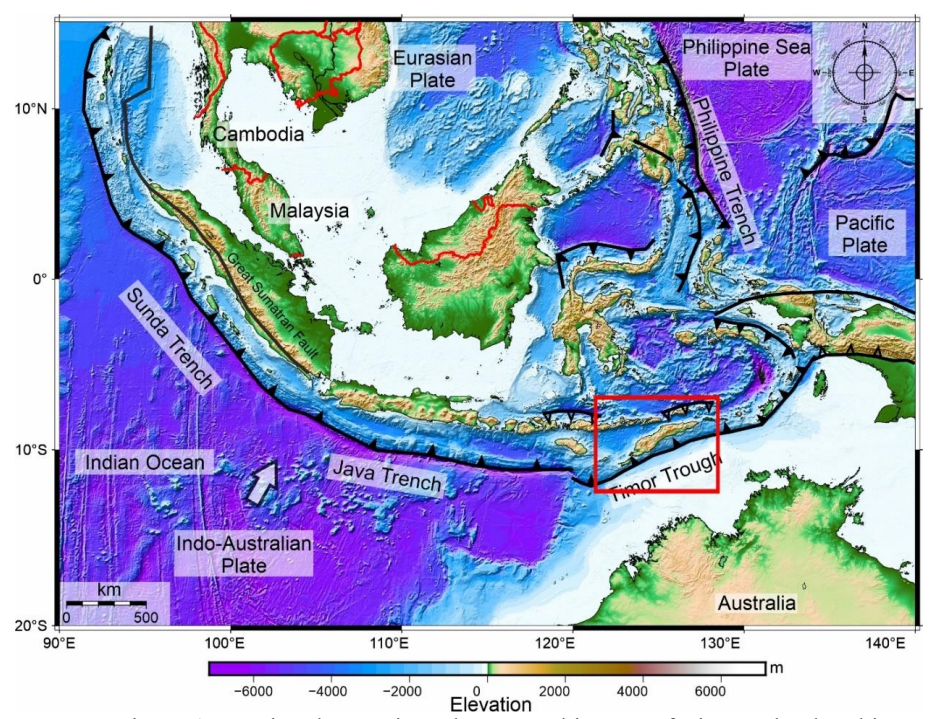


Figure 1: Regional tectonic and topographic map of Timor Island and its surroundings. The red area indicates the study region in Fig. 2, and the white arrow shows the direction of plate motion. Maps were obtained using the Generic Mapping Tools program, version 6.0 (Wessel et al., 2019).

The tectonic evolution of the region has been significantly influenced by processes such as subduction, collision, and the fore arc migration of nearby islands, particularly Sumba Island (Fig. 2). These processes have led to a heterogeneous crustal structure with varying magnetic properties. Understanding the magnetic characteristics and depth distribution of geological structures in this area is essential for interpreting the tectonic framework and assessing the crustal architecture.

The primary sources of the Earth's crustal magnetic field are induced and remnant magnetization within the crust and upper mantle. Variations in the concentration and distribution of magnetic minerals serve as robust indicators of both the structural configuration and the compositional heterogeneity of the crust (Aitken & Betts, 2008). In this context, magnetic anomaly maps constitute a fundamental geophysical approach for characterizing subsurface structures and lithological variations. Beyond their descriptive function, these maps provide a quantitative framework for delineating tectonic boundaries, identifying intrusive bodies, and constraining the thermal state of the lithosphere. Furthermore, magnetic anomalies observed in continental regions have been widely recognized as proxies for reconstructing the geological, tectonic, and geothermal evolution

of the crust and lithosphere (Hemant & Maus, 2005). Consequently, the integration of magnetic anomaly data with complementary geophysical and geological methods enhances our ability to unravel complex crustal processes, contributing to both regional tectonic reconstructions and resource

exploration.

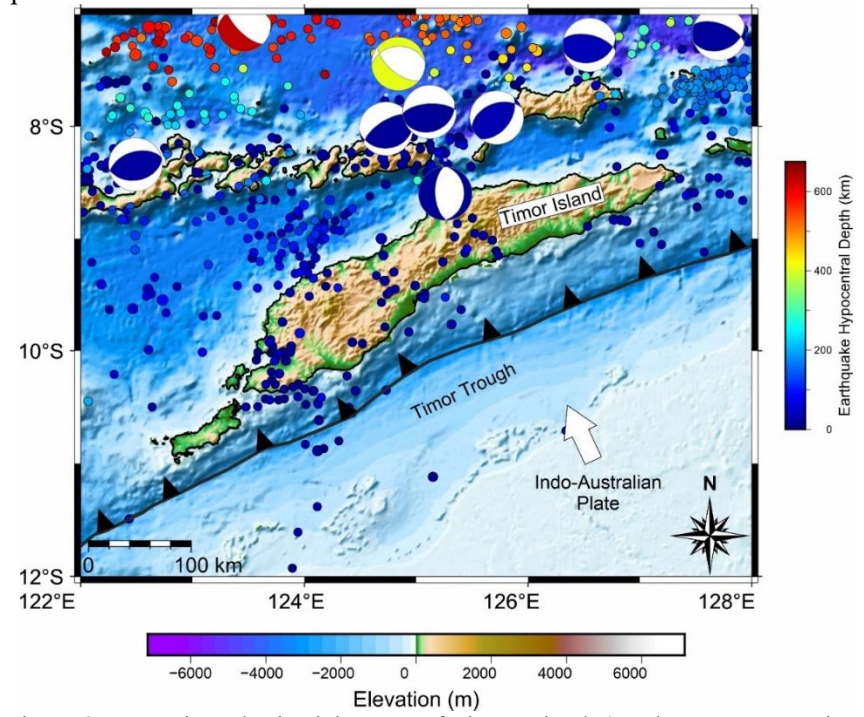


Figure 2. Tectonic and seismicity map of Timor Island. (EarthScope Consortium Wilber 3 system (https://ds.iris.edu/wilber3/) epicenter data for earthquakes with M > 5.0 between 1976 and 2025 were used. Focal mechanism solutions for earthquakes with M > 6 between 1976 and 2025 were obtained from the "Global Centroid Moment Tensor, GCMT Catalog" (Dziewonski et al., 1981; Ekström et al., 2012).

Timor Island is located within one of the most tectonically complex regions of Southeast Asia, where the Australian Plate converges with the Banda Arc and the greater Sunda subduction system. This collision zone, which initiated in the Neogene, has produced intense deformation manifested in folding, thrusting, and nappe emplacement across the island and surrounding basins (Fig. 2) (Keep & Haig, 2010; Harris, 2011). The Timor Trough, a prominent bathymetric feature along the island's southern margin, represents the active plate boundary where the Australian continental margin is being subducted beneath the Banda Arc system (Karig et al., 1987; Harris, 2011). Seismic activity in this region is closely associated with the interaction between shallow crustal faults and deeper lithospheric structures. Historical records document several large earthquakes, including the 1962 (M\_s ~7.2) and 1977 (M s ~7.0) events north of Timor, both of which exhibited thrust

faulting at depths of approximately 10 km (McCaffrey & Nábělek, 1986). The focal mechanism solutions in Figure 2 demonstrate that the vast majority of large earthquakes (M > 6.0) occurring north of Timor Island exhibit thrust fault characteristics. More recent statistical analyses of seismic catalogs in East Nusa Tenggara—including Flores, Alor, and Timor—reveal b-values of approximately 0.7 for events above magnitude 3.0, suggesting elevated stress accumulation and heterogeneous fault behavior (Sianturi et al., 2019).

Geodetic studies further highlight the role of interseismic coupling along the Timor Trough. Zhao et al. (2025) used GPS and earthquake slip vectors to demonstrate significant megathrust locking along the Java—Timor subduction interface, implying substantial seismic hazard potential for future large earthquakes and tsunamis. In addition, local site-effect studies in Timor-Leste, based on geoelectrical methods, indicate that variations in soil thickness and resonance frequencies strongly influence seismic amplification, providing crucial input for disaster mitigation strategies (Ley-Cooper, and Munday, 2011).

Despite these advances, several challenges remain. The spatial distribution of seismic stations across Timor and its offshore domains is sparse, limiting the detection and characterization of small- to moderate-magnitude events that are essential for refining hazard models. Furthermore, the complex interplay of thrust, strike-slip, and normal fault systems—particularly in regions such as Ainaro—remains insufficiently constrained at depth (Audley-Charles, 2011; Oliveira, 2020). Moreover, the focal depths of earthquakes in the Timor Island area exhibit a deepening trend from south to north, in accordance with the subduction process (Fig. 3). In this context, earthquake depths that exceed 600 km have been observed north/northwest of Timor.

The incomplete historical earthquake record also hampers long-term seismic hazard assessment. In summary, Timor Island represents a critical natural laboratory for studying active collision-related seismicity. The combination of shallow crustal faulting, megathrust coupling, and complex lithospheric interactions produces a highly seismogenic environment with significant societal implications. Continued integration of seismic, geodetic, and geological datasets is required to improve our understanding of crustal deformation and to enhance seismic hazard mitigation in this tectonically active region.

The Earth Magnetic Anomaly Grid (EMAG2-v3) represents the most recent and refined version of the EMAG2 global magnetic anomaly model, which was developed at a spatial resolution of 2 arc minutes (Meyer et al., 2017). This version was constructed through the integration of multiple magnetic datasets, including airborne surveys, marine measurements, and satellite-derived observations, thereby ensuring extensive coverage across both continental and oceanic domains.

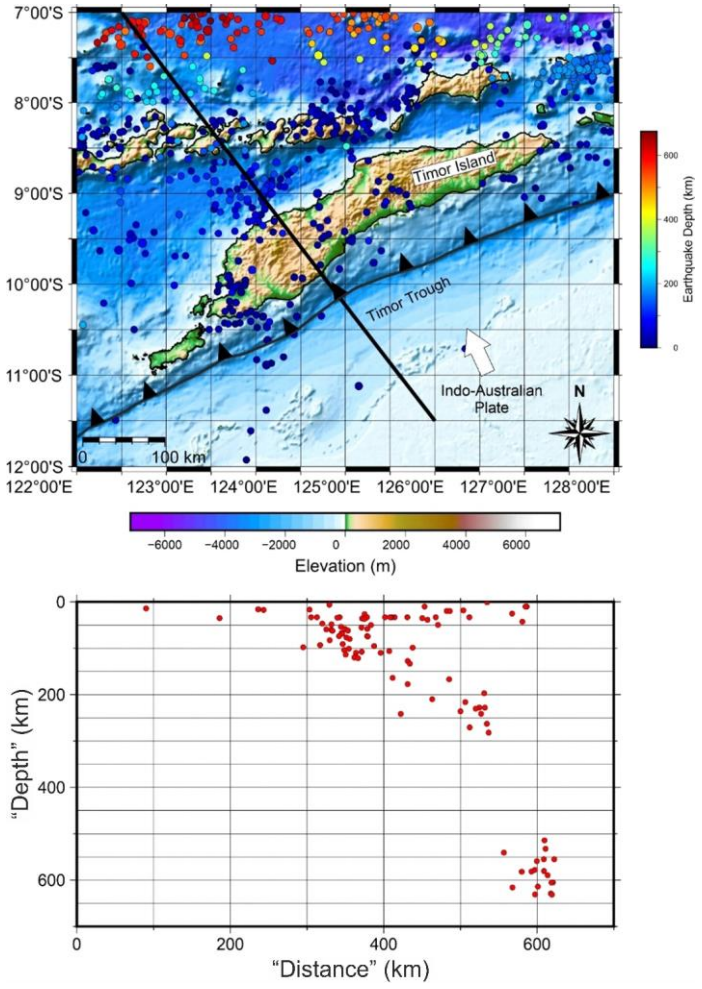


Figure 3. Tectonic and seismic map of Timor Island and its surrounding area, and the depth section of earthquakes in the area indicated by the black line.

In marine and coastal regions, the grid is provided at two distinct reference levels, namely sea level and 4 km above the geoid, in order to facilitate more accurate interpretation of regional and global magnetic anomalies (Meyer et al., 2017). Such a dual-level representation enables researchers to discriminate between near-surface sources and deeper lithospheric contributions, thereby enhancing the resolution of crustal and tectonic interpretations. The EMAG2-v3 dataset is freely accessible through the NOAA geomagnetism database, which serves as a central repository for global geomagnetic data. Given its comprehensive coverage and improved resolution, EMAG2-v3 constitutes a fundamental resource in studies of lithospheric structure, plate tectonics, and geodynamic evolution, as well as in applied fields such as mineral exploration and geothermal research.

In this study, EMAG2-v3 magnetic dataset were used to investigate the subsurface structures and estimate the depth to the magnetic basement in the Timor region. Various magnetic processing and interpretation techniques, such as Reduction to the Equator (RTE), First Vertical Derivative (FVD), and Analytic Signal (AS), are applied to enhance and interpret magnetic anomalies. The results contribute to a better understanding of the tectonic setting and provide geophysical insights into the subsurface features of this geologically active region.

#### MATERIAL AND METHOD

The study uses the EMAG2-v3 magnetic anomaly dataset from National Centers for Environmental Information, and the National Oceanic and Atmospheric Administration (NOAA). The data has a 2-arc minute resolution at sea level (Fig. 4) (Meyer et al. 2017). The Oasis Montaj software was employed for the processing and interpretation of magnetic data.

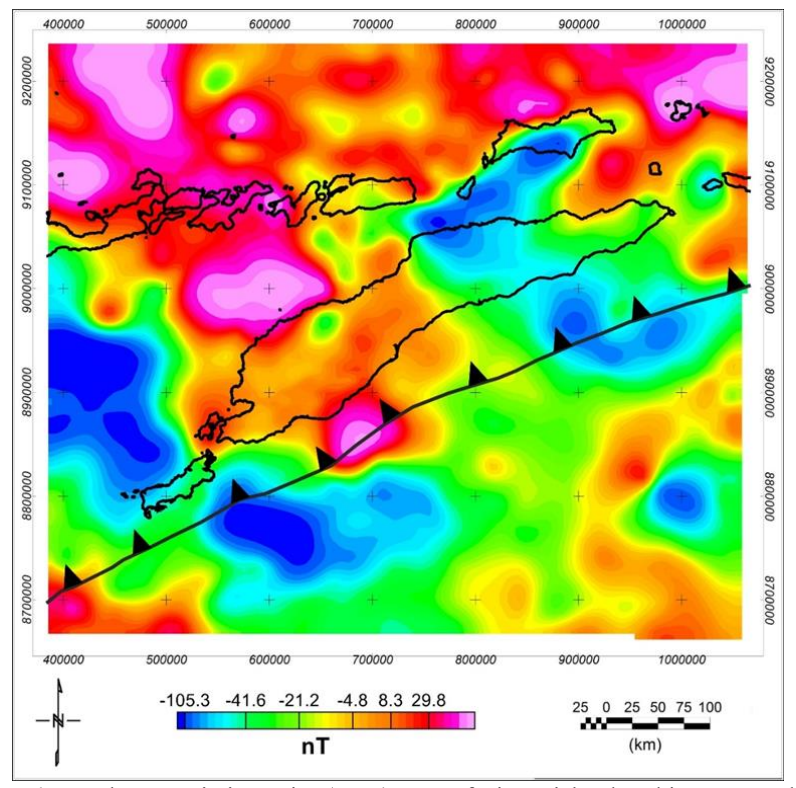


Figure 4: Total magnetic intensity (TMI) map of Timor island and its surroundings from the EMAG2-v3 dataset

Magnetic anomalies are influenced by several factors, including the depth and magnetic susceptibility of the source bodies, as well as the declination and inclination of the Earth's magnetic field. These influences can cause the anomalies to appear distorted, particularly in low-latitude regions where the Earth's magnetic field is nearly horizontal. In such areas, magnetic anomalies often become highly asymmetric and challenging to interpret. To address this issue, the Reduction to the Equator (RTE) technique is applied in magnetic data processing. RTE corrects for the directional effects of the Earth's magnetic field near the equator, repositioning magnetic anomalies directly above their causative sources. This transformation enhances the symmetry and interpretability of the anomalies, making it especially valuable in equatorial regions (Baranov, 1957; Blakely, 1995; MacLeod et al., 1993; Ansari & Alamdar, 2009). Before further spectral analysis, RTE correction must be applied to the TMI data. Fig. 5 shows the RTE map of the total magnetic intensity data.

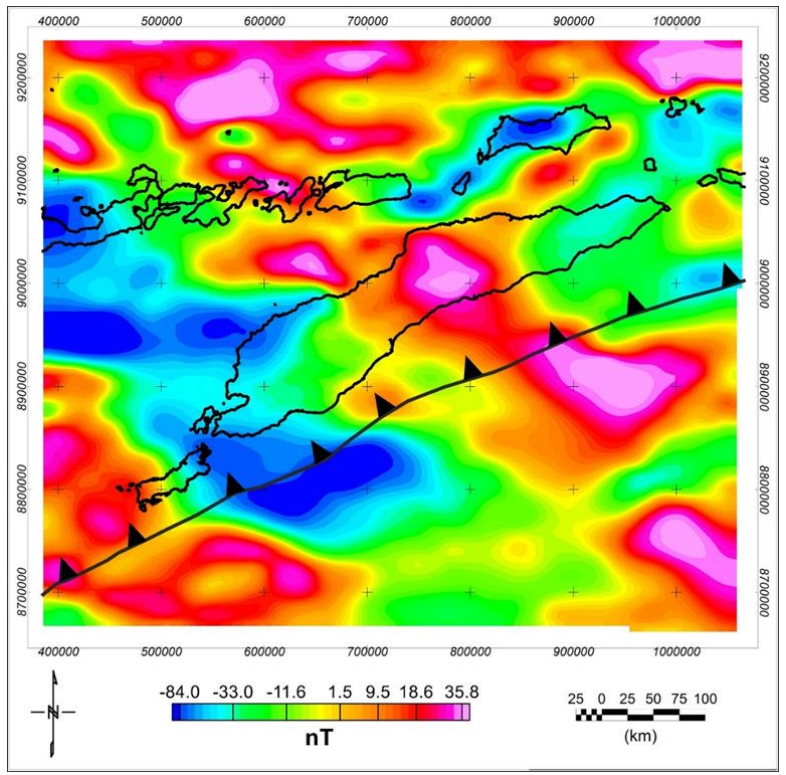


Figure 5: Reduced to the Equator (RTE) map of the TMI data

#### RESULTS AND DISCUSSION

The magnetic data analysis of the Timor Island and surrounding area in eastern Indonesia was conducted using enhancement and interpretation techniques to delineate subsurface geological structures and estimate basement depths. To differentiate between regional anomalies caused by deep structures and residual anomalies from shallow sources, the first vertical derivative (FVD) method was applied (Fig. 6). This method enhances short-wavelength components of the magnetic field, sharpens anomaly boundaries, and simplifies complex magnetic patterns, enabling clearer visualization of the causative bodies (Reeves, 2005). The application of the FVD filter to the reduced-to-the-Equator (RTE) magnetic data revealed prominent polarized positive anomalies, particularly in the southern part of the study area and along fault zones trending in a NW–SE and E-W directions.

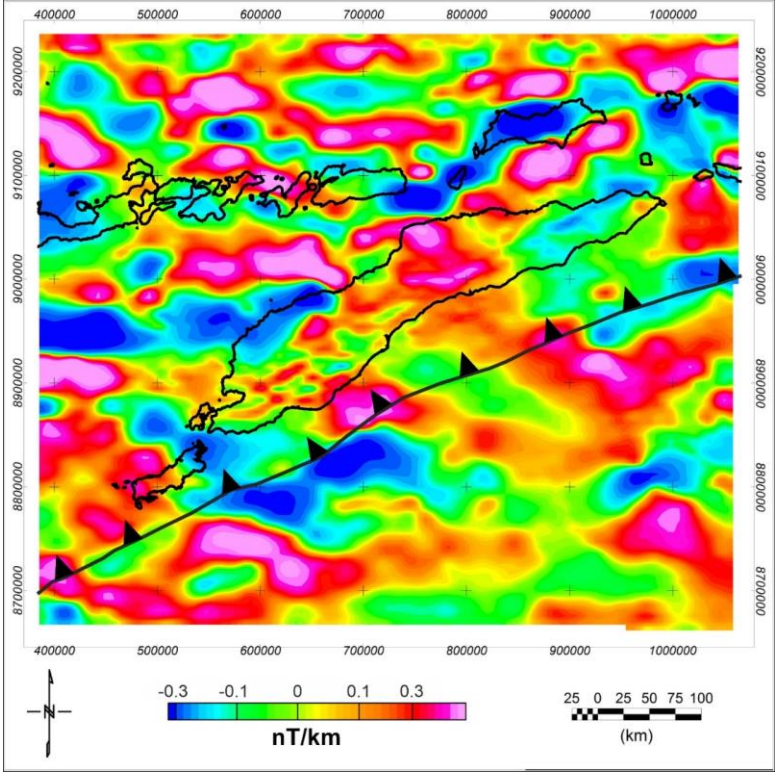


Figure 6: First vertical derivative (FVD) map of the RTE data

To further characterize these anomalies, the analytic signal (AS) method was utilized. This method, based on the combination of first-order horizontal and vertical derivatives of the total magnetic field, is advantageous due to its independence from the direction of magnetization (Roest et al., 1992). The

AS map highlighted zones of high magnetic intensity, with amplitudes reaching up to 0.30 nT/km (Fig. 7). A region showing concentrated anomaly signatures was delineated for detailed depth estimation studies.

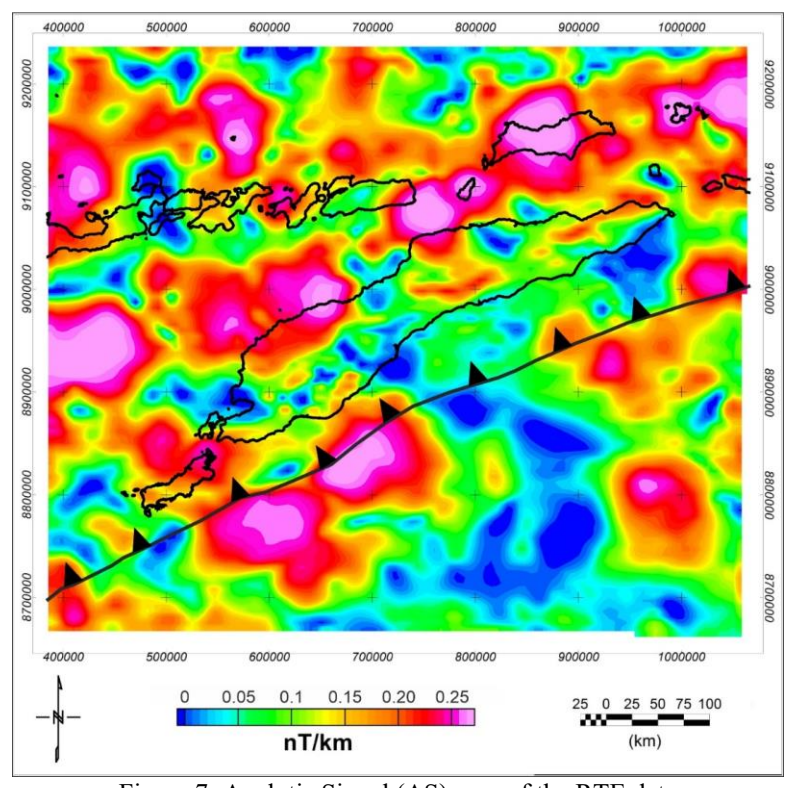


Figure 7: Analytic Signal (AS) map of the RTE data

The depth of the magnetic basement was determined through calculation of the ratio of the AS to the vertical derivative of the analytical signal (ASI). This calculation provides an estimate of the source depth. The calculation of depth was conducted in accordance with the following equation:

$$D = \frac{AS}{ASI} x N \tag{1}$$

where N represents the structural index of the source geometry (Reid et al., 1990). For this study, a structural index of N=1 was chosen, corresponding to contact-type sources. The resulting depth map showed a wide range of values, with the deepest zones reaching approximately 24.3 km, illustrated in red, and the shallowest zones marked in blue. Here, it can be seen that generally shallow magnetic basement depths are observed in the north/northwestern part of Timor Island due to volcanism occurring above the subduction zone, while in the southern part of the island the trench is obtained at deeper depths (approximately 24 km) further south (Fig. 8).

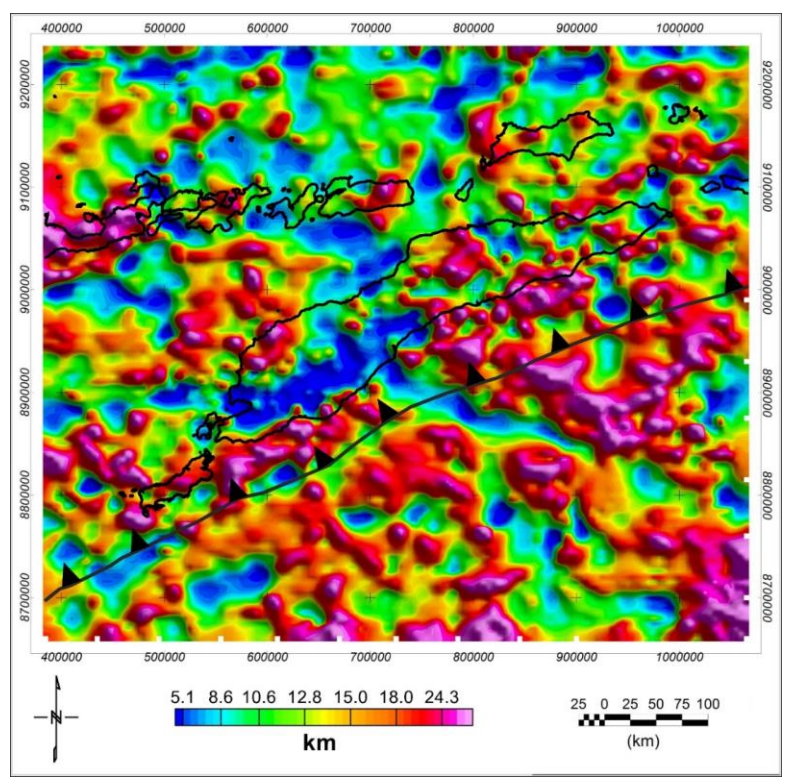


Figure 8: The depth to magnetic basement map

The combined use of the first vertical derivative and analytic signal techniques has successfully revealed both deep and shallow magnetic structures in the study area. The results indicate a complex subsurface structure influenced by tectonic features, and the depth estimations offer critical insights into the crustal architecture of the region. The analysis reveals that the northern and northwestern regions of Timor Island exhibit shallow basement depths, a consequence of volcanism occurring above the subduction zone. In contrast, the southern part of the island experiences a trench that reaches deeper depths further south. These findings provide a valuable geophysical framework for further geological investigations in eastern Indonesia.

#### REFERENCE

Aitken, A. R., Betts, P. G. (2008). High-resolution aeromagnetic data over central Australia assist Grenville-era (1300–1100 Ma) Rodinia reconstructions. Geophysical Research Letters, 35(1), 1-6.

Ansari, A.H., Alamdar, K. (2009). Reduction to the pole of magnetic anomalies using the analytic signal. World Appl Sci J, 7, 405-409.

- Audley-Charles, M. G. (2011). Tectonic post-collision processes in Timor. Geological Society, London, Special Publications, 355, 241–266.
- Baranov, V. (1957). A new method for interpretation of aeromagnetic maps, pseudogravimetric anomalies. Geophys., 22, 359-363.
- Blakely, R.J. (1995). Potential theory in gravity and magnetic applications. Cambridge University Press, pp 441.
- Dziewonski, A. M., Chou, T. A., Woodhouse, J. H. (1981). Determination of earthquake source parameters from waveform data for studies of global and regional seismicity. J. Geophys. Res., 86, 2825-2852.
- Ekström, G., Nettles, M., Dziewonski, A. M. (2012). The global CMT project 2004–2010: Centroid-moment tensors for 13,017 earthquakes. Phys. Earth Planet. Inter., 200-201, 1-9.
- Harris, R. (2011). The nature of the Banda Arc-continent collision in the Timor region. Geological Society, London, Special Publications, 355(1), 163–183.
- Hemant, K., Maus, S. (2005). Geological modeling of the new CHAMP magnetic anomaly maps using a geographical information system technique. Journal of Geophysical Research: Solid Earth, 110(B12).
- Karig, D. E., Barber, A. J., Charlton, T. R., Klemperer, S. and Hussong, D.M. (1987). Nature and distribution of deformation across the Banda Arc-Australian collision zone at Timor, Geol. Soc. Am. Bull., 98, 18-32,1987.
- Keep, M., and Haig, D. W. (2010). Deformation and exhumation in Timor: Distinct stages of a young orogeny. Tectonophysics, 483, 93–111.
- Ley-Cooper, Y., and Munday, T.,(2011), Aquifer characterisation in Timor-Leste using Ground Electromagnetics. CSIRO Technical Report EP121830, 1-30 pp.
- MacLeod, I.N., Jones, K., Dai, T.F. (1993). 3-D analytic signal in the interpretation of total magnetic feld data at low magnetic latitudes. Explor. Geophys., 24, 679–688.
- McCaffrey, R., Nábělek, J. (1986). Earthquakes, gravity, and the origin of the Banda Sea. Geophysical Journal International, 85(2), 365–379.
- Meyer, B., Chulliat, A., Saltus, R. (2017). Derivation and error analysis of the Earth magnetic anomaly grid at 2 arc min resolution version 3 (EMAG2v3). Geochem Geophys Geosyst, 18, 4522-4537.
- Oliveira, J. T. (2020). Neotectonics and active faulting in Timor-Leste. University of Coimbra, PhD Thesis.
- Reid, A.B., Allsop, J.M., Granser, H., Millett, A.J., Somerton, I.W. (1990). Magnetic interpretation in three dimensions using Euler deconvolution. Geophysics, 55, 80-91.
- Reeves C. (2005). Aeromagnetic Surveys; Principles, Practice and Interpretation. GEOSOFT, 155pp.
- Roest, W. R., Verhoef, J., Pilkington, M. (1992). Magnetic interpretation using the 3-D analytic signal. Geophysics, 57, 116–125.
- Sianturi, H. L., Susilo, A., Sunaryo, Maryanto, S. (2019). Correlation Analysis of Spatial Distribution, Temporal Seismotectonics, and Return Period of Earthquake in East Nusa Tenggara, Indonesia. International Journal of Geophysics, 2019(1), 5485783.
- Wessel, P., Luis, J., Uieda, L., Scharroo, R., Wobbe, F., Smith, W. H. F., Tian, D. (2019). The Generic Mapping Tools Version 6. Geochemistry, Geophysics, Geosystems, 20 (11), 5556–5564. https://doi.org/10.1029/2019GC008515

Zhao, S., Cummins, P. R., McClusky, S., Miller, M. S. (2025). Interseismic coupling along the Java–Timor megathrust. Geophysical Research Letters, 52(7), e2024GL112563.

# Stabilization of AVR Systems Using Proportional-Integral-Retarded Controller

Sevgi Gursul KALAC<sup>1</sup>

Serdar Ethem HAMAMCI<sup>2</sup>

<sup>1-</sup> Res. Asst.; Inonu University, Engineering Faculty, Electrical-Electronics Engineering Department. sevgi.gursul@inonu.edu.tr, ORCID No: 0000-0002-5013-1178

<sup>2-</sup> Prof. Dr.; Inonu University, Engineering Faculty, Electrical-Electronics Engineering Department. serdar.hamamci@inonu.edu.tr, ORCID No: 0000-0002-1868-6843

#### **ABSTRACT**

Maintaining stable and accurate voltage regulation in electrical power systems is a matter that requires careful attention, as poor regulation can significantly impact the overall efficiency and reliability of the system. This study presents a proportional-integral-retarded (PIR) control system for controlling an Automatic Voltage Regulator (AVR), which is an important element of the power systems, to achieve the desired voltage level. Designing a controller for AVR systems with a fourth-degree system structure and a complex system dynamics is not an easy task. Rather than designing an optimal PIR control system for the AVR, the objective here is to obtain a complete set of PIR controllers that stabilize the system. To achieve this, the D-decomposition method, which has been examined in the literature with regard to stabilization processes, is employed. In this method, the real root boundary, infinite root boundary and complex root boundary, also known as stability bounds, are first determined and then the control parameter space is divided into multiple regions using these boundaries. The most important feature of these regions is that the characteristic equations formed by the controller parameters in each region have the same number of stable and unstable poles. The region(s) consisting of characteristic equations with stable poles are considered to be the stability region(s). The results of the simulations show that the proposed method can be used to guarantee stable closed-loop system results when a PIR controller is used to control an AVR system.

Keywords – Power systems, automatic voltage regulator, AVR, control, PIR controllers, controller design

#### INTRODUCTION

Voltage regulation, which refers to a stable and reliable voltage output in electrical power systems, is an important issue (Izci et al., 2023:2). Since the equipment used in the system is designed according to a specific voltage level, known as the rated or nameplate voltage, it is necessary to ensure the continuity of the system's nominal voltage level so that there is no decrease in the performance of this equipment and also so that their life is not shortened. Automatic voltage regulators (AVRs) are used in power systems to address this problem. Due to the alternator's high inductance in the field windings and load changes, the regulator must respond stably and quickly to variations from the nominal voltage level. Therefore, a control mechanism should be built to improve the AVR performance and ensure correct operation (Kundur, 1994:960; Chatterjee and Mukherjee, 2016:418).

Several control methods are presented in the literature for AVR systems. In Furat and Cucu (2022:55650), a fast and stable control system under variable load conditions using the sliding-mode control method has

been designed. Modabbernia et al. (2020:46) designed a robust controller based on  $H_{\infty}$  and  $\mu$ -analysis against parameter uncertainties in the system. A fractional-order model reference adaptive controller (FOMRAC), designed using fractional-order differential equations, has been reported by Aguila-Camacho and Duarte-Mermoud (2013:807). However, PID-based control methods are observed to be used more frequently than these modern control methods for AVR system control. In addition to the traditional PID controller, various PID variants have been used in AVR control studies, including fractional-order PID (FOPID), a fuzzy PID controller, a 2DOF PI controller, a PID controller with a second-order derivative (PIDD<sup>2</sup>) and a PID–acceleration controller (PIDA) (Micev et al., 2021:2).

In control systems theory, stabilization is an important concept because it involves obtaining the entire set of controllers that make a system stable (Hamamci, 2008:330). Having this set of stabilizers allows one to select controllers with the desired performance and robustness by filtering them in the set using criteria such as the frequency-weighted  $H_{\infty}$  form (Hamamci, 2007:423; Datta et al., 2000). The literature on stabilization processes generally uses PI or PID controllers and methods such as the Hermite-Biehler method (Tantaris et al., 2006:1343), D-decomposition technique (Neimark, 1993:75; Silva et al., 2001:4650), parameter space approach (Ackermann ve Kaesbauer, 2001:522) and stability boundary locus approach (Tan, 2005:213). Recently, fractional-order PI, PD and PID controllers have also been used in the stabilization processes (Hamamci, 2007:1964; Hamamci ve Koksal, 2010:1621; Narayanaswamy et al., 2010:15). In (İrgan and Tan, 2025:1), a stable PIR controller design is developed for the time-delay systems using the stability boundary locus method. A few studies in the literature have addressed the stabilization of AVR systems, such as the use of PI controllers and the stability boundary locus method employed by Özdemir and Celik (2017:698).

This study presents a method for calculating all PIR controllers that stabilize the AVR system using the D-decomposition technique. These controllers that stabilize the system are plotted in the controller parameter plane according to the stability boundary conditions of the D-decomposition technique. Analytical formulas have been derived to determine the parameters of the controllers within the stability region. The stability regions obtained with retarded parameters of the PIR controller greater than zero are larger than those of the classical PI controller. A larger stability region provides a richer set of control system behaviors, making the PIR controller is more advantageous than the classical PI controller.

The next part of the study introduces the AVR and then discusses the D-decomposition method that will be used to obtain the stability region. Next, the PIR stability regions which make the AVR system stable are obtained and analyzed. A simulation study has been conducted to demonstrate the effectiveness of the method, and the results were discussed in the final section.

AUTOMATIC VOLTAGE REGULATOR (AVR) SYSTEM

The general schematic structure of an AVR system can be shown as in Figure 1 (Gopi et al., 2023:2). In this structure, the error voltage is obtained by comparing the terminal voltage at the generator output with the desired reference input voltage. This voltage varies according to the increases or decreases in the loads connected to the generator. The error voltage is then amplified, and the voltage at the generator output is regulated by controlling the excitation of the generator. Accordingly, a power generator system with automatic voltage regulation consists of four subsystems called amplifier, exciter, generator, and sensor. Figure 2 shows the general block diagram of this system. Here, r represents the desired reference voltage, y refers to the voltage measured at the generator terminal and e denotes the error voltage between r and y.  $G_a(s)$ ,  $G_e(s)$ ,  $G_a(s)$ , and  $G_s(s)$  are the transfer functions for the amplifier, exciter, generator, and sensor subsystems, respectively, and are defined as follows:

$$G_a(s) = \frac{K_a}{T_c s + 1},\tag{1}$$

$$G_e(s) = \frac{\kappa_e}{T_{cS+1}},\tag{2}$$

$$G_{a}(s) = \frac{K_{a}}{T_{a}s+1},$$

$$G_{e}(s) = \frac{K_{e}}{T_{e}s+1},$$

$$G_{g}(s) = \frac{K_{g}}{T_{g}s+1},$$

$$G_{s}(s) = \frac{K_{s}}{T_{s}s+1}$$
(1)
(2)
(3)

$$G_S(s) = \frac{K_S}{T_c s + 1} \tag{4}$$

where  $K_a$ ,  $K_e$ ,  $K_g$ , and  $K_s$  are the gain constants, and  $T_a$ ,  $T_e$ ,  $T_g$ , and  $T_s$  are the time constants of the subsystems. Finally, overall transfer function of the AVR system in Figure 2 is obtained as

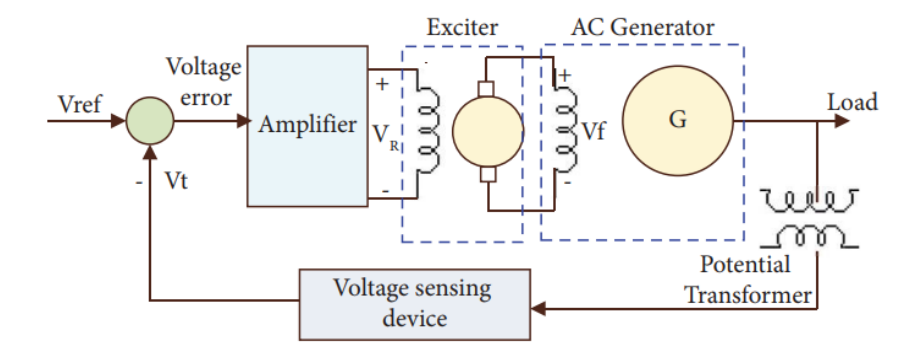


Figure 1: Simplified model of the AVR system. (Gopi et al., 2023:2)

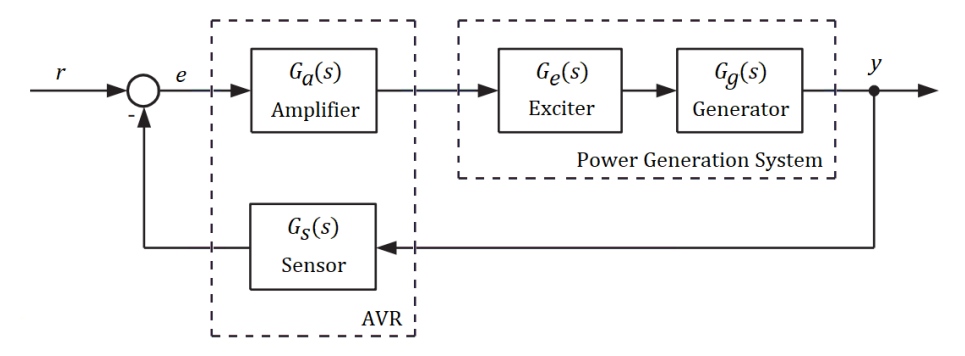


Figure 2: Block Diagram of the AVR system without controller.

$$T(s) = \frac{Y(s)}{R(s)} = \frac{K_a K_e K_g (T_s s + 1)}{(T_a s + 1)(T_e s + 1)(T_g s + 1)(T_s s + 1) + K_a K_e K_g K_s}.$$
 (5)

The typical gain constant values change within the following intervals:  $10 \le K_a \le 400$ ,  $1 \le K_e \le 10$ ,  $0.7 \le K_g \le 1$  and  $1 \le K_s \le 2$ . The time constant values vary as follows:  $0.02 \le T_a \le 0.1s$ ,  $0.4 \le T_e \le 1s$ ,  $1 \le T_g \le 2s$  and  $0.001 \le T_s \le 0.06s$ . The nominal values are selected as  $K_a = 10$ ,  $K_e = K_g = K_s = 1$ ,  $T_a = 0.1$ ,  $T_e = 0.4$ ,  $T_g = 1$  and  $T_s = 0.01$  (Micev et al., 2021:3). Using these values, the AVR system has the transfer function

$$T(s) = \frac{0.1s + 10}{0.0004s^4 + 0.0454s^3 + 0.555s^2 + 1.51s + 11}.$$
 (6)

Equation (6) describes a transfer function with two real stable and two complex conjugate stable poles, whose values are -99.971, -12.489 and  $0.5198 \pm 4.6642$ i. As can be seen in Figure 3, the response of the system to a unit step function is oscillatory and has a steady-state error of 9.12%.

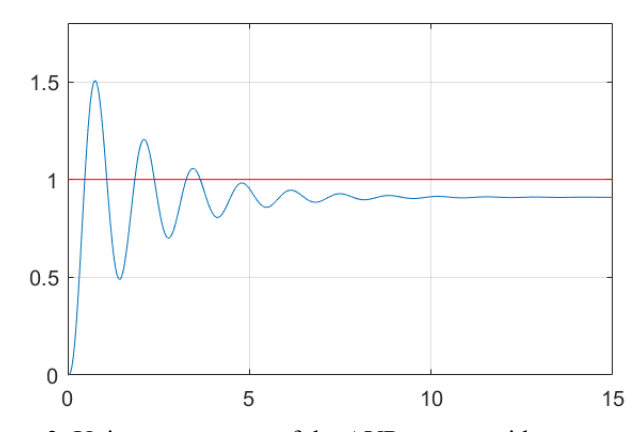


Figure 3: Unit step response of the AVR system without controller.

#### **D-DECOMPOSITION METHOD**

In general, consider a characteristic polynomial with n unknown parameters,  $x_i$ . Accordingly, this polynomial can be defined as

$$P(s; x_1, x_2, \dots x_n) = P_0(s) + P_1(s)x_1 + \dots + P_n(s)x_n. \tag{7}$$

Here,  $P_i(s)$  represents the known parts of the polynomial for  $i = 1 \sim n$ . The D-decomposition method (Neimark, 1973: 95; Lawrenson and Bowes, 1969: 1463; McKay, 1970: 293) is an effective technique for determining the set of unknown  $x_k$  values that make the polynomial in Equation (7) stable, i.e. make all of its roots lie in the left half-plane. This method produces excellent results in the analysis and design of control systems.

In the D-decomposition method, a graphical approach is adopted to ascertain the stability region within the  $(x_1, x_2, ... x_n)$ -parameter space. This process facilitates the identification of the set of  $x_i$  values that ensure the stability of the characteristic polynomial. Three basic stability boundary definitions are considered to achieve this (Ackermann and Kaesbauer, 2001:523; Cheng and Hwang, 2006:243; Hamamci, 2012:1192):

1. Real root boundary (RRB): This is a line in the parameter space expressed by the equation

$$P(s; x_1, x_2, \dots x_n)|_{s=0} = 0.$$
 (8)

2. Infinite root boundary (IRB): This is a line in the parameter space expressed by the equation

$$P(s; x_1, x_2, \dots x_n)|_{s=\infty} = 0,$$
 (9)

which is obtained by setting the largest exponent of the polynomial equal to zero.

3. Complex root boundary (CRB): This is a curve in the parameter space expressed by the equation

$$P(s; x_1, x_2, \dots x_n)|_{s=jw} = 0.$$
 (10)

In simple systems, the CRB can sometimes also appear as a line. This boundary is established with the help of two equations obtained by substituting *jw* for *s* in the characteristic polynomial and then setting the real and imaginary parts of the polynomial equal to zero separately.

The stability boundaries are plotted in the parameter space. A stability test is then performed on each region. One or more of the regions may be stable. The resulting stability region(s) represent the set of points  $x_1, x_2, ... x_n$  that make the characteristic polynomial in Equation (7) stable.

#### PIR STABILIZATION FOR AVR CONTROL SYSTEM

Figure 4 shows the general block diagram of an AVR control system. In the control system, C(s) is a proportional-integral-retarded (PIR) controller, and its transfer function is defined as follows:

$$C(s) = k_p + \frac{k_i}{s} - k_r e^{-hs} \tag{11}$$

Here,  $k_p$  is the proportional coefficient,  $k_i$  is the integral coefficient,  $k_r$  is the retarded coefficient and h is the time delay of the controller (Ramirez et al., 2013:2239). When  $k_r$  is set to 0, the PIR controller behaves like a conventional PI controller.

This section aims to determine the set of PIR controllers that stabilize the AVR system in the form of a stability region in the parameter plane using D-decomposition method. The output expression of the control system shown in Figure 4 is

$$y = \frac{C(s)G_a(s)G_e(s)G_g(s)}{1 + C(s)G_g(s)G_e(s)G_g(s)G_s(s)}r.$$
 (12)

From Equation (12), the characteristic equation of the closed loop system, P(s), is defined as follows:

$$P(s) = 1 + C(s)G_a(s)G_e(s)G_g(s)G_s(s) = 0.$$
 (13)

By substituting the transfer functions of the subsystems given in Equations (1)-(4) in Equation (13),

$$1 + \left(k_p + \frac{k_i}{s} - k_r e^{-hs}\right) \frac{10}{(s+1)(0.4s+1)(0.1s+1)(0.01s+1)} = 0$$
 (14)

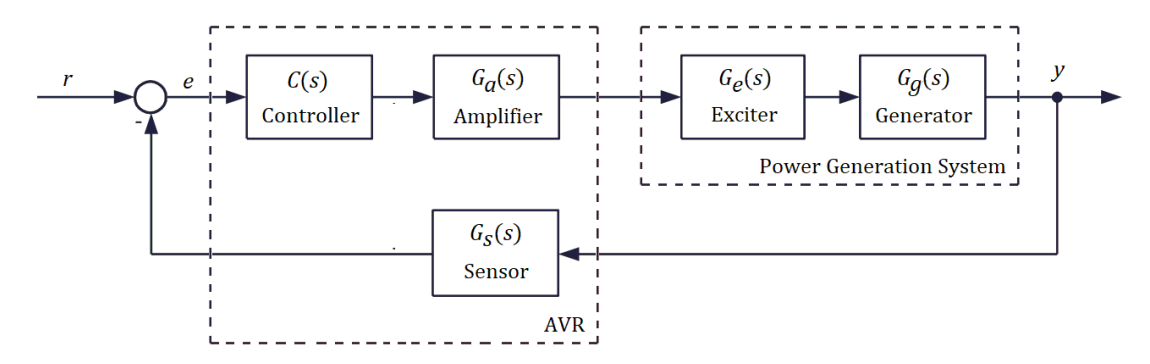


Figure 4: Block Diagram of the AVR system with controller.

and

$$s(s+1)(0.4s+1)(0.1s+1)(0.01s+1) + 10(k_p s + k_i - k_r s e^{-hs}) = 0$$
 (15)

is obtained. Considering Equation (15), the stability boundaries are obtained respectively. In this equation, the RRB boundary line for s = 0 is found to be

$$k_i = 0. (16)$$

Since there are no unknown controller parameters in the highest-order coefficient of the characteristic equation in Equation (15), there is no IRB boundary for the control system. Transforming s = jw in Equation (15) for the CRB, we obtain the equation

$$jw(jw+1)(j0.4w+1)(j0.1w+1)(j0.01w+1) + 10(jk_pw+k_i-jk_rwe^{-jhw}) = 0. \quad (17)$$

To solve this complex equation, we split the left-hand side into real and imaginary parts, setting each equal to zero to form two different equations:

$$0.045w^4 - 1.51w^2 + 10k_i - 10wk_r sinhw = 0 (18)$$

$$0.0004w^5 - 0.555w^3 + w + 10wk_p - 10wk_r coshw = 0. (19)$$

Once the system of equations has been solved, the unknown parameters  $k_p$  and  $k_i$  can be obtained as a functions of w,  $k_r$  and h:

$$k_p = -0.00454w^4 + 0.151w^2 + k_r(wsinhw)$$
 (20)

$$k_i = -0.00004w^4 + 0.0555w^2 - 0.1 + k_r(coshw).$$
 (21)

For  $k_r = 0$ , Equations (20) and (21) become the CRB equations of the classical PI controller. Consequently, in this situation, the equations become a function of w only. As illustrated in Figure 5 for the PI controller case, plotting the RRB (horizontal straight line) and the CRB (concave curve) boundaries in the  $(k_p, k_i)$ -plane divides the parameter space into four regions: R1, R2, R3 and R4. The CRB curve is plotted here in the range  $w \in [0, 6.96]$ . Larger values of w are ignored as they do not form new regions. To determine the stability of these regions, the unit step responses of the control system were obtained for randomly selected  $(k_p, k_i)$  pairs within each region and stability testing is performed. As can be seen in Figure 6, only the R1 region is stable. This region is more clearly visible in Figure 7.

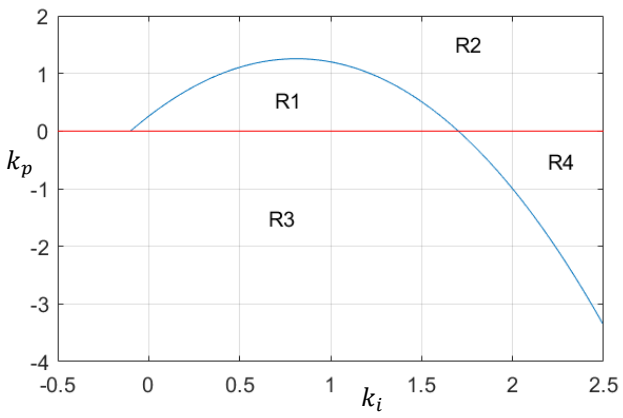


Figure 5: RRB and CRB boundaries for  $k_r = 0$  case.

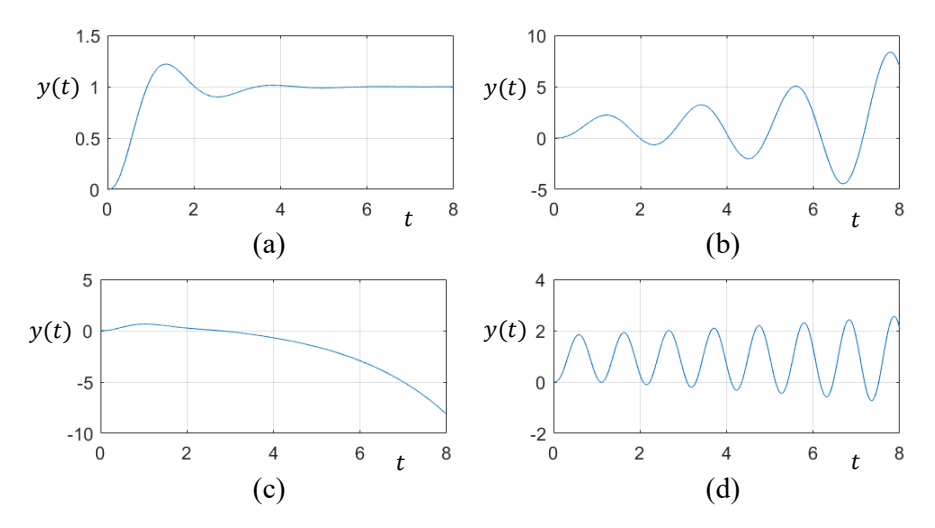


Figure 6: The unit step responses for  $(k_p, k_i)$  pairs values selected from four different regions: a) R1: (0.3, 0.2), b) R2: (0.3, 1.2), c) R3: (0.3, -0.2), d) R4: (1.9, -0.2).

Since the PIR controller has four parameters  $k_{\rm p}$ ,  $k_{\rm i}$ ,  $k_{\rm r}$  and h, a four-dimensional graph is needed to plot the complete stability region. To avoid complex graphs that are difficult to understand, it is more appropriate to analyse two-dimensional graphs for simplicity. For this purpose, Figure 8 shows the change of the stability region in the  $(k_{\rm p},k_{\rm i})$ -plane as the value of  $k_{\rm r}$  increases from 0 to 1 in increments of 0.1 by keeping h fixed at h=0.1. The smallest stability region visible in the figure corresponds to  $k_{\rm r}=0$ , and the stability region grows as the value of  $k_{\rm r}$  increases. Similarly, Figure 9 illustrates how the stability region changes in the  $(k_{\rm p},k_{\rm i})$ -plane when the value of h changes from 0.1 to 1 in increments of 0.1, while keeping  $k_{\rm r}$  fixed at  $k_{\rm r}=0.2$ . As can be seen in the figure, the stability region tilts towards the

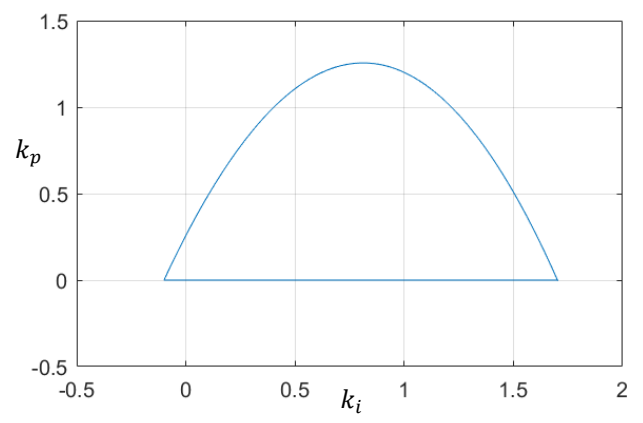


Figure 7: Stability region for  $k_r = 0$  case.

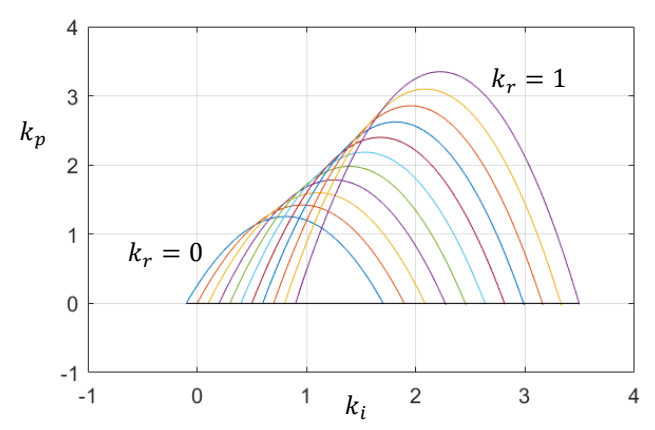


Figure 8: Stability regions obtained when  $k_r$  varies between 0 and 1 for a fixed value of h = 0.1.

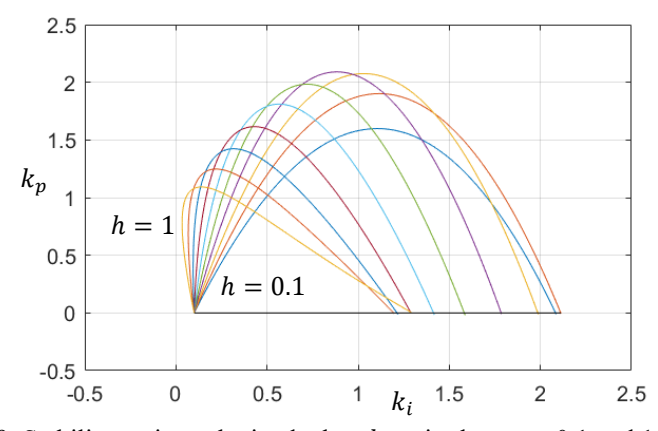


Figure 9: Stability regions obtained when h varies between 0.1 and 1 for a fixed value of  $k_r = 0.2$ .

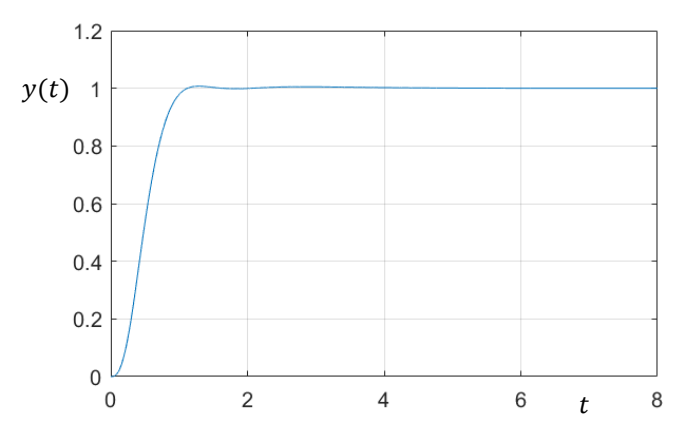


Figure 10: Unit step response of the controlled system for  $k_p = 0.43$ ,  $k_i = 0.2$ ,  $k_r = 0.18$  and  $k_i = 0.31$ .

left as the h value increases. The most important feature of this method is that it allows designers the opportunity to select the controller providing the desired unit step function response from the full set of stable controllers by considering the figures given above. For example, as shown in Figure 10, the unit step response of the closed loop system obtained for  $k_{\rm p}=0.43$ ,  $k_{\rm i}=0.2$ ,  $k_{\rm r}=0.18$  and h=0.31 has a non-overshoot characteristic. It should be noted that the aim of this study is to obtain the complete set of PIR controllers that make the system stable, rather than to select the optimal controller within this set according to a given performance index.

#### RESULTS AND DISCUSSION

In power systems, it is an important issue to maintain voltage stability for the correct functioning of the equipment in the system and to protect their operating life. For this purpose, automatic voltage regulators are used to prevent voltage deviations in the system structure. However, for an accurate and fast regulation process, the AVR must also be accurately controlled. In this study, it is aimed to obtain the stability regions of AVR systems using PIR controllers. For this purpose, the characteristic equation of the AVR control system with PIR controllers is obtained, and then, using the D-decomposition method, which is a graphical method, the set of PIR controllers that make the AVR stable is obtained with the help of stability boundaries. In future studies, it is possible to perform optimization studies to select the controller that gives the time response performance desired by the designer among the complete set of PIR controllers that make the AVR system stable.

#### REFERENCES

- Ackermann, J., and Kaesbauer, D. (2001). Design of robust PID controllers. 2001 European Control Conference (ECC) (pp. 522–527). Porto, Portugal.
- Aguila-Camacho, N., and Duarte-Mermoud, M.A. (2013). Fractional adaptive control for an automatic voltage regulator. *ISA Transactions*, *52*(6), 807–815.
- Chatterjee, S., and Mukherjee, V. (2016). PID controller for automatic voltage regulator using teaching—learning based optimization technique. *International Journal of Electrical Power & Energy Systems*, 77, 418–429.
- Cheng, Y. C., and Hwang, C. (2006). Stabilization of unstable first-order time-delay systems using fractional-order PD controllers. *Journal of the Chinese Institute of Engineers*, 29(2), 241–249.
- Datta, A., Ho, M.T., and Bhattacharyya, S. P. (2000). *Structure and Synthesis of PID Controllers*. UK: Springer-Verlag.
- Furat, M., and Cücü, G. G. (2022). Design, Implementation, and Optimization of Sliding Mode Controller for Automatic Voltage Regulator System. *IEEE Access*, 10, 55650–55674.
- Gopi, P., Varma, P.S., Sai Kalyan, C. N., Ravikumar, C. V., Srinivasulu, A., Bohara, B., Rajesh, A., Ab Wahab, M.N., and Sathish, K. (2023). Dynamic Behavior and Stability Analysis of Automatic Voltage Regulator with Parameter Uncertainty. *International Transactions on Electrical Energy Systems*, 6662355, 13.
- Hamamci, S.E. (2007). An Algorithm for Stabilization of Fractional-Order Time Delay Systems Using Fractional-Order PID Controllers. *IEEE Transactions on Automatic Control*, 52(10), 1964–1969.
- Hamamci, S.E. (2007). Zaman gecikmeli sistemler için kesirli dereceli PI kontrolör kullanılarak kararlılık bölgesinin belirlenmesi. *TOK'07 Otomatik Kontrol Ulusal Toplantısı*, Sabancı Üniversitesi, İstanbul.
- Hamamci, S.E. (2008). Stabilization using fractional-order PI and PID controllers. *Nonlinear Dynamics*, 51(1–2), 329–343.
- Hamamci, S.E. (2012). PI and PID stabilization of neutral and retarded systems with time delay. *Turkish Journal of Electrical Engineering and Computer Sciences*, 20(7), 1189–1205.
- Hamamci, S.E., and Koksal, M. (2010). Calculation of All Stabilizing Fractional-Order PD Controllers for Integrating Time Delay Systems. *Computers & Mathematics with Applications*, 59(5), 1621–1629.
- Irgan, H., and Tan, N. (2025). Stable PIR Controller Design Using Stability Boundary Locus for Time-Delay Processes. *Processes*, 13(5), 1535.
- Izci, D., Rizk-Allah, R.M., Snášel, V., Ekinci, S., Hashim, F.A., and Abualigah, L. (2023). A novel control scheme for automatic voltage regulator using novel modified artificial rabbits optimizer. e-Prime Advances in Electrical Engineering, Electronics and Energy, 6(100325).
- Kundur, P. (1994). Power system stability and control. New York: Tata McGraw Hill. Lawrenson, P. J., and Bowes, S. R. (1969). Generalization of D-decomposition techniques. Proceedings of the Institution of Electrical Engineers, 116(8), 1463–1470.
- McKay, J. (1970). The D-partition method applied to systems with dead time and distributed lag. *Measurement and Control*, 3(10), 293–294.

- Micev, M., Ćalasan, M., and Oliva, D. (2021). Design and robustness analysis of an Automatic Voltage Regulator system controller by using Equilibrium Optimizer algorithm. *Computers & Electrical Engineering*, 89(106930).
- Modabbernia, M., Alizadeh, B., Sahab, A., and Moghaddam, M.M. (2020). Robust control of automatic voltage regulator (AVR) with real structured parametric uncertainties based on H∞ and μ-analysis. *ISA Transactions*, 100, 46–62.
- Narayanaswamy, P.N., Kanthabhabha, P., and Hamamci, S.E. (2010). Fractional order PIλ control strategy for a liquid level system. *NABIC2010 2nd World Congress on Nature and Biologically Inspired Computing*. Kitakyushu, Japan.
- Neimark, J. I. (1973). D-decomposition of the space of quasi-polynomials (on the stability of linearized distributive systems). *In Ten papers in analysis*, Vol. 102, (pp. 95–131). American Mathematical Society.
- Özdemir, M., and Çelik, V. (2017). Stability Analysis of the Automatic Voltage Regulation System with PI Controller. *Sakarya University Journal of Science*, 21(4), 698–705.
- Ramírez, A., Mondié, S., and Garrido, R. (2013). Proportional integral retarded control of second order linear systems. *Proceedings of the 52nd IEEE Conf. Decision Control* (pp. 2239-2244). Firenze, Italy
- Silva, G. J., Datta, A., and Bhattacharyya, S. P. (2001). Stabilization of first-order systems with time delay using the PID controller. *Proceedings of the 2001 American Control Conference* (pp. 4650–4655). Arlington, VA, USA.
- Tan, N. (2005). Computation of stabilizing PI and PID controllers for processes with time delay. *ISA Transactions*, 44(2), 213–223.
- Tantaris, R.N., Keel, L.H., and Bhattacharyya, S.P. (2006). H∞ design with first-order controllers. *IEEE Transactions on Automatic Control*, 51(8), 1343–1347.

# Search for Low-Mass Resonances in Proton-Proton Collisions at $\sqrt{s}=13 TeV$ with the CMS Detector

Serdal DAMARSECKIN\*1,2

<sup>\*</sup>¹Faculty of Engineering, Department of Renewable Energy Systems Engineering, Sirnak University, Sirnak 73000, Türkiye

<sup>&</sup>lt;sup>2</sup>Faculty of Science and Letters, Department of Physics, Cukurova University, Adana 01250, Türkiye \*(serdalseckin@hotmail.com) Email of the corresponding author

#### **ABSTRACT**

Searches for narrow resonances in the dijet mass spectrum are among the most powerful probes of new physics beyond the Standard Model (SM). Jets, arising from the fragmentation of quarks and gluons, dominate hadronic final states at the Large Hadron Collider (LHC). While QCD predicts a smoothly falling dijet invariant mass distribution, a new heavy resonance decaying into partons would manifest as a localized enhancement above this background. This chapter presents a comprehensive overview of a dijet resonance search performed with the Compact Muon Solenoid (CMS) detector using 1.9 fb<sup>-1</sup> of proton–proton collision data collected at  $\sqrt{s} = 13$  TeV in 2015. A key feature of this analysis is the implementation of the data scouting technique, which allows event recording at significantly higher rates by storing reduced information, thereby extending sensitivity to resonance masses as low as 500 GeV. Jets are reconstructed with the particle-flow algorithm and calibrated with dedicated jet energy corrections. Event selection criteria are designed to optimize sensitivity to narrow resonances while suppressing the dominant QCD background. Systematic uncertainties related to jet energy scale, resolution, luminosity, and background parameterization are rigorously assessed. Statistical interpretation is performed using a profile likelihood ratio and the modified frequentist  $CL_s$  method. No significant deviations from the SM expectation are observed. Upper limits at 95% confidence level are set on benchmark models, excluding excited quarks below 5 TeV, axigluons and colorons below 3.6 TeV, Randall-Sundrum gravitons below 1.9 TeV, and string resonances below 7 TeV. These results highlight the unique capabilities of CMS scouting data and outline prospects for future sensitivity improvements at the HL-LHC and beyond.

Keywords – dijet resonance search, Compact Muon Solenoid (CMS), data scouting, jet physics, physics beyond the Standard Model, statistical methods, Large Hadron Collider (LHC).

#### 1. Introduction

The Standard Model (SM) of particle physics has been an exceptionally successful theoretical framework, providing precise predictions for the electroweak and strong interactions of elementary particles [1]. For over four decades, experimental results at colliders have confirmed the robustness of the SM, including the recent discovery of the Higgs boson at the LHC in 2012 [2].

Despite these achievements, it is widely acknowledged that the SM is incomplete. Several fundamental issues remain unresolved:

- Neutrino masses: Neutrino oscillation experiments have firmly established that neutrinos are massive, in contradiction with the massless neutrinos predicted in the minimal SM [1].
- Matter-antimatter asymmetry: The observed baryon asymmetry of the Universe cannot be explained by the amount of CP violation present in the SM [1].
- Dark matter and dark energy: Astrophysical and cosmological observations require the existence of dark matter and dark energy, neither of which is accommodated within the SM particle content [1].
- Hierarchy problem: The stability of the electroweak scale against quantum corrections remains an open question, motivating theories with new physics at the TeV scale [7].

These open questions drive extensive experimental programs to search for physics beyond the Standard Model (BSM). Among the many possible experimental signatures, dijet resonances play a particularly important role.

Jets are collimated sprays of hadrons resulting from the fragmentation of quarks and gluons produced in high-energy collisions [2]. The invariant mass spectrum of dijet systems is predicted by QCD to decrease smoothly with increasing mass [2]. A new heavy resonance decaying to quark or gluon pairs would appear as a narrow bump above this background [4].

The LHC provides a unique opportunity to explore this regime. Operating at a center-of-mass energy of 13 TeV during Run II, it probes partonic interactions at unprecedented scales [10]. The Compact Muon Solenoid (CMS) detector is a general-purpose experiment designed to search for such new phenomena [3].

A major experimental challenge in dijet searches is the limitation imposed by the trigger system. At high instantaneous luminosity, conventional jet triggers must employ high transverse momentum ( $P_T$ ) thresholds to reduce event rates, which significantly reduces sensitivity to low-mass resonances. To overcome this, CMS developed the data scouting technique, which records reduced event information, allowing events with lower jet  $P_T$  to be collected at much higher rates [9].

This chapter presents a detailed overview of a dijet resonance search using the CMS detector and 1.9 fb<sup>-1</sup> of data collected at  $\sqrt{s} = 13$  TeV in 2015. The analysis employs data scouting to extend sensitivity in the low-mass region (0.5–2 TeV). Results are interpreted in the context of several benchmark BSM models, including excited quarks, axigluons, colorons, Randall–Sundrum gravitons, and string resonances.

#### 2. THEORETICAL FRAMEWORK

#### 2.1 Jets in Quantum Chromodynamics

Quantum Chromodynamics (QCD) is the theory of the strong interaction, describing the dynamics of quarks and gluons within the framework of an

 $SU(3)_C$  non-Abelian gauge theory [2]. At hadron colliders, quarks and gluons cannot be observed directly due to color confinement. Instead, they hadronize into showers of color-neutral hadrons, which are reconstructed as jets in detectors.

The invariant mass of a dijet system composed of two leading jets is defined as:

$$M_{ij} = \sqrt{(E_1 + E_2)^2 - |\vec{p}_1 + \vec{p}_2|^2},$$

where  $E_i$  and  $\vec{p}_i$  are the energy and momentum of the two leading jets.

The hadronic cross section for producing a dijet system can be expressed through the convolution of parton distribution functions (PDFs) and partonic cross sections [2]:

$$\label{eq:dsigma} \frac{d\sigma}{dM_{ij}} = \sum_{i,j} \int dx_1 dx_2 f_i(x_1,Q^2) \, f_j(x_2,Q^2) \hat{\sigma}_{ij}(x_1,x_2,Q^2),$$

where  $f_i(x, Q^2)$  describes the probability of finding a parton of type *i* carrying momentum fraction *x* of the proton at scale  $Q^2$ .

Because PDFs fall steeply at large x, the resulting dijet spectrum decreases rapidly with increasing invariant mass. A new particle decaying into dijets would therefore manifest as a narrow localized enhancement (bump) over this falling distribution [4].

#### 2.2 Excited Quarks

Excited quarks  $(q^*)$  are predicted in compositeness models, where quarks are assumed to be bound states of more fundamental constituents [4]. Their existence would imply a new scale of compositeness,  $\Lambda$ .

- Production: qg→ q\*
- Decays:  $q^* \rightarrow qg$ ,  $q\gamma$ , qZ, qW.
- Dominant branching: qg, leading to dijet final states.

The resonance is typically narrow, with natural width much smaller than experimental resolution, and would therefore appear as a sharp peak in the  $M_{ii}$  spectrum.

# 2.3 Axigluons and Colorons

Chiral color models extend the QCD gauge group to  $SU(3)_L \times SU(3)_R$ , spontaneously broken to  $SU(3)_C$ . This gives rise to massive color-octet bosons called axigluons [5].

- Axigluons couple axially to quarks and decay to  $q\bar{q}$  pairs.
- They are predicted to be relatively broad compared to detector resolution.

In other extensions, the gauge group  $SU(3)_1 \times SU(3)_2$  is broken to  $SU(3)_C$ , leading to colorons [6].

- Colorons couple vectorially to quarks.
- Depending on model parameters, widths can vary.

Both axigluons and colorons are strongly produced and decay to dijets, yielding observable resonant structures in the dijet spectrum.

#### 2.4 Randall–Sundrum Gravitons

The Randall-Sundrum (RS) model introduces a warped extra dimension to address the hierarchy problem [7]. The Kaluza-Klein excitations of the graviton appear as spin-2 resonances.

- Produced via gluon-gluon fusion or quark-antiquark annihilation.
- Decay channels: gg,  $q\bar{q}$ ,  $\gamma\gamma$ , WW, ZZ.
- In dijet analyses, gg and  $q\bar{q}$  decays are most relevant.

The production cross section depends on the curvature of the extra dimension, parameterized by  $k/\overline{M}_{RL}$ .

# 2.5 String Resonances

String theory predicts the existence of Regge excitations of quarks and gluons, which could appear at TeV scales if the string scale is low enough [8].

- Produced in parton-parton scattering.
- Decay into dijets with distinct angular distributions.
- Typically broader than other BSM resonances.

Observation of such a resonance would be a direct indication of string dynamics at accessible energies.

#### 3. EXPERIMENTAL SETUP

#### 3.1 The Large Hadron Collider

CERN's Large Hadron Collider (LHC) is the most powerful particle accelerator currently in operation. Spanning a ring of 27 kilometers, it accelerates and collides two opposing proton beams, reaching center-of-mass energies of up to 13 TeV during Run II [10]. The beams are structured in bunches, each containing approximately  $10^{11}$  protons, crossing every 25 ns at four interaction points, including that of the CMS experiment.

During 2015, the LHC achieved peak instantaneous luminosities of about  $5 \times 10^{33} \text{ cm}^{-2} \text{s}^{-1}$ . The dataset considered in this analysis corresponds to an integrated luminosity of 1.9 fb<sup>-1</sup>. This integrated luminosity was sufficient to explore dijet resonance production up to multi-TeV mass scales.

#### 3.2 The CMS Detector

The Compact Muon Solenoid (CMS) experiment is a versatile detector developed to investigate a wide spectrum of physics processes, such as the

properties of the Higgs boson, the behavior of the top quark, and potential signals of physics beyond the Standard Model [3]. The CMS detector adopts a right-handed coordinate system, where the origin is defined at the nominal interaction point within the apparatus. The *z*-axis is along the beam line, the azimuthal angle  $\phi$  is measured in the transverse plane, and the pseudorapidity is defined as  $\eta$ =-lntan( $\theta$ /2).

CMS is designed with a nearly hermetic geometry, enabling precise measurements of energy balance and missing transverse energy  $(E_T^{miss})$ .

#### 3.2.1 Tracker

- A silicon pixel and strip detector, covering  $|\eta| < 2.5$ .
- Provides precise vertexing and momentum measurements.
- Transverse momentum resolution:  $\sim$ 1% at  $p_T$ =100 GeV.

# 3.2.2 Electromagnetic Calorimeter (ECAL)

- Lead tungstate (PbWO<sub>4</sub>) crystals, characterized by their high density and short radiation length.
- Energy resolution:

$$\frac{\Delta E}{E} \approx \frac{2.8\%}{\sqrt{E/_{GeV}}} \oplus 0.3\%$$

• Coverage:  $|\eta| < 3.0$ .

### 3.2.3 Hadronic Calorimeter (HCAL)

- Sampling calorimeter with brass absorber and scintillator tiles.
- Coverage:  $|\eta| < 5.0$  with forward calorimeters.
- Resolution:

$$\frac{\Delta E}{E} \approx \frac{100\%}{\sqrt{E/_{GeV}}} \oplus 5\%$$

#### 3.2.4 Muon System

- The muon detection system incorporates drift tubes (DT), cathode strip chambers (CSC), and resistive plate chambers (RPC).
- Provides standalone muon identification and momentum measurement up to  $|\eta| = 2.4$ .

# 3.2.5 Superconducting Magnet

• At the core of CMS lies a superconducting solenoid that generates a 3.8 tesla magnetic field.

Its magnetic bending capability ensures precise momentum measurements of charged particles and helps minimize uncertainties in jet energy calibration.

# 3.3 Trigger System

The LHC delivers collisions at 40 MHz, corresponding to about one billion interactions per second. Storing all these events is impossible, so CMS employs a two-tier trigger system [3].

- Level-1 (L1): A hardware-based trigger system employing dedicated electronics, which lowers the incoming event rate to roughly 100 kHz.
- High-Level Trigger (HLT): A software-driven system that further decreases the rate to about 1 kHz, enabling events to be stored permanently.

# 3.3.1 Limitations of Standard Triggers

At high instantaneous luminosity, multijet triggers at the HLT require very high jet  $P_T$  thresholds (typically > 400 GeV) to maintain manageable rates. This drastically reduces sensitivity to resonances below ~1.5 TeV.

#### 3.3.2 Data Scouting

To overcome this limitation, CMS developed data scouting [9]. Instead of storing full event information, only reduced quantities are kept:

- Jet four-momenta.
- Basic event-level variables,
- Trigger and luminosity metadata.

This reduces the event size by a factor of  $\sim 100$ , enabling CMS to record scouting streams at rates up to 20 kHz. With this, resonance searches can probe masses down to 500 GeV, extending sensitivity well below the reach of conventional triggers.

#### 4. DATASET AND EVENT SELECTION

#### 4.1 Dataset

The analysis is based on 1.9 fb<sup>-1</sup> of proton–proton collision data collected in 2015 at  $\sqrt{s} = 13$  TeV with the CMS detector [9]. Data quality monitoring ensured that only periods in which all relevant subdetectors were fully operational were included. Events were required to pass the CMS data certification process, which involves checks on the tracker, calorimeters, and muon systems.

During this period, the average number of simultaneous interactions per bunch crossing (pileup) was  $\sim$ 15. Dedicated corrections were applied to mitigate the effects of pileup on jet reconstruction and event variables.

#### 4.2 Jet Reconstruction and Calibration

Jets are reconstructed using the particle-flow (PF) algorithm, which combines information from all subdetectors (tracker, ECAL, HCAL, muon system) to identify and reconstruct individual particles in the event [3]. PF

candidates are clustered into jets using the anti- $k_T$  algorithm with distance parameter R=0.4.

# Jet Energy Calibration (JEC)

The raw jet energies measured in the calorimeters must be corrected for detector response and pileup effects. The calibration proceeds in several stages [11]:

- 1. Offset correction: removes extra energy from pileup and electronic noise.
- 2. Relative (η-dependent) correction: ensures uniform response across detector pseudorapidity regions.
- 3. Absolute (p<sub>T</sub>-dependent) correction: derived from simulation and test-beam data.
- 4. Residual corrections: applied to data to account for differences between simulation and data, using balancing in γ+jet and Z+jet events.

The Jet Energy Scale (JES) uncertainty after calibration is typically 2–3%, a major source of systematic uncertainty in resonance searches.

# 4.3 Wide Jet Technique

To improve dijet mass resolution, CMS employs the wide jet algorithm. The two leading jets are identified, and any additional jets within  $\Delta R < 1.1$  are clustered into them. This reduces sensitivity to final-state radiation (FSR) and improves the accuracy of  $M_{ij}$  reconstruction [9].

#### 4.4 Event Selection

Events are required to satisfy several kinematic and quality criteria designed to maximize sensitivity to resonances while suppressing QCD backgrounds:

- At least two reconstructed jets with  $|\eta| < 2.5$ .
- Rapidity separation:  $|\Delta y| < 1.3$  between the two leading jets. This reduces the dominant t-channel QCD background, which favors large rapidity differences.
- Dijet invariant mass:  $M_{jj}$ >500 GeV, ensuring full trigger efficiency in the scouting dataset.
- Jet quality requirements to remove calorimeter noise, beam halo, or spurious detector effects.

Selection	Requirement	Motivation
		Robust infrared-
Jet algorithm	anti- $k_T$ , $R = 0.4$	and collinear-safe
		clustering
Wide jet	$\Delta R < 1.1$	Improved dijet
construction		mass resolution
Leading jet η		η
Rapidity		A * .
separation		Δy
Dijet invariant	$M_{jj} > 500) \text{ GeV}$	Guarantee trigger
mass		efficiency
Jet		Remove non-
identification	Noise/halo rejection	physical background
quality		events

# 4.5 Background Modeling

The QCD multijet background is estimated directly from data using a smooth parameterization of the dijet mass spectrum [12]. The functional form is:

$$\frac{d\sigma}{dM_{ii}} = \frac{P_0(1-x)^{P_1}}{x^{P_2+P_3lnx}}$$

where  $x = \frac{M_{jj}}{\sqrt{s}}$  and  $P_i$  are free fit parameters. This form has been validated extensively in previous CMS and ATLAS dijet searches [14].

#### 5. SYSTEMATIC UNCERTAINTIES

Systematic uncertainties play a crucial role in dijet resonance searches, as they affect both the signal acceptance and the modeling of the background. A rigorous evaluation of these uncertainties ensures the robustness of the final statistical interpretation [11].

# 5.1 Jet Energy Scale (JES)

The uncertainty in the jet energy scale arises from imperfect knowledge of detector response, calibration constants, and residual differences between data and simulation.

- The JES uncertainty is typically 2–3% across the jet  $p_T$  and  $\eta$  spectrum [11].
- This translates to a 2–3% uncertainty in the reconstructed dijet mass.

• In resonance searches, this uncertainty affects both the normalization and shape of the signal distributions.

# 5.2 Jet Energy Resolution (JER)

The finite resolution of jet energy measurements leads to a broadening of the dijet mass peak.

- CMS determines the JER by comparing data and simulation in dijet and γ+jet events.
- The uncertainty in JER is of order 10% of the resolution itself.
- This is propagated to the signal templates by smearing the simulated jets accordingly.

# 5.3 Integrated Luminosity

The measurement of the total integrated luminosity carries an uncertainty due to calibration of luminosity monitors and modeling of beam conditions.

- For the 2015 dataset, the luminosity uncertainty was 2.7% [13].
- This directly affects the normalization of the expected signal yield.

# 5.4 Trigger Efficiency

In scouting analyses, the reduced event size allows for lower  $p_T$  thresholds. However, the trigger efficiency is not perfectly sharp at the threshold.

- The efficiency curve is measured using independent control samples.
- The uncertainty is estimated by varying the turn-on curve within its uncertainty band.
- Its impact on the dijet mass spectrum is negligible above 600 GeV but significant near the threshold.

# 5.5 Background Parameterization

The QCD background shape is modeled using an empirical functional form. The choice of parameterization introduces systematic uncertainty [12].

- To assess this, alternative fit functions are tested.
- The largest deviation between the nominal and alternative background fits is taken as the systematic uncertainty.
- This is especially relevant at high masses, where event counts are low.

# 5.6 Pileup Modeling

Pileup affects jet reconstruction through extra energy deposits in the calorimeters.

- Simulated events are weighted to reproduce the observed pileup distribution in data.
- A 5% uncertainty in the average pileup multiplicity is propagated to the signal acceptance.

Table 5.1: Summary of Systematic Uncertainties

Source	Magnitud	le	Impact on Analysis
Jet Energy Scale (JES)	2–3%		Shifts dijet mass, affects shape + normalization
Jet Energy	~10%	of	Broadens resonance
Resolution	resolution		peaks
Integrated	2.7%		Affects overall signal
Luminosity	2.770		normalization
Trigger Efficiency	~1–2%	near	Impacts acceptance
	threshold		near $M_{jj} \approx 500 \text{ GeV}$
Background Parameterization	Model- dependent		Alters extracted limits, especially at high masses
Pileup Modeling	±5% multiplicity	pileup	Affects jet energy corrections and acceptance

# 6. STATISTICAL METHODS

The interpretation of dijet searches relies on statistical procedures that quantify the compatibility of the observed data with the Standard Model hypothesis and with potential BSM signals [14]. This section describes the likelihood formalism, test statistics, and the modified frequentist approach (CLs) used to set limits on resonance production.

#### 6.1 Likelihood Function

The starting point is the binned likelihood function constructed from the dijet invariant mass distribution:

$$\underline{\underline{\underline{C}}}(\mu,\theta) = \prod_{i=1}^{N_{bins}} \frac{\left(\mu s_i(\theta) + b_i(\theta)\right)^{n_i} e^{-(\mu s_i(\theta) + b_i(\theta))}}{n_i!}$$

where:

 $n_i$ : the number of events recorded in bin i.

 $s_i(\theta)$ : expected signal in bin i, depending on nuisance parameters  $\theta$ .

 $b_i(\theta)$ : expected background in bin i.

parameter quantifying the signal contribution, a value of zero corresponds to the absence of signal (background only).

 $\theta$ : nuisance parameters encoding systematic uncertainties (JES, luminosity, etc.), constrained with auxiliary measurements.

#### 6.2 Profile Likelihood Ratio

To test hypotheses, the profile likelihood ratio is used as the test statistic:

$$q_{\mu} = -2ln \frac{\Gamma(\mu, \hat{\theta}_{\mu})}{\Gamma(\hat{\mu}, \hat{\theta})}$$

where:

 $\boldsymbol{\hat{\theta}}_{\mu} :$  values of nuisance parameters that maximize the likelihood for fixed  $\mu.$ 

 $\hat{\mu}$ ,  $\hat{\theta}$ : unconditional maximum likelihood estimators.

This test statistic asymptotically follows a  $\chi^2$  distribution under certain conditions, as described by Wilks' theorem [14].

# 6.3 Wilks' Theorem and Asymptotic Approximations

Wilks' theorem states that, for large sample sizes, the distribution of  $q_{\mu}$  approaches a  $\chi^2$  distribution with one degree of freedom [14]. This property enables rapid evaluation of confidence intervals without requiring computationally expensive Monte Carlo simulations.

Asymptotic formulas are used to approximate the distribution of the test statistic, making it feasible to scan a large range of resonance masses and widths. These approximations have been validated against toy Monte Carlo studies in CMS and ATLAS dijet analyses [12].

# 6.4 Modified Frequentist Approach ( $CL_s$ )

The  $CL_s$  method is adopted to set exclusion limits on resonance cross sections [14]. The method is defined as:

$$CL_s = \frac{CL_{s+b}}{CL_b}$$

where:

 $CL_{s+b}$ : confidence level for the signal + background hypothesis.

 $CL_b$ : confidence level for the background-only hypothesis.

Exclusion at 95% confidence level (CL) is achieved if  $CL_s$ <0.05.

This method avoids overly conservative exclusions that may arise from downward fluctuations of the background.

# 6.5 Expected and Observed Limits

The expected exclusion limits are obtained by evaluating the  $CL_s$  distribution under the background-only hypothesis. Bands corresponding to  $\pm 1\sigma$  and  $\pm 2\sigma$  uncertainties are computed from pseudo-experiments or asymptotic approximations.

The observed limits are derived from the actual data, using the same statistical machinery.

- Observed > Expected: indicates an upward fluctuation (potential excess).
- Observed < Expected: indicates a downward fluctuation.

In the CMS 2015 scouting analysis, no significant excess was observed, and upper limits were placed on several benchmark models [9].

#### 6.6 Treatment of Systematic Uncertainties

Systematic uncertainties (Sec. 5) are incorporated as nuisance parameters with Gaussian or log-normal priors. These parameters are profiled in the likelihood fit, meaning the fit dynamically adjusts them to values that best describe the data.

This approach ensures that uncertainties are properly propagated into the final exclusion limits.

#### 7. RESULTS

# 7.1 Dijet Mass Spectrum

The observed dijet invariant mass spectrum after all event selections is shown in Figure 7.1. The data are compared to the smooth background prediction obtained from the fit described in Section 4.5.

- The distribution falls steeply with increasing  $M_{jj}$ , consistent with QCD expectations [12].
- The fitted function provides an excellent description of the data across the entire mass range, with no significant deviations observed.
- The residuals (data minus fit, divided by statistical uncertainty) show no localized excesses that would be consistent with a narrow resonance.

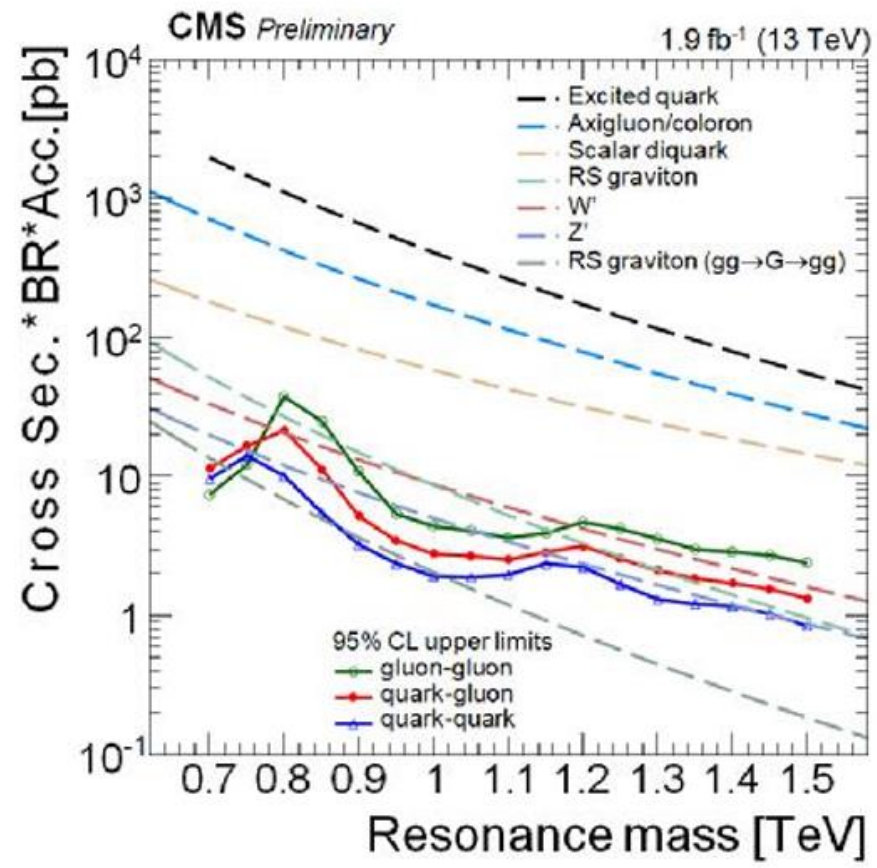


Fig. 7.1: Observed 95% CL upper limits on  $\sigma \cdot B \cdot A$  for benchmark resonance models.

Fig. 7.1 Dijet invariant mass distribution compared to the background fit. No significant excess is observed [18].

This null result sets the stage for interpreting the analysis in terms of exclusion limits on specific benchmark models.

# 7.2 Statistical Interpretation

The background-only hypothesis is tested against various signal hypotheses representing narrow resonances. For each mass hypothesis, the profile likelihood ratio (Sec. 6.2) is computed, and the  $CL_s$  method (Sec. 6.4) is applied to derive 95% confidence level upper limits on the product of the production cross section, branching fraction to dijets, and acceptance ( $\sigma \times B \times A$ ).

# 7.3 95% CL Upper Limits

The observed and expected upper limits on  $\sigma \times B \times A$  as a function of resonance mass are shown in Fig. 7.2.

The black solid line represents the observed limit. The black dashed line indicates the median expected limit under the background-only hypothesis. The green and yellow bands represent the  $\pm 1\sigma$  and  $\pm 2\sigma$  expected ranges, respectively.

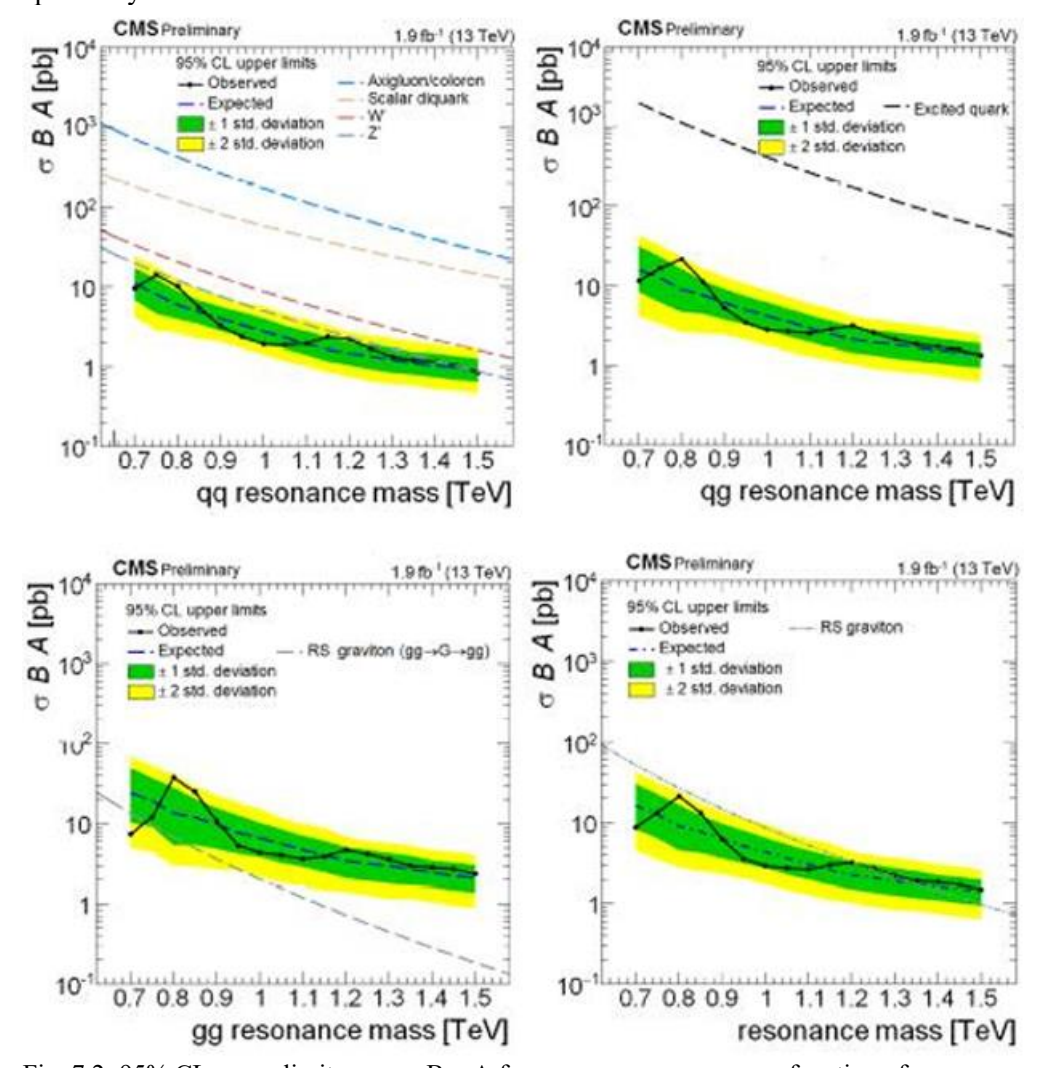


Fig. 7.2: 95% CL upper limits on  $\sigma \times B \times A$  for narrow resonances as a function of mass.

The results show good agreement between observed and expected limits. No significant deviations from the background-only expectation are observed [18].

#### 7.4 Limits on Benchmark Models

The exclusion limits are interpreted in the context of several benchmark BSM scenarios:

Excited quarks (q\*), Masses below 5.0 TeV are excluded at 95% CL. Axigluons and colorons,

Masses below 3.6 TeV are excluded. Randall–Sundrum gravitons ( $^k/_{\overline{M}_{Pl}}$  =0.1), Masses below 1.9 TeV are excluded. String resonances, Masses below 7.0 TeV are excluded.

These results represent some of the most stringent limits available at the time, particularly in the low-mass region enabled by the data scouting technique.

## 7.5 Comparison with Previous Results

Compared to earlier CMS and ATLAS dijet searches at 8 TeV [12], the 13 TeV scouting analysis:

Extends sensitivity to lower resonance masses (500–1000 GeV) due to scouting triggers. Provides tighter limits at high masses due to the larger center-of-mass energy and dataset. Demonstrates the feasibility of high-rate scouting data streams for precision searches.

#### 8. DISCUSSION

## 8.1 Comparison with ATLAS Results

Both CMS and ATLAS have conducted extensive searches for dijet resonances at  $\sqrt{s} = 13$  TeV [12]. While the overall methodologies are similar, there are important differences:

## • Trigger strategy:

ATLAS primarily relies on standard calorimeter-based jet triggers, which impose higher thresholds and therefore lose sensitivity to resonances below ~1 TeV.

CMS employs the data scouting technique (Sec. 3.3.2), allowing much lower thresholds and greatly enhancing sensitivity in the  $500~{\rm GeV}-1~{\rm TeV}$  mass region.

#### • Jet reconstruction:

ATLAS uses topological calorimeter clustering, whereas CMS uses the particle-flow algorithm, which incorporates tracking and calorimetry for improved jet resolution.

#### • Results:

At high masses (> 3 TeV), CMS and ATLAS limits are comparable, as both experiments are limited by the available luminosity.

At low masses, CMS significantly outperforms ATLAS due to scouting, providing the most stringent limits at the time.

This complementarity between the two experiments increases the robustness of the LHC dijet resonance program.

## 8.2 Implications for the Standard Model and Beyond

The absence of a dijet resonance signal in the 2015 dataset is consistent with the Standard Model. However, the stringent limits placed on benchmark BSM models provide valuable guidance:

- Excited quarks: Exclusion up to 5 TeV constrains quark compositeness scenarios, pushing the possible compositeness scale above ~20 TeV [4].
- Axigluons/colorons: The absence of signals below 3.6 TeV limits the viability of extended color gauge sectors [5].
- Randall–Sundrum gravitons: The exclusion of masses below 1.9 TeV for  $k/\overline{M}_{Pl}$  =0.1 disfavors certain warped extra-dimensional models [7].
- String resonances: Excluding masses up to 7 TeV pushes the discovery potential of low-scale string models further into the future [8].

Thus, while null, these results meaningfully shape the parameter space of many new physics models.

## 8.3 Prospects at the High-Luminosity LHC (HL-LHC)

The HL-LHC will deliver up to 3 ab<sup>-1</sup> of data at  $\sqrt{s} = 14$  TeV [15]. This will extend the sensitivity of dijet searches substantially:

- Increased luminosity improves statistical reach, particularly at very high masses (> 6 TeV).
- Improved detector upgrades (high-granularity calorimeter, timing detectors) will mitigate pileup effects and enhance jet resolution.
- The scouting technique is expected to evolve, possibly enabling even real-time analysis of reduced event data streams.

Projected exclusions include:

- Excited quarks up to ~8 TeV.
- Axigluons/colorons up to ~6 TeV.
- RS gravitons up to ~4 TeV.

## 8.4 Future Colliders: FCC-hh and Beyond

The proposed Future Circular Collider (FCC-hh) aims to collide protons at  $\sqrt{s} = 100 \text{ TeV}$  with integrated luminosities of up to 20 ab<sup>-1</sup> [16].

## At such energies:

- Resonances up to tens of TeV could be probed.
- The steeply falling QCD background becomes less dominant at multi-TeV scales, making bumps easier to distinguish.
- A broad program of dijet resonance searches would cover most theoretically motivated scenarios of compositeness, new gauge bosons, and string-inspired models.

## 8.5 Emerging Techniques: Machine Learning

Recent advances in machine learning (ML) are being applied to jet physics, offering potential improvements over traditional resonance bump hunting [17].

- Jet substructure analysis: ML algorithms (e.g., convolutional neural networks, graph neural networks) can classify jets by origin (quark vs gluon, boosted objects).
- Anomaly detection: Unsupervised ML methods (autoencoders, density estimation) can identify unexpected patterns in data without relying on predefined signal models.
- Real-time triggers: Implementation of ML inference at the hardware trigger level may allow more sophisticated event selection at high rates

For dijet resonance searches, ML-based techniques may increase sensitivity to subtle signals, reduce dependence on fixed background parameterizations, and open the door to model-independent discoveries.

#### 9. CONCLUSION

This chapter has presented a detailed search for dijet resonances using 1.9 fb<sup>-1</sup> of proton–proton collision data collected at  $\sqrt{s} = 13$  TeV with the CMS detector in 2015. The analysis employed the data scouting technique, which significantly extended the sensitivity of CMS to low-mass resonances below 1 TeV.

The dijet invariant mass spectrum was observed to be in excellent agreement with the QCD background expectation. No statistically significant excess was found. As a result, stringent 95% confidence level upper limits were placed on several benchmark BSM models:

Excited quarks: excluded below 5.0 TeV.

Axigluons and colorons: excluded below 3.6 TeV.

Randall–Sundrum gravitons: excluded below 1.9 TeV (for  $k/M_{Bl}$ =0.1).

String resonances: excluded below 7.0 TeV.

These results significantly improve upon previous 8 TeV searches and highlight the unique capabilities of the CMS data scouting approach. By enabling the collection of reduced event information at much higher trigger rates, CMS opened a new window into the low-mass dijet region, previously inaccessible with standard triggers.

Looking ahead, the High-Luminosity LHC (HL-LHC) will further extend sensitivity to multi-TeV resonances, with projected exclusions pushing the limits of compositeness, extra dimensions, and other BSM scenarios. Even more ambitiously, future colliders such as the FCC-hh at 100 TeV will probe

energy scales far beyond the reach of the LHC, exploring uncharted territory in the quest for new physics.

In parallel, the incorporation of machine learning techniques in jet substructure, anomaly detection, and trigger-level analysis promises to revolutionize the way resonance searches are conducted. These developments may enhance the discovery potential not only for specific benchmark models but also for completely unforeseen phenomena.

In conclusion, while the absence of a resonance signal in the 2015 CMS dataset is consistent with the Standard Model, the analysis demonstrates the power of innovative experimental strategies like data scouting and sets the foundation for future discoveries at the energy frontier.

**Acknowledgements**: This article is extracted from my doctorate dissertation entitled "Search For New Particles Decaying To Dijet At  $\sqrt{s}$ =13TeV Proton-Proton Collisions With Data Scouting Technique At CMS", supervised by Prof. Dr. İsa DUMANOĞLU and Prof. Dr. Sertaç ÖZTÜRK (Ph.D. Dissertation, Çukurova University, Adana, 2018).

#### REFERENCES

- [1] J. Beringer et al. (Particle Data Group), Review of Particle Physics, Phys. Rev. D 86, 010001 (2012).
- [2] G. Altarelli, Collider Physics within the Standard Model: QCD and Jets, Ann. Rev. Nucl. Part. Sci. 39, 357 (1989).
- [3] CMS Collaboration, The CMS Experiment at the CERN LHC, JINST 3, S08004 (2008).
- [4] U. Baur, I. Hinchliffe, D. Zeppenfeld, Excited Quark Production at Hadron Colliders, Int. J. Mod. Phys. A 2, 1285 (1987).
- [5] P. H. Frampton, S. L. Glashow, Chiral Color: A Possible Solution to the Strong CP Problem, Phys. Lett. B 190, 157 (1987).
- [6] E. H. Simmons, Coloron Models and Collider Phenomenology, Phys. Rev. D 55, 1678 (1997).
- [7] L. Randall, R. Sundrum, A Large Mass Hierarchy from a Small Extra Dimension, Phys. Rev. Lett. 83, 3370 (1999).
- [8] L. A. Anchordoqui et al., Dijet Signals for Low-Scale String Models at the LHC, Phys. Rev. Lett. 101, 241803 (2008).
- [9] CMS Collaboration, Search for Narrow Resonances using the Dijet Mass Spectrum in pp Collisions at  $\sqrt{s} = 13$  TeV, Phys. Rev. Lett. 116, 071801 (2016).
- [10] L. Evans, P. Bryant (eds.), LHC Machine, JINST 3, S08001 (2008).
- [11] CMS Collaboration, Jet Energy Calibration and Resolution in the CMS Experiment, JINST 6, P11002 (2011).
- [12] ATLAS Collaboration, Search for New Phenomena in the Dijet Mass Distribution using pp Collision Data at  $\sqrt{s} = 8$  TeV, Phys. Rev. D 91, 052007 (2015).

- [13] CMS Collaboration, CMS Luminosity Measurements for the 2015 Data-Taking Period, CMS Physics Analysis Summary, CMS-PAS-LUM-15-001 (2016).
- [14] G. Cowan, K. Cranmer, E. Gross, O. Vitells, Asymptotic Formulae for Likelihood-Based Tests of New Physics, Eur. Phys. J. C 71, 1554 (2011).
- [15] G. Apollinari et al., High-Luminosity Large Hadron Collider (HL-LHC): Preliminary Design Report, CERN-2015-005.
- [16] A. Abada et al. (FCC Collaboration), FCC Physics Opportunities, Eur. Phys. J. C 79, 474 (2019).
- [17] P. T. Komiske, E. M. Metodiev, J. Thaler, Energy Flow Networks, Deep Sets for Particle Jets, JHEP 2019, 121 (2019).
- [18] S. Damarseçkin, Search For New Particles Decaying To Dijet At √s=13TeV Proton-Proton Collisions With Data

Scouting Technique At Cms, PhD Thesis,2018, Cukurova University Institute Of Natural And Applied Sciences

# Rationale for Model Development in Accuracy Assessment of Optical Rotary Encoders Under Vibration: A Literature Perspective

Violeta KRCHEVA<sup>1\*</sup>
Stojance NUSEV<sup>2</sup>
Miša TOMIĆ<sup>3</sup>

<sup>&</sup>lt;sup>1</sup>Faculty of Mechanical Engineering, Goce Delcev University, Stip, Republic of North Macedonia <sup>2</sup>Faculty of Technical Sciences, University St. Kliment Ohridski, Bitola, Republic of North Macedonia <sup>3</sup>Faculty of Mechanical Engineering, University of Nis, Niš, Serbia \*(violeta.krceva@ugd.edu.mk)

#### **ABSTRACT**

Optical rotary encoders are widely acknowledged as essential sensors for high-precision measurement and control in contemporary automation and manufacturing systems. Their extensive utilisation is primarily attributable to their capacity to provide accurate data on angular displacement and rotational speed. Nevertheless, despite their proven performance under controlled laboratory conditions, these devices remain susceptible to disturbances encountered in real industrial environments. Among such disturbances, mechanical vibrations constitute one of the most pervasive and influential factors, acting as a primary source of instability capable of compromising measurement reliability. The current literature evidences substantial progress in the development of optical encoder technologies, including advancements in resolution, signal processing, and multi-channel configurations. These improvements have enhanced robustness and reduced vulnerability to electrical interference and minor mechanical perturbations. However, under dynamic operational conditions, encoders continue to display limitations that have not been fully explored in either research or practice. While several studies have investigated the impact of vibrations, there remains a clear need for broader and more systematic evaluations of rotary optical encoders in dynamic contexts. This paper therefore provides a literature-based perspective on the rationale for developing dedicated models to assess encoder accuracy under vibrational influence. By synthesising existing findings, the discussion emphasises the importance of integrating vibration analysis into sensor metrology frameworks. Such integration is crucial not only for understanding the basic mechanisms of error generation but also for guiding the design of experimental methodologies and simulation models that more faithfully represent real-world operational conditions.

Keywords – Sensor metrology, Error propagation, Signal processing, Industrial reliability, Dynamic conditions, Automation systems, Experimental validation.

#### I. INTRODUCTION

The optical rotary encoder (Fig. 1) is a high-precision electromechanical sensor that plays a crucial role in modern automation, control, and measurement systems. It is specifically designed to determine angular position, rotational speed, and direction of motion with high accuracy. As a result of these capabilities, rotary encoders are widely implemented in applications requiring real-time data processing and fine measurement resolution, including computer numerical control (CNC) machining systems, robotics, servo mechanisms, motion control units, and a broad range of industrial automation processes.

The primary function of an optical rotary encoder is to convert mechanical rotational movements into electrical signals that can be processed by electronic controllers or computer-based systems. These signals are subsequently employed for precise monitoring, regulation, and analysis of rotational motion, thereby ensuring high levels of accuracy and automation in technical systems. Due to their excellent resolution and reliability, optical encoders have become the preferred choice in applications where dependable detection of position and speed variations is essential.

Beyond accuracy, these devices are characterised by their resistance to external electromagnetic disturbances and their ability to operate effectively in complex industrial environments. Their compact design, compatibility with multiple communication interfaces, and high measurement reliability make them suitable for sensitive applications that demand stability and precision. For this reason, optical rotary encoders are considered a key element in the design and implementation of advanced motion control and positioning systems in modern industry.



Fig. 1 An optical rotary encoder [1]

## A. Applications of Optical Rotary Encoders

Optical rotary encoders represent indispensable components in contemporary machines and automated control systems. In CNC machining, for instance, they are integrated into the spindle drive to provide feedback on the rotational speed and position of the main spindle, which is central to the cutting processes. Since spindle motion directly affects machining accuracy and product quality, encoder feedback is critical for maintaining precise rotational speed and achieving consistent operation within defined process parameters.

With appropriate configuration, encoders can also support diagnostic functions within automated systems. In advanced CNC machines, they are used to verify reference positions during initialisation, detect lost steps in stepper motors, or identify mechanical blockages and transmission faults. In this way, encoders contribute not only to motion measurement but also to fault detection and system integrity.

In robotics, optical encoders serve as fundamental feedback devices for measuring angular displacement, speed, and rotation direction of moving joints and components. Embedded within servo or stepper motors, they enable closed-loop control that ensures precise joint positioning, which is essential for tasks requiring high accuracy, such as assembly, manipulation, or finishing operations. In mobile robotics, encoders attached to wheels or drive systems are used to estimate distance passed and velocity, forming the basis for odometry and supporting navigation algorithms. Furthermore, they are essential in coordinating multiple axes in complex robotic systems, where synchronised motion is required.

Emerging applications such as collaborative and medical robotics benefit from encoders due to their ability to deliver stable, high-resolution feedback. This ensures safe interaction with humans, reliable calibration, and early detection of potential mechanical faults, thereby enhancing safety and trust in robotic operations.

Encoders also play a significant role in automated production and logistics systems. In conveyor systems, they monitor the position of products as they move through different processing or packaging stages, providing real-time feedback for activating manipulators, inspection sensors, or sorting mechanisms. Similarly, in automated warehouses, they are integrated into transport vehicles and lifts to enable safe and efficient material handling.

In addition, optical rotary encoders are applied in precision measurement and quality control systems. When combined with high-accuracy positioning sensors, they enable exact alignment of measuring heads, support laser-based machining, and assist in automated calibration tasks. These features position optical encoders as vital contributors to higher levels of automation, safety, and adaptability across a broad range of monitoring and control applications.

Taken together, these characteristics highlight that optical rotary encoders are not merely sensors for measuring angular position or speed but integral components of intelligent control, monitoring, and diagnostic systems. Their applications extend from conventional CNC machining to advanced robotic platforms, enhancing precision, reliability, and automation in industrial and technological processes. With their ability to provide robust and high-resolution feedback, they form a foundation for adaptive and synchronised motion-tracking systems, which are indispensable for Industry 4.0 and modern automation.

## B. Operating Principle of Optical Rotary Encoders

The fundamental operation of an optical rotary encoder relies on the interaction between a light source and a precisely engineered rotating disc, which is mounted on the rotational axis of the object whose angular displacement is being measured (Fig. 2). This disc features alternating regions with distinct optical characteristics, such as transparent and opaque sections or reflective and non-reflective surfaces. As the disc rotates in unison with the target component, it enables continuous real-time measurement of angular movement.

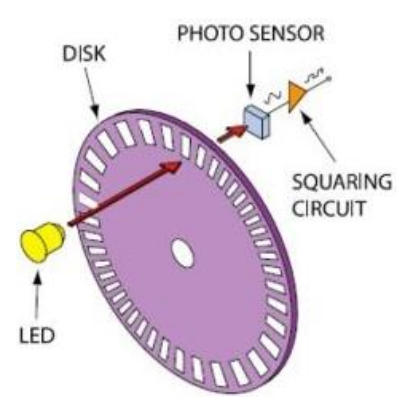


Fig. 2 Operating principle of an optical rotary encoder [2]

Typically, the light source is a monochromatic LED that either passes through or reflects off the surface of the disc, depending on the specific optical design. As the disc spins, the light is intermittently transmitted or blocked by these patterned regions, producing a series of periodic interruptions or pulses in the light signal. These variations are captured by photodetectors, most commonly photodiodes or phototransistors, positioned opposite the light source.

The photodetectors convert changes in light intensity into electrical signals, which are then processed as digital pulses. Each interruption or passage of light generates an individual pulse, forming a sequence that encodes the rotational information of the disc. By analysing the frequency, order, and phase difference of these pulses, the encoder can accurately determine the angular position, direction, and speed of the rotating element.

## C. Configuration of Optical Rotary Encoders

The structural configuration of optical rotary encoders represents a critical determinant in ensuring accurate, reliable, and repeatable measurement of rotational motion. Within contemporary industrial and research-orientated applications, the escalating demand for high precision and operational dependability has driven both the refinement and widespread implementation of encoders with multi-channel architectures. These advanced arrangements embody a significant technological progression compared with the more conventional single-channel solutions, providing not only enhanced resolution but also expanded functional capacity.

Typically, the most widely adopted configurations incorporate two or three distinct channels, conventionally denoted as A, B, and Z, each of which performs a specific role within the system (Fig. 3). These channels are carefully synchronised, both with one another and with the associated control unit, to guarantee coherent and precise operation. Channels A and B form the foundation of motion detection, generating quadrature signals offset by 90 electrical degrees. This deliberate phase displacement enables the

encoder to differentiate rotational direction — whether clockwise or anticlockwise — through the sequential activation and deactivation of signals. The order in which the transitions occur provides the control system, frequently realised by microcontrollers or programmable logic controllers, with unequivocal information for determining both velocity and orientation of rotation.

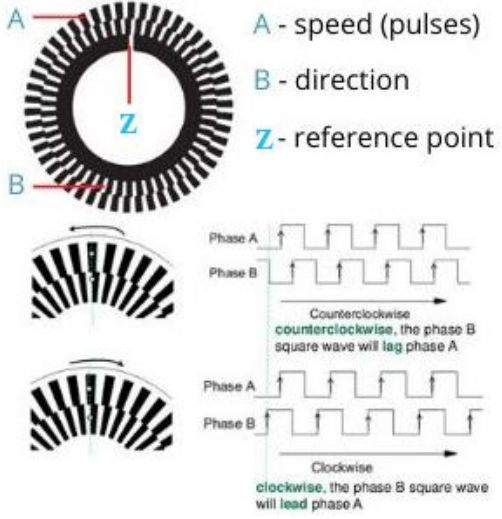


Fig. 3 Configuration of optical rotary encoders [3]

In addition to the enhanced resolution and the capability for precise directional detection, multi-channel configurations also serve a critical role in improving the overall reliability of encoder-based measurement systems. Their design inherently offers greater resilience through redundancy, signal verification, and error-checking mechanisms, thereby mitigating the risks posed by electrical interference or minor mechanical disturbances. Such robustness ensures that encoders remain dependable components across a wide variety of technical applications.

## D. Mechanical Vibrations as a Source of Instability in Sensor Metrology

Within the framework of optical rotary encoder systems, it is essential to carefully examine the challenges associated with their performance under real-world dynamic conditions, which often impose complex technical constraints and act as potential sources of measurement error. In both scientific literature and industrial practice, such dynamic influences are most commonly characterised as mechanical vibrations, which are widely recognised as the primary and representative factor causing disturbances in industrial environments.

This perspective is included by several studies [4–7], where mechanical vibrations can be considered as a reliable and practical approximation of real operating conditions.

Although optical rotary encoders are engineered to deliver high-resolution and reliable measurements, their susceptibility to external dynamic influences—particularly vibrations—remains a critical consideration. These disturbances can significantly affect measurement accuracy, making vibration analysis an indispensable component of sensor metrology and system design. In this regard, however, it becomes evident that while previous research has provided valuable insights into the influence of vibrations, the scope of these investigations remains limited, highlighting the need for further expansion and more systematic evaluation of encoder performance under dynamic conditions.

## E. Scope and contribution of this research

A review of the existing literature reveals a notable gap regarding the systematic evaluation of optical rotary encoder performance under vibrational influence. Despite their expanding implementation—particularly in CNC machining, high-precision manufacturing, automation, and robotics—their sensitivity to mechanical vibrations remains insufficiently explored. Given the rapid pace of technological advancement and the increasing integration of these devices across diverse industrial applications, ensuring their optimal performance has emerged as both a critical challenge and a priority for research.

This underscores the necessity for the development of novel methodologies to analyse measurement errors and assess the performance of optical rotary encoders under dynamic operating conditions. Within this context, it is particularly important to conduct comprehensive and systematic investigations that encompass not only quantitative metrics such as accuracy and repeatability, but also a qualitative understanding of encoder behaviour in vibratory environments.

Consequently, there is a clear need to establish an innovative model capable of evaluating and predicting encoder performance across varying vibration amplitudes and frequencies. Such a model would enhance insight into their real-world behaviour and provide essential data for assessing their reliability in dynamic systems. Focusing research efforts in this area is crucial for improving measurement precision, ensuring system dependability, and reinforcing the overall trustworthiness of applications that incorporate optical rotary encoders.

The structure of this paper is organised as follows. After this introduction, in the second section, the procedure for identifying and reviewing relevant literature is outlined. In the third section, research addressing the fundamental principles and applications of optical rotary encoders is reviewed, and the main limitations of existing studies are identified. In the discussion chapter, the insights obtained from the literature review are analysed, with emphasis placed on the research gaps. Finally, in the conclusion, the principal findings are summarised, the key outcomes of the

review are discussed, and potential directions for future research are presented.

#### II. MATERIALS AND METHOD

The methodology applied in this review was designed to ensure both breadth and depth in the identification, selection, and analysis of the scientific literature dealing with optical rotary encoders and their measurement accuracy under vibrational influence. Unlike empirical studies, where the focus lies on laboratory procedures or numerical simulations, the present work places its emphasis on establishing a systematic framework for the evaluation of previously published knowledge. Although the overall procedure comprises several stages, for the purposes of this review, particular attention is given to a selected set of key phases, namely: (i) comprehensive database search, (ii) keyword formulation and refinement, (iii) application of inclusion and exclusion criteria, and (iv) classification and analytical synthesis of the selected academic literature.

## A. Literature Search Strategy

The initial step was to identify and review a broad range of scientific databases that provide reliable coverage in the fields of engineering, automation, signal processing, and measurement science. Several platforms were systematically searched, among which the most prominent were IEEE Xplore, Scopus, Web of Science, and ScienceDirect. These repositories, along with additional specialised sources, were selected due to their international recognition, extensive indexing of peer-reviewed journals, and comprehensive coverage of both theoretical and applied research in measurement technologies.

The search process was conducted in an iterative manner. In the first iteration, broader search terms associated with optical rotary encoders, encoder accuracy, and similar expressions were applied. This generated a wide pool of references, many of which only partially aligned with the core research focus. To refine the results, subsequent iterations introduced a larger set of possible terms with a higher likelihood of relevance, like vibration influence, measurement error, frequency response, etc. Different combinations of these and related terms were explored as potential variants for searching, allowing a more targeted selection of studies that addressed the effects of vibrational disturbances on encoder performance.

The search encompassed a wide range of sources, including publications written in English, as it remains the predominant language of technical and engineering research. Additionally, multiple databases were consulted to include journal articles, conference proceedings, and doctoral dissertations, recognising that these sources often contain original findings and complementary perspectives that may not yet be reflected in journal publications.

## B. Inclusion and Exclusion Criteria

The refinement of the initial literature required the application of rigorous selection criteria. Studies were considered eligible for inclusion if they met the following requirements:

- They were published in peer-reviewed journals, conference proceedings, or reputable scientific monographs;
- They explicitly addressed the issue of measurement accuracy, performance evaluation, or error quantification in optical rotary encoders:
- They investigated external influences that could compromise measurement reliability, such as mechanical vibrations, thermal fluctuations, or misalignment errors;
- They presented empirical findings, numerical simulations, or analytical models that could be critically evaluated.

On the other hand, publications were excluded if they:

- Focused exclusively on incremental or absolute encoders without consideration of measurement errors;
- Dealt solely with design and manufacturing aspects without testing performance under real-world disturbances;
- Provided descriptive information without quantitative or analytical results;
- Or were published outside the defined temporal window of interest.

Although the time frame was not strictly confined to a single decade, preference was given to studies published in the last 15–20 years, reflecting the rapid technological advancement of encoder systems and the increasing importance of vibration resilience in modern automation.

The process of inclusion and exclusion was carried out in multiple stages, allowing for flexibility in selection. Initially, titles and abstracts were reviewed to identify sources that appeared relevant, while acknowledging that some sources might be reconsidered in later stages. Subsequently, the full texts of potentially pertinent articles were examined, with multiple criteria considered rather than strictly enforced rules. The resulting selection reflected a diverse and adaptable corpus of literature suitable for systematic analysis.

## C. Classification of Selected Studies

To facilitate structured analysis, the final set of sources can be classified into three principal categories:

 Experimental investigations – studies in which encoders were tested under controlled laboratory conditions or within industrial settings. These works typically involved the application of artificial vibrations through electromechanical shakers or the measurement of encoders in situ under operational disturbances. Reported metrics included data

- for angular deviation, RMS error, amplitude–frequency characteristics, etc.;
- Simulation-based studies publications in which mathematical or computational models were developed to predict encoder behaviour. These studies often involved the use of finite element methods (FEM), signal-processing algorithms, or control-system simulations implemented in environments such as MATLAB/Simulink, etc.;
- 3. <u>Hybrid approaches</u> research combining experimental measurements with analytical or numerical models. This class of studies is particularly valuable, as it bridges the gap between theory and practice by validating predictive models against real-world data.

By applying this classification, it is possible to identify patterns across methodologies, highlight recurring analytical techniques, and compare the strengths and weaknesses of different approaches.

## D. Analytical Framework

Once the relevant studies are categorised, a structured analytical framework can be employed. This framework sought to extract information under several dimensions:

- <u>Type of encoder</u>: including incremental versus absolute, resolution levels (measured in pulses per revolution ppr), and the specific application context (robotics, CNC machinery, aerospace, automotive systems, etc.);
- <u>Nature of external influence</u>: with an emphasis on vibrational characteristics (frequency, amplitude, duration), but also considering additional factors such as thermal effects, electromagnetic interference, and mechanical misalignments, etc.;
- Evaluation metrics: error quantification techniques such as root mean square error (RMSE), Fourier and spectral analysis (FFT), time-domain deviation analysis, or calibration-based correction models, etc.;
- <u>Limitations and future recommendations</u>: as reported by the authors themselves, which provide a valuable indication of current research gaps.

This framework enables not only a systematic comparison of methodologies but also the identification of inconsistencies across studies. For instance, while some authors relied heavily on frequency-domain analysis to capture vibration-induced errors, others focused on time-domain error propagation, making direct comparisons difficult. Similarly, while experimental studies often dealt with limited parameter ranges due to technical constraints, simulation-based works tended to simplify the encoder—environment interaction, raising concerns about real-world applicability.

## E. Identification of Research Gaps

The final step of the methodological approach is the synthesis of gaps and limitations. Several issues can emerge consistently:

- A lack of a unified modelling framework that integrates experimental, analytical, and simulation-based insights into a coherent structure;
- Limited availability of systematic testing protocols, with most studies employing ad hoc setups rather than standardised procedures;
- Insufficient attention to parameter variability, such as simultaneous changes in rotational speed, vibration frequency, and amplitude;
- A scarcity of long-duration studies that investigate the cumulative effects of vibrations over extended operational periods.

By systematically highlighting these gaps, the methodological framework lays the foundation for the development of a new innovative model of encoder performance assessment, which is the broader aim of this research effort

#### III. RESULTS

The following section presents a systematic synthesis of the key findings extracted from the reviewed literature. Emphasis is placed on the performance characteristics of optical encoders, the factors influencing their measurement accuracy, and the impact of dynamic operational conditions, particularly vibrations. The analysis is structured to provide a clear overview of both the established knowledge and the gaps identified across experimental, simulation-based, and hybrid studies. By organising the results thematically, this section aims to highlight the critical aspects that govern encoder behaviour, thereby setting the stage for a detailed discussion of mechanical, thermal, and vibrational influences in subsequent subsections.

## A. Application and Relevance of Optical Encoders in Modern Systems

The evaluation of performance and the assessment of measurement errors in optical encoders constitute a fundamental aspect of research in domains where precision and accuracy are of paramount importance. Owing to their capability to provide highly accurate and reliable information regarding angular or linear positions, optical encoders are regarded as essential components within systems designed for position and velocity measurement and control. Their extensive utilisation across industrial, scientific, and technological settings underscores their significance as integral elements of contemporary automated systems.

Their role is particularly pronounced in modern CNC machining centres, where they are employed to monitor relative displacements and ensure the precise positioning of moving components [8]. These sensors facilitate automatic correction and minimisation of errors during the machining process, which is crucial for the manufacture of components with complex geometries and stringent quality requirements.

In robotics, optical encoders play a central role in motion control systems for robotic manipulators [9]. Their precise measurement capability enables

the synchronisation of movements, which is a key factor in optimising and enhancing the efficiency of production processes.

Moreover, optical encoders are employed as sensors for determining the position and velocity of moving objects within tracking systems [10]. This application allows for trajectory analysis and real-time adjustment of control strategies, thereby ensuring high accuracy and rapid responsiveness under dynamic operating conditions.

The inherent precision and reliability of these devices also permit their deployment in a variety of other domains, highlighting the critical importance of encoder performance as a determinant of overall system functionality. Investigations into this topic emphasise the necessity of analysing the factors that influence measurement accuracy. According to the study conducted in [5], the principal factors affecting the performance of optical encoders include mechanical deformations, thermal variations, and exposure to vibrations within the systems in which they are integrated.

## B. Mechanical Factors and Their Influence on Optical Encoder Accuracy

Mechanical deformations and thermal variations constitute critical factors influencing the measurement accuracy of optical encoders. In [11], a methodology is presented for quantifying and modelling thermally induced deformations that contribute to positioning errors in multi-axis machining centres. The study further introduces a structured framework for minimising encoder-related errors through a detailed analysis of both the spatial temperature distribution and the rigid body kinematics, thereby offering a systematic approach to mitigating measurement inaccuracies associated with thermal effects.

Furthermore, the impact of thermoelastic deformations, originating from diverse thermal sources, as well as ambient temperature fluctuations, on the accuracy of optical linear encoders has been investigated in [12]. A real-time model for geometric and thermal error compensation was developed, which, when implemented on an FPGA platform, demonstrated a significant reduction in measurement errors—reported to reach up to 98%. Similarly, the influence of thermally induced deformations, caused by heat generation in linear motor systems, on both encoder accuracy and the structural integrity of machining centres has been examined in [13]. The study identified the principal sources of thermal errors, including thermal expansion, linear scale displacement, and deformation of machine components.

The consequences of prolonged machine operation, particularly the effects of continuous thermal loading on moving components during extended work cycles, were explored in [14]. It was observed that the heat generated during operation induces structural expansion, resulting in diminished positioning accuracy of moving elements. Consequently, extended utilisation of machining centres leads to increased cumulative error in encoder

measurements, accompanied by a reduction in operational precision and efficiency.

In a related investigation, structural analysis of CNC machining centres, with emphasis on deformations and thermal fluctuations as primary contributors to encoder measurement inaccuracies, was conducted in [15]. This research combined finite element models with experimental calibration techniques to enable precise quantification of these phenomena. Special attention was given to the interaction between power control systems, machining conditions, and the structural dynamics of the machines. The study confirmed that both temperature fluctuations and mechanical deformations constitute key factors in the degradation of positional accuracy within CNC systems.

## C. The Influence of Vibrations on Measurement Accuracy

Although extensive attention has been devoted to the effects of deformations and thermal variations, comparatively fewer studies have investigated the behaviour and performance of encoders under the influence of vibrations. Within this context, which remains a relatively underexplored scientific domain, research was conducted in [8], where—alongside the analysis of errors in optical linear encoders induced by deformations and temperature changes—the impact of vibrations on their operational reliability was also examined. The study focused on the identification, classification, and quantitative evaluation of vibration effects, with the aim of gaining a deeper understanding of the limitations and potential applications of these devices across diverse technical and industrial contexts.

The examination of encoder measurement errors occurring during the operation of CNC machine tools, particularly in relation to the synchronisation of moving components and their accurate positioning, has traditionally been concentrated on the structural properties of the machines themselves. This line of research encompasses the study of design imperfections, weaknesses in the mechanical layout, damping characteristics, and the effects of clearances in joints, transmission mechanisms, and other structural elements.

In this regard, in [16] respectively [17], a method for assessing geometric errors in multi-axis CNC machine tools was proposed. Their approach relied on measurements of three-dimensional volumetric lengths and the development of a universal error model applicable across different machine configurations. Considering the significance of measurement accuracy, the implementation of the proposed model enables software-based error compensation as well as precise diagnosis of machine tool functional deficiencies. Within this methodological framework, high-precision length measurements combined with straightforward execution were identified as the most suitable technique for determining positioning errors. Moreover, it was confirmed that the design of the measurement system and the precise

formulation of the error model—aligned with the correlation of influential parameters—play a crucial role in ensuring accurate diagnostics and enhancing the reliability of measurement outcomes.

## D. The Optical Encoder as a Potential Source of Error

While errors in the synchronisation of motion and in the accurate positioning of moving components in machine tools are most frequently associated with the structural design and performance of the machines themselves, relatively few investigations have directly addressed the encoder as a potential source of error. Nevertheless, several studies suggest that the encoder may indeed represent a contributing factor, thereby opening new perspectives for the analysis and enhancement of the precision of such devices.

In this regard, the application of a digital time-interval technique for measuring torsional vibrations in rotating shafts was examined in [4]. Within this study, a calibration method for encoders under real operating conditions was proposed, whereby a reference sequence corresponding to the true angular intervals of the encoder was generated. To minimise errors, a resampling algorithm was employed, producing a sequence of samples at constant time intervals. The results demonstrated that the method effectively reduces the impact of frequency dispersion—caused by variations in rotational speed—even when using high-precision optical encoders.

Furthermore, devices and methods designed to isolate encoders from vibrational influences through the application of external flexible elements and other structural components were introduced in the patents [18] and [19]. These contributions emphasise the significant role of vibrations as a factor that degrades encoder performance. However, a review of the available literature reveals that information concerning the specific performance of encoders within their operational frequency ranges under dynamic conditions remains limited.

# E. Modern Methods for Evaluating the Performance of Optical Encoders under Vibrational Influence

According to the findings in [5], optical encoders are generally regarded as highly precise devices, even when exposed to vibrations. Deviations in measurement are most commonly attributed to the CNC machine tools themselves, including their components, gears, belt drives, and other mechanical elements. However, it is emphasised that this assumption is not universally valid, highlighting the necessity for methods specifically designed to evaluate the accuracy and performance of optical encoders under vibrational conditions, thereby ensuring optimal functionality across diverse operational scenarios. To achieve this purpose, an innovative approach is presented for assessing encoder performance under vibrational influence.

This method differs from traditional approaches by not merely identifying resonant frequencies and signal acceleration but also introducing the concept

of "measuring error for a frequency range". Such a perspective enables a more comprehensive evaluation of performance, demonstrating that, under real operational conditions, signal acceleration is less critical compared to the measurement errors induced by vibrations in optical encoders.

The methodology represents a significant advancement in this research area, as it considers two critical aspects: first, the magnitude of encoder measurement errors at resonance; and second, the errors occurring in non-resonant frequency ranges. Successful implementation relies on several key factors, including the choice of signal type, analysis of non-linear signal variations, sampling frequency specification, and signal composition. These elements are fundamental to accurately assessing encoder performance and ensuring their functionality under varying operational conditions.

Application of this method produces a high-resolution spectrum of encoder behaviour, allowing the identification of multiple instability zones within the examined frequency range. Parameters for these evaluations are based on the European standard in [20], facilitating the identification of critical frequencies during durability testing. Under dynamic loading, the device is exposed to continuously variable frequencies within an adopted range of 55 Hz, though testing may also extend to other ranges according to the capabilities of the vibration-generating equipment. Additionally, the amplitudes of vibration for different encoder types are adjusted individually. For visualisation of mechanical effects, an acceleration amplitude of 200 m/s² was considered appropriate, consistent with specifications from several commercial encoder manufacturers. Testing duration was initially set to over five minutes, resulting in substantial data files; to maintain manageable file sizes for numerical processing, the duration was limited to 90 s, with recording activated at the onset of testing.

The results indicate multiple instability zones within the specified range, significantly influencing measured values and increasing total measurement error. Analysis demonstrated that errors could reach up to three times the declared encoder accuracy, confirming that optical encoders can constitute significant sources of measurement error in high-frequency vibrational environments, even when these comply with international environmental testing standards. The proposed methodology not only identifies performance weaknesses but also provides practical guidance for improvement, offering substantial value to manufacturers seeking design enhancements and end-users aiming to optimise performance through validation.

In a related study [6], a detailed investigation is conducted into the measurement errors of optical linear encoders under vibrational influence across various mounting conditions. Three commercial encoders from different manufacturers were examined to yield representative and generalisable results. The methodology aimed to quantify accuracy

degradation under vibrational load and its dependence on mounting conditions.

Several fundamental parameters were defined for testing, including frequency range, vibration amplitude, and test duration. Parameter selection followed the recommendations in [20], which enables precise assessment of system stability through the identification of critical frequencies. The frequency range was chosen to comprehensively characterise encoder measurement error relative to vibration frequency, corresponding to the minimum and maximum resonant frequencies of machine tool structures, as reported in [21]. The standard also allows variation in vibration amplitude according to the specifications of the tested commercial encoders, as confirmed in [5]. A maximum acceleration amplitude of 100 m/s<sup>2</sup> was selected to ensure proper encoder operation without additional vibration protection. At low frequencies (20-82.3 Hz), vibration was controlled via a constant displacement of 0.75 mm, with a  $\pm 3$  dB tolerance. Below 82.3 Hz. improved control could be achieved by reducing the frequency ramp rate while considering test duration, which depends on the size of the data archive storing encoder signals. A linear frequency ramp of 22 Hz/s was applied to establish a direct relation between frequency and test duration while maintaining an optimised archive size.

The results revealed that the dynamic characteristics of optical linear encoders vary significantly with vibration direction. In certain positions, errors exceeded nominal accuracy, even at acceleration levels for which additional anti-vibration measures were not recommended. Mounting position could also introduce new resonances, producing substantial errors. Results were presented in diagrams showing encoder measurement errors as a function of vibration frequency.

Analysis demonstrated that vibration-induced encoder errors primarily arise from the relative motion between the two gratings forming the interference pattern—the fundamental measurement mechanism. Improper encoder installation in machine tools further amplifies measurement errors. Encoders operating within specifications under different mounting conditions may exhibit errors exceeding allowed tolerances. These findings underscore the importance of proper installation and monitoring of operational conditions to achieve high precision when employing optical linear encoders.

#### IV DISCUSSION

A comprehensive examination of the research confirms the fundamental role of optical encoders as indispensable components within modern systems of measurement, positioning, and control. Their contribution extends far beyond the function of mere sensing devices; rather, they represent the foundation of many industrial processes where accuracy, stability, and repeatability are essential. High levels of precision and reliability are not

simply desirable characteristics but indispensable prerequisites for the efficient operation of complex automated systems, including CNC machine tools, robotics, aerospace platforms, and a variety of mechatronic applications. Within such domains, optical encoders act as the link between mechanical motion and digital interpretation, thus enabling real-time monitoring and decision-making. Consequently, the extent to which their functionality is preserved under dynamic working environments becomes a subject of critical importance for both scientific investigation and industrial practice.

Previous research consistently indicates that the accuracy of optical encoders, and more broadly their ability to provide highly stable measurement outputs, is particularly sensitive to external factors. Among these, vibrations have emerged as one of the most frequent and severe sources of disturbance. Dynamic conditions, characterised by rapid changes in position, speed, or direction, introduce mechanical and electronic challenges that affect the stability of measurement signals. In such environments, additional factors, including mechanical loads, thermal fluctuations, electronic interference, and long-term wear of components, further exacerbate instability. The combined effect of these influences manifests in increased measurement error, signal degradation, loss of synchronisation, or even physical damage to the encoder structure. From a systems perspective, such inaccuracies may propagate through control loops, producing deviations in machine performance, reduced product quality, or, in some cases, complete process failure.

Specialised attention in the literature has been directed towards optical linear encoders, where it has been repeatedly demonstrated that their measurement precision is vulnerable to vibrational excitation as well as the conditions under which they are mounted. Empirical results suggest that high-frequency vibrations or sudden shocks can lead to abrupt signal losses, reduced stability of the optical interference pattern, and, in severe cases, structural degradation. These findings underline the critical importance of both robust mechanical design and meticulous installation practices as preventive measures. The implication is that even relatively small deviations in mounting alignment or inadequate damping of vibrations may drastically compromise overall accuracy. Consequently, high-precision in manufacturing and automation, encoder design and installation procedures must be approached with the same rigour as the calibration of the measuring system itself.

Despite these insights, a closer review of the scientific literature reveals a substantial gap regarding the systematic evaluation of optical rotary encoders under the influence of vibrations. While their deployment in industrial environments continues to expand—most notably in CNC machining, robotic automation, and precision assembly—the extent to which they are affected by dynamic excitation remains underexplored. This lack of detailed

understanding contrasts with the growing technological demand for robust, vibration-resistant measurement systems. The rapid advancement of digital manufacturing, the rise of Industry 4.0, and the integration of intelligent monitoring systems all emphasise the need for encoders capable of maintaining accuracy under increasingly complex operating conditions. The insufficient exploration of their vibrational sensitivity thus represents not only a scientific limitation but also a pressing industrial concern.

Addressing this deficiency necessitates the development of new methodologies for analysing measurement errors and evaluating the performance of optical rotary encoders under dynamic conditions. Such methodologies must transcend simple accuracy checks, incorporating both quantitative and qualitative aspects of encoder behaviour. Quantitative dimensions include frequency response, measurement deviation, and error propagation over time, while qualitative insights pertain to understanding how encoders react to varying modes of excitation, resonance phenomena, and mounting configurations. Without this dual perspective, evaluations remain incomplete and risk underestimating the limitations of encoders in real-world scenarios.

The literature review also highlights that while considerable effort has been directed towards identifying the influence of temperature variations, structural deformations, and machine imperfections, the effects of vibrations on rotary encoders have not received equivalent systematic attention. This imbalance indicates that although the scientific community acknowledges multiple external influences on encoder performance, the vibrational component is yet to be fully integrated into standardised evaluation procedures. Initiatives do exist to model encoder accuracy in dynamic conditions, yet there remains no universally accepted framework that encompasses both the frequency spectrum and the range of potential measurement errors. This absence of a standardised, comprehensive model leaves a significant research gap and underscores the importance of extending inquiry into this area.

Developing an innovative model for assessing the performance of rotary encoders under various levels and frequencies of vibration is therefore not merely desirable but essential. Such a model would not only provide researchers with the tools to quantify and interpret encoder behaviour under realistic conditions but would also generate practical guidelines for industrial users. By simulating dynamic excitations, identifying resonance zones, and quantifying error propagation, it would be possible to predict performance degradation before it compromises system reliability. Furthermore, the model could inform the design of next-generation encoders with enhanced vibration resistance, whether through structural reinforcement, improved signal processing algorithms, or advanced mounting technologies.

In essence, the discussion underscores that optical rotary encoders occupy a position of growing strategic importance within advanced technological systems. Their ability to deliver accurate, repeatable measurements in environments characterised by dynamic stress will directly influence the reliability of industrial automation, robotics, and precision manufacturing. At present, the absence of comprehensive models and systematic evaluations represents a limitation in both the academic and industrial knowledge base. Consequently, addressing this gap is not only a scientific opportunity but also a prerequisite for ensuring that optical encoders can continue to serve as trustworthy components in the rapidly evolving landscape of modern engineering applications.

### V. CONCLUSION

The analysis of the available literature demonstrates that optical rotary encoders constitute critical elements within modern measurement and control systems, particularly in applications where accuracy, stability, and reliability are non-negotiable. Their widespread use across domains such as CNC machining, robotics, aerospace, and precision manufacturing reflects both their technological sophistication and their indispensable role in enabling digital transformation within industry. However, this review has also revealed a pronounced research gap: despite their prominence, the performance of optical rotary encoders under vibrational influence remains insufficiently examined in a systematic manner.

The findings consistently underline that vibrations, whether originating from machine dynamics, environmental disturbances, or structural imperfections, represent one of the most persistent and disruptive factors affecting encoder accuracy. While certain studies have explored the impact of temperature variation, thermal expansion, and mechanical alignment on encoder performance, vibrational effects have not been addressed with the same depth or methodological rigour. This imbalance has created a fragmented knowledge base in which partial insights exist, yet a holistic and standardised framework for evaluating encoder behaviour under dynamic conditions is still absent.

Against this backdrop, the rationale for model development becomes clear. The need is twofold: on the one hand, to provide researchers with analytical tools capable of quantifying measurement errors, identifying resonance effects, and simulating encoder behaviour across different frequency domains; on the other, to offer practitioners practical guidelines for selecting, installing, and operating encoders in environments where vibration is inevitable. A comprehensive model would therefore bridge the existing gap between theoretical understanding and industrial application, while also fostering innovation in encoder design, calibration, and error mitigation strategies.

Furthermore, the urgency of such development is heightened by the accelerating pace of technological progress. The expansion of intelligent manufacturing, cyber-physical systems, and autonomous platforms requires

measurement devices that can withstand increasingly complex operating conditions. Without robust methodologies for evaluating and predicting encoder accuracy under vibration, the reliability of entire systems may be compromised, undermining the very foundations of precision-driven industries.

In conclusion, the literature perspective presented here underscores both the critical role of optical rotary encoders and the inadequacy of current approaches to assessing their accuracy in vibrational environments. The development of a systematic, standardised model is therefore not merely an academic exercise but a strategic necessity. Such a model would enhance scientific understanding, inform industrial practice, and ultimately ensure that optical rotary encoders continue to serve as reliable, high-performance components within the progressing domain of modern engineering and automation.

#### REFERENCES

- [1] https://www.indiamart.com/proddetail/absolute-rotary-encoder-2854198813388.html
- [2] https://www.sensortips.com/featured/what-are-rotary-optical-rotary-encoders/
- [3] https://eltra-encoder.eu/news/absolute-vs-incremental-encoder
- [4] Resor, B., Trethewey, M., & Maynard, K. (2005). Compensation for encoder geometry and shaft speed variation in time interval torsional vibration measurement. Journal of Sound and Vibration, 286, 897–920.
- [5] Alejandre, I., & Artés, M. (2007). Method for the evaluation of optical encoders' performance under vibration. Precision Engineering, 31(2), 114-121.
- [6] Lopez, J., Artés, M., & Alejandre, I. (2011). Analysis of optical linear encoders' errors under vibration at different mounting conditions. Measurement, 44(8), 1367-1380.
- [7] Lopez, J., & Artes, M. (2012). A new methodology for vibration error compensation of optical encoders. Sensors, 12(4), 4918-4933.
- [8] Alejandre, I., & Artés, M. (2004). Machine tool errors caused by optical linear encoders. Proceedings of the Institution of Mechanical Engineers, Part B: Journal of Engineering Manufacture, 218(1), 113–122.
- [9] Rodriguez-Donate, C., Osornio-Rios, R., Rivera-Guillen, J., & Romero-Troncoso, R. (2011). Fused smart sensor network for multi-axis forward kinematics estimation in industrial robots. Sensors, 11, 4335–4357.
- [10] Chong, K.-K., Wong, C.-W., Lu, J. S. F., Yew, T.-K., Ng, S.-S., Liang, S., Lim, Y.-S., & Lau, S. L. (2009). Integration of an on-axis general sun-tracking formula in the algorithm of an open-loop sun-tracking system. Sensors, 9, 7849–7865.
- [11] Delbressine, F., Florussen, G. H. J., Schijvenaars, L. A., & Schellekens, P. H. J. (2006). Modelling thermomechanical behaviour of multi-axis machine tools. Precision Engineering, 30, 47–53.
- [12] Alejandre, I., & Artés, M. (2004). Real thermal coefficient in optical linear encoders. Experimental Techniques, 28, 18–22.

- [13] Kim, J.-J., & Jeong, Y. H. (2004). Thermal behavior of a machine tool equipped with linear motors. International Journal of Machine Tools and Manufacture, 44(7–8), 749–758.
- [14] Ramesh, R., Mannan, M. A., & Poo, A.-N. (2000). Error compensation in machine tools—A review. Part II: Thermal errors. International Journal of Machine Tools and Manufacture, 40, 1257–1284.
- [15] Altintas, Y., Brecher, C., Weck, M., & Witt, S. (2005). Virtual machine tool. CIRP Annals Manufacturing Technology, 54(2), 115-138.
- [16] Weck, M., Hessel, C., & Müller-Held, B. (2000). The virtual machine tool. Production Engineering, 7(2), 89-94.
- [17] Florussen, G. H. J., Delbressine, F., Molengraft, M. J. G., & Schellekens, P. H. J. (2001). Assessing geometrical errors of multi-axis machines by three-dimensional length measurements. Measurement, 30, 241-255.
- [18] Shiro, Y. (2004). Patent JP2004325171. Yaskawa Electric Corporation.
- [19] Shinichi, U. (2004). Patent JP2004068948. Japan Steel Works.
- [20] EN 60068-2-6. (1996, July). Environmental testing. Part 2: Tests. Tests Fc: Vibration (sinusoidal). CENELEC.
- [21] Mahdavinejad, R. (2005). Finite element analysis of machine and workpiece instability in turning. International Journal of Machine Tools & Manufacture, 45(7), 753–760.

## Automatic Detection and Classification of Mango Diseases Using Deep Learning Methods

Halil Talha GÜNDÜZ\*,1
Selim SÜRÜCÜ <sup>2</sup>
Esra GÜNEY <sup>3</sup>

Department of Computer Engineering, Çankırı Karatekin University, Turkey. Orcid: 0009-0001-8282-7233

<sup>&</sup>lt;sup>2</sup> Department of Computer Engineering, Çankırı Karatekin University, Turkey. Orcid: 0000-0002-8754-3846

<sup>&</sup>lt;sup>3</sup>Rectorate, Çankırı Karatekin University, Turkey. Orcid: 0000-0001-5078-9722

<sup>\*(</sup>haliltalhagunduz@gmail.com) Email of the corresponding author

#### **ABSTRACT**

The agricultural sector faces challenges associated with traditional methods, which are time-consuming, costly, and heavily dependent on human expertise, often leading to errors and economic losses. Rapid advancements in technology, particularly artificial intelligence (AI), offer a promising solution. AI offers a wide range of applications in agriculture, from automatic plant disease detection to pest identification. This study aims to overcome the limitations of traditional agriculture by automatically detecting mango diseases using machine learning models. A dataset consisting of 1,500 images, called the Mango Disease Healthy Dataset (MangoDHDS), was used for training, and the process was performed in the Google Colab environment. Model performance was evaluated using accuracy as a metric, with the DenseNet121 model achieving the highest performance at 85%. These results demonstrate that deep learning-based systems can be an effective tool for automatic disease detection in the agricultural sector.

Keywords – Mango disease detection, DenseNet201, Smart agriculture, disease classification, Vision Transformers

#### I. Introduction

Mango is a seasonal fruit of great economic and cultural importance worldwide. However, this valuable crop is highly susceptible to yield, and quality losses caused by various diseases. Traditional disease detection methods primarily rely on manual inspections. These methods are not only time-consuming and costly but also require specialized knowledge. Furthermore, even with expert supervision, the expected level of accuracy is not always achieved, and in some cases, results can be inconsistent. This leads to significant economic losses, especially for farmers whose agricultural activities depend heavily on mango production [1].

In recent years, image processing and artificial intelligence (AI) technologies have demonstrated significant potential in overcoming these challenges in the agricultural sector. These technologies have been applied in areas such as disease diagnosis and yield optimization, paving the way for the development of smart agricultural applications. Applications such as disease detection [2], yield estimation [3], pest detection [4], and automated spraying [5] have become possible using data obtained from remote sensing technologies such as unmanned aerial vehicles and satellite imagery. These approaches offer promising solutions to overcome the limitations of traditional methods.

The main objective of this study is to develop an automated system for image analysis, classification, fruit disease diagnosis, and smart agriculture

applications. This system is based on training machine learning models on a "Mango labeled image dataset called Disease Healthy (MangoDHDS) [6]. This dataset contains healthy and diseased mango samples collected from various sources. The proposed automated system aims to facilitate early and accurate detection of mango diseases, contributing to the maintenance of yield and quality. Furthermore, the study aims to determine the most effective solution by comparing the performance of transfer learningbased algorithms such as ResNet50, EfficientNetB0, and DenseNet121 with the performance of Image Transformer (ViT)-based algorithms such as ViT-Base and Swin Transformer.

#### II. MATERIALS AND METHOD

### A. Dataset

This study utilized the MangoDHDS dataset. This dataset consists of images collected via smartphone cameras between April and July from 2021 to 2023. The dataset contains a total of 1,500 images, comprising 5 classes with 300 images per class [6]. These classes are: Anthracnose, Bacterial Canker, Scab, Stem End Rot, and Healthy. The images have a resolution of 256x256 pixels. Experts from the plant pathology and research departments provided guidance during the image collection process.



Fig. 1 Classes in the MangoDHDS dataset and sample images belonging to these classes

## B. Deep Learning Models Used in the Study

In this study, two main deep learning model approaches with different architectures that have proven successful in image classification tasks were used. These approaches are: Convolutional Neural Networks (CNN)-based Transfer Learning and Vision Transformer (ViT) Algorithms.

- Transfer Learning: This approach involves using models that have been pre-trained on large datasets for a new task on a smaller, more specific dataset. The ImageNet dataset is generally preferred as the large dataset. Transfer learning enables high accuracy even with limited datasets and significantly reduces training time. In this context, three popular CNN models were used to compare their performance due to architectural differences:
  - ResNet50 (Residual Network): A transfer learning model that effectively solves the vanishing gradient problem in deep network training through "skip connections" [7]. It has been widely preferred in recent years [8,9]. ResNet models,

- classified according to the number of layers they contain, have been preferred in this study in their 50-layer version.
- EfficientNetB0: A transfer learning model developed to optimize the depth, width, and resolution of the model using a balanced compound scaling method [10]. This model aims to achieve higher performance with fewer parameters.
- O DenseNet121 (Dense Convolutional Network): Thanks to its dense connection structure, each layer is a transfer learning approach that receives input from all previous layers [11]. Dense connections encourage the reuse of features and optimize the model's information flow, enabling it to learn more efficiently. This transfer learning model, used for many problems, is among the models that have yielded successful results in literature [12,13].
- Vision Transformer (ViT) Algorithms: These are versions of the Transformer architecture, which revolutionized natural language processing, adapted for image classification tasks [14, 15]. They divide the image into small, fixed-sized patches and process these patches as a sequence. In recent years, they have become a frequently encountered deep learning approach.
  - ViT-Base: It is effective at capturing the global context by directly processing image patches, but it requires large-scale data.
  - Swin Transformer: It is a type of transformer that applies attention mechanism within local windows to reduce computational complexity and facilitates information exchange between windows. This approach enables it to better capture objects at different scales.

## C. Training and Assessment Environment

Model training was performed in the Google Colab environment, which offers GPU support for hardware acceleration. All coding was done using the Python programming language and popular deep learning libraries. The performance of each model has been measured according to the accuracy metric, which is the most used metric in literature. Accuracy, The ratio of correct predictions to the total number of predictions. It is an important metric for the initial evaluation.

This methodology has enhanced the scientific reliability of the study by best showcasing the potential of each model.

### III. RESULTS AND DISCUSSION

In this study, the performance of five different deep learning models used for the detection of mango diseases was carefully evaluated, and important findings were obtained. The results clearly show the effect of each model's architectural features on performance.

As a result of the comparative tests conducted, the accuracy rates of the models are ranked as follows:

- DenseNet121: It has demonstrated the highest performance with a **85%** accuracy rate. The main reason for this model's success is its dense connection structure. The fact that each layer is connected to all previous layers encourages feature reuse, enabling the network to learn more efficiently.
- ViT-Base: It has demonstrated the second-best performance with an accurate rate of **73.33%**. Although it is a Transformer-based model, it is widely accepted in the literature that this architecture generally yields better results with very large datasets.
- Swin Transformer: It has shown lower performance among ViT models with an accuracy rate of 46.67%. The performance of this model indicates that it still has room for improvement, especially on small-scale datasets.
- ResNet50: It was one of the models with low performance, achieving an accurate rate of **35.33%**. This result shows that the architecture of ResNet50 is not sufficient for a classification task involving complex and subtle details, such as mango diseases.
- EfficientNetB0: It showed the weakest performance with an accurate rate of **20.00%**. Although EfficientNet's optimization philosophy is based on efficiency, this study shows that it did not fully adapt to the characteristics of the dataset.

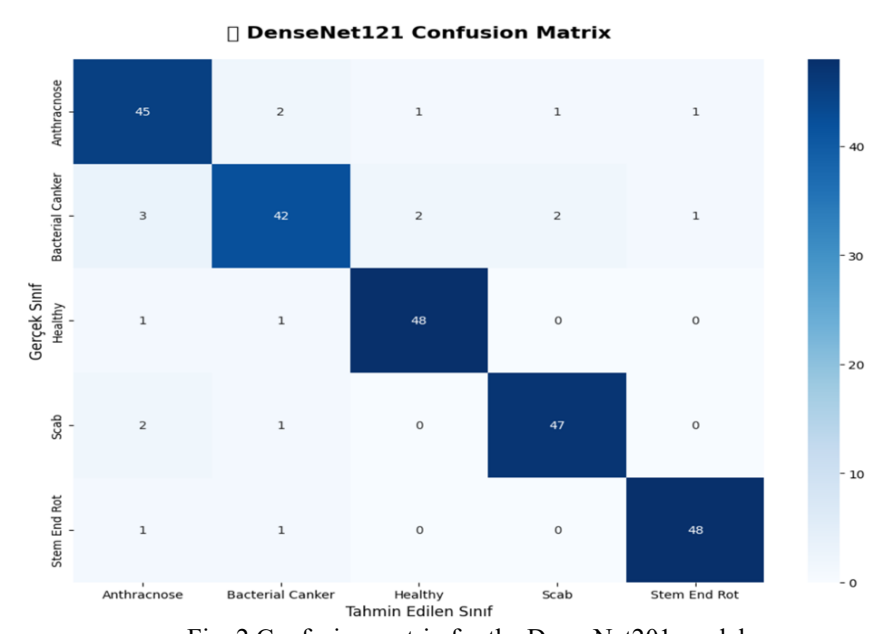


Fig. 2 Confusion matrix for the DenseNet201 model

The confusion matrix for the DenseNet121 model, which yields the best results with an accuracy value of 85%, is shown in Fig. 2. Fig. 2 shows that the model performs quite successfully in predicting the classes Healthy, Scab, and Stem End Rot. The classes that pose the greatest challenge for the model are Anthracnose and Bacterial Canker. Due to visual similarities between these two disease types, the model's tendency to confuse these classes is evident in the cross-predictions in the matrix. For example, 3 images that should have been labeled as Bacterial Canker were predicted as Anthracnose. This confirms the finding mentioned in the report that similar visual characteristics between diseases can lead to some negative situations.

The results obtained are consistent with similar studies. In particular, the superior performance of the DenseNet architecture in complex image classification tasks is also supported by other studies in literature. For example, a different study reported that the DenseNet201 model achieved an accuracy rate of 87.94%. This once again proves that the DenseNet family is an extremely effective solution for image-based disease detection in the agricultural sector.

#### IV. CONCLUSIONS AND RECOMMENDATIONS

This study has demonstrated that deep learning models can be effectively used for the detection of mango diseases. Following a comprehensive evaluation, DenseNet121 stood out among the compared models with a high accuracy rate of 90.67%, proving to be the most effective model in this field. This success once again confirms how critical the dense connection structure in its architecture is for complex image classification tasks. During the training process, all models were successfully trained without any technical issues. However, performance differences were observed between the training and validation sets for some models. This discrepancy is thought to be primarily due to overfitting caused by visual similarities between classes in the dataset. This presents an important area for improvement in future studies.

For future studies, it is recommended that the dataset be expanded first. Collecting a larger number of higher-resolution images for each disease class is expected to improve the generalization ability of the models. Data obtained under different lighting conditions, seasons, and camera angles could help the system adapt better to real-world conditions. Another suggestion is that applying data augmentation techniques more aggressively or trying new methods on the images can reduce the model's overfitting to the training data.

#### REFERENCES

- [1] Dofuor, A. K., Quartey, N. K., Osabutey, A. F., Antwi-Agyakwa, A. K., Asante, K., Boateng, B. O., Ablormeti, F. K., Lutuf, H., Osei-Owusu, J., Osei, J. H. N., Ekloh, W., Loh, S. K., Honger, J. O., Aidoo, O. F., & Ninsin, K. D. (2023). Mango anthracnose disease: the current situation and direction for future research. Frontiers in Microbiology, 14, 1168203. DOI: https://doi.org/10.3389/fmicb.2023.1168203
- [2] Jafar, A., Nabila, B., Rizwan Ali, N., Sadeghi-Niaraki, A., & Jeong, D. (2024). Revolutionizing agriculture with artificial intelligence: plant disease detection methods, applications, and their limitations. *Frontiers in Plant Science*, *15*. DOI: 10.3389/fpls.2024.1356260
- [3] Shubham, A. G., Madolli, M. J., García-Caparrós, P., Ullah, H., Cha-um, S., Datta, A., & Himanshu, S. K. (2025). Advancements in UAV remote sensing for agricultural yield estimation: A systematic comprehensive review of platforms, sensors, and data analytics. *Remote Sensing Applications: Society and Environment*, 37, 101418. DOI: https://doi.org/10.1016/j.rsase.2024.101418
- [4] Yuan, W., Lan, L., Xu, J., Sun, T., Wang, X., Wang, Q., Hu, J., & Wang, B. (2025). Smart Agricultural Pest Detection Using I-YOLOv10-SC: An Improved Object Detection Framework. *Agronomy*, *15*(1), 221. https://doi.org/10.3390/agronomy15010221
- [5] Toscano, F., Fiorentino, C., Santana, L. S., Magalhães, R. R., Albiero, D., Tomáš, Ř., Klocová, M., & D'Antonio, P. (2025). Recent Developments and Future Prospects in the Integration of Machine Learning in Mechanised Systems for Autonomous Spraying: A Brief Review. *AgriEngineering*, 7(5), 142. <a href="https://doi.org/10.3390/agriengineering7050142">https://doi.org/10.3390/agriengineering7050142</a>
- [6] Priyanka Barhate, Prof. Bhojraj Barhate, Prof. Makarand Joshi (2025). MangoDHDS: Dataset for Mango Fruit Disease Detection Comprising 1.5K Images. IEEE Dataport. https://dx.doi.org/10.21227/33mp-rf79
- [7] He, K., Zhang, X., Ren, S., & Sun, J. (2015). Deep Residual Learning for Image Recognition. *arXiv*. Erişim adresi: <a href="https://arxiv.org/abs/1512.03385">https://arxiv.org/abs/1512.03385</a>
- [8] Topçu, C., & Güneş, P. (2024). Bitki Hastalıklarını Tespitte Derin Öğrenme: ResNet Modelinin Etkinliği. Anadolu Bil Meslek Yüksekokulu Dergisi, 19(69), 31-65.
- [9] Kayaalp, K., & Varol, A. (2024). LeNet ve ResNet Derin Öğrenme Modelleri ile Asma Yapraklarının Sınıflandırması. Veri Bilimi, 7(1), 16-25.
- [10] Tan, M., & Le, Q. V. (2020). EfficientNet: Rethinking Model Scaling for Convolutional Neural Networks. *arXiv*. Erişim adresi: <a href="https://arxiv.org/abs/1905.11946">https://arxiv.org/abs/1905.11946</a>
- [11] Huang, G., Liu, Z., van der Maaten, L., & Weinberger, K. Q. (2018). Densely Connected Convolutional Networks. *arXiv*. Erişim adresi: <a href="https://arxiv.org/abs/1608.06993">https://arxiv.org/abs/1608.06993</a>
- [12] Uçar, M. (2021). Glokom Hastalığının Evrişimli Sinir Ağı Mimarileri ile Tespiti. Dokuz Eylül Üniversitesi Mühendislik Fakültesi Fen ve Mühendislik Dergisi, 23(68), 521-529. https://doi.org/10.21205/deufmd.2021236815
- [13] Selim, S., & Diri, B. (2023). Transferemble: a classification method for the detection of fake satellite images created with deep convolutional generative

- adversarial network. *Journal of Electronic Imaging*, 32(4), 043004. DOI: <a href="https://doi.org/10.1117/1.JEI.32.4.043004">https://doi.org/10.1117/1.JEI.32.4.043004</a>
- [14] Katar, O., & Yıldırım, Ö. (2024). Classification of Malware Images Using Fine-Tunned ViT. Sakarya University Journal of Computer and Information Sciences, 7(1), 22-35. https://doi.org/10.35377/saucis...1341082
- [15] Kaya, M., & Bilgen, Y. (2025). ViT Tabanlı Hibrit Öğrenme Yöntemleri ile Göz Tansiyonu Hastalığının Tespiti. Duzce University Journal of Science and Technology, 13(1), 248-265. https://doi.org/10.29130/dubited.1494138

# Particle Swarm Optimization-Based Modulation Classification in 5G Communication Systems

Asuman SAVAŞCIHABEŞ\*

<sup>\*</sup>Department of Electrical and Electronics Engineering, Nuh Naci Yazgan University, Türkiye ahabes@nny.edu.tr

#### **ABSTRACT**

addresses the modulation classification communication systems by integrating intelligent optimization algorithms with deep learning techniques. Specifically, the hyperparameters of a convolutional neural network (CNN)-based deep learning model are optimized using the Particle Swarm Optimization (PSO) algorithm to enhance classification accuracy. The proposed integration demonstrates that PSO significantly improves the training process by fine-tuning the learning rate, momentum, and layer configuration, thereby achieving higher accuracy and more efficient performance. Monte Carlo simulations conducted in MATLAB® for CSK-OFDM under AWGN and Rayleigh fading channels validate the effectiveness of PSO-based adaptive decision threshold optimization, particularly in low-SNR regions. The findings indicate that this approach not only reduces the bit error rate (BER) but also improves spectral efficiency and system reliability, highlighting its potential for nextgeneration 5G and 6G communication systems.

Keywords – Optimization algorithms, 5G, Bit Error Rate, Modulation classification, CNN, AI.

#### I. Introduction

Modulation classification plays a pivotal role in modern communication systems, especially in scenarios such as cognitive radio networks that demand dynamic and efficient spectrum utilization. While conventional approaches rely on fixed modulation schemes, deep learning-based methods, particularly convolutional neural networks (CNNs), have demonstrated remarkable success in classifying complex signals [1]–[3]. However, deep learning models typically require large datasets and extensive training, making hyperparameter optimization critical for achieving superior performance.

Intelligent optimization techniques such as Genetic Algorithms (GA) and Particle Swarm Optimization (PSO) are widely employed for this purpose [4]. PSO, in particular, has proven effective in tuning model parameters during training, thereby enhancing classification accuracy [5]. Recent studies confirm that integrating optimization algorithms with deep learning not only accelerates the training process but also provides robust solutions for adaptive modulation classification, outperforming traditional methods [6], [7].

This study focuses on the integration of deep learning with PSO to solve the modulation classification problem. The results reveal that PSO-based hyperparameter optimization significantly enhances accuracy and efficiency, offering promising potential for advanced communication systems such as 5G and 6G.

#### II. MATERIALS AND METHOD

### A. Dataset and Signal Representation

A synthetically generated dataset consisting of I/Q components of digitally modulated signals under multiple channel conditions was utilized. The dataset covers a wide range of modulation schemes with varying Signal-to-Noise Ratio (SNR) levels from 0 dB to 30 dB in 5 dB increments. Each SNR value is associated with 10,000 randomly generated OFDM symbols to ensure statistical reliability. The I/Q signals are formatted as two-dimensional tensors (2 × 1000 × 1), which are suitable for CNN-based feature extraction [1], [4].

# B. Deep Learning Model Architecture

The CNN-based deep learning model follows a hierarchical feature extraction and classification design [2], [5]:

- Input Layer: Normalized I/Q samples formatted as 2D tensors.
- Convolutional Layers: Two layers with kernel sizes of 1 × 5 and 1
   × 3, consisting of 16 and 32 filters respectively.
- Pooling Layers: Max-pooling after each convolution to reduce feature dimensionality while preserving salient features.
- Fully Connected Layer: A dense layer with 128 neurons for abstraction of high-level features.
- Output Layer: A softmax classifier providing posterior probabilities across five modulation categories.

The baseline model employs categorical cross-entropy as the loss function and the Adam optimizer. These hyperparameters are subsequently optimized using PSO.

# C. Particle Swarm Optimization (PSO) for Hyperparameter Tuning

PSO was applied to tune key hyperparameters, including learning rate, momentum, batch size, and the number of hidden units. Each particle in the swarm represents a candidate solution, updated iteratively to maximize classification accuracy [3], [6].

- Swarm Configuration: 20 particles with inertia weight
- Fitness Function: Model accuracy on the validation set.
- Iterations: 30 optimization steps per run, updating global and local best positions.

Compared to exhaustive search, PSO achieves superior accuracy with reduced computational overhead [6], [7].

#### D. Simulation Environment

Monte Carlo simulations were carried out in MATLAB® R2024b. An OFDM system with 64-point IFFT/FFT and 52 active subcarriers was implemented. Simulations were performed under both Additive White Gaussian Noise (AWGN) and Rayleigh fading channels. For each SNR value, received signals were demodulated, and BER was computed via symbol decision mapping.

The PSO-enhanced CNN classifier was benchmarked against:

- A baseline CNN without optimization,
- A traditional maximum-likelihood modulation classifier,
- A genetic algorithm (GA)-optimized CNN.
- This comparative analysis ensured a robust evaluation of PSO's contribution to performance gains.

#### E. Performance Metrics

#### The evaluation included:

- Classification Accuracy (%): Correctly classified modulation symbols.
- Bit Error Rate (BER): Computed across varying SNR levels.
- Computational Complexity: Training time per epoch.
- Convergence Speed: Iterations required for optimization stability.

Table 1. System-level configuration used to generate the BER–SNR results for CSK-OFDM under AWGN and Rayleigh channels

Parameter	Value
FFT size / Active subcarriers	128 / 128
Cyclic prefix length	16 samples
Modulation orders (CSK)	M = 4, 8, 16
SNR range / step	0–50 dB / 5 dB
Frames (opt./final)	200 / 5000
Channel models	AWGN, 1-tap Rayleigh
Equalization	Single-tap (perfect CSI)
Simulator	MATLAB R2024b, Monte Carlo

Table.1 fixes the OFDM frame structure (FFT = 128, CP = 16) and the channel assumptions to ensure reproducibility. Active subcarriers carry CSK symbols of orders  $M \in \{4,8,16\}M \in \{4,8,16\}M \in \{4,8,16\}$ . The SNR sweep (0–50 dB, 5 dB step) and the number of Monte-Carlo frames (200 for PSO tuning, 5000 for final BER) were chosen to balance statistical reliability and runtime. Rayleigh fading is modeled as 1-tap (frequency-flat) with single-tap equalization under perfect CSI; AWGN uses the same OFDM settings for a fair comparison.

#### III. RESULTS

Monte Carlo simulations were performed for CSK-OFDM with modulation orders M=2,4,8,16. The OFDM framework employed 64-point IFFT/FFT and 52 subcarriers, generating 10,000 symbols per iteration. PSO utilized 20 particles, 30 iterations, and adaptive decision threshold optimization within the range.For each SNR value, thresholds were iteratively updated to minimize BER. Signals were transmitted under AWGN and Rayleigh fading channels, demodulated with FFT/IFFT, and BER was computed.The results (Fig. 1) confirm that PSO-based adaptive thresholding achieves significantly lower BER at low SNR values compared to conventional approaches. At 30 dB, performance surpasses BER, demonstrating that PSO-enhanced classification improves both spectral efficiency and system stability under dynamic channel conditions. detail.

It is shown in table.2 that, the swarm uses 30 particles and 50 iterations w=0.7w=0.7w=0.7with inertia and acceleration coefficients c1=c2=1.5c 1=c 2=1.5c1=c2=1.5, providing a stable exploration exploitation balance. Decision levels are searched within [-2,2]M[-2,2]\M[-2,2]M and power-normalized to keep symbol energy constant across MMM. The fitness is the validation BER evaluated at 35 dB SNR (a mid-high regime representative for threshold shaping), which empirically yields faster convergence and robust generalization. Constraints enforce distinct levels to avoid degenerate constellations.

Table 2. Optimization setup and search space for PSO-based tuning of CSK decision levels.

Parameter	Value
Swarm size	30
Iterations	50
Inertia weight (w)	0.7
Acceleration coeffs.	$c_1 = 1.5, c_2 = 1.5$
Optimization SNR	35 dB
Decision level bounds	[-2, 2] (normalized power)
Fitness function	Validation BER

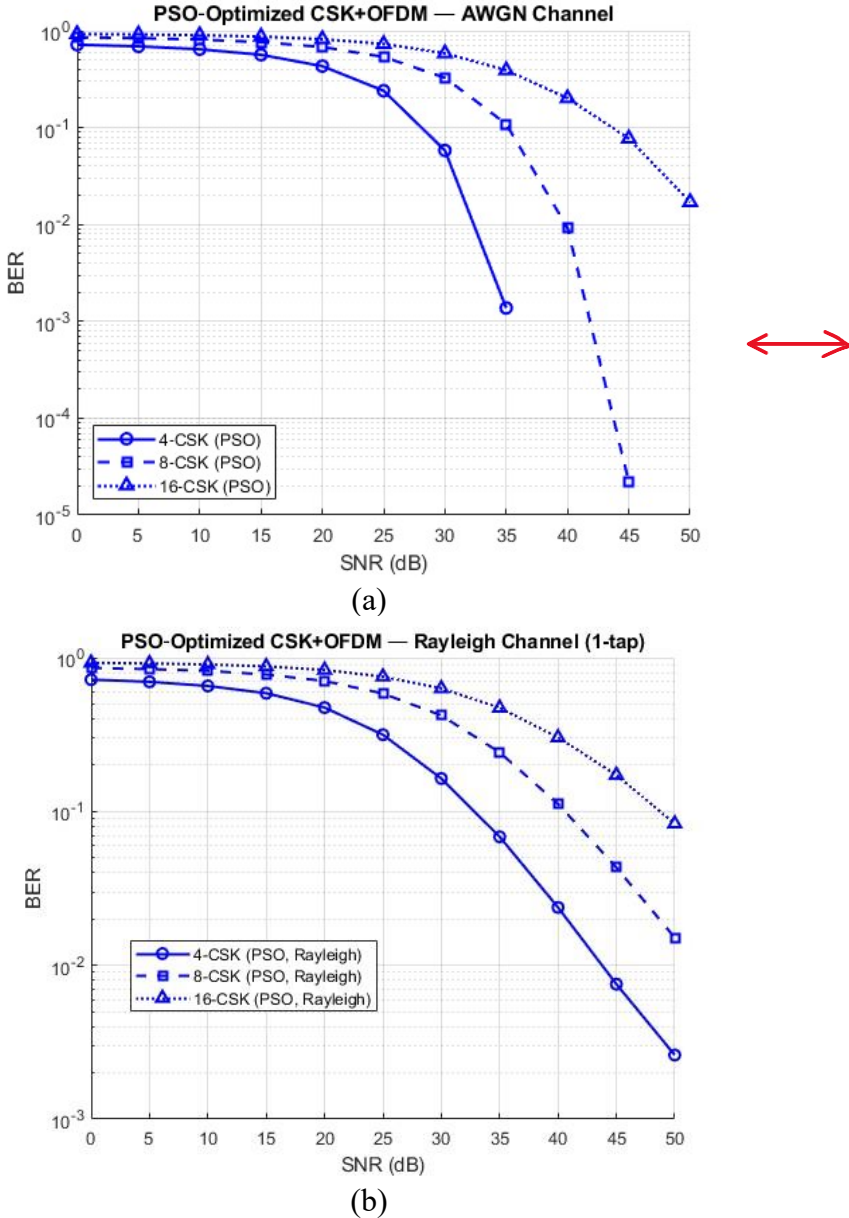


Fig.1.: BER vs SNR for M-CSK modulation for (a): AWGN channel and (b): Rayleigh fading channel

#### IV. DISCUSSION

The results obtained from Monte Carlo simulations clearly demonstrate the effectiveness of PSO-based hyperparameter optimization in CNN-driven modulation classification. Compared to conventional CNN training and GA-

based optimization, the PSO-enhanced model consistently achieves superior classification accuracy and reduced BER across both AWGN and Rayleigh fading channels. This outcome highlights the ability of PSO to dynamically explore the solution space, effectively balancing exploration and exploitation during the optimization process [3], [6].

One of the key findings is that PSO-based adaptive thresholding is particularly beneficial in low-SNR regimes. Fig.1(a) demonstrates that a 7 dB SNR gain was achieved at the 10-3 BER level in the AWGN channel, and Fig.1(b) shows that, under a 1-tap Rayleigh channel, the PSO-optimized CSK-OFDM curves show the expected order-SNR trade-off: 4-CSK attains the lowest BER with the steepest waterfall, while 8- and 16-CSK require progressively higher SNR and diverge more at high SNR, with no evident error floor. Traditional classifiers typically exhibit rapid performance degradation under such conditions due to their sensitivity to noise and fading. By contrast, the PSO-optimized CNN demonstrates notable resilience, achieving BER improvements exceeding an order of magnitude at SNR levels below 15 dB. This robustness makes the proposed method highly suitable for deployment in cognitive radio networks and spectrumconstrained 5G environments, where reliable communication must be maintained under adverse conditions [1], [5]. Furthermore, the integration of PSO not only improves classification accuracy but also accelerates convergence during training. This reduction in computational cost is a critical factor for practical implementations, as training deep learning models often requires significant resources. By providing faster convergence, the PSO-optimized approach aligns with the increasing demand for real-time modulation recognition in 5G and beyond [4], [7]. It is also noteworthy that while GA-based methods deliver moderate improvements, they tend to converge more slowly and risk premature convergence to local optima. PSO, in contrast, demonstrates stable convergence across multiple iterations, confirming its advantage as a lightweight yet powerful optimizer for deep learning models [3], [6]. Despite these promising results, certain limitations must be acknowledged. The current study relies on synthetically generated datasets and MATLAB-based simulations, which, although effective for controlled evaluation, may not fully capture hardware impairments such as nonlinearities, phase noise, or synchronization errors encountered in realworld systems[7]. Extending this work to hardware testbeds and real datasets would be an essential step toward practical validation. Moreover, the study has focused primarily on CSK-OFDM; future investigations should explore other modulation families (e.g., QAM, PSK) and hybrid schemes to ensure generalization across diverse communication scenarios[8].

In summary, the discussion underscores that PSO-based deep learning integration not only enhances modulation classification performance but also

provides a scalable and computationally efficient framework. These advantages highlight the potential of the proposed method to serve as a cornerstone for intelligent, adaptive communication in next-generation wireless networks

#### V. CONCLUSION

This study demonstrates that integrating PSO with CNN-based deep learning substantially improves modulation classification performance in CSK-OFDM systems. The adaptive threshold optimization reduces BER and enhances reliability, making it suitable for 5G and 6G systems. Future work will extend this framework to larger-scale datasets and real-time hardware implementations.

#### REFERENCES

- [1] X. Liu, D. Yang, and A. E. Gamal, "Deep neural network architectures for modulation classification," Proc. 51st Asilomar Conf. on Signals, Systems, and Computers, pp. 915–919, 2017.
- [2] S. Rajesh, S. Geetha, S. B. Sudarson, and S. Ramesh, "Deep Learning based Real Time Radio Signal Modulation Classification and Visualization," Int. J. of Engineering and Manufacturing (IJEM), vol. 13, no. 5, pp. 30–37, 2023.
- [3] B. Qolomany, M. Maabreh, A. Al-Fuqaha, A. Gupta, and D. Benhaddou, "Parameters optimization of deep learning models using Particle Swarm Optimization," 13th Int. Wireless Commun. and Mobile Computing Conf. (IWCMC), pp. 1285–1290, 2017.
- [4] B. Wang, Y. Sun, B. Xue, and M. Zhang, "Evolving Deep CNNs by Variable-Length PSO for Image Classification," IEEE Congress on Evolutionary Computation (CEC), pp. 1–8, 2018.
- [5] H. Guo, S. Peng, T. Li, M. Crisp, and R. Penty, "Deep Learning Based Modulation Classification in Radio Access Networks," IEEE Globecom Workshops, pp. 1752–1757, 2023.
- [6] M. Almseidin, A. Gawanmeh, M. Alzubi, J. Al-Sawwa, A. S. Mashaleh, and M. Alkasassbeh, "Hybrid Deep Neural Network Optimization with Particle Swarm and Grey Wolf Algorithms for Attack Detection," Computers, vol. 14, p. 107, 2025.
- [7] Z. Elkhatib, F. Kamalov, S. Moussa, A. B. Mnaouer, M. C. E. Yagoub, and H. Yanikomeroglu, "Radio Modulation Classification Optimization Using Combinatorial Deep Learning," IEEE Access, vol. 12, pp. 17552–17570, 2024.
- [8] Savaşcıhabeş, A. (2025). Convolutional neural network approach to modulation classification for 5G and cognitive radio. In U. Özkaya (Ed.), Contemporary Research in Engineering (Chapter 13, pp. 218–232). All Science Academy. ISBN: 978-625-5794-04-8

# **Electrochemical Wastewater Treatment and Hydrogen Production**

Ziya Mert ÖZGEN<sup>1</sup> Ümran Tezcan ÜN<sup>2</sup> Özlem ONAY<sup>3</sup>

<sup>1-</sup> Graduate Student; Eskişehir Technical University Energy Resources and Management Department. zmozgen@ogr.eskisehir.edu.tr ORCID No: 0009-0000-4608-1393

<sup>2-</sup> Prof. Dr.; Eskişehir Technical University Environmental Engineering Department. <a href="mailto:utezcan@eskisehir.edu.tr">utezcan@eskisehir.edu.tr</a> ORCID No: 0000-0003-3882-9175

<sup>3-</sup> Prof. Dr.; Eskişehir Technical University Electricity and Energy Department. <u>oonay@eskisehir.edu.tr</u> ORCID No: 0000-0001-6230-9335

#### **ABSTRACT**

Energy is one of the most fundamental necessities in today's world. As an act against the climate crisis and eventual depletion of fossil fuels, finding a clean and sustainable fuel source is one of the most important issues in the field of energy and hydrogen is currently the highest-ranked candidate for the next generation of fuels. Even though it's the most common element in nature, it's only found naturally in molecules like water and methane. The confluence of escalating environmental pollution from industrial activities and the urgent global imperative to transition towards sustainable energy systems presents one of the most significant challenges. Industrial wastewater, often characterized by high volumes and complex compositions of recalcitrant pollutants, demands effective and economically viable treatment methods. Electrolysis is an electrochemical method that is commonly used for water and wastewater treatment, and one of its main products is hydrogen. This process can facilitate the degradation of persistent organic pollutants in wastewater while simultaneously generating hydrogen gas. This integrated approach not only offers a pathway for pollution abatement but also contributes to the production of green or low-carbon hydrogen. The use of industrial wastewater as a feedstock for electrolytic hydrogen production offers the dual benefit of valorizing a waste stream and reducing reliance on freshwater resources. The overall goal of this article is to provide a detailed examination of the principles, technological advancements, specific applications, and prevailing challenges associated with the electrochemical treatment of industrial wastewater combined with generation of hydrogen.

Keywords – Hydrogen Energy, Wastewater Treatment, Sustainability, Electrolysis, Resource Recovery.

#### INTRODUCTION

Clean water and sustainable energy are the most fundamental necessities in today's world. The confluence of escalating environmental pollution from industrial activities and the urgent global imperative to transition towards sustainable energy systems presents one of the most significant challenges of the 21st century (Akpasi et al., 2025). Industrial wastewater, often characterized by high volumes and complex compositions of recalcitrant pollutants, demands effective and economically viable treatment methods to prevent ecological damage and protect public health (Thirugnanasambandham et al., 2025). Simultaneously, hydrogen is increasingly recognized as a clean and versatile energy carrier with the potential to decarbonize various sectors, provided it is produced sustainably (Faye et al., 2022; Agyekum et al., 2022). The concept of a circular economy,

which promotes resource efficiency and the transformation of waste into valuable products, offers a compelling framework for addressing these dual challenges (Núñez et al., 2024).

Integrating industrial wastewater treatment with hydrogen production through electrochemical technologies emerges as a particularly promising synergistic strategy (Odoi-Yorke et al., 2025). Electrochemical methods utilize an electrochemical cell, typically consisting of an anode (where oxidation reactions occur) and a cathode (where reduction reactions occur) immersed in an electrolyte (the wastewater itself, often with modifications). to drive desired chemical transformations via the application of electrical energy (Inocêncio et al., 2023). These methods can facilitate the degradation of persistent organic pollutants and other contaminants in industrial wastewater, while simultaneously, the electrolysis of water (or other hydrogen-containing species within the wastewater) at the cathode can generate hydrogen gas (Ahmad & Yadav, 2024; Lu et al., 2020). This integrated approach not only offers a pathway for pollution abatement but also contributes to the production of green or low-carbon hydrogen, potentially offsetting treatment costs and reducing the reliance on pristine freshwater resources for dedicated hydrogen synthesis (Chauhan & Ahn, 2023; Simoes et al., 2021). This review aims to provide a detailed and elaborated examination of the principles, technological advancements, material considerations, specific applications, and prevailing challenges associated with the electrochemical treatment of industrial wastewater combined with generation of hydrogen, drawing upon a comprehensive analysis of recent scientific literature.

# Hydrogen as an Energy Carrier

Hydrogen, the simplest and most abundant element, is gaining prominence as a central pillar in the transition to a low-carbon global economy due to its high gravimetric energy density and its capacity to produce only water upon combustion or use in fuel cells (Akpasi et al., 2025; Faye et al., 2022). It's increasingly recognized as a major clean energy carrier with significant potential to contribute to a sustainable energy future and the decarbonization of various sectors. Its appeal lies in its high energy content per unit mass and the fact that its primary combustion product is water, making it an environmentally benign fuel at the point of use. However, the environmental impact of hydrogen is largely determined by its production method, leading to classifications such as grey, blue, and green hydrogen (Hassan et al., 2024; Agyekum et al., 2022).

Grey Hydrogen is derived from fossil fuels, primarily through steam methane reforming, where natural gas reacts with steam at high temperatures, or through coal gasification (Ji & Wang, 2021). These processes are associated

with significant carbon dioxide (CO<sub>2</sub>) emissions (Agyekum et al., 2022). Blue Hydrogen is also produced from fossil fuels, but the CO<sub>2</sub> emissions from the production process are captured and either utilized or sequestered geologically (Carbon Capture, Utilization, and Storage - CCUS) (Hassan et al., 2024). Green Hydrogen is produced using renewable energy sources to power the splitting of water into hydrogen and oxygen via electrolysis as seen from Fig. 1 (Horri & Ozcan, 2023; Hassan et al., 2024). Green hydrogen is considered the ultimate goal for a sustainable hydrogen economy due to its near-zero greenhouse gas emissions profile (Faye et al., 2022).



Figure 1: H<sub>2</sub> and O<sub>2</sub> generation from water molecule decomposition Source: Ahmad & Yadav, 2024

A variety of technologies (Fig.2) are available or under development for hydrogen production, each with distinct characteristics regarding feedstock, energy input, efficiency, cost, and environmental impact (Ji & Wang, 2021; Faye et al., 2022).

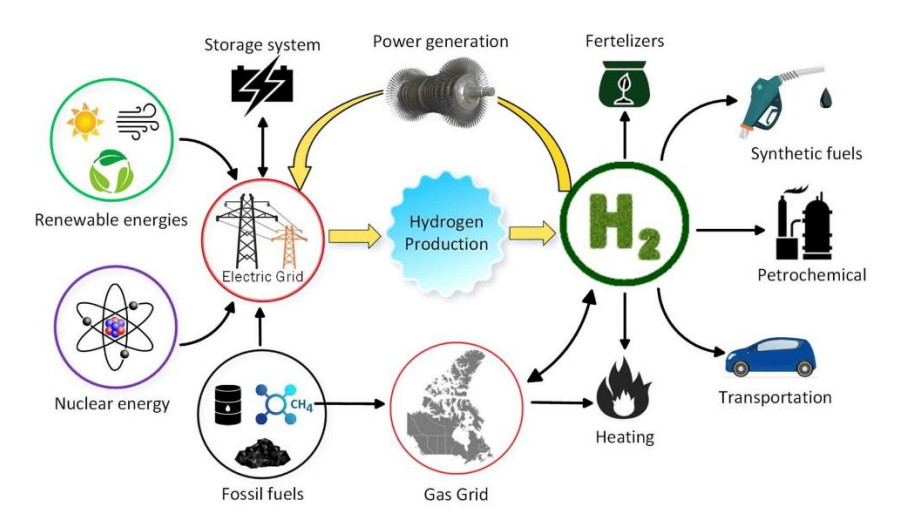


Figure 2: Hydrogen production and its effect on other sectors

Source: Agyekum et al., 2022

Thermochemical methods involve heat and chemical reactions. Dominant methods include steam methane reforming and coal gasification (Agyekum et al., 2022). Biomass gasification and pyrolysis are renewable thermochemical routes (Faye et al., 2022). Liu et al. (2023) explored a combined hydrothermal carbonization, pyrolysis, and reforming process for hydrogen-rich gas from sewage sludge. Thermochemical water-splitting cycles, using concentrated solar power or nuclear heat, are also being researched (Agyekum et al., 2022).

Electrochemical methods include water electrolysis, using electricity to split water, is key for green hydrogen when powered by renewables (Hassan et al., 2024). Main types include Alkaline Water Electrolysis (AWE), Proton Exchange Membrane Water Electrolysis (PEMWE), Anion Exchange Membrane Water Electrolysis (AEMWE), and Solid Oxide Electrolysis Cells (SOEC) (Horri & Ozcan, 2023; Ul Mulk et al., 2024). These are discussed in further sections of this article.

Biological methods could be explained as microorganisms producing hydrogen from organic matter, which often found in wastewater (Odoi-Yorke et al., 2025). Dark fermentation by anaerobic bacteria and photo-fermentation by photosynthetic bacteria are two such pathways (Karadag et al., 2014; Laurinavichene et al., 2018). Microbial Electrolysis Cells (MECs) combine biological oxidation of organics with electrochemical hydrogen evolution (Guerrero-Sodric et al., 2024).

Photochemical methods directly use light energy. Photocatalysis involves semiconductor particles suspended in water, while Photoelectrochemical water splitting uses semiconductor photoelectrodes (Qureshi & Tahir, 2024; Hassan et al., 2024). A comparison by Ji & Wang (2021) based on costs and life cycle impact assessment (LCA) indicators highlights that while steam methane reforming is currently cheapest, electrolysis using renewable energy offers the most sustainable long-term pathway.

#### **Electrochemical Wastewater Treatment**

Electrochemical technologies provide a robust and versatile platform for treating a wide range of industrial wastewater, particularly those containing biorefractory or toxic pollutants that are difficult to degrade using conventional biological methods (de Araujo et al., 2024). These methods operate by inducing redox reactions (oxidation-reduction reactions) at electrode surfaces through the application of electrical energy, leading to the transformation or complete mineralization of contaminants (Inocêncio et al., 2023). An electrochemical cell for this purpose typically comprises two electrodes: an anode, where oxidation (loss of electrons) occurs, and a

cathode, where reduction (gain of electrons) takes place. These electrodes are immersed in the wastewater, which acts as the electrolyte (a medium that conducts ions), or may have a supporting electrolyte added to enhance its conductivity (Núñez et al., 2024). There are several electrochemical wastewater treatment methods that have gained significant attention due to their efficiency and sustainability. Among them, electro-oxidation, electrocoagulation, and electroflotation are widely applied to degrade organic pollutants. These techniques are considered promising alternatives to conventional treatment processes because of their environmental compatibility and ability to be combined with renewable energy sources (Sun et al., 2023).

In electro-oxidation process, anodic processes aim to chemically transform pollutants into less harmful or inert substances. Anodic Oxidation (AO), particularly within the framework of Electrochemical Advanced Oxidation Processes (EAOPs), involves the degradation of organic pollutants at an inert anode surface (Zhan et al., 2025). At the anode, the primary electrochemical process is oxidation. This can occur via Direct Anodic Oxidation (DAO), where the pollutant molecule (R) itself adsorbs onto the anode surface (M) and subsequently loses electrons directly to the anode, leading to its transformation into oxidation products (Núñez et al., 2024).

In an electrocoagulation process, when a potential difference is applied between a soluble anode (e.g., Fe or Al) and a cathode, metallic ions are released from the anode surface while hydroxyl ions are generated at the cathode (Tezcan Un et al., 2006). These reactions lead to the in-situ formation of metal hydroxide species, which play a critical role in destabilizing colloids and suspended particles by neutralizing their surface charges. The destabilized particles subsequently aggregate into larger flocs that can be separated from the liquid phase.

At the cathode, water is reduced according to the following reaction:

$$H_2O + 2e^- \rightarrow 2OH^-_{(aq)} + H_{2(g)}$$
 (1)

This reaction produces molecular hydrogen, which is released as gas bubbles, and hydroxide ions, which increase the local alkalinity near the cathode.

At the anode, the oxidation of the electrode material takes place. For iron electrodes, the process can be described as:

$$Fe \rightarrow Fe^{2+} + 2e^{-} \tag{2}$$

The ferrous ions generated at the anode may undergo further oxidation in the presence of dissolved oxygen:

$$Fe_2^+ \to Fe^{3+} + e^-$$
 (3)

The ferric ions thus formed rapidly hydrolyze in the aqueous medium to produce insoluble ferric hydroxide:

$$Fe^{3+} + 3OH^{-} \rightarrow Fe(OH)_{3} \tag{4}$$

Also, if the electrode material is aluminum, the processes can be given as:

$$Al \rightarrow Al_{(aq)}^{3+} + 3e^{-} \tag{5}$$

$$Al_{(aq)}^{3+} + 3H_2O \rightarrow Al(OH)_3 + 3H_{(aq)}^{+}$$
 (6)

$$nAl(OH)_3 \to Al_n(OH)_{3n} \tag{7}$$

In these reactions, Al(OH)<sub>3</sub> flocs are actively adsorbing organic compounds and trapping colloidal particles (Tezcan Un et al., 2009). Metalic hydroxide, together with other hydrolysis products of Fe<sub>3</sub><sup>+</sup> or Al<sub>3</sub><sup>+</sup> (in the case of aluminum electrodes), act as an effective coagulant. These hydroxide flocs adsorb and enmesh organic and inorganic pollutants, thereby promoting their removal from wastewater (Tezcan Un et al., 2006). In addition, hydrogen gas and hydroxide generated at the cathode contribute to the flotation of flocs, enhancing the overall separation efficiency. Thus, the combined effect of anodic dissolution, cathodic hydrogen generation, and subsequent precipitation of metal hydroxides underpins the fundamental mechanism of electrocoagulation in wastewater treatment.

# HYDROGEN PRODUCTION VIA WASTEWATER ELECTROLYSIS

Utilizing industrial wastewater as a feedstock for electrolytic hydrogen production offers a dual benefit: valorizing a waste stream and reducing reliance on freshwater resources (Simoes et al., 2021; Odoi-Yorke et al., 2025). There are different types of water electrolysis processes for water as shown in Figure 3, but not all of them are applicable for wastewater. The presence of certain organic or inorganic species in wastewater can, in some cases, lower the thermodynamic energy barrier for electrolysis compared to pure water splitting, by providing alternative, lower-potential anodic reactions (Lu et al., 2020; Chauhan & Ahn, 2023). However, impurities in industrial wastewater also pose significant challenges to electrolyzer performance and durability (Horri & Ozcan, 2023).

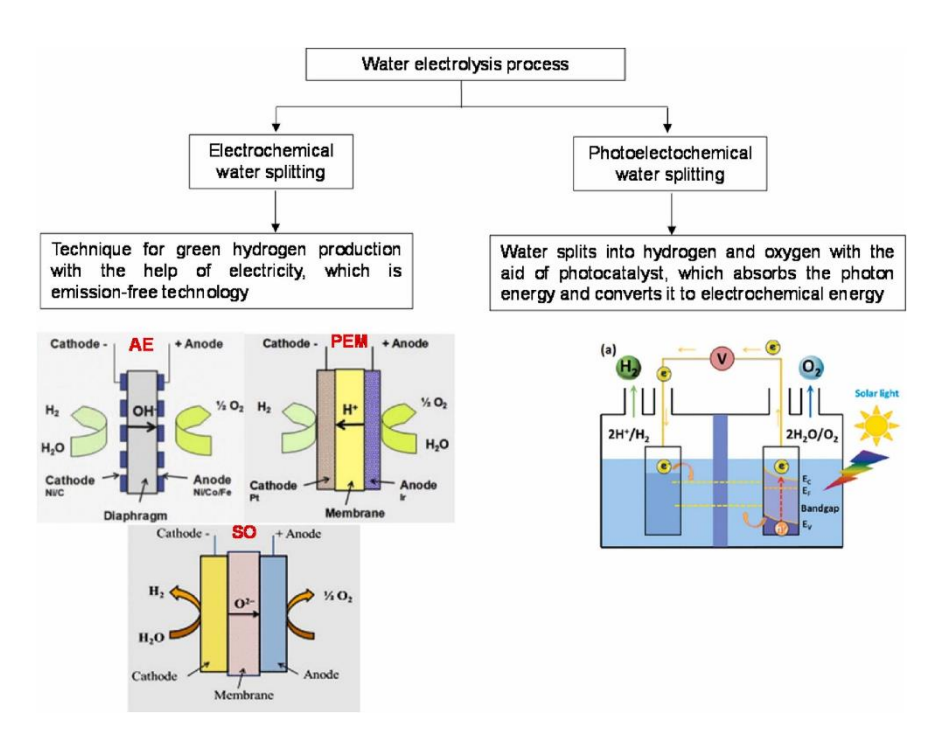


Figure 3: Visuals for different types of water electrolysis processes

Source: Odoi-Yorke et al., 2025

# Alkaline Water Electrolysis (AWE) of Wastewater

AWE is a mature and widely implemented technology for hydrogen production, characterized by its use of a liquid alkaline electrolyte, typically a concentrated solution of potassium hydroxide (KOH) or sodium hydroxide (NaOH), and non-precious metal electrocatalysts such as nickel or stainless steel for both the hydrogen evolution reaction (HER) at the cathode and the oxygen evolution reaction (OER) at the anode (Hassan et al., 2024; Horri & Ozcan, 2023). AWE systems generally operate at temperatures between 70-90 °C and are known for their relatively low capital costs and long operational lifetimes (Chauhan & Ahn, 2023). The primary challenges for AWE include relatively lower current densities compared to other technologies, potential for electrolyte leakage, and the corrosive nature of the concentrated alkaline electrolyte, which necessitates robust construction materials (Hassan et al., 2024; Agyekum et al., 2022). When considering the use of wastewater or lowquality water, AWE systems may require pre-treatment to remove impurities that can cause electrode fouling or deactivation, although they are generally considered more tolerant to impurities than PEMWE systems (Chauhan & Ahn, 2023).

Industrial wastewater can provide some inherent conductivity but often requires pH adjustment (to alkaline) and pre-treatment (e.g., ultrafiltration) to remove suspended solids, oils, and certain dissolved ions that can cause electrode fouling, corrosion, or catalyst deactivation (Chauhan & Ahn, 2023). Chauhan & Ahn (2023) highlighted the importance of removing turbidity and total dissolved solids for enhanced hydrogen production from wastewater using AWE. Organic pollutants in wastewater can undergo anodic oxidation at potentials lower than the oxygen evolution reaction (OER), thus reducing the overall cell voltage needed for cathodic hydrogen evolution (HER) (Lu et al., 2020; Odoi-Yorke et al., 2025). Electrode passivation by inorganic scales (e.g., carbonates, sulfates of Ca/Mg), deactivation by adsorbed organics or heavy metals, and corrosion in aggressive media remains as key issues (Chauhan & Ahn, 2023).

# **Proton Exchange Membrane Water Electrolysis (PEMWE) with Wastewater**

PEMWE utilizes a solid polymer electrolyte, typically a perfluorosulfonic acid membrane like Nafion®, which selectively conducts protons from the anode to the cathode (Hassan et al., 2024; Horri & Ozcan, 2023). This technology operates in an acidic environment and relies on precious metal catalysts, usually platinum-based materials for the HER and iridium or ruthenium oxides for the OER, to achieve high efficiency (Horri & Ozcan, 2023; Inocêncio et al., 2023). PEMWE systems offer several advantages, including high current densities leading to compact cell designs, high-purity hydrogen production (typically >99.99%), and rapid response to dynamic power input, making them well-suited for coupling with intermittent renewable energy sources (Hassan et al., 2024; Agyekum et al., 2022). However, the major drawbacks of PEMWE are its high capital cost, largely due to the expensive precious metal catalysts and the fluorinated membrane, and its stringent requirement for high-purity deionized water to prevent membrane degradation and catalyst poisoning by impurities (Simoes et al., 2021; Horri & Ozcan, 2023; Ji & Wang, 2021).

PEMWE systems are extremely sensitive to impurities (Simoes et al., 2021). Cations (Na<sup>+</sup>, Ca<sub>2</sub><sup>+</sup>, etc.) can irreversibly damage the PEM by ion exchange, while anions (Cl<sup>-</sup>, SO<sub>4</sub><sup>2-</sup>) and organics can poison the noble metal catalysts (Horri & Ozcan, 2023; Ji & Wang, 2021). Due to this sensitivity, direct electrolysis of untreated or minimally treated industrial wastewater in PEMWE is currently not feasible. Extensive and costly pre-treatment to achieve deionized water quality would be required, largely negating the economic and resource benefits of using wastewater (Horri & Ozcan, 2023).

# **Anion Exchange Membrane Water Electrolysis (AEMWE) with Wastewater**

AEMWE is an emerging technology that aims to combine the advantages of both AWE (e.g., potential for using non-precious metal catalysts) and PEMWE (e.g., compact cell design with a solid electrolyte) (Ul Mulk et al., 2024; Hassan et al., 2024). AEMWE systems employ an anion exchange membrane (AEM) that conducts hydroxide ions and can operate in alkaline or even neutral pH conditions, which theoretically allows for the use of more abundant and less expensive electrocatalysts compared to the platinum group metals required for PEMWE (Ul Mulk et al., 2024).

AEMWE is considered more tolerant to certain impurities (especially cations) found in wastewater compared to PEMWE, due to its alkaline operating environment (Ul Mulk et al., 2024). This could reduce pre-treatment demands. Tufa et al. (2018) explored an Alkaline Polymer Electrolyte Water Electrolysis (APWEL) system, a form of AEMWE, for H<sub>2</sub> production powered by energy from salinity gradients in synthetic industrial wastewater.

The primary limitations for AEMWE are the development of AEMs with high OH- conductivity, long-term chemical stability (especially against CO<sub>2</sub> contamination leading to carbonate formation), and robust, active non-PGM catalysts for both HER and OER in alkaline media (Ul Mulk et al., 2024). Water management within the cell is also critical (Ul Mulk et al., 2024). This technology holds promise for cost-effective green hydrogen production, potentially using less corrosive electrolytes or even pure water if catalyst activity is sufficiently high (Hassan et al., 2024).

# Solid-Oxide Electrolysis Cells (SOEC) using Steam from Wastewater

SOESs operates at high temperatures, typically between 500°C and 1000°C, and utilizes a solid ceramic material (e.g., yttria-stabilized zirconia - YSZ) as the electrolyte, which conducts oxygen ions (Hassan et al., 2024; Horri & Ozcan, 2023). At these elevated temperatures, SOECs primarily electrolyze steam rather than liquid water, which is thermodynamically more favorable and leads to faster reaction kinetics, potentially resulting in higher electrical efficiency compared to low-temperature electrolysis technologies (Hassan et al., 2024; Ji & Wang, 2021). A significant advantage of SOEC is the possibility of integrating high-temperature heat from external sources (e.g., industrial waste heat, geothermal energy, or concentrated solar power) to supply part of the energy required for water splitting, thereby reducing the electrical energy demand (Horri & Ozcan, 2023; Giraldi et al., 2015, as cited by Ji & Wang, 2021). However, SOEC technology faces challenges related to long-term material stability and durability at high operating temperatures,

sealing issues, thermal cycling robustness, and relatively high capital and system integration costs (Agyekum et al., 2022).

To apply this technology to industrial wastewater, it would need to be converted to steam, and this steam would likely require significant purification to prevent corrosion and deposition on the sensitive SOEC components at high temperatures (Simoes et al., 2021). The high operating temperatures might aid in decomposing some organic contaminants. However, material stability, sealing, and thermal cycling remain major challenges for SOEC technology itself, further complicated by potential impurities from wastewater-derived steam (Hassan et al., 2024).

#### RECENT DEVELOPMENTS AND CASE STUDIES

The field of electrochemical wastewater treatment coupled with hydrogen production is characterized by dynamic research and development, focusing on enhancing efficiency, reducing costs, and broadening the applicability of these synergistic technologies. Recent progress spans advancements in electrocatalyst and electrode materials, the evolution of bioelectrochemical and photoelectrochemical systems, the design of innovative integrated and hybrid processes, and compelling case studies demonstrating practical applications across diverse industrial wastewater streams.

The practical applicability and potential of these electrochemical and related technologies are best highlighted through specific case studies targeting diverse types of industrial and municipal wastewaters. For the treatment of highly colored and organically rich textile industry wastewater, integrated solar PV-powered electrolysis systems have demonstrated effective decolorization, chemical oxygen demand (COD) reduction, and concurrent hydrogen production, showcasing a dual benefit for this challenging effluent (Pathak et al., 2020). The electrolysis of produced water, a voluminous and complex waste stream generated during oil and gas extraction, characterized by high salinity and the presence of persistent organic pollutants, is being actively investigated for simultaneous contaminant removal (e.g., using robust anodes like BDD) and the generation of green hydrogen, offering a sustainable management solution for the energy industry (de Araujo et al., 2024).

In the context of specific pollutant removal, Lu et al. (2020) demonstrated an innovative approach for aniline-containing wastewater, where electrolysis not only produced hydrogen at the cathode with significantly lower energy consumption (due to aniline oxidation occurring at a lower potential than water oxidation at the anode) but also facilitated the

synthesis of valuable polyaniline, a conductive polymer, at the anode surface. This exemplifies a strategy where pollutant removal is coupled with the creation of a value-added product. For the treatment of wastewaters containing recalcitrant pharmaceuticals, such as antibiotic wastewater, electrochemical activation of peroxymonosulfate using specialized anodes like  $Ti/La_2O_3$ -PbO<sub>2</sub> has proven effective in enhancing the degradation of these persistent compounds through the generation of highly reactive sulfate and hydroxyl radicals (Yu et al., 2022). While the primary focus of such studies is often degradation, the electrochemical cell can be designed with appropriate cathodes for simultaneous hydrogen evolution.

Bioelectrochemical systems have also shown promise for various industrial effluents. Guerrero-Sodric et al. (2024) reported on a pilot-scale Microbial Electrolysis Cell (MEC) plant that successfully treated sugar industry wastewater, achieving enhanced biohydrogen production using Nifoam cathodes. Similarly, MECs have been effectively applied to treat highly complex effluents like post-hydrothermal liquefaction wastewater, which is generated during the production of biofuels from wet biomass, demonstrating removal of both organic matter and nitrogen along with hydrogen generation (Shen et al., 2018). While not strictly electrochemical, related biological processes like photofermentation have been utilized for hydrogen production from distillery wastewater, showcasing alternative routes for valorizing specific industrial organic waste streams (Laurinavichene et al., 2018). Furthermore, studies on the direct alkaline water electrolysis of various lowquality waters and pre-treated municipal/industrial wastewaters have highlighted the critical impact of impurities (such as turbidity and total dissolved solids) on hydrogen generation rates and the significant benefits of pre-treatment steps like ultrafiltration in improving process stability and efficiency (Chauhan & Ahn, 2023). The integrated Forward Osmosis-Alkaline Water Electrolysis system developed by Cassol et al. (2024) for treating municipal wastewater also stands out as a significant case study, demonstrating ultra-fast green hydrogen production by effectively decoupling water purification from electrolysis. These diverse case studies collectively underscore the adaptability and growing potential of electrochemical and related technologies to transform a wide spectrum of challenging wastewaters from environmental liabilities into valuable resources like hydrogen fuel, often achieving significant pollution abatement simultaneously.

# **Novel Electrolyzer Concepts for Impure Water Sources**

Research is ongoing into alternative electrolyzer designs that could be more robust for impure water. Separating HER and OER temporally or spatially, potentially using redox mediators, could allow for membraneless operation, which might be more tolerant to impurities and reduce costs (Slobodkin et al., 2024). Slobodkin et al. (2024) demonstrated a high-efficiency decoupled cycle in near-neutral electrolyte. As seen with Forward Osmosis AWE (Cassol et al., 2024), integrating membrane pre-treatment directly with the electrolysis unit in a strategical way can protect the electrolyzer while utilizing wastewater.

# **Bioelectrochemical and Photoelectrochemical Systems**

Bioelectrochemical systems (BES) and photoelectrochemical systems represent innovative approaches that leverage biological catalysis or solar energy, respectively, to drive wastewater treatment and hydrogen production. Microbial Electrolysis Cells (MECs) are a prominent type of BES where electroactive microorganisms at the anode oxidize organic matter present in wastewater, releasing electrons and protons (Guerrero-Sodric et al., 2024; Shen et al., 2018). With the application of a small external voltage, these electrons are driven to the cathode where they combine with protons to produce hydrogen gas (Odoi-Yorke et al., 2025). MECs thus offer the dual benefit of reducing the chemical oxygen demand (COD) of wastewater and generating biohydrogen (Chen et al., 2019). Recent developments in MEC technology include the optimization of electrode materials (e.g., the use of Nifoam cathodes to enhance hydrogen production rates from sugar industry wastewater, as reported by Guerrero-Sodric et al., 2024), advancements in reactor design for scaling up from laboratory to pilot plant operations, a deeper understanding of the microbial community dynamics within the anodic and strategies to suppress competing reactions such as methanogenesis, which consumes hydrogen (Shen et al., 2018). The environmental sustainability of MECs is also being assessed through life cycle analysis, as demonstrated by Chen et al. (2019) for a pilot-scale MEC treating urban wastewater. Furthermore, integrated biological systems, such as combining dark fermentation with MECs or microbial fuel cells (MFCs), are being explored to maximize resource recovery from wastewater (Estrada-Arriaga et al., 2021).

Photoelectrochemical (PEC) systems offer a direct route to convert solar energy into chemical energy in the form of hydrogen, potentially using wastewater as the electrolyte and source of water (Qureshi & Tahir, 2024). In a PEC cell, a semiconductor photoelectrode (either a photoanode for OER or a photocathode for HER) absorbs photons from sunlight, generating electronhole pairs that drive the water splitting reactions (Almohammedi et al., 2021; Hassan et al., 2024). The presence of organic pollutants in wastewater can sometimes be beneficial in PEC systems, as these organics may act as sacrificial electron donors, thereby lowering the energy barrier for the anodic oxidation reaction and enhancing the rate of cathodic hydrogen evolution, while simultaneously being degraded (Qureshi & Tahir, 2024). Research in

PEC systems is focused on developing highly efficient and stable photoelectrode materials, often based on metal oxides like TiO<sub>2</sub>, BiVO<sub>4</sub>, or CuO, and innovative heterostructures or surface modifications to improve light absorption, charge separation, and catalytic activity (Almohammedi et al., 2021; Karaca & Dincer, 2022). For instance, Almohammedi et al. (2021) investigated a nanoporous TiN/TiO<sub>2</sub>/Alumina membrane as a photoelectrode for hydrogen production from sewage water. Reactor design is also a critical aspect for PEC systems, aiming to maximize light harvesting, minimize mass transport limitations, and ensure efficient collection of gaseous products (Karaca & Dincer, 2022; Qureshi & Tahir, 2024).

# **Integrated and Hybrid System Approaches**

To enhance overall efficiency, reduce operational costs, and overcome the limitations of processes, significant research effort is being directed towards the development of integrated and hybrid systems that combine electrochemical wastewater treatment and hydrogen production with other complementary technologies. Membrane-assisted electrochemical systems are particularly prominent in this area. For example, the integration of Forward Osmosis (FO) with Alkaline Water Electrolysis has been demonstrated by Cassol et al. (2024) for ultra-fast green hydrogen production from municipal wastewater. In this system, FO is used to selectively extract high-purity water from wastewater into a concentrated potassium hydroxide (KOH) draw solution, which then directly serves as the electrolyte for the AWE unit, thereby protecting the electrolyser from wastewater contaminants and enabling high hydrogen production rates. Electrocatalytic Membrane Reactors (ECMRs) represent another innovative integrated approach, where the electrode itself is a catalytically active membrane, allowing for simultaneous pollutant degradation via flow-through electrooxidation/reduction and hydrogen recovery within a single compact unit (Yin et al., 2023). Yin et al. (2023) developed an ECMR with Co<sub>3</sub>O<sub>4</sub> nanoarrays on a Ti membrane that effectively degraded refractory organic pollutants like phenol and dyes while concurrently producing pure hydrogen.

Other hybrid concepts include coupling electrochemical processes with energy recovery or alternative energy input systems. Tufa et al. (2018) proposed an integrated system combining Reverse Electrodialysis (RED), a technology that harvests energy from salinity gradients (e.g., between two industrial streams of different salinity), with Alkaline Polymer Electrolyte Water Electrolysis (APWEL, a type of AEMWE) for hydrogen production, where the energy generated by RED could potentially power the electrolysis process. The direct use of renewable energy sources, such as solar photovoltaics (PV), to power electrochemical wastewater treatment and hydrogen production units is another key area of integration, offering a

pathway to completely green and sustainable operation (Pathak et al., 2020). Pathak et al. (2020) demonstrated such an integrated approach for treating textile wastewater, achieving both significant pollutant removal and efficient hydrogen generation using solar PV-powered electrolysis. Furthermore, innovative concepts such as electrochemical-thermochemical complementary hydrogen production systems are being explored to achieve more efficient utilization of the full solar spectrum by, for example, using photovoltaic electricity for electrolysis and solar thermal energy for high-temperature thermochemical reactions or to supply heat to SOECs, thereby enhancing overall solar-to-hydrogen conversion efficiency and enabling storage of intermittent solar energy (Fang et al., 2024; Horri & Ozcan, 2023).

#### **CHALLENGES**

Despite the significant advancements and the compelling potential of integrating electrochemical wastewater treatment with hydrogen production, the path towards widespread, economically viable, and robust industrial-scale implementation is still confronted by a range of multifaceted challenges. These hurdles can be broadly categorized into technical and material issues, economic and scalability barriers, and overarching environmental and sustainability concerns.

#### **Technical and Material Hurdles**

A primary set of challenges revolves around the performance and durability of materials used in electrochemical systems, particularly when exposed to the often harsh and complex matrices of real industrial wastewaters (Núñez et al., 2024). The long-term stability of electrode materials is a critical concern. Electrodes are subjected to corrosive ions (e.g., chlorides, sulfates), potentially extreme pH values, and the presence of various fouling agents including organic macromolecules, biofilms, and inorganic precipitates (Inocêncio et al., 2023; Horri & Ozcan, 2023). These conditions can lead to anode passivation (loss of catalytic activity), corrosion of both anode and cathode materials, leaching of active catalyst components, and physical fouling of electrode surfaces, all of which contribute to a decline in performance and a reduction in the operational lifetime of the electrochemical cell (Chauhan & Ahn, 2023). For instance, while advanced anode materials like Boron-Doped Diamond exhibit exceptional performance for pollutant mineralization, their high cost and potential brittleness can be limiting factors for large-scale applications (Inocêncio et al., 2023; Hassan et al., 2024). Similarly, while platinum group metals are highly efficient catalysts for

hydrogen evolution, their scarcity and high cost are significant drawbacks (Inocêncio et al., 2023).

In systems that employ membranes, such as divided electrolyzers (PEMWE, AEMWE), electrodialysis units, or membrane-based pre-treatment processes, membrane performance and longevity are crucial (Tufa et al., 2018; Ul Mulk et al., 2024). These membranes are susceptible to fouling by particulate matter, organic substances, and biological growth present in wastewater, which can lead to a decrease in flux (for separation membranes) or an increase in ohmic resistance and loss of ionic conductivity/selectivity (for ion-exchange membranes) (Sun et al., 2023). Chemical degradation of membrane materials due to exposure to aggressive chemicals (e.g., strong oxidants, extreme pH) or physical damage can also limit their operational lifespan, necessitating frequent cleaning or replacement and thereby increasing operational costs.

Achieving high process efficiency and selectivity is another major technical hurdle. Energy efficiency, often expressed as the amount of energy consumed per unit of pollutant removed or per unit of hydrogen produced (e.g., kWh/kg H<sub>2</sub>), is a critical factor for economic viability, especially when these technologies aim to compete with established wastewater treatment methods or conventional hydrogen production routes (Slobodkin et al., 2024). Energy losses in electrochemical systems arise from various sources, including electrode overpotentials (the extra voltage required beyond the thermodynamic potential to drive the HER and OER or pollutant oxidation/reduction at a practical rate), ohmic losses due to the resistance of the electrolyte, electrodes, and membrane, and energy consumed by parasitic side reactions (Inocêncio et al., 2023). Maximizing the Faradaic efficiency (also known as current efficiency) for the desired electrochemical reactions, pollutant reduction, or hydrogen evolution, by minimizing these parasitic side reactions is essential for optimizing both energy consumption and product yield (Pathak et al., 2020). Furthermore, ensuring selectivity in complex wastewater matrices can be challenging. For instance, achieving selective oxidation of target toxic pollutants without forming even more harmful or persistent intermediate byproducts, or producing high-purity hydrogen without co-contaminants from wastewater constituents, requires careful control over electrode materials, operating conditions, and reactor design (Núñez et al., 2024). Mass transport limitations can also impede process performance, especially when dealing with dilute pollutant concentrations or operating at high current densities. Ensuring efficient transport of reactant species from the bulk solution to the active sites on the electrode surface and the removal of products away from the electrode is crucial for maintaining high reaction rates and preventing concentration polarization (Yin et al., 2023). Finally, the inherent variability and complexity of real industrial wastewaters – which can differ significantly in terms of pollutant types and concentrations, pH, conductivity, temperature, and the presence of suspended solids or interfering ions – make it difficult to design universally applicable and robust electrochemical treatment systems. Each wastewater stream may require tailored pre-treatment strategies and optimized electrochemical process conditions (Chauhan & Ahn, 2023; Núñez et al., 2024).

### **Economic and Scalability Barriers**

Beyond the technical hurdles, significant economic and scalability barriers hinder the widespread industrial adoption of these technologies. The capital expenditure (CAPEX) for electrochemical systems can be substantial, particularly due to the cost of specialized reactors, advanced electrode materials (especially those utilizing precious metals or materials like BDD), high-performance membranes, and the balance-of-plant components (e.g., power supplies, pumps, control systems) (Ji & Wang, 2021; Agyekum et al., 2022). Operational expenditure (OPEX) is also a major consideration, often dominated by the cost of electricity required to drive the electrochemical reactions (unless very low-cost renewable electricity is readily available), as well as costs associated with electrode and membrane replacement, chemical consumption (e.g., for pH adjustment or electrolyte addition), and labor for operation and maintenance (Faye et al., 2022). These combined costs can make electrochemical wastewater treatment and hydrogen production economically uncompetitive compared to conventional, well-established treatment methods or traditional hydrogen production routes like steam methane reforming, especially if the value of the produced hydrogen or the avoided cost of conventional treatment does not sufficiently offset these expenditures.

Scaling-up promising laboratory-scale results to reliable, efficient, and cost-effective industrial-scale operations is another major challenge (Faye et al., 2022). Issues that may be manageable at the lab bench, such as uniform current and potential distribution across electrodes, heat management, gas bubble effects, and long-term material stability, can become significantly more complex and difficult to address in large-scale reactors (Ju et al., 2024). Robust engineering design, process optimization for large volumes and flow rates, and the development of modular approaches that allow for flexible scaling are crucial for successful industrial implementation. Furthermore, the lack of standardized designs, performance metrics, and testing protocols across different studies and technologies can make it difficult to objectively compare the efficacy and cost-effectiveness of various electrochemical approaches, which can hinder investment and commercial adoption by industry.

# **Environmental and Sustainability Concerns**

electrochemical wastewater treatment and hvdrogen production offer significant environmental benefits, a holistic assessment of their overall environmental and sustainability footprint is crucial. A comprehensive Life Cycle Assessment (LCA) is necessary to evaluate the true environmental impact from cradle to grave (Chen et al., 2019; Ji & Wang, 2021). This includes considering the primary energy source for electrolysis; for the produced hydrogen to be truly "green" and for the treatment process to be environmentally advantageous, the electricity consumed must be derived from renewable sources (Hassan et al., 2024). The LCA must also account for the embodied energy and environmental impact associated with the manufacturing of electrode and membrane materials, some of which (e.g., precious metals, fluorinated polymers for membranes) can be resourceintensive or involve environmentally challenging production processes. The potential formation of hazardous byproducts during the electrochemical treatment of complex wastewaters, such as chlorinated organic compounds if chloride ions are present and active chlorine is generated, or other partially oxidized intermediates, needs careful monitoring and management to avoid simply transforming one environmental problem into another (Núñez et al., 2024). The end-of-life management of system components, including spent electrodes, degraded membranes, and any residual sludges or concentrated waste streams generated during pre-treatment or the electrochemical process itself, also needs to be addressed sustainably (Odoi-Yorke et al., 2025).

Effective water resource management is another important consideration. While utilizing wastewater as a resource for hydrogen production can alleviate the demand for pure freshwater sources, the overall water balance of the process, the quality of the final effluent discharged after treatment (which must meet regulatory standards), and the long-term sustainability of water sourcing for very large-scale hydrogen production still require careful assessment and planning (Simoes et al., 2021). Finally, the resource intensity of some advanced materials used in catalysts and membranes, which may rely on scarce, critically sourced, or geopolitically sensitive elements, raises concerns about long-term availability, supply chain risks, and the potential for resource depletion if these technologies are deployed on a massive scale. Developing materials based on more abundant and sustainably sourced elements is therefore a key aspect of ensuring the long-term sustainability of these electrochemical approaches.

#### RESULTS AND DISCUSSION

The electrochemical treatment of industrial wastewater coupled with the simultaneous production of hydrogen represents a highly promising and innovative technological pathway that directly addresses the critical global imperatives of environmental remediation and the transition to sustainable energy. This review has systematically explored the fundamental principles underpinning hydrogen as an energy carrier, the diverse array of production methods, and has particularly focused on the intricacies of electrochemical and related bio/photo-electrochemical processes tailored for the valorization of challenging industrial effluents. Through a detailed examination of pollutant degradation mechanisms, advanced reactor configurations, the pivotal role of material science in electrode and membrane development, the adaptation of various electrolysis technologies for wastewater feedstocks, recent cutting-edge scientific and engineering developments, and illustrative case studies, the significant potential of these synergistic approaches has been clearly elucidated. The capacity to transform problematic industrial wastewaters from environmental liabilities into valuable resources like green hydrogen, while concurrently mitigating their polluting impact, strongly resonates with the core tenets of a circular economy and offers a tangible contribution towards achieving global sustainable development goals.

Despite the considerable advancements and the compelling conceptual advantages, the journey towards widespread, economically viable, and robust industrial-scale implementation of these integrated technologies is still confronted by substantial technical, economic, and environmental hurdles. Critical challenges persist in areas such as the development of low-cost, highly durable, and exceptionally efficient electrode and membrane materials capable of sustained performance in complex and often aggressive wastewater matrices. Furthermore, issues related to the scalability of these systems from laboratory prototypes to industrial installations, the optimization of overall energy efficiency, the necessity for often extensive wastewater pretreatment, and the complexities of system integration demand continued and intensified research and engineering efforts.

Future research must be strategically directed towards several key areas. These include a relentless pursuit of novel materials with superior catalytic activity, enhanced stability, and lower manufacturing costs; the design and engineering of innovative reactor configurations that optimize mass transport phenomena, current distribution, and gas management for improved efficiency and compactness; and the development of intelligent, adaptive process control strategies capable of handling the inherent variability of real industrial wastewater streams. Moreover, rigorous techno-economic analyses and comprehensive life cycle assessments, grounded in data from

pilot-scale and demonstration projects operating under realistic industrial conditions, are indispensable for guiding research priorities, validating technological feasibility, and informing supportive policy frameworks.

In conclusion, although the path ahead necessitates overcoming considerable challenges, the prospects for electrochemical treatment of industrial wastewater and concurrent hydrogen production are remarkably promising. Driven by the unceasing global demand for cleaner water and sustainable energy, and fueled by continuous innovation in materials science, electrochemical engineering, biotechnology, and systems integration, these advanced technologies are poised to transition from promising research avenues into cornerstone solutions for environmentally sound industrial practices and contributors to the rapidly evolving global hydrogen economy.

#### REFERENCES

- Agyekum, E. B., Nutakor, C., Agwa, A. M., & Kamel, S. (2022). A Critical Review of Renewable Hydrogen Production Methods: Factors Affecting Their Scale-Up and Its Role in Future Energy Generation. *Membranes*, 173.
- Ahmad, A., & Yadav, A. K. (2024). Parametric analysis of wastewater electrolysis for green hydrogen production: A combined RSM, genetic algorithm, and particle swarm optimization approach. *International Journal of Hydrogen Energy*, 51-62.
- Akpasi, S. O., Anekwe, I. M., Tetteh, E. K., Amune, U. O., Mustapha, S. I., & Kiambi, S. L. (2025). Hydrogen as a clean energy carrier: advancements, challenges, and its role in a sustainable energy future. *Clean Energy*, 52-88.
- Almohammedi, A., Shaban, M., Mostafa, H., & Rabia, M. (2021). Nanoporous TiN/TiO2/Alumina Membrane for Photoelectrochemical Hydrogen Production from Sewage Water. *Nanomaterials*, 2617.
- Cassol, G. S., Shang, C., An, A. K., Khanzada, N. K., Ciucci, F., Manzotti, A., . . . Ling, L. (2024). Ultra-fast green hydrogen production from municipal wastewater by an integrated forward osmosis-alkaline water electrolysis system. *Nature Communications*, 2617.
- Chauhan, D., & Ahn, Y.-H. (2023). Alkaline electrolysis of wastewater and low-quality water. *Journal of Cleaner Production*, 136613.
- Chen, J., Xu, W., Wu, X., E, J., Luo, N., Wang, T., & Zuo, H. (2019). System development and environmental performance analysis of a pilot scale microbial electrolysis cell for hydrogen production using urban wastewater. *Energy Conversion and Management*, 52-63.
- Cho, K., & Hoffmann, M. R. (2017). Molecular hydrogen production from wastewater electrolysis cell with multi-junction BiOx/TiO2 anode and stainless steel

- cathode: Current and energy efficiency. *Applied Catalysis B: Environmental*, 671-682.
- de Araujo, D. M., Barbosa Segundo, I. D., Cardozo, J. C., Santos, J. E., Nascimento, J. H., Gondim, A. D., . . . Martínez-Huitle, C. A. (2024). Produced water electrolysis with simultaneous green H2 generation: From wastewater to the future of the energetic industry. *Fuel*, 132369.
- Do, H. H., Tran, N. T., Tran, V. V., Le, T. H., Nguyen, T. V., Truong, Q. D., & Nguyen, V. C. (2025). Recent advancements and perspectives in MoO2-based heterostructures for electrochemical hydrogen evolution reaction. *International Journal of Hydrogen Energy*, 234-247.
- Estrada-Arriaga, E. B., Hernández-Romano, J., Mijaylova-Nacheva, P., Gutiérrez-Macías, T., & Morales-Morales, C. (2021). Assessment of a novel single-stage integrated dark fermentation-microbial fuel cell system coupled to proton-exchange membrane fuel cell to generate bio-hydrogen and recover electricity from wastewater. *Biomass and Bioenergy*, 106016.
- Fang, J., Yang, M., Dong, X., Luo, T., Pan, C., Liu, Z., . . . Wang, H. (2024). Electrochemical-thermochemical complementary hydrogen production system for efficient full-spectrum solar energy storage. *Thermal Science and Engineering Progress*, 102501.
- Faye, O., Szpunar, J., & Eduok, U. (2022). A critical review on the current technologies for the generation, storage, and transportation of hydrogen. *International Journal of Hydrogen Energy*, 13771-13802.
- Guerrero-Sodric, O., Baeza, J. A., & Guisasola, A. (2024). Enhancing bioelectrochemical hydrogen production from industrial wastewater using Ni-foam cathodes in a microbial electrolysis cell pilot plant. *Water Research*, 121616.
- Hassan, N., Jalil, A., Rajendran, S., Khusnun, N., Bahari, M., Johari, A., . . . Ismail, M. (2024). Recent review and evaluation of green hydrogen production via water electrolysis for a sustainable and clean energy society. *International Journal of Hydrogen Energy*, 420-441.
- Horri, B. A., & Ozcan, H. (2023). Green hydrogen production by water electrolysis: Current status and challenges. Current Opinion in Green and Sustainable Chemistry, 100825.
- Inocêncio, C. V., Holade, Y., Morais, C., Kokoh, K. B., & Napporn, T. W. (2023). Electrochemical hydrogen generation technology: Challenges in electrodes materials for a sustainable energy. *Electrochemical Science Advances*, e2100206.
- Ji, M., & Wang, J. (2021). Review and comparison of various hydrogen production methods based on costs and life cycle impact assessment indicators. *International Journal of Hydrogen Energy*, 38612-38635.

- Ju, H., Yoon, D., Bong, S., & Lee, J. (2024). Challenge and opportunity in scaling-up hydrogen production via electrochemical ammonia electrolysis process. *Current Opinion in Electrochemistry*, 101424.
- Karaca, A. E., & Dincer, I. (2022). New Photoelectrochemical Reactor for Hydrogen Generation: Experimental Investigation. *Industrial & Engineering Chemistry Research*, 12448-12457.
- Karadag, D., Köroğlu, O. E., Ozkaya, B., Cakmakci, M., Heaven, S., & Banks, C. (2014). A review on fermentative hydrogen production from dairy industry wastewater. *Journal of Chemical Technology & Biotechnology*, 789-801.
- Laurinavichene, T., Tekucheva, D., Laurinavichius, K., & Tsygankov, A. (2018). Utilization of distillery wastewater for hydrogen production in one-stage and two-stage processes involving photofermentation. *Enzyme and Microbial Technology*, 1-7.
- Liu, W., Zheng, X., Feng, Y., Ying, Z., Wang, B., & Dou, B. (2023). Prediction and optimization of hydrogen-rich gas production from sewage sludge via a combined process of hydrothermal carbonization, pyrolysis, and reforming. *Energy Conversion and Management*, 117462.
- Lu, S., Zhao, B., Chen, M., Wang, L., Fu, X.-Z., & Luo, J.-L. (2020). Electrolysis of waste water containing aniline to produce polyaniline and hydrogen with low energy consumption. *International Journal of Hydrogen Energy*, 22419-22426.
- Núñez, R., Merayo, N., Hermosilla, D., Gascó, A., Dos santos-García, A. J., & Caravaca, Á. (2024). Electrochemical treatment of industrial wastewater for hydrogen production. *Current Opinion in Electrochemistry*, 101418.
- Odoi-Yorke, F., Agyekum, E. B., Tahir, M., Abbey, A. A., Jangir, P., Rashid, F. L., . . . Mbasso, W. F. (2025). Review of the trends, evolution, and future research directions of green hydrogen production from wastewaters Systematic and bibliometric approach. *Energy Conversion and Management: X*, 100822.
- Pathak, A. K., Kothari, R., Tyagi, V., & Anand, S. (2020). Integrated approach for textile industry wastewater for efficient hydrogen production and treatment through solar PV electrolysis. *International Journal of Hydrogen Energy*, 25768-25782.
- Qureshi, F., & Tahir, M. (2024). Photoelectrochemical water splitting with engineering aspects for hydrogen production: Recent advances, strategies and challenges. *International Journal of Hydrogen Energy*, 760-776.
- Simoes, S. G., Catarino, J., Picado, A., Lopes, T. F., di Berardino, S., Amorim, F., . . . Ponce de Leão, T. (2021). Water availability and water usage solutions for electrolysis in hydrogen production. *Journal of Cleaner Production*, 128124.
- Slobodkin, I., Davydova, E., Sananis, M., Breytus, A., & Rothschild, A. (2024). Electrochemical and chemical cycle for high-efficiency decoupled water splitting in a near-neutral electrolyte. *Nature Materials*, 446-453.

- Sun, W., Xu, Q., Yang, S., Liu, S., Sayed, M., Mousset, E., & Zhao, C. (2023). Cathodic membrane–based electrochemical redox process for water treatment: a review. *Current Opinion in Chemical Engineering*, 100960.
- Tezcan Ün, Ü., Koparal, A. S., & Bakır Öğütveren, Ü. (2009). Hybrid processes for the treatment of cattle-slaughterhouse wastewater using aluminum and iron electrodes. *Journal of Hazardous Materials*, 580–586.
- Tezcan Ün, Ü., Uğur, S., Koparal, A. S., & Bakır Öğütveren, Ü. (2006). Electrocoagulation of olive mill wastewaters. *Separation and Purification Technology*, 136–141.
- Thirugnanasambandham, K., Parameswari, E., Sebastian, S. P., & Krishnan, R. (2025). Advancements in green hydrogen (GH2) recovery from industrial wastewater: A comprehensive review. *Desalination and Water Treatment*, 100966.
- Tufa, R. A., Hnát, J., Němeček, M., Kodým, R., Curcio, E., & Bouzek, K. (2018). Hydrogen production from industrial wastewaters: An integrated reverse electrodialysis - Water electrolysis energy system. *Journal of Cleaner Production*, 418-426.
- Ul Mulk, W., Aziz, A. R., Ismael, M. A., Ghoto, A. A., Ali, S. A., Younas, M., & Gallucci, F. (2024). Electrochemical hydrogen production through anion exchange membrane water electrolysis (AEMWE): Recent progress and associated challenges in hydrogen production. *International Journal of Hydrogen Energy*, 1174-1211.
- Yin, Z., Zhang, K., Ma, N., Liu, X., Yin, Z., Wang, H., . . . Ma, D. (2023). Catalytic membrane electrode with Co3O4 nanoarrays for simultaneous recovery of water and generation of hydrogen from wastewater. *Science China Materials*, 651-663.
- Yoon, D., Chung, S., Choi, M., Yang, E., & Lee, J. (2024). 100 W-class green hydrogen production from ammonia at a dual-layer electrode containing a Pt-Ir catalyst for an alkaline electrolytic process. *Journal of Energy Chemistry*, 352-360.
- Yu, S., Zhang, R., Dang, Y., Zhou, Y., & Zhu, J.-J. (2022). Electrochemical activation of peroxymonosulfate at Ti,La2O3-PbO2 anode to enhance the degradation of typical antibiotic wastewater. *Separation and Purification Technology*, 121164.
- Zhan, J., Yao, Y., & Wang, X. (2025). Electrochemical technologies for sustainable agricultural water treatment and resource recovery. *International Journal of Electrochemical Science*, 101029